The environments and progenitors of extreme supernovae in the low-redshift universe

by

Kirsty Taggart

A thesis submitted in partial fulfilment of the requirements of

Liverpool John Moores University

for the degree of

Doctor of Philosophy

July 2020

Declaration

The work presented in this thesis was carried out at the Astrophysics Research Institute, Liverpool John Moores University. Unless otherwise stated, it is the original work of the author.

Some of the photometry in Table 2.4 was reduced by Dan Perley and the implementation of the ZTF-marshal interface presented within Chapter 3.4 was aided by Ashot Bagdasaryan.

While registered as a candidate for the degree of Doctor of Philosophy, for which submission is now made, the author has not been registered as a candidate for any other award. This thesis has not been submitted in whole, or in part, for any other degree.

NOVEMBER 29, 2020

Abstract

Core-collapse supernovae (CCSNe) are the explosive endpoints of massive ($>8\,\mathrm{M_\odot}$) stars that manifest as a bright optical display that lasts for a period of weeks to several months, leaving behind a stellar-mass black hole or a neutron star corpse.

Currently supernova science is in a phase of unprecedented activity and productivity, with a new generation of wide-field survey telescopes that scan the entire night sky every few days. As a result, we have begun to discover huge diversity in the observational and physical explosion properties of supernovae that do not neatly fit into the standard classification scheme derived nearly a century ago. Some supernovae produce relativistic jets and are accompanied by long-duration gamma-ray bursts (LGRBs), and superluminous supernovae (SLSNe) have radiated luminosities that exceed CCSNe by an order of magnitude, suggesting an energetic and poorly understood explosion mechanism.

In this thesis, I take advantage of new unbiased supernova samples to provide insights into the explosive endpoints of massive stars through their host galaxy environments. I use public imaging surveys to gather multi-wavelength photometry for a spectroscopically-complete sample of 150 CCSN host galaxies from the All-Sky Automated Survey for Supernovae (ASAS-SN) and fit the resulting spectral energy distributions (SEDs) to derive stellar masses and integrated star formation rates. I find that 33^{+4}_{-4} per cent of CCSNe take place in dwarf galaxies (stellar mass, $M_* < 10^9\,\mathrm{M_\odot}$) and 2^{+2}_{-1} per cent in dwarf starburst galaxies (specific star formation rate, sSFR $> 10^{-8}$ yr^{-1}).

CCSNe provide a census of all massive star formation. Thus, this new CCSN

catalogue is an ideal 'control' sample to compare with exotic supernovae (SLSNe and LGRBs) at low redshift. I reanalyse SLSN and LGRB hosts from the literature (out to $z < 0.3$) in a homogeneous way to compare against the CCSN host sample. I conclude that the relative SLSN-I to CCSN supernova rate is increased in low-mass galaxies and at high specific star formation rates. These parameters are strongly covariant, and it was not possible to securely identify which factor (low mass or high sSFR) was more strongly associated with an enhanced SLSN or LGRB rate.

In addition, I present my work to help to build future supernova catalogues with the Zwicky Transient Facility (ZTF), including the Bright Transient and Superluminous Supernova surveys. I have integrated the Liverpool Telescope with ZTF which allows follow-up spectroscopy and photometry to be requested and reduced via an automated reduction and image-subtraction pipeline. These new transient catalogues will be larger, and they will provide better control of systematics, enabling detailed future studies.

KIRSTY TAGGART   NOVEMBER 29, 2020

Publications

In the course of completing the work presented in this thesis, the following paper has been submitted for publication in a refereed journal:

1. *Core-collapse, superluminous, and gamma-ray burst supernova host galaxy populations at low redshift: the importance of dwarf and starbursting galaxies*
   Taggart, K. & Perley, D. A., 2020, MNRAS, submitted

Whilst writing this thesis, K. Taggart has also contributed to the following publications, which are focused on topics related to this thesis work:

1. *A nearby super-luminous supernova with a long pre-maximum & "plateau" and strong C II features*
   Anderson, J. P., Pessi, P. J., Dessart, L., Inserra, C., Hiramatsu, D., **Taggart, K.**, et al., 2018, A&A, 620, A67

2. *The fast, luminous ultraviolet transient AT2018cow: extreme supernova, or disruption of a star by an intermediate-mass black hole?*
   Perley, D. A., Mazzali, P. A.; Yan, L., Cenko, S. B; Gezari, S., **Taggart, K.**, et al., 2019, MNRAS, 484, 1031

3. *The Zwicky Transient Facility Bright Transient Survey I: Spectroscopic Classification and the Redshift Completeness of Local Galaxy Catalogs*
   Fremling, U. C., Miller, A. A., Sharma, Y., Dugas, A., Perley, D. A., **Taggart, K.**, et al., 2020, ApJ, 895, 32

4. *Host Galaxies of Type Ic and Broad-lined Type Ic Supernovae from the Palomar Transient Factory: Implication for Jet Production*
Modjaz, M. et al. (inc. **Taggart, K.**), 2020, ApJ, 892, 153

5. *Four (Super)Luminous Supernovae From the First Months of the ZTF Survey*
Lunnan, R., Yan, L., Perley, D. A., Schulze, S., **Taggart, K.**, et al., ApJ, 901, 61

6. *Seventeen Tidal Disruption Events from the First Half of ZTF Survey Observations: Entering a New Era of Population Studies*
van Velzen, S., Gezari, S., Hammerstein, E., Roth, N.; Frederick, S., Ward, C., Hung, T., Cenko, S. B., Stein, R., Perley, D. A., **Taggart, K.**, et al., ApJ, submitted

7. *GROWTH on GW190425: Searching thousands of square degrees to identify an optical or infrared counterpart to a binary neutron star merger with the Zwicky Transient Facility and Palomar Gattini IR*
Coughlin M. W., et al. (inc. **Taggart, K.**), 2019, ApJ, 885, L19

8. *GROWTH on S190814bv: Deep Synoptic Limits on the Optical/Near-Infrared Counterpart to a Neutron Star-Black Hole Merger*
Andreoni I., et al. (inc. **Taggart, K.**), 2020, ApJ, 890, 131

9. *ZTF Early Observations of Type Ia Supernovae I: Properties of the 2018 Sample*
Yao Y., et al. (inc. **Taggart, K.**), 2019, ApJ, 886, 152

10. *Early Ultra-Violet observations of type IIn supernovae constrain the asphericity of their circumstellar material*
Soumagnac, M. T., et al. (inc. **Taggart, K.**), ApJ, 889, 51

11. *A high-energy neutrino coincident with a tidal disruption event*
Stein R., et al. (inc. **Taggart, K.**), Nature Astronomy, submitted

12. *SN2020bvc: a Broad-lined Type Ic Supernova with a Double-peaked Optical Light Curve and a Luminous X-ray and Radio Counterpart*
Ho, A. Y. Q., et al. (inc. **Taggart, K.**), ApJ, 902, 22

13. *Kilonova Luminosity Function Constraints based on Zwicky Transient Facility Searches for 13 Neutron Star Mergers*
Kasliwal, M. M., et al. (inc. **Taggart, K.**), ApJ, submitted

14. *Helium-rich Superluminous Supernovae from the Zwicky Transient Facility*
Yan, L., Perley, D., Schulze, S., Lunnan, R., Sollerman, J., De, K., Chen, Z., Fremling, C., Gal-Yam, A., **Taggart, K.**, et al., ApJ, 902, 8

Kirsty Taggart   November 29, 2020

Acknowledgements

First and foremost, I would like to thank my supervisor, Dan Perley, for being a terrific advisor. He has been a patient and inspiring mentor throughout my studies, demonstrating what a brilliant and hard-working scientist can achieve.

I have really enjoyed working on my PhD at the Astrophysics Research Institute. The department is very friendly and welcoming, and it has been such a privilege to interact with so many inspiring scientists. Specifically, thank you to Shiho, who went above and beyond to arrange funding to cover my international fees. I will be forever grateful for this opportunity.

Thank you to Anna, Danielle, Caroline and Maureen (the lifeblood of the ARI) for keeping the department running so seamlessly. Thanks also to Stuart, Dan, and Ben for providing invaluable technical help, including when water cascaded down (like a waterfall) onto my laptop during write up. You really can't make these things up! I am also fortunate to have worked with such lovely office mates (Jon, Seb, Egidijus, Hannah, Silvia and Maisie). One of my highlights was taking some of you to see the Manx wallabies. Finally, thanks to Phil, whose daily department e-mails brightened my day during COVID lockdown when this thesis was written.

Thank you to Janet Chen and Patricia Shady for arranging for me to observe at the MPE telescope. It was a unique and unforgettable experience. Thank you to the ZTF team for letting me join such a stimulating and exciting project. Particularly thanks to Mansi Kasliwal and Christoffer Fremling for supporting me to visit Caltech – it was a real privilege.

I am grateful to have had many great friendships throughout my life. Silvia, I dearly miss our numerous (and much needed) coffee trips! Thanks to Dan for the Sunday writing sessions and excellent lunches out, which made the process of job applications a whole lot more bearable. Thanks to my co-COVID compadre Seb for the motivational calls during lockdown/write-up. You were exceptionally tolerant when my main topic of conversation was my varied attempts to block the Sun from overheating my flat.

To Emmy, my oldest friend – I always look forward to visiting the Isle of Man when you're around. To my other Manx friends Abi, Hayley and Robert, we will always be the four musketeers. You have been amazing friends throughout my life, and for that, I am very grateful. To Emily (PA galaxy), who I have known from our undergrad years at Sheffield. Ever since we were lab partners in second year, our friendship has truly blossomed. We have been through so much together (Australia, travelling, exam revision, our Master's project, and embarking on this PhD journey). I am lucky to have done it all alongside you –you are a true inspiration.

Finally, it is with deep gratitude that I thank my parents, brother and boyfriend, for their unconditional love and unwavering support. To my Aunty 'Tatty', you've been such a big part of my life, and I can always rely on you to make me a bit silly. I simply could not have done this without you all. And, to my Grandad, Harry, who first showed me what true passion for a subject and that the world (and in this case, the Universe) is full of exciting problems waiting to be explored. I really wish you were here to read this ♡.

Kirsty Taggart   November 29, 2020

Contents

List of Tables

List of Figures

Chapter 1

Introduction

1.1 The lives of massive stars

1.1.1 Birth

Giant clouds of gas and dust (10^3–10^6 M$_\odot$) are the birth sites of stars. Their high column densities shield them from incoming cosmic rays and interstellar radiation, and without these heating sources, the clouds remain extremely cool (tens of Kelvin). This allows the hydrogen (and small amounts of other species) to exist in a molecular form in giant molecular clouds. Turbulent motions inside these molecular clouds cause them to fragment into self-gravitating pre-stellar cores of roughly $\sim$1 M$_\odot$. These cores individually undergo collapse to form single stars or more commonly binary or low-number multiple star systems (Duchêne & Kraus, 2013).

The distribution function of *individual* stellar masses within a newly formed stellar cluster is governed by the initial mass function (IMF). It is worth noting that the mass distribution will be altered as stars evolve, especially if they suffer significant mass-loss in their evolution. The first empirical parametrisation of the IMF was done by Salpeter (1955) for stars in the solar neighbourhood. The number

of stars that form within a given mass range, $\xi(m)dm$, takes the form of a power law:

$$\xi(m) \propto \left(\frac{m}{M_\odot}\right)^\alpha \qquad (1.1)$$

Where $\alpha=-2.35$ for the Salpeter (1955) slope.

Nowadays the most commonly adopted models are the Kroupa (2001) three-part power-law extension to the Salpeter (1955) IMF and the Chabrier (2003) log-normal IMF (see Fig. 1.1 for a schematic).[1] In galactic-field studies, the shape of the IMF is observed to be universal (Bastian et al., 2010). However, the upper mass limit ($\sim$150 M$_\odot$; Figer, 2005; Koen, 2006) is observationally challenging to constrain, and it is unclear whether this mass cut is statistical or perhaps physical in nature.

For example, there are some indications from resolved studies that the 30 Doradus region in the Large Magellanic Cloud (LMC) can form stars with stellar masses between 100–300 M$_\odot$ (Crowther et al., 2016). There have also been hints the IMF may vary in different extragalactic environments. For example, with redshift, star-formation rate such as a top-heavy IMF in starburst galaxies, or metallicity (e.g. Weidner et al., 2011; Hopkins, 2018).

The IMF shape suggests that the overwhelming majority of stars are low-mass (0.1–0.5 M$_\odot$). Below the low-mass stellar boundary ($<$0.1 M$_\odot$) are sub-stellar brown dwarfs, which span a mass range between about 0.01–0.08 M$_\odot$. Brown dwarfs never attain a high enough central temperature to fuse hydrogen, but are often included in IMF estimates. The number of stars by mass drops rapidly (seemingly as a power law). This means that massive stars ($>$8 M$_\odot$) that explode as supernovae are exceedingly rare – they make up less than $\sim$1 per cent of all stars formed within the star cluster. In addition, massive stars correspond to the upper tail of the power-law stellar mass distribution, therefore very high-mass

---

[1]For the purposes of this thesis, I will use the Chabrier (2003) initial mass function.
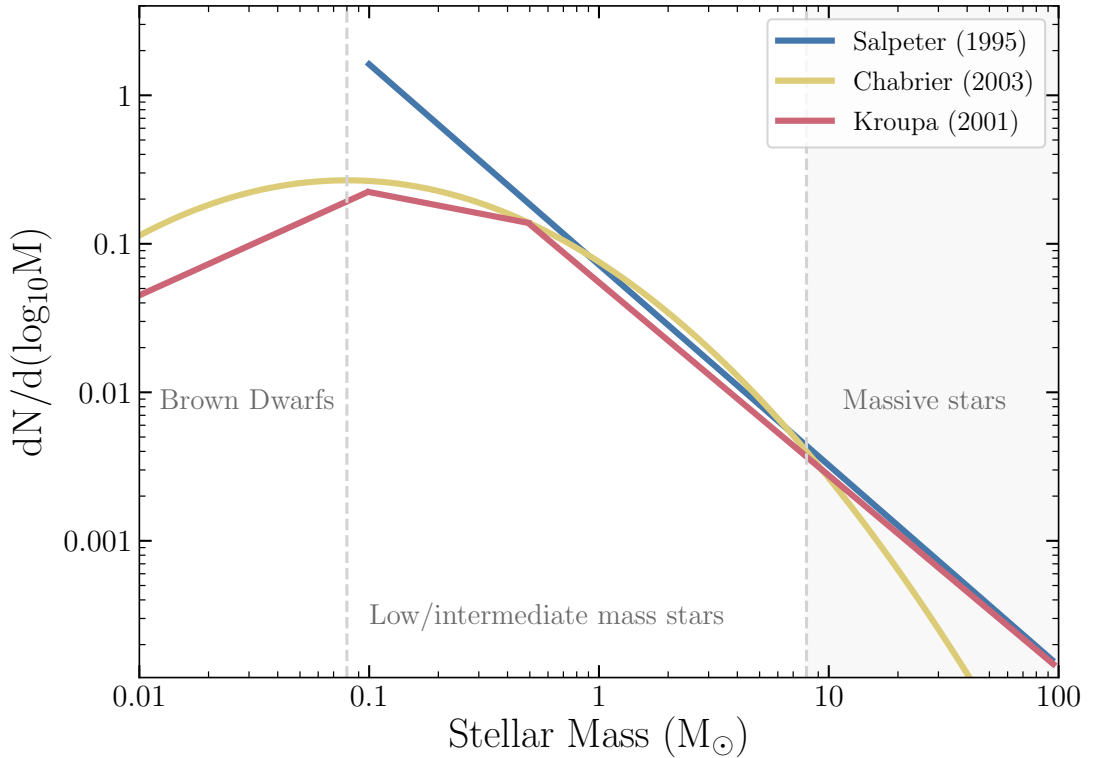
Figure 1.1: A schematic with common parameterisations of the IMF. The Salpeter (1955) slope (α=–2.35) is in blue, three-part power-law (Kroupa, 2001) in pink (α =–0.3,α =–1.3,α =–2.3) and the Chabrier log-normal turnover (Chabrier, 2003) in yellow.

early O-type stars ($\sim$32–128 M$_\odot$) are even rarer than early B-type stars ($\sim$8–16 M$_\odot$) (Zinnecker & Yorke, 2007).

Even though most stars in the Universe are low-mass ($<$0.5 M$_\odot$), the luminosity output of a newly formed stellar cluster is dominated by high-mass stars. From birth, high-mass stars will strongly influence their environment, and this has strong implications on the star formation process. Once one (or more) massive O or early B-type stars have formed within their parent molecular cloud, they will begin to emit huge amounts of UV radiation, which in turn photoionises their local molecular hydrogen environment. Photoionisation reduces the amount of neutral hydrogen available for star formation and creates an H II region of ionised hydrogen concentrated around the massive star. The ionising UV radiation together with mechanical stellar winds and outflows from massive stars will expel any remaining gas that has not already formed stars (on a timescale comparable

to the massive star lifetime) and ultimately destroy, or at least disrupt, the parent molecular cloud, stopping the star formation process (e.g. Whitworth, 1979). In this thesis, I will concentrate on the most massive stars (>8 M$_\odot$), which undergo dramatic evolution, ending their lives in the explosions we call supernovae.

1.1.2 Evolution[2]

Independent of their initial mass, all stars spend the majority ($\sim$90 per cent) of their lifetime on the Main Sequence (MS). During this phase, they fuse hydrogen to helium in their stellar core at temperatures exceeding 10^7 K. This nuclear fusion reaction results in a small change of mass (the mass of helium is less than the sum of the masses of four individual hydrogen nuclei), and by the Einstein mass-energy relation, this mass difference is released as energy. The thermal energy released by fusion will balance the inward force of the star's self-gravity, allowing the star to remain in hydrostatic equilibrium during the MS.

A star's initial mass governs its time spent in this early evolutionary phase. Empirically, for the majority of stars the luminosity of a star (L) on the MS scales with the initial mass (M) as approximately L$\sim$M$^{3.5}$ (e.g. Harwit, 1988). The lifetime of a star is the ratio of the amount of fuel (stellar mass) versus the rate at which it burns its fuel (i.e., its luminosity); therefore the MS lifetime can be approximated to $\tau_{\mathrm{MS}}\sim$ M$^{-2.5}$. Somewhat paradoxically, this means that low and intermediate-mass stars (<8 M$_\odot$) spend longer in this phase and have much longer lives than massive stars. A star like our Sun (1 M$_\odot$) will remain on the MS for approximately 10 billion years, whereas a massive star will spend a small fraction of this time on the MS – only a few tens of millions of years, or even less.[3]

---

[2]This chapter is based on single-star evolutionary theory. However, binary interactions play an important role in the evolution of massive stars. Sana et al. (2012) find that almost three-quarters of massive stars will interact (be stripped by, accrete mass from, or merge) with a nearby companion star prior to core-collapse.

[3]It is important to note that in massive stars exceeding $\sim$20 M$_\odot$ the mass–luminosity relation flattens due to the increased radiation pressure relative to gas pressure. This sets a minimum stellar lifetime of $\sim$2 Myrs even for *very* high mass (200–500 M$_\odot$) stars (Yusof et al., 2013).

For stars more massive than 1.3 $M_\odot$, the temperature in the star's core exceeds $\sim 1.4 \times 10^7$ K. Therefore, the carbon, nitrogen and oxygen (CNO) cycle is the dominant nuclear reaction in the MS phase (whereas the proton–proton chain is dominant for stars with masses less than about 1.1 $M_\odot$). The CNO cycle gives rise to a series of reactions that convert hydrogen to helium with the help of carbon, nitrogen, and oxygen acting as catalysts. The CNO cycle depends strongly on temperature ($\propto T^{17}$), so the reactions are centrally concentrated, and a steep temperature gradient makes the core fully convective. Convection brings new hydrogen fuel into the core and disperses the newly-formed helium throughout the core (for extensive reviews on the pre-supernova evolution of massive stars see Burbidge et al. 1957; Weaver et al. 1978; Woosley et al. 2002; Heger et al. 2005).

Outside the core, the temperature is too low to burn hydrogen, so when a MS star has exhausted the hydrogen in its core, hydrogen-burning stops altogether. The loss of energy generation causes the star to move out of hydrostatic equilibrium and slowly contract, increasing the central density and pressure. In turn, this will cause another phase of hydrogen burning in a shell around the core boundary. The shell gradually burns its way outwards into fresh fuel, and the star does not collapse because the overlying hydrogen-burning shell maintains its temperature. The star evolves off the MS and usually becomes a hydrogen-rich red supergiant (RSG) for massive stars with initial stellar masses between 8–25 $M_\odot$. For very massive stars (>25–500 $M_\odot$), they do not become a RSG, but undergo a brief period of intensive mass loss, losing their outer hydrogen envelope to become a WR star (Wolf & Rayet, 1867). WR stars have strong mass-loss rates ($\sim 10^{-5}$ $M_\odot\,yr^{-1}$; Nugis & Lamers, 2000) from stellar winds.

The temperature in the stellar core soon becomes hot enough to fuse helium into carbon. Unlike low-mass stars, fusion does not stop after core helium fusion, and the star begins a complex evolutionary pathway.[4] A series of burning episodes

---

[4]Here I refer the reader to Chapter 1.3.1 which discusses the fate of very massive stars (>130 $M_\odot$) at low-metallicity. These stars are theorised to undergo explosive carbon burning during their evolution, leading to the complete disruption of the star as a Pair Instability SN and

occurs where one element is burned in the core, while the ashes of the various burning stages are burned in successive shells surrounding the core. Each burning episode becomes shorter and shorter as lighter elements are fused into heavier elements, ultimately culminating in core silicon burning to form iron (^{56}Fe) in the core. However, ^{56}Fe is stable against fusion reactions because the nuclear binding energy per nucleon (i.e., the lowest mass per nucleon) peaks at ^{56}Fe.

1.1.3 Terminal end point as a core-collapse supernova

In this section, I outline the fundamental physics involved in the core collapse of a massive star. Despite several decades of research, the core-collapse explosion mechanism is still uncertain and an area of active research. This reflects the complex nature of the problem. Computational modelling of CCSNe has been carried out over several decades (e.g. Colgate & White, 1966; Wilson, 1985; Bruenn, 1985; de Nisco et al., 1998; Janka, 2012), but requires detailed physics at every scale, from general relativity to fluid dynamics and nuclear and neutrino physics. Additionally, the properties of the progenitor stars vary and so too will the explosion model. Only in the last decade have we had the required computational power for 3D core-collapse supernova simulations (e.g. Hanke et al., 2013; Janka et al., 2016; Müller et al., 2016; Wongwathanarat et al., 2015; Chen et al., 2020). Each simulation needs ~50 million CPU hours, running for months on highly-parallelised computers (Müller & Smartt, 2017).

Up to this point in a star's life, its self-gravity has been balanced by energy generation from nuclear fusion. But once nuclear fusion in the core has been terminated, the delicate balance maintaining hydrostatic equilibrium is disrupted. The core contracts and the compressed gas becomes degenerate – the star is now entirely supported by the degeneracy pressure of electrons. In this state, matter is so dense that further compaction would require electrons to occupy the same

---

potentially a SLSN. Chapter 1.3.2 also discusses the explosive end points of stars between 95–130 $M_\odot$ that undergo pulsational instabilities in their evolution that lead to large mass ejection and may be responsible for SLSNe-II.

energy states, but the Pauli exclusion principle forbids this.

Meanwhile, lighter elements continue to burn in shells above the degenerate iron core, dumping their iron ashes into the core. The core grows in mass until it exceeds the maximum white dwarf mass known as the Chandrasekhar mass (1.4 $M_\odot$), where even electron degeneracy pressure is insufficient to support the core. Once the core surpasses this critical mass, the star begins to collapse under its own self-gravity. The core temperature and density increases and in these extreme conditions, two dominant physical processes occur: photodisintegration and neutronisation.

Photodisintegration – High core temperatures ($T \sim 10^{11}$ K) cause energetic photons to break down all the iron peak elements back into a mixture of helium, protons and neutrons. This unravels the evolutionary work of millions of years of nuclear fusion in the star.

The dissociation of the most abundant form of iron would take the form:

$$\gamma + {}^{56}\text{Fe} \rightarrow 13({}^4\text{He}) + 4\text{n} \quad (-124 \text{ MeV}) \tag{1.2}$$
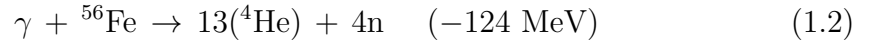
And at slightly hotter core temperatures ($T > 2 \times 10^{11}$ K) the ^{4}He formed in the dissociation of iron is itself photodissociated:

$$\gamma + {}^4\text{He} \rightarrow 2\text{p} + 2\text{n} \quad (-28 \text{ MeV}) \tag{1.3}$$
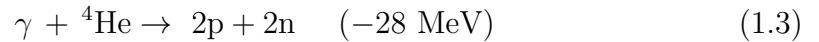
Neutronisation – In the process, the central region reaches such high densities that free protons and electrons are pushed together to form neutrons and neutrinos. As neutrinos are weakly interacting, they escape freely from the star and carry away the binding energy of the core. Pressure support decreases, and the star undergoes further collapse, producing even more neutrons.

$$p + e^- \rightarrow n^+ + \nu_e \tag{1.4}$$

These endothermic reactions deplete the energy of the system and the associated pressure reduction accelerates the stellar collapse. Moreover, the rates of photo-disintegration and neutronisation increase rapidly with temperate, setting up the runaway collapse of a star. The result of these two processes build up a highly neutron-rich core, undergoing a rapid change in state to form a proto-neutron star.

The inner core ($\sim$0.5 M$_\odot$) collapses more slowly than the outer core (which is collapsing at supersonic speeds), and this infall occurs until the density of the material reaches that of nuclear matter ($\sim$10^{15} g cm^{-3}). In the same way as before, the degeneracy pressure (only this time exerted by neutrons) prevents further gravitational collapse, but this alone is not enough, and the strong nuclear force plays a more significant role in supporting the core. The inner core stiffens as a result of the repulsion of the strong force, but it overshoots this mark and bounces back. The outer accreting material hits this wall, launching a shock wave that propagates outwards in a so-called 'core bounce'. The shock propagates first through the proto-neutron star core and then outwards into the iron core, colliding with infalling iron in the outer core. This causes the shock to lose the initial energy gained from the rebound due to photodissociation of iron peak nuclei into free nucleons and by rapid neutrino losses once the shock reaches densities of $\sim$10^{11} g cm^{-3}. These severe energy losses (along with the pressure of the infalling outer core) stall the shock, preventing it moving outwards beyond a radius of 100–200 km.

The stalled shock must be regenerated, and this shock will go on to rip the outer layers of the star apart. However, despite decades of explosion modelling, the mechanism responsible for this is poorly understood. Neutrino-driven heating (Colgate & White, 1966; Bethe & Wilson, 1985) is the most commonly invoked mechanism to regenerate the stalled shock and to power the explosion. In this model, neutronisation produces many neutrinos. Ordinarily neutrinos interact weakly with matter, but the extreme density of the collapsing star means that they cannot escape, and instead they deposit their energy just above the core.

This neutrino-driven heating causes violent convection motions which raises the pressure and establishes a pressure gradient which re-energises the explosion and moves the material beyond 150 km where the shock initially stalled (Janka, 2012, 2017).

The newly formed shock wave propagates out of the iron core and through the stellar envelope at speeds as high as 10 per cent of the speed of light. The shock wave compresses and heats the envelope to such a degree (the interior $\sim$3,000 km is heated to $>5\times10^9$ K; Woosley et al., 2002) that it causes the explosive nuclear burning of many intermediate-mass elements (e.g. oxygen, silicon, neon and carbon) that will power the late-time light curve (^{56}Fe, ^{56}Co and ^{56}Ni).

In the classical view, for single stars of solar metallicity with M_{ZAMS} <40 $M_{\odot}$, neutron degeneracy pressure combined with the strong nuclear force halts further gravitational collapse, leaving a dense ball of neutron-rich material, merely a few kilometres in radius (a so-called neutron star). Whereas for stars with M_{ZAMS} > 40 $M_{\odot}$, the neutron-rich core is more massive (typically $\sim$2 $M_{\odot}$) and exceeds the Tolman–Oppenheimer–Volkoff (TOV) critical mass limit for neutron-degenerate matter (Oppenheimer & Volkoff, 1939). Beyond the TOV mass limit, not even neutron degeneracy pressure can prevent this object from collapsing even further. Once it collapses to within its Schwarzschild radius it forms a gravitational singularity, with infinite density and zero radius. Such an object is called a black hole. The gravity of this object is so strong that not even light can escape and they cause minute distortions in the fabric of space-time.

However, the emerging picture from simulations suggests that there is no single mass division for producing either a neutron star or a black-hole (e.g. O'Connor & Ott, 2011; Ugliano et al., 2012; Sukhbold & Woosley, 2014; Müller et al., 2016). There is broad qualitative agreement that the likelihood a massive star explodes is a function of its density structure (e.g. O'Connor & Ott, 2011; Ugliano et al., 2012; Sukhbold & Woosley, 2014), which can be characterised by its compactness. Stars below $\sim$20 $M_{\odot}$ seem to explode as supernovae and above this limit, stars have a tendency to collapse directly to a black hole without a visible

core-collapse supernova explosion as a so-called 'failed supernovae' (Fryer, 1999; Kochanek et al., 2008) But perhaps counterintuitively a star's compactness is not a monotonic function of its birth mass – it can change with stochastic variations in the progenitor and a variety of factors that effect the mass-loss of the progenitor such as metallicity, rotation and binary interactions. Thus, in some mass regions (between 20–120 $M_\odot$) there might be 'islands of explodability' that produce successful explosions and neutron stars (O'Connor & Ott, 2011; Ugliano et al., 2012; Sukhbold & Woosley, 2014; Clausen et al., 2015; Ertl et al., 2016). The predicted lack of high-mass supernova progenitors, coupled with the lack of direct progenitor detections of stars with masses exceeding $\sim 17\ M_\odot$ may mean that very massive progenitors ($>17\ M_\odot$) of supernovae are rare (Smartt, 2015), a result now known as the 'red supergiant problem'. In single-star evolution this is controversial because it is unlikely that the envelope of a 17–30 $M_\odot$ RSG star can be removed by quiescent winds (Beasor et al., 2020).

Supernova light curve – The first observable light from a core-collapse supernova is when the shock reaches and breaks out of the outermost layers of the stellar envelope in a 'shock breakout'. This can take anywhere between a few hours up to a day, depending on progenitor radius. Next, the electromagnetic display begins, as a brief flash of X-ray/UV radiation. The flash occurs on timescales of a few hours after shock break out when the expanding material has a small area and reaches temperatures $>10^5$ K. This is followed by UV/optical radiation as the emission from the expanding material cools on the timescale of a day. This early-time emission has been predicted for several decades (Colgate, 1968; Klein & Chevalier, 1978; Falk, 1978), but the rapid timescale makes it difficult to observe. Thus, shock break out has only recently been observed in X-ray (Soderberg et al., 2008), UV (Gezari et al., 2015; Schawinski et al., 2008) and possibly in optical light (e.g. Garnavich et al., 2016). However, the post-breakout shock cooling can be more easily captured and has been observed for many SNe including SN 1987A (e.g. Ensman & Burrows, 1992).

After shock breakout, the outer hydrogen envelope is left completely ionised.

Ionised hydrogen is opaque and traps radiation with a photon diffusion timescale of thousands of years. But since the outer layers of the star are expanding the area of the photosphere is increased and begins to cool. After a few days, the outer layers of the ionised hydrogen envelope have expanded and cooled (T<6,000 K) enough that the ionised hydrogen can recombine to neutral hydrogen near the photosphere, removing the opacity. A recombination front begins in the outer layers and over time is forced deeper and deeper into the star. This means that photons from the hotter inner regions of the hydrogen envelope can begin to escape, since neutral hydrogen is transparent to radiation at most wavelengths. For stars with extended envelopes (depending on the radius, mass and density profile of the recombining hydrogen layer), this results in a light curve plateau, the defining property of Type IIP SNe (discussed in Section 1.2.2). The plateau occurs because initially the photospheric radius changes slowly, causing minimal cooling and the recombination energy release maintains the temperature at T$\sim$6,000 K. However, when the photosphere does begin to expand significantly, the diffusing radiation is cooled, and the luminosity declines rapidly. After the recombination front has passed through the entire hydrogen envelope, the shock energy is dissipated, the plateau phase (where present) ends and the light curve drops sharply.

The late-time light curve of a supernova is driven by radioactive decay of ^{56}Ni synthesised in the supernova explosion and the products of its decay:

$$^{56}_{28}\text{Ni} \rightarrow \, ^{56}_{27}\text{Co} + \text{e}^+ + \nu_\text{e} + \gamma \quad (\tau_{1/2} = 6.02 \text{ days})$$

$$(1.5)$$

$$^{56}_{27}\text{Co} \rightarrow \, ^{56}_{26}\text{Fe} + \text{e}^+ + \nu_\text{e} + \gamma \quad (\tau_{1/2} = 77.7 \text{ days})$$
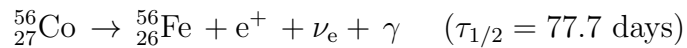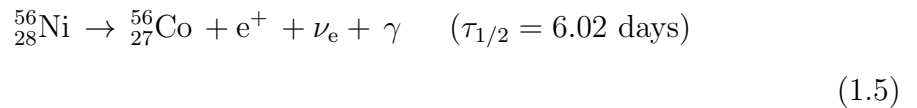
^{56}Ni has a radioactive half-life of less than a week. When it radioactively decays, the gamma-ray and positron emission deposits energy into the supernova ejecta, producing the characteristic exponentially declining tail that follows the ^{56}Co decay rate. The shape of the light curve will vary depending on: the mass of the

envelope (higher mass means a longer diffusion timescale for photons to escape from the expanding ejecta, therefore wider light curve), the radius of the pre-supernova star, energy of the explosion, degree of mixing, and the mass of ^{56}Ni produced in the explosion, which ultimately depends on the progenitor mass. A more massive progenitor will typically produce a broader light curve and a more luminous peak.

The majority ($\sim$99 per cent) of the energy budget of supernovae is released in the form of neutrinos. Neutrinos only weakly interact with matter, therefore escape freely and are only observable for nearby SNe (e.g. Ando et al., 2005). They carry away $\sim$10^{53} erg of the energy liberated by gravitational collapse. Of the remaining 1 per cent of the supernova energy budget, typically $\sim$10^{51} erg is released as kinetic energy of the expanding ejecta and only $\sim$10^{49} erg is released as optical light. Typically a supernova fades over a few months to years, leaving behind a shock-filled bubble (which lasts thousands of years) and a compact neutron star or black hole remnant.

1.2   Observational properties of supernovae

1.2.1   History of supernova detection and dedicated searches

Supernovae have been observed, recorded and studied for nearly 2000 years. Due to their brightness and relatively long-duration in optical light, they have played an essential role in the early development of astronomy as a science and to the history of science as a whole. Only five supernovae have been observed in our Milky Way galaxy; SN 185 is the earliest supernova in human records. It was recorded as a 'guest star' by Chinese astronomers (e.g. Zhao et al., 2006) and due to its proximity to Earth, the supernova would have been visible for many months with the naked eye alone.

Almost a century later, another Galactic supernova was discovered by astronomers

hired by the Chinese imperial courts as human scanners of the night sky. Astronomers stood on observatory platforms positioned around the city and developed sophisticated maps of the night sky. Any changes were carefully recorded to inform and warn the emperor of anything that might herald an invasion. On the 4th of July, in 1054, they identified a new 'guest star' in the sky (e.g. Collins et al., 1999). The position of the 'star' and the relative brightness with time was recorded. The supernova has since been pinpointed to the Crab Nebula (Messier 1) which is believed to be the supernova remnant (Lundmark, 1921; Duyvendak, 1942; Mayall & Oort, 1942). The pulsing neutron star (a pulsar) embedded in the supernova remnant was the first to be connected to a supernova remnant and is the only pulsar with a known birth date. The value of careful observations to posterity is so clearly demonstrated in this case!

Since then, several other Galactic supernovae have been discovered with the naked eye – the most recent being Kepler's supernova in 1604 (e.g. Baade, 1943). It was not until the 19th century that the first extragalactic supernova (SN 1885A) was discovered in the Andromeda galaxy (although it was not fully recognised until later on; de Vaucouleurs & Corwin, 1985).

Pioneering theoretical work in the field was undertaken by Walter Baade and Fritz Zwicky who first proposed that supernovae are the transition of normal stars to neutron stars and coined the term 'super-novae' (Baade & Zwicky, 1934). Fritz Zwicky also conducted the first dedicated search for supernova (the 'supernova search patrol') using the 18-inch Schmidt Telescope at Palomar Observatory (Zwicky, 1938). This arduous search manually compared photographic plates of the same patch of sky to pinpoint any new point sources appearing in the images. Between the years 1921–1973, Zwicky discovered over 100 supernovae in total (e.g. Zwicky, 1938), making it the most supernovae discovered by any single person and pushing the boundaries of what was then achievable with the available technology – an impressive record that held for many decades.

Towards the end of the 20th century, new digital image sensor technology (CCDs;

Boyle & Smith 1970) was becoming available.[5] The first application of CCDs within astronomy was in the late 1970s, which improved the efficiency of searches due to their superior sensitivity compared with photographic plates. By the 1990s, several dedicated robotic transient searches were underway. These searches were made possible by cheaper and more powerful computers, which allowed large-scale image processing and digital image-subtraction for automated transient detection. The Berkeley Automated Supernova Search (Perlmutter et al., 1992) which was later succeeded by Katzman Automatic Imaging Telescope at Lick Observatory (Filippenko et al., 2001) used a galaxy-targeted search that enabled the detection of a few tens of events per year.

In 1987, the Large Magellanic Cloud (LMC) hosted SN 1987A, which was visible with the naked eye, exploding a mere ∼50 kpc from Earth (e.g. Arnett et al., 1989; Woosley, 1988). By this point, there had been significant progress achieved in theoretical predictions of supernova explosions and technical advances in observational techniques. The vast leap in understanding meant that the observations could be fully exploited and tested against theoretical predictions and 1987A became the most scrutinised supernova in history (e.g. Trimble, 1988).

SN 1987A is the only core-collapse supernova whose progenitor has been detected spectroscopically as well as photometrically (Sanduleak, 1970; Rousseau et al., 1978). One of the main surprises was when the progenitor star was unexpectedly identified as a blue supergiant (rather a red supergiant as predicted by standard stellar evolutionary theory at the time) (Arnett, 1987; Woosley et al., 1987; Saio et al., 1988). Stellar evolutionary models later predicted that low metallicity, fast rotation or binarity could cause a blue supergiant star to explode as a core-collapse supernova (e.g. Podsiadlowski, 1992; Vanbeveren et al., 2013).

In addition, SN 1987A provided the first direct evidence of supernova neutrino emission (Aglietta et al., 1987; Hirata et al., 1987; Bionta et al., 1987) in the final stage of core-collapse of a massive star. Core-collapse models predicted that

---

[5]Boyle and Smith were awarded the 2009 Nobel Prize in Physics for their invention: `https://www.nobelprize.org/prizes/physics/2009`.

∼99 per cent of the total gravitational energy released in core-collapse is emitted in the form of neutrinos. By coincidence, some experiments in particle physics were capable of detecting neutrinos, and a pulse of ∼20 extragalactic neutrinos were detected a few hours before the supernova appeared in optical light after its shock breakout, dramatically illustrating this theory to be true (e.g. Arafune & Fukugita, 1987; Bahcall et al., 1987). SN 1987A has helped answer some of the questions relating to early-time supernova luminosity and its subsequent radioactive decay (e.g. Arnett et al., 1989; Woosley, 1988), but it has opened up many more.

1.2.2 Supernova classification scheme

The first observational attempt at spectral supernova classification was made by Minkowski (1941), who noted types I and II based on the presence (II) or absence (I) of hydrogen emission lines in the spectra of supernovae at maximum light. This nomenclature is still used today, but was derived before we fully understood the explosion mechanisms behind supernovae. It later emerged that a subset of hydrogen-deficient supernovae (type Ia's) were not related to the death of massive stars, but were from an entirely different physical mechanism – their luminosities are powered by the decay of ^{56}Ni produced by the thermonuclear runaway explosion of a carbon-oxygen white dwarf (Hoyle & Fowler, 1960; Whelan & Iben, 1973; Nomoto et al., 1984).

A general overview of the most common subtypes of supernova can be found in Filippenko (1997) and a schematic of the main subtypes is shown in Fig. 1.2. In this thesis, I will outline the observational characteristics of the most common classes below which are physically split in thermonuclear Ia supernovae and core-collapse supernovae:

Ia supernovae – SNe Ia are defined by the strong silicon absorption feature (6355 Å) in their spectra at maximum light. SN Ia are a remarkably homogeneous class; they exhibit similar spectral and photometric properties. Specifically, they
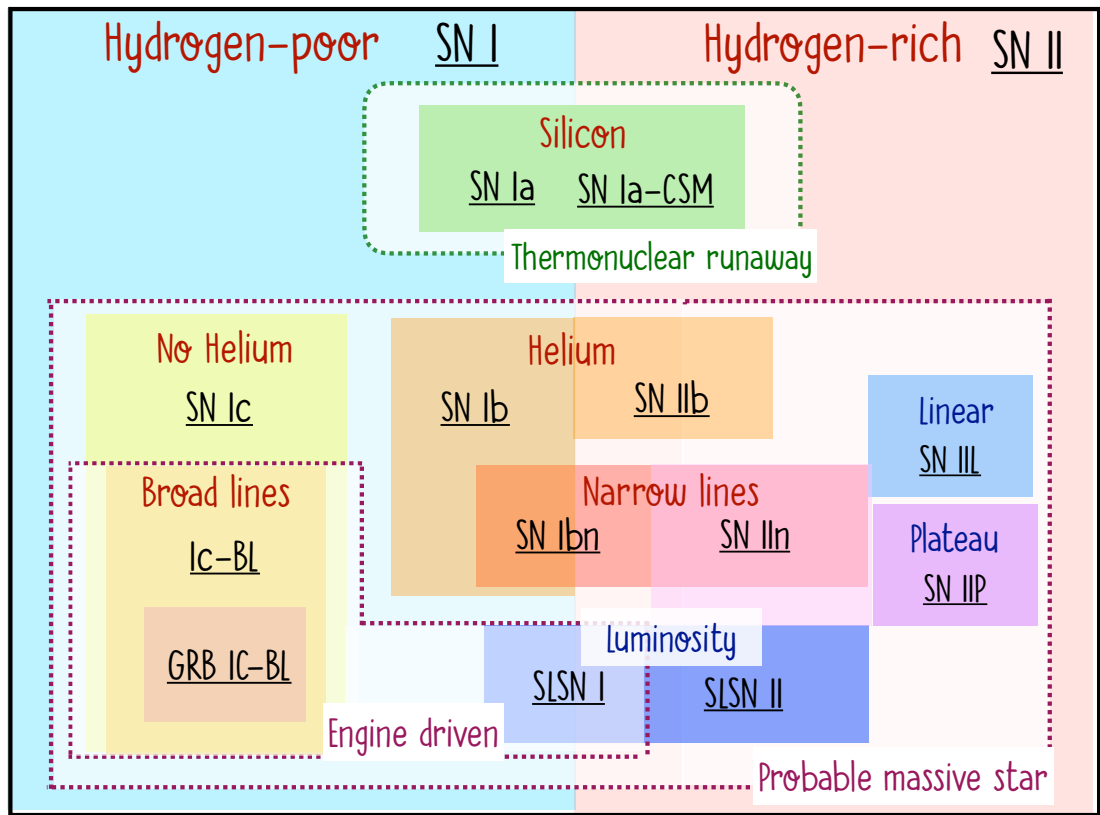
Figure 1.2: Schematic of all supernova classifications of all SN subtypes used within this thesis. SN are classified via the presence or absence of certain spectroscopic features (red) or via light curve features (blue). The dotted lines indicate the physical origins of the supernova subtypes.

have uniform absolute luminosities $M_v \sim$–19.1, with a dispersion of 0.3 mag (e.g. Hamuy et al., 1996). Moreover, their peak brightness is systematically correlated with other light curve properties, which have allowed them to be standardised. The most prominent correlation is the so-called Phillips relation between the width of the light curve and its peak brightness (Phillips, 1993). This was used to bring any Type Ia supernova peak magnitude to a standard candle value, making them extraordinary cosmological distance measures, which were later used to discover the accelerated expansion of the Universe (Riess et al., 1998).[6]

Although this class is the most homogeneous, some diversity is present. There are three main types of peculiar Ia's, commonly referred to as the first supernova discovered within each respective subclass (1991bg-like, 1991T-like and 2002cx-like; Filippenko et al., 1992; Li et al., 2003). These peculiar Ia's make up about $\sim$30 per cent of all Ia's in volume-limited samples (Li et al., 2011a). Super-luminous 1991T-like objects represent around $\sim$9 per cent, sub-luminous 1991bg-like objects represent around $\sim$15 per cent, and $\sim$5 per cent are 2002cx-like with faint luminosities, but with spectra similarities to 1991T-like (Li et al., 2011a). In addition, new surveys are discovering supernovae in sufficient numbers, allowing rare and hitherto unrecognised populations to be found. For example, some Ia SNe show evidence for supernova ejecta interaction with a slow-moving dense circumstellar material (CSM), evidenced by narrow hydrogen emission lines as well exhibiting spectroscopic features of a SN Ia (Dilday et al., 2012; Silverman et al., 2013).

In magnitude-limited surveys, because of their bright absolute luminosities, SNe Ia are the most commonly discovered supernova class. For example, in the ZTF magnitude-limited survey, they make up about $\sim$72 per cent of the sample (Fremling et al., 2020). Whereas even though CCSNe are the most abundant extra-galactic transient in volume-limited surveys (Li et al., 2011b), only $\sim$26 per cent of SNe in a magnitude-limited survey are CCSNe[7] because they are much less

---

[6]This discovery led to the Nobel Prize in Physics in 2011: https://www.nobelprize.org/prizes/physics/2011/press-release/.

[7]The remaining $\sim$2 per cent of SNe in the ZTF magnitude-limited survey are SLSNe.

luminous that Ia SNe.

The common consensus is that a carbon-oxygen white dwarf accretes material from a binary companion until temperature and density ignite a thermonuclear runaway explosion, as a type Ia supernova. The nature of the exploding carbon-oxygen white dwarf has been confirmed with observations of the nearby SN Ia 2011fe (Nugent et al., 2011), but identifying the binary companion is still an unsolved problem. The binary companion star could be a non-degenerate star (anything from a MS star, to a more evolved RG), or it could be a degenerate white dwarf (Hillebrandt & Niemeyer, 2000) and it is likely that both channels are in operation, although the ratio between their rates is unclear.

Core-collapse supernovae – All other types of supernova are thought to be related to massive stars. Fig. 1.3 shows a diagram of the spectral lines used as a classification diagnostic for the most common types of core-collapse supernova. The most common sub-classes are: SNe **II**, **IIn** and **IIb** which display hydrogen Balmer lines in their spectra, whereas **Ib**, **Ibn**, **Ic** and **Ic-BL** have hydrogen-deficient spectra. The conventional picture suggests that type II supernovae arise from RSG stars with initial stellar masses between $\sim$8–20 $M_{\odot}$ whose progenitors retain most their hydrogen envelope prior to their explosion. Whereas type I supernovae arise from initially more massive progenitor stars that shed their hydrogen envelopes through stellar winds or binary interaction.

Hydrogen-rich supernovae are by far the most common type of core-collapse supernova (e.g. Smith et al., 2011). The Balmer lines exhibit P-Cygni profiles with an absorption and emission component in the spectral line profile of hydrogen (typically 3,000–10,000 km s^{-1}), indicating rapid expansion velocities of material in the supernova in a gaseous envelope.

Early work studying type II SNe found they fell into two distinct classes based on the shape of their late-time optical light curve (Barbon et al., 1979). The light curve (in magnitude-space) either shows a 'plateau' with constant brightness for $\sim$100 days (IIP) or a 'linear' decline (IIL). The primary physical difference

between these sub-types is due to the hydrogen envelope mass at the epoch of explosion (Popov, 1993). IIP supernovae typically have larger hydrogen envelopes than IIL whose progenitors must have already lost a large fraction of their envelope. Thus IIP's have more energy deposited from hydrogen recombination in the ejecta, resulting in the distinct plateau. Recently there has been additional observational and theoretical work focusing on the IIP/IIL distinction and some studies question whether there is actually any evidence for two distinct classes, as opposed to a continuum of light curve behaviour (e.g. Anderson et al., 2014; Eldridge et al., 2018).
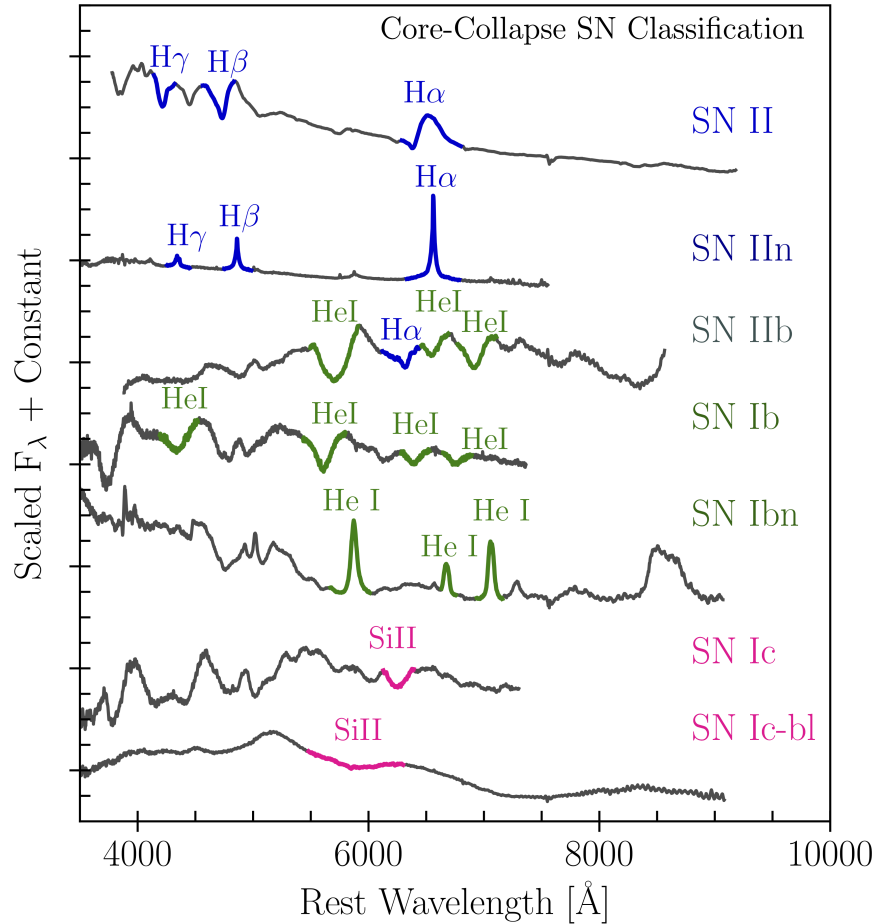
Figure 1.3: A diagram showing spectral classifications of core-collapse supernova from Modjaz et al. (2019).

Hydrogen-deficient supernovae shed their hydrogen-rich stellar envelope partially (retaining a few tenths of a solar mass) or entirely prior to their explosion. The resulting spectrum shows Balmer lines which fade quickly in its evolution or

lack Balmer lines entirely. These so-called stripped-envelope supernova (SE-SN; Filippenko, 1997) are classified based on helium lines in their spectra, either as helium-rich (Ib and IIb) or helium-poor (Ic). The mass stripping occurs as a result of either metallicity-driven ($\dot{M} \propto Z^{0.6-0.8}$; Vink et al., 2001) stellar winds (Maeder & Meynet, 2000) from very massive ($M_{ZAMS} > 25$ $M_\odot$) WR progenitors or via mass transfer in close binary systems (Podsiadlowski et al., 1992). The latter requires a less massive primary star ($M_{ZAMS} < 20$ $M_\odot$). Both channels are likely to contribute to SE-SNe, but statistically, single massive WR stars are rare, therefore they are unlikely to account for the observed fraction of SE-SNe, so the binary system scenario could be more common (Smith et al., 2011).

A small fraction of type Ic SE-SNe have broad spectral absorption features. They are given the additional label 'BL' in their classification. Ic-BL SNe are rare and account for only a few per cent of the core-collapse supernova population (Smith et al., 2011). Their broadened lines are caused by fast expansion velocities of the supernova ejecta. Their line widths are typically between 15,000–30,000 km s^{-1} at maximum light, with median line widths $\sim$9,000 km s^{-1} broader than their Ic cousins (Modjaz et al., 2016). In addition, some Ic-BL SNe have been associated with low-redshift long-duration gamma-ray bursts (LGRBs) or X-ray flashes (XRF) (Galama et al., 1998; Hjorth et al., 2003; Stanek et al., 2003; Woosley & Bloom, 2006). These so-called 'engine-driven' SNe are powered by a rapidly-spinning, newly formed compact object (sometimes termed the 'central engine'): either a rapidly spinning and highly magnetised neutron star ('magnetar'; Ostriker & Gunn, 1971) or a rapidly rotating black hole undergoing fallback accretion (Dexter & Kasen, 2013). This SN-GRB connection has been cemented with $\sim$20 additional observations of Ic-BL SNe coincident with LGRBs (Cano et al., 2017b). However, despite this tight association, many SN Ic-BL are frequently found blindly in optical surveys without any association with a LGRB detection, and it is not yet firmly established whether all LGRBs occur in association with SN Ic-BL.

Of the 5 local LGRBs reported without SNe ($z < 0.3$), two are highly-publicised

events from 2006 for which a SN was ruled out to deep limits, LGRBs 060505 and 060614 (Fynbo et al., 2006; Gal-Yam et al., 2006; Della Valle et al., 2006; Gehrels et al., 2006). These LGRBs appear to have genuinely different progenitors and/or explosion mechanisms from ordinary SN-associated long-duration GRBs. The remaining events (LGRBs 050826, 080517 and 111225A) have relatively poor constraints on the extinction column towards the LGRB and/or on the presence of a SN peaking 1–3 weeks after the event (e.g. Stanway et al., 2015).

Stars exploding within dense CSM show emission features associated with interaction and are referred to as 'interacting supernovae'. Massive stars often lose a significant fraction of their initial mass (e.g. Chugai & Danziger, 1994), particularly in their post-MS evolution. Mass-loss occurring shortly before the star explodes as a supernova builds shells of CSM. The high-velocity supernova ejecta collides with and shocks the slow-moving CSM. When the ionised CSM recombines, it emits strong and narrow (typically 500–1,000 km s^{-1}) emission lines atop of intermediate and broad bases (typically 1,000–5,000 km s^{-1}), These supernovae are given a designation with an 'n'. Type Ibn have narrow helium lines, while IIn have narrow hydrogen lines.

To some extent, all supernovae are interacting with their environment because space is not a vacuum. Some level of interaction will naturally occur when the supernova ejecta ploughs into the surrounding ISM. However, whether this can be detected shortly after explosion depends on the density of the surrounding material. Interacting supernovae have strong emission lines and are therefore at the upper end of the CSM density continuum. These supernovae are diverse in their observational properties since there is not a single evolutionary pathway nor one specific progenitor type.

In addition, 'flash' spectroscopy (Gal-Yam et al., 2014; Kochanek, 2019) of young (taken within hours of the supernova explosion) type II supernovae has revealed emission features directly related to the effects of the shock-breakout flash on the material immediately surrounding the progenitor (e.g. Niemela et al., 1985; Gal-Yam et al., 2014), capturing a narrow time window between the collapse of a

core and the ejecta sweeping up the surrounding environment. Ionising photons produced in the shock break out from the stellar surface ionise the surrounding CSM or an extended progenitor wind, which recombines and radiates strong high-ionisation emission lines. Within hours to days, the CSM is swept up by the SN ejecta propagating outwards, and these lines weaken substantially.

1.2.3   Current supernova search effort

The supernova search effort has evolved significantly, even over the past few years, revealing a huge diversity in explosions. We are now in the all-sky era: where larger CCDs are relatively cheap, gigapixel detectors are used frequently, and increased computing power has now made it viable to survey the entire night sky on timescales of a few days. Accompanying this is rapid reporting of transient discoveries and classifications to the global community of astronomers, allowing the detection and public announcement of thousands of supernovae per year.

The first steps in this 'all-sky era' were taken in 2013 by the All-Sky Automated Survey for Supernovae (ASAS-SN; Shappee et al., 2014), using small (14-cm) robotic survey telescopes distributed across the globe. ASAS-SN automatically surveys the entire visible sky to a magnitude depth of $\sim$18 mag in g-band. Since ASAS-SN is reasonably shallow, the discovered SNe are bright, and the rate of discovery means that most of these supernovae are spectroscopically accessible for classification, even with reasonably small telescopes. The Zwicky Transient Facility (ZTF; Bellm et al., 2019; Graham et al., 2019) began in 2018 and followed a similar philosophy to ASAS-SN, but is scanning the entire northern hemisphere every three nights in g and r-band, to a much fainter depth of 20.5 magnitudes, discovering thousands of SNe. This exponential increase in supernova discoveries will only continue with more new facilities coming online, such as the BlackGEM survey (Bloemen et al., 2015) and GOTO (Dyer et al., 2018) whose primary goals are for gravitational wave counterpart detection, but will discover many young transients in the process, particularly during LIGO/VIRGO downtime

when attention is focused on SN follow-up. Surveys such as Young Supernova Experiment (YSE; Jones et al., 2019) are combining public optical light curve data from ASAS-SN and ZTF with Pan-STARRS data for higher cadenced and deeper observations. Finally, in the next few years, the Vera Rubin Observatory will come online (VRO; Ivezic et al., 2008), generating an estimated 10^7 alerts per night. This will enable an order of magnitude more supernova discoveries ($\sim 10^3$ SNe per night)[8] than any current survey, meaning even the rarest transients like SLSNe, will be discovered in the thousands ($\sim 10^4$ yr^{-1}; Villar et al., 2018).

1.3 Observed properties and explosion models of exotic supernovae

As well as an exponential increase in the number of supernovae, the combination of deep, wide-field and high cadence observation means that surveys are now sensitive to transients spanning a much broader range of luminosity and timescale. This increase in discovery efficiency is now being coupled with more systematic classification and follow-up, allowing large statistical samples of supernovae to be built and for rare types of supernova to be pinpointed, revealing a more diverse picture than the classical supernova types outlined in Chapter 1.2.2.

One remarkable discovery that did not fit in this scheme was intrinsically bright ($M \lesssim -20$) and extremely rare (1 in 1,000 CCSNe; Quimby et al., 2013; Prajs et al., 2017) superluminous supernovae (SLSNe) that reach luminosities at least an order of magnitude brighter than ordinary core-collapse supernova (Quimby et al. 2011; Gal-Yam 2012; see Gal-Yam 2019 and Inserra 2019 for recent reviews). They also show distinctions from CCSNe in their spectroscopic properties and in their light curve evolution (discussed later in this chapter) which may point to a different progenitor or explosion mechanism. Thus, they have captivated the supernova community because their immense intrinsic brightness makes them inviting can-

---

[8]VRO predicted supernova discoveries obtained from: https://www.lsst.org/science/transient-optical-sky/supernovae.

didates for high-redshift cosmological applications (Inserra et al., 2020), and they provide a means to study new explosion channels of super-massive stars.

1.3.1 Hydrogen-poor superluminous supernovae

Light curve – SLSNe-I are hot and blue in their early evolution, with UV-bright light curves. They reach peak absolute magnitudes between $-22.5 < \mathrm{M}_g < -20$ mag (De Cia et al., 2018; Lunnan et al., 2018) compared to stripped-envelope supernovae which typically peak between $-17 < \mathrm{M}_g < -19$ mag (e.g. Richardson et al., 2014; Taddia et al., 2018).

The overall evolution and shape of SLSN light curves vary significantly between events. Rises are gradual and linear with rise times spanning between 20 to hundreds of days, with even the most fast-rising events exceeding the typical stripped-envelope rise time 13–22 days (Taddia et al., 2018). Often some undulations are present before peak with extremely hot temperatures ($\sim$25,000 K) (e.g. Nicholl & Smartt, 2016) that rapidly cool which may be attributed to shock-cooling emission due to shock break out through an extended stellar envelope. Two or more peaks are often visible (e.g. Yan et al., 2015, 2017; Vreeswijk et al., 2017), implying the operation of some additional mechanism. Similarly, following maximum light, their light curve decline times vary but tend to decline at a rate >0.03 mag day^{-1} (Quimby et al., 2011).

Spectra – In a similar way to the supernova classification scheme outlined in Section 1.2.2, SLSNe-I are defined as superluminous supernovae whose spectra are hydrogen-deficient at maximum light (whereas SLSNe-II are hydrogen-rich). However, their spectroscopic properties show unique characteristics when compared to hydrogen-deficient core-collapse supernovae.

At early times their spectra are characterised by a hot and blue continuum (T$\sim$20,000 K), with weak metal lines imprinted with UV absorption features bluewards of 2800 Å. Outside of the UV, broad O II features in the blue part
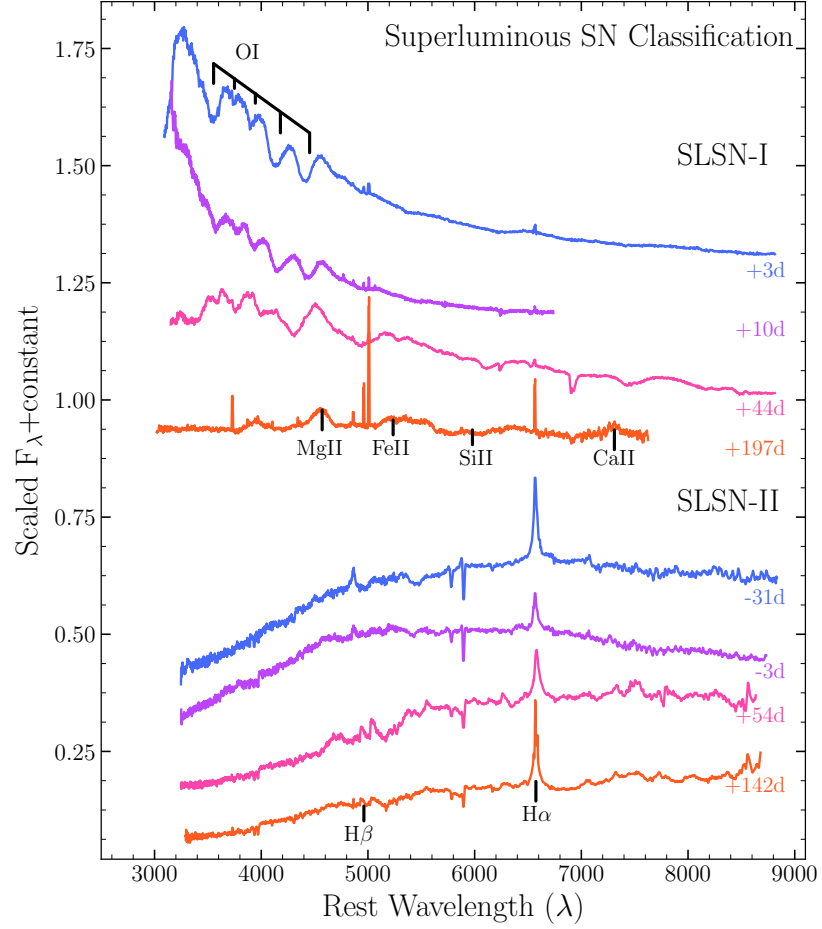
Figure 1.4: A diagram showing spectral features of SLSNe. The spectra evolve from hot to cool photospheric ($\gtrsim$14 d), to late-time nebular emission ($\gtrsim$100 d). Spectra of SN2016eay, the SLSN-I, are from Kangas et al. (2017); Nicholl et al. (2017a) and at first have a blue continuum, with strong O I features and then later Mg II, Fe II, Ca II and S II emission features appear. The spectra of the SLSN-II, SN2006gy, are from Smith et al. (2007, 2010).

of the optical spectrum at ~4100 and 4400 Å give the spectra its characteristic 'W'-shaped spectra feature, unique to SLSNe (see Fig. 1.4). These spectral features are the result of highly-excited states. In recent years, these spectroscopic features are being used to classify SLSNe, without a stringent luminosity cut (Quimby et al., 2018). Later in their evolution, the photosphere expands and cools to ~10,000 K. By this point, the spectra begin to resemble ordinary Ic SNe, as heavily blended absorption lines of Ca II 7300 Å, Mg II 4571 Å, Fe II 5169 Å and Si II 5972 Å become apparent (see Fig. 1.4). In general, SLSNe-I have broad absorption features, with expansion velocities similar to Ic-BL SN (Liu et al.,

2017).

Many months after the explosion, SLSNe enter the nebular phase. The ejecta become optically thin to continuum photons, giving us the ability to look deep into the star's interior. As is the case in Ic SNe, forbidden emission lines dominate SLSN-I nebular spectra. However, there are differences: SLSNe-I show stronger Fe II 5169 Å than Ic SNe, more similar to LGRB SNe indicating potentially a more massive progenitor causing a significant fraction of Fe II in the ejecta. O I is stronger in SLSNe than both LGRB SNe and Ic SNe, respectively. The presence of a low-velocity OI line from deep in the ejecta requires central instabilities which cause clumping. Some SLSNe have high O II/O I ratios, which indicate high ionisation (Lunnan et al., 2014; Inserra et al., 2017).

Proposed explosion mechanisms– Producing a luminous and long-lived supernova requires a gradual energy injection into the supernova ejecta sustained over many months. The mechanism that powers this energy injection is still uncertain, and several theoretical mechanisms could play a role in the production of SLSNe-I.

For stripped-envelope SNe, their energy source is from the radioactive decay of the ^{56}Ni synthesised in the explosion. Thus, a simple explanation of the power source driving SLSNe could be the *radioactive decay* of several solar masses ($\sim$10 M$_\odot$) of ^{56}Ni (Gal-Yam et al., 2009). This amount of ^{56}Ni could be produced by an extremely massive progenitor star ($\sim$100 M$_\odot$) that retains a large stellar core before collapse (Moriya et al., 2010; Young et al., 2010). However, retaining a large stellar core is difficult during a star's lifetime due to sizeable mass losses (e.g. Smith, 2014).

One variant on the radioactive decay model is the *Pair-Instability* SN model that was first theorised in the mid-nineteen-sixties (PISN; Fowler & Hoyle, 1964; Barkat et al., 1967; Rakavy & Shaviv, 1967). PISNe occur during the late evolutionary burning phases of super-massive *and* metal-poor stars (130–250 M$_\odot$; $\sim$0.2 Z$_\odot$; Yusof et al., 2013). When the massive ($>$63 M$_\odot$ Heger & Woosley,

2002) core ignites carbon burning, the core temperature approaches 10^9 K. At these temperatures (since photon energies are distributed according to the Planck function) a fraction of the photons will have enough energy (>1 MeV, the pair production threshold in the rest frame) to begin electron-positron pair production. This gamma-ray energy is channelled into the rest mass energy that may have otherwise gone into maintaining pressure support in the core and causes dynamical instability with a rapid core contraction.

The electron-positron pairs produced in the explosive burning can annihilate, creating neutrinos which escape from the star. This leads to a drop in radiation pressure support, causing a dynamical instability. The star can no longer maintain pressure support and begins to implode. The core contraction increases the temperature beyond a few 10^9 K, and the star ignites explosive nuclear burning (primarily of oxygen), which releases enough energy to reverse the implosion entirely. This leads to the complete disruption of the star in a PISN explosion. For stars with slightly lower initial masses (95–130 $M_\odot$), explosive oxygen burning does not disrupt the whole star, but creates strong pulsations in a pair instability supernova (PPISN). Later in this chapter I will discuss PPISNe as possible candidates to power SLSNe-II.

Population III stars are hypothesised to be the first generation of stars to form in the Universe. As such they are composed entirely of primordial gas (hydrogen, helium and very small amounts of light elements lithium and beryllium) left over from cosmological nucleosynthesis and they generate the first metals.[9] Population III stars have historically been invoked as candidates for PISNe because they lack metal coolants and have reduced line-driven mass loss, meaning they are they are extremely massive (>100 $M_\odot$; Bromm et al., 1999) and are more likely to retain an extensive stellar core at late evolutionary stages. Recent hydrodynamical simulations indicate that ∼25 per cent of population III stars will explode as

---

[9]Whereas, Population I stars are younger, metal-rich stars that are typically found in the spiral arms or disk of a galaxy and Population II stars are older and more metal-poor (in comparison to Population I) stars and are found in the halo and nuclear bulge of a galaxy, and in globular clusters.

PISNe (Hirano et al., 2015). Initially it was thought that PISNe must only occur in exceptionally metal-poor stars, but some models suggest that if the magnetic fields are strong, stars lose less stellar mass by stellar winds therefore a PISN may be possible at solar metallicities (Georgy et al., 2017; Petit et al., 2017).

A PISN explosion of a massive core (Heger & Woosley, 2002) produces several solar masses of ^{56}Ni and injects more than ten times the explosion energy of the canonical core-collapse supernovae mechanism. Fortunately, radioactive decay is well-studied, so this theoretical scenario is easily testable by examining SLSN light curves (e.g. Quimby et al., 2011). If more ^{56}Ni is produced in the explosion, the diffusion times for radiation in the ejecta will be increased because iron-group elements have a high opacity. This high opacity should manifest as a slow rise to peak in the optical light curve. Moreover, when more ^{56}Ni is produced in the explosion, the peak luminosity of the light curve is brighter, and the late-time light curve decay should be consistent with the radioactive decay of ^{56}Co (i.e. 0.01 mag day^{-1}; Pastorello et al., 2010). The light curves of PISN are predicted to rise on a timescale of >100 days (Kasen & Bildsten, 2010) but the observed light curves of SLSNe rise much faster (eg., Inserra et al., 2013). The decay times (>0.03 mag day^{-1}) of SLSN light curves decline a few times faster than radioactive ^{56}Co decay (Quimby et al., 2011). Thus, the ejecta mass (derived from the light curve width) is smaller than the inferred ^{56}Ni mass and is therefore nonphysical (e.g. Quimby et al., 2011; Chomiuk et al., 2011; Gal-Yam, 2012).

The most convincing observational case for a PISN was SN 2007bi (Gal-Yam et al., 2009), which showed a core mass of ∼100 M$_\odot$ and >3 M$_\odot$ of ^{56}Ni produced in the explosion, in line with the predictions from PISN models. One of the distinguishing features of PISNe is that they show a slow rise to peak, as well as a slow decline, but unfortunately SN 2007bi lacked pre-peak data to test this prediction (e.g. Nicholl et al., 2013). Another example is SN 2016iet (Gomez et al., 2019) has an inferred mass and metallicity predicted by PISNe models. However, despite these observations, the vast majority of SLSNe cannot be explained by radioactive decay of ^{56}Ni.

The majority (∼70–90 per cent) of stars form in clusters (Lada & Lada, 2003). In the early stages of cluster formation, the dynamical evolution of these clusters are dominated by massive stars. Dynamical friction causes stars to concentrate towards the cluster centre and this drives the system to collapse. The extreme densities result in successive collisions and mergers which may produce super-massive stars containing the entire mass of the collapsing cluster core. These massive stars could have rapid rotation rates and end their life as SLSNe and LGRBs (van den Heuvel & Portegies Zwart, 2013).

Also, a small fraction of SLSNe-I show signs of interaction with non-hydrogen CSM. Thus, interaction may also play a part in producing some H-deficient SLSN explosions (Chatzopoulos & Wheeler, 2012; Sorokina et al., 2016; Vreeswijk et al., 2017). In this scenario, the energy source is the kinetic energy of the ejecta itself (e.g. Smith, 2014). The supernova ejecta ploughs into and shock-heats the hydrogen-deficient CSM. The ionised CSM produces X-ray emission (e.g. Pan et al., 2013), and when the ionised CSM recombines, the energy is re-radiated as optical photons.

It is also essential to note that late-time interaction with hydrogen-rich CSM does occur in a small fraction (∼15 per cent) of SLSNe (Yan et al., 2015, 2017), and therefore does contribute at least some additional luminosity. For example, in the small sample of three events from Yan et al. (2017), hydrogen emission is not present after peak until at least 70 days into its evolution. These events have been interpreted as the interaction with CSM at large radii from the progenitor ($\sim 10^{11}$ km) that must have been ejected several decades prior to the explosion. However, most SLSN-I display no sign of interaction, and require another explanation.

The *engine-driven scenario* would provide a long-lived energy source behind the fast-moving ejecta, keeping it hot and luminous. The central engine is proposed to be a either a rapidly rotating and highly magnetised neutron star ('magnetar'; Ostriker & Gunn, 1971) or fallback accretion onto a rapidly rotating black hole (Dexter & Kasen, 2013). In general, the magnetar model is usually favoured, because the fallback accretion model would require 100's of $M_\odot$ accretion material

to produce the required energy.

Ostriker & Gunn (1971) first proposed that highly magnetised neutron stars could energise supernovae by injecting their rotational energy into the ejecta or remnant. Maeda et al. (2007) created a magnetar model to apply to supernovae and this model was developed by Kasen & Bildsten (2010); Woosley (2010); Metzger et al. (2015) to apply to SLSNe. Massive stars have higher rotation rates than low-mass stars, with typical equatorial velocities between 150–200 kms^{-1} during hydrogen burning (e.g. Fukuda, 1982). If massive stars have sufficient rotational energy when the star collapses to form a neutron star it is born with a spin period of $\sim$1 ms because angular momentum is conserved. Fast rotation rates cause a strong magnetic field and approximately 10 per cent of neutron stars are born as magnetars with exceptionally high magnetic field strengths of the order B$\sim$10^{14}–10^{15} G (see Kaspi & Beloborodov, 2017, for a recent review).

The newly formed magnetar spins down, injecting a significant fraction of the rotational energy via strong magnetic coupling of the stellar envelope with the proto-neutron star, which in turn magnetically slows down its rotation. The spin-down power is injected over a short timescale (seconds) and causes a magnetically driven wind. The wind acts as a piston on the expanding supernova ejecta behind the supernova shock and severely heats the ejecta, creating an expanding bubble of hot plasma (e.g. Kasen & Bildsten, 2010; Woosley, 2010; Metzger et al., 2015).

If SLSNe are associated with a central engine, then we may expect isotropic radio emission from the inner nebula years after the explosion, once the ejecta becomes sufficiently transparent to free-free absorption at radio frequencies (e.g. Omand et al., 2018). Until recently, radio studies of SLSNe have been fruitless (e.g. 2015bn, 2017egm; Nicholl & Smartt, 2016; Bose et al., 2018b), but late-time radio emission from one nearby SLSN has been recently detected (PTF10hgi; Eftekhari et al., 2019) and this lends further support to the magnetar explanation of SLSNe.

Attempts to locate a high energy X-ray counterpart in SLSNe have mainly led to upper limits (Margutti et al., 2017) with limiting X-ray luminosities between

10^{40}–10^{45} erg s^{-1}, with the exception of two SLSNe (SCP06F6, PTF12dam; Levan et al., 2013; Margutti et al., 2018). SCP06F6 was too bright in X-rays to be entirely attributed to CSM interaction, leading to suggestions that a central engine might be responsible for this energy (Levan et al., 2013). However, such significant X-ray or radio emission does not seem to be common among SLSNe-I.

1.3.2 Hydrogen-rich superluminous supernovae

SLSNe-II are not nearly as well studied as SLSNe-I, in part because they seem to be rarer, but also more focus has been placed on understanding the physical explosion mechanism behind SLSNe-I largely due greater challenges describing them physically and exciting prospects of testing extreme physical models.

Light curve– SLSNe-II have peak absolute magnitudes of M∼–21 in the optical and have similar rise and decay times as SLSNe-I (Gal-Yam, 2019). It is unclear whether they are the luminous end of the continuous SN IIn luminosity function, or they are a distinct population. Their light curve shapes are diverse, probably reflecting variations in the supernova ejecta mass and mass-loss processes of the progenitors, causing differences in CSM density and structure.

Spectra– SLSN-II have strong hydrogen emission features within their spectra. The majority of SLSN-II have narrow hydrogen emission lines similar to those of less luminous SNe IIn, indicating their luminosities are predominantly powered by interaction of supernovae ejecta with CSM – a mechanism that is more clearly understood than the exotic explosion mechanisms evoked for SLSNe-I. However, some SLSN-II have retained some form of hydrogen rich envelope prior to their explosion as seen via broad hydrogen emission, but have weak to little interaction.

Proposed explosion mechanisms– Understanding the mechanism behind SLSN-II is a complex problem because the radiation emitted from the core is reprocessed by the envelope of material. Since most SLSN-II show signatures of interaction it is natural to assume that these supernova are powered by the SN ejecta's kinetic

energy being transferred to thermal energy. The luminosity of CSM interaction depends on the rate that CSM enters the forward shock which depends on the progenitor's mass loss rate (Smith, 2017). SLSN-II typically emit $\sim 10^{51}$ erg of electromagnetic energy and at these energies, there is just enough kinetic energy to power these explosions within the energy budget of the standard core-collapse supernova model via interaction and efficient conversion to thermal energy required. Most supernovae with these energies probably represent the most extreme cases of mass loss pre-expelled by an ultra-massive star progenitor star before the explosion (Chevalier & Irwin, 2011; Ginzburg & Balberg, 2012; Moriya et al., 2013), while 'normal' type IIn SNe are likely to originate from a lower density and/or asymmetric CSM morphology. (Chevalier & Irwin, 2011; Ginzburg & Balberg, 2012; Moriya et al., 2013).

However, SLSNe-II with energies more than 10^{51} erg require CSM interaction *and* a hyper-energetic explosion. The *Pulsational Pair-Instability* explosion (PPISNe; Woosley et al., 2007; Chatzopoulos & Wheeler, 2012) has been proposed to explain these SLSNe-II. This mechanism is related to the aforementioned PISNe, but occurs in stars with lower birth masses (95–130 $M_\odot$) with less massive cores (30–63 $M_\odot$). Similarly to PISNe, interior instabilities arise due to extreme core temperatures. Energetic photons cause spontaneous electron–positron production sapping energy from the core and causing it to collapse. But unlike PISNe, the energy released in these reactions is insufficient to unbind the entire star, but results in a series of pulsational mass ejections.

The core stabilises when the mass ejected is sufficient and the core cools, until contraction causes the core to ignite once again, renewing the cycle of electron–positron production. The star may pulsate several times prior to final core-collapse on timescales lasting days to ten thousand years and amounting to several solar masses of the star's envelope. As a result, shells of material are built up over time around the progenitor star, often at large radii. The remnant will eventually stabilise, and continue nuclear fusion until the iron core-collapses and produces a supernova. The supernova ejecta collides with circumstellar material

surrounding the star (Woosley, 2017), leaving a 35–45 $M_\odot$ black hole. SN 2016aps has a large combined ejecta and CSM mass ($>$50 $M_\odot$) and an energy $>10^{52}$ erg, consistent with a super-massive star in the energy range where one may expect a hyper-energetic explosion as a PPISN or PISN (Nicholl et al., 2020).

1.3.3 Long-duration gamma-ray burst supernovae

Long-duration gamma-ray bursts (LGRBs) were first observed by the US Military Vela satellites when searching for nuclear detonations by the Soviet Union in the late nineteen-sixties. When it was realised they were of 'cosmic origin', they were finally declassified and published by Klebesadel et al. (1973). LGRBs are brief, typically lasting from a few seconds to several hours, but extremely luminous flashes (kinetic luminosities exceeding 10^{53} erg s^{-1}) of high-energy radiation. They are associated with the formation of a relativistic jet (Lorentz factor, $\gamma >$ 100) from a 'central engine' (a fast-spinning neutron star or black hole) at the centre of a collapsing and rapidly rotating massive stellar core. The jet punches a hole in the stellar envelope and produces the observed gamma-rays far outside the progenitor star. The gamma-ray emission is confined to a collimated beam with an opening angle of $<$10 degrees. This means than an observer will only see the gamma-rays within a narrow window when they are aligned with the LGRB axis. The prompt phase of gamma-ray emission is then followed by afterglow emission generally associated with shocks as the relativistic jet decelerates into the surrounding matter (see reviews by Gehrels et al. 2009; Kumar & Zhang 2015; Schady 2017).

Light curve– The majority of LGRB radiation is initially concentrated in gamma-rays during the burst. The characteristic rest-frame energy peaks at around 300 keV. Usually, the prompt emission is followed by afterglow radiation that peaks across the electromagnetic spectrum, at first in X-ray and then progressively out through the UV, optical, IR, microwave and radio, lasting days to even years. Gamma-ray emission light curves last 10–100's of seconds, but some 'ultra-long'

LGRB light curves appear on timescales more than 7,000 seconds (e.g. LGRB 101225A; Thöne et al., 2011; Levan et al., 2014). Their gamma-ray light curves are rather heterogeneous – some have smooth single pulses, whereas others have multiple peaks and have substructure; there is no characteristic shape. These rapid variations place strong constraints on the size and nature of the progenitor because the objects cannot vary faster than the time it takes for electromagnetic radiation to travel across them, meaning the LGRB energy is emitted across a small region.

Spectra– The spectra of LGRBs are hard, with energy emission >200 keV. Their spectra can be modelled with a power law (Band et al., 1993), indicating a non-thermal emission, from synchrotron radiation or inverse-Compton scattering.

Proposed explosion mechanisms– Traditionally, the *Collapsar Model* (Woosley, 1993) was used to explain LGRBs. In this scenario, a massive and rapidly rotating star undergoes core-collapse to a black hole before an outgoing shock is launched. The high angular momentum part of the star is channelled into forming a disk orbiting the black hole. Viscous processes allow accretion of this material from the disk onto the black hole. This rapid accretion drives a relativistic jet perpendicular to the rotational plane producing an LGRB. The associated SN occurs from the wind lost from the accreting disk.

However, more recently there has been a significant shift of focus to the *Magnetar Model* where the energy input from a rapidly spinning neutron star (with a period of the order of a millisecond) is sufficient to power an LGRB. The model is similar to the one invoked for SLSNe, but the magnetar has a much stronger magnetic field and quicker spin-down, meaning the energy is released on a rapid timescale, allowing the jet to break out of the star (Metzger et al., 2011, 2015). In LGRBs the timescale is likely to be minutes or less, whereas for SLSNe it may be days or more. A magnetar is favoured in some LGRBs that show extended afterglow emission (e.g. Metzger et al., 2011; Knust et al., 2017).

Given the low LGRB rate compared to CCSNe, we know there must be special

circumstances to produce an LGRB progenitor. The observed association between LGRBs and Ic-BL SNe (e.g. Woosley & Bloom, 2006; Hjorth & Bloom, 2012; Cano et al., 2017a) suggest the progenitors must lose their hydrogen envelope and most of their helium envelope before death. However, beyond this, the exact progenitor mass and the compact object formed is an open problem (e.g. Levan et al., 2016).

Rotating cores are a prerequisite for all LGRB models. Binary progenitor channels can lead to rapidly rotating stars because angular momentum is transferred (e.g. Stanway et al., 2016; Cantiello et al., 2007). Most models involve stellar mergers which are efficient at converting orbital rotation to spin rotation. This production channel involves progenitor stellar masses that are appreciably lower than single star models. Single stars efficiently lose their angular momentum due to stellar winds therefore a metal-poor progenitor is favoured for single star models. Low metallicity stars have efficient mixing that keeps them quasi-chemically homogeneous (and the outer hydrogen envelope is mixed and fused into alpha elements) in their evolution (e.g. Woosley & Bloom, 2006; Yoon & Langer, 2005). This means they do not evolve through the RSG phase with associated strong mass loss and are able to maintain their rapid rotation rate. For the single star models, Wolf-Rayet (WR) stars (>25 M$_\odot$) are usually invoked as candidate progenitors. WR stars are compact, allowing a jet to maintain enough energy to break out of the star. Ultra–long bursts that have been associated with bright Ic SNe (Greiner et al., 2015) could be explained by the engine-driven explosions of stars of much larger radii.

1.4 Observational supernova progenitor & explosion constraints

1.4.1 Direct progenitor detections

The most reliable way to connect the various types of supernova explosions to their progenitor stars is via deep pre-explosion imaging of the supernova site – ideally from the *Hubble Space Telescope* or with adaptive optics ground-based imaging (Smartt, 2009). The method is relatively simple: pre and post-explosion images are accurately registered on a sub-pixel scale, and a candidate progenitor is identified at the precise location of the supernova explosion. Post-explosion imaging confirms the absence of the progenitor after the supernova has faded and by measuring the star's brightness before it explodes, one can determine its initial mass.

Considerable progress has been made in the most abundant types of core-collapse supernova (type II). The progenitors of IIP SNe have been pinpointed to single red supergiant stars (Smartt, 2009). These stars have initial stellar masses between $\sim$10–17 $M_\odot$ and still retain most their hydrogen envelope as RSGs before the explosion as IIP SNe, albeit with a lack of progenitors at the expected higher mass end $\sim$17–20 $M_\odot$ limit. Five type IIb progenitors have direct progenitor detections, with initial masses that seem to be higher than those of IIP supernovae. For all IIb direct detections, binary progenitors seem the most plausible progenitor scenario (Maund et al., 2004; Folatelli et al., 2014, 2015; Kilpatrick et al., 2017).

It has been suggested that luminous blue variable stars (LBVs) are connected to IIn SNe. In single-star evolutionary theory, LBVs are evolved, massive O-type stars undergoing periods of extreme mass loss, expelling their hydrogen envelope in a rapid transition to a WR star. Thus LBVs were deemed to be only a short transitional phase in stellar evolution and not a possible endpoint of a massive star before core-collapse (Maeder & Meynet, 2000). It is now emerging that binary

interactions could play an essential role in producing an LBV star, through mass gain from a nearby stellar companion or via stellar mergers (Smith, 2017).

SN 2005gl is the only robust direct detection of a Type IIn supernova progenitor to date. The progenitor was very luminous (Gal-Yam et al., 2007; Gal-Yam & Leonard, 2009) and the only observed precedent for this luminosity is an LBV. There are also plenty of reasonably strong indirect arguments in favour of an LBV-like progenitor for IIn SNe. For example, IIn spectra have strong interaction lines which supports extreme mass loss and some SNe such as SN 2009ip and SN 2015bh have shown non-terminal precursor outbursts (Elias-Rosa et al., 2016; Thöne et al., 2017).

However, less progress has been made amongst hydrogen-poor stripped-envelope supernovae, mainly because these events are less common and their progenitors are optically fainter than RSGs. Eldridge et al. (2013) did an extensive search of all nearby 12 Ib/c progenitors; all the sites lack a significant direct detection. Although in recent years there have been some recent hints at a Ib/c progenitor detection, further observations are required for a definitive assessment of the nature of their progenitors. For example, the progenitor mass of SN iPTF13bvn, a type Ib (Cao et al., 2013; Groh et al., 2013; Folatelli et al., 2016), was constrained to an upper limit of <25 M$_\odot$, ruling out a Wolf-Rayet progenitor or an early O-type star, but could be consistent with a binary system (Eldridge et al., 2015). A potential progenitor of type Ic SN 2017ein was detected in pre-explosion imaging (Kilpatrick et al., 2018; Van Dyk et al., 2018). The point source was consistent with a high initial mass $\sim$50 M$_\odot$ progenitor or a binary model with a primary star $<$60 M$_\odot$. However, the source was marginally extended and consistent with a stellar cluster. Therefore late-time observations are necessary to confirm that this is the progenitor.

In practice, even though direction detection is a powerful method, there have only been a few dozen progenitor detections because there must be existing pre-explosion imaging of sufficient spatial resolution to pinpoint a progenitor. Only a small fraction of the sky has been surveyed at the required depth and resolution

– so most SNe do not have pre-explosion imaging in the archive. In addition, progenitor studies are often hindered due to spatial crowding within stellar clusters. There are also several complicating factors that make the interpretation of the progenitor detection difficult. One must estimate the stellar mass from a colour-magnitude diagram and apply a correction to estimate an initial supernova progenitor mass, but this is often unreliable due to uncertainties in fitting their SEDs (e.g. WR stars have diverse temperatures and radii leading to different SEDs). In addition, inference of the progenitor initial mass strongly depends on stellar evolution assumptions (e.g. mixing lengths, mass loss rates, metallicity, rotation, multiplicity) of the models that are used to infer the ZAMS properties from the pre-explosion ones.

This method is also limited by the local supernova rate. The maximum distance at which a standard RSG SN progenitor can be resolved and detected is $\sim$20 Mpc (Smartt, 2009).[10] At this distance, a single *HST*/WFC3 pixel (plate scale of 0.04 arcseconds per pixel) subtends $\sim$3.9 pc. This method cannot be used for rare or distant transients, so it is highly unlikely that pre-explosion imaging will ever uncover the progenitor properties of SLSN or LGRBs due to a combination of their low volumetric rate (Quimby et al., 2013; Prajs et al., 2017) and their high-redshift nature: the closest SLSN discovered to date is at a distance of $\sim$110 Mpc (SN 2018bsz; Anderson et al., 2018) and the closest LGRB-SN is at $\sim$40 Mpc (SN 1998bw; Galama et al., 1998). Progenitors of SLSNe and LGRBs remain poorly understood, and this motivates the use of indirect methods to probe supernova progenitor properties and to constrain their poorly understood explosion mechanism.

---

[10] This distance limit will vary for different SN progenitors. For example, the IIn LBV detection (Gal-Yam et al., 2007) was at 66 Mpc because LBVs are brighter than RSGs. In contrast, this distance is closer for WR stars (the anticipated progenitors of Ibc's), and for SN Ia's the distance is closer still.

1.4.2 Historical overview of supernova host galaxies

One way to constrain supernova models is to analyse the properties of the galaxies they inhabit to search for trends in morphology, colour, chemical composition, and star-formation. These trends can be tied to the mass and age of the underlying stellar populations to make inferences about the SN progenitor star or to test the predictions of specific models. Some models predict a population that predominantly explodes in specific environments, such as in dense star clusters or at low-metallicity.

Host galaxy studies can be conducted on two scales, either globally considering the properties of the galaxy as a whole, or locally considering the environment at the precise location of the supernova explosion. Host galaxy studies have the advantage that they can be done out to cosmological distances and unlike supernova light curve and spectral studies, gathering data for host studies is not limited to a critical time window.

Global properties– The first host galaxy studies investigated the nature of SN progenitors primarily based on global galaxy properties such as luminosities, morphologies, and association with star-formation that largely constrain whether a progenitor is young or old.

Since CCSN progenitors evolve to their evolutionary end-point rapidly in less than 10^7 years, it was expected that most would explode in their birth environment in star clusters or OB associations (Duchêne & Kraus, 2013). As a consequence, the first supernova surveys searched for CCSNe by targeting late-type spiral or irregular galaxies with active star formation. They found CCSNe preferentially located in the spiral arms of galaxies (e.g. Maza & van den Bergh, 1976; Bartunov et al., 1994) and in bright regions of active star formation (e.g. van Dyk, 1992) with young stellar populations (e.g. Van Dyk et al., 1999). Moreover, they are *rarely* in early-type environments with little star formation, unless a recent merger or interaction has caused some presence of a young stellar population in the galaxy (Hakobyan et al., 2008). This evidence means that CCSNe are associated with

the youngest, and most massive stars.

In contrast, SNe Ia are found across a broader range of environments, within early *and* late-type hosts. Albeit their rate seems to be enhanced in younger stellar populations, with higher star-formation rates compared to passive systems with no star formation (e.g. Mannucci et al., 2005; Sullivan et al., 2006). SN Ia that explode in strongly star-forming galaxies tend to be intrinsically brighter than those that explode in galaxies with little ongoing star formation. The origin of such variations is unknown, but it could imply that there are multiple explosion channels. The first channel could be from a younger, single-degenerate progenitor that explodes within a few hundred million years, and the second could be a double-degenerate channel that produces SNe Ia on longer time scales of thousands of years (e.g. Maoz et al., 2010).

This host galaxy work was extended to the hosts of LGRBs and SLSNe. Early indications showed stark differences in the global properties of SLSN and LGRBs from ordinary core-collapse supernova hosts and to the bulk population of star-forming galaxies. $\sim$50 per cent of CCSNe are in grand design spiral galaxies ($0.28 < z < 1.3$) and the other $\sim$50 per cent are in irregulars, whereas the spiral fraction is only $\sim$10 per cent for LGRBs ($0.09 < z < 1.2$; Svensson et al., 2010) and is similarly low for SLSNe. The remaining $\sim$90 per cent of the SLSNe and LGRBs generally occur in faint and compact galaxies with irregular structure (Fruchter et al., 2006; Le Floc'h et al., 2003; Neill et al., 2011; Lunnan et al., 2014; Angus et al., 2016). The median half-light radius of LGRBs is only $\sim$1700 pc (Lyman et al., 2017), and for SLSNe it is only $\sim$900 pc (Lunnan et al., 2015). These studies concluded that this preference for compact, low-mass galaxies is the result of a progenitor or explosion mechanism that forms preferentially at low-metallicity because the metallicities of galaxies decrease with lower stellar masses (e.g. Tremonti et al., 2004). This could point to many of the proposed scenarios to explain SLSNe and LGRBs such as a super-massive star that only occurs at low-metallicity, or a rapidly rotating star that forms a magnetar. A summary of the requirements is shown in Table 1.1 and described in Section 1.4.3.

Local properties– Two similar analysis methods were developed to study the correlation between the locations of transients with respect to the overall light distribution in their hosts, independent of galaxy morphology. The normalised cumulative rank method (NCR; James & Anderson, 2006) and the fractional light approach (F_{light}; Fruchter et al., 2006). These pixel-based methods use host galaxy images and firstly sort all the pixels in the transient host in ascending order of surface brightness. The pixels are summed cumulatively and normalised by the total sum of the host pixels. The brightness of the transient pixel is placed within this fractional light distribution and F_{light} corresponds to the fraction of pixels fainter than or equal to the pixel containing the explosion. If the explosions purely trace the distribution of light, one would expect F_{light} values to be uniformly distributed between 0 and 1. Fruchter et al. (2006) analysed LGRBs in rest frame UV or blue light (observed primarily in *STIS* and *HST V*-band filters) which predominantly traces the light from massive stars. They found that LGRBs are strongly associated with the brightest regions (with F_{light} values skewed towards 1) of their hosts and are more strongly associated with star formation, whereas CCSNe trace the light uniformly (Fruchter et al., 2006; Svensson et al., 2010).

In studies of nearby compact starburst galaxies, bright H II regions are often comprised of many O-type and WR stars (Hadfield & Crowther, 2006). Therefore LGRBs were linked to deaths of massive stars that explode in their birth environment (Fruchter et al., 2006). This coupled with the fact that LGRBs are typically found in low-mass compact galaxies was used to suggest that the fundamental difference between LGRBs and CCSNe is a combination of their progenitor mass and metallicity (e.g. Fruchter et al., 2006; Wolf & Podsiadlowski, 2007) because if metallicity alone was the difference then within the faintest galaxies, LGRBs would trace the UV light distribution in the same way as CCSNe do in dwarf galaxies.

SLSNe-I were also studied using the F_{light} technique on rest-frame UV *HST* images by Lunnan et al. (2015) who found that the locations are more strongly associated with host light than CCSNe, but are less strongly associated than LGRBs,

indicating potentially a somewhat older, lower mass progenitor for SLSNe.

However, most SLSNe and LGRBs lie at $z > 0.1$ where they are spatially unresolved and this makes it difficult to precisely determine the progenitor mass and to distinguish between $\sim$10–25 M$_\odot$ progenitors and super-massive progenitors $\sim$25–250 M$_\odot$. Since CCSNe are much more common than SLSNe and LGRBs there are larger samples at low redshift, and so the physical sizes probed by pixel based methods are much smaller. Anderson et al. (2012) also investigated differences in the CCSN population in rest frame NUV and Hα. They found an increasing association with Hα emission from SN II$\rightarrow$Ib$\rightarrow$Ic, suggesting a possible increasing mass sequence for CCSN progenitors with Ic SNe having the most massive progenitors. However, Crowther (2013) argues that this method is sensitive to the varying properties and duty cycles of H II regions. Most of the CCSN sample from Anderson et al. (2012) are in high-mass galaxies with high star formation rates, and are associated with massive H II regions with duty cycles of $\sim$20 Myr. Thus the association, or lack of association with star formation suggests only that type II CCSN and type Ic SNe have different minimum progenitor mass thresholds of $\sim$8 M$_\odot$ and $\sim$12 M$_\odot$ respectively. Whereas to provide stronger constraints for high-mass ($>$50–100 M$_\odot$) progenitors, one would require a sample of CCSNe in isolated and shorter-lived ($\sim$3–5 Myr) H II regions (Crowther, 2013).

Neill et al. (2011) and Fruchter et al. (2006) first suggested that the lack of SLSNe and LGRBs in luminous, high-mass galaxies was because they are suppressed at high metallicities. More recently, increasingly sophisticated approaches have been used to investigate these initial findings by studying the metallicities and star-formation properties in more detail.

1.4.3   Metallicity

The metallicities of host galaxies allow specific constraints to be placed on chemical enrichment and the underlying ages and metallicities of the stellar population at the supernova site. Each explosion and progenitor channel for CCSNe, SLSNe

Table 1.1: Progenitor models and predictions for SLSNe-I, SLSNe-II and LGRB. All progenitor masses are initial masses. Host predictions are loosened considerably if binary channels are considered because mass and rotation can be transferred.

Model	Variant	Transient			Progenitor requirement and host predictions
		SLSN-I	SLSN-II	LGRB	
Radioactive Decay	CCSN	☑	☑	☒	**Single Star:** High-mass $\sim$100 M$_\odot$ star, <0.5 Z$_\odot$ or rapid rotation causing homogeneous evolution.
	PISN	☑	☒	☒	**Single Star:** 130–250 M$_\odot$, <0.2 Z$_\odot$ or rapid rotation causing homogeneous evolution youngest stellar populations. **Binary Channel**: Dynamical interactions in young clusters in starburst galaxies.
Central Engine	Magnetar	☑	☒	☑	**Single Star:** $\sim$20 M$_\odot$ but rapidly rotating, <0.3 Z$_\odot$. **Binary Channel:** Lower mass and higher metallicity threshold than single-star channel.
	Blackhole (Collapsar)	☒	☒	☑	**Single Star:** Could require very massive star >20 M$_\odot$ but rapidly rotating, <0.3 Z$_\odot$. **Binary Channel:** Lower mass and higher metallicity threshold than single-star channel.
Interaction	CCSN	Partly	☑	☒	**Single Star:** Contributes to SLSN-I luminosity but could entirely power SLSN-II. Requires significant mass loss for dense CSM could be enhanced at higher metallicity and with a super-massive star.
	PPISN	☒	☑	☒	**Single Star:** 90–130 M$_\odot$, <0.3 Z$_\odot$ to retain mass, starburst preference.

and LGRBs (see Table 1.1) will be formed more easily in certain conditions. For example, certain models require a highly stripped hydrogen-poor star, some need a super-massive star, while others require a rapidly rotating progenitor. Another complicating factor is that the progenitor can be single, or could be formed through binary channels that cause the progenitor star to be stripped by, accrete mass from, or merge with a close companion. The initial formation requirements for binary channels are more complex than the single-star models, but they are also more flexible given that mass and rotation can be transferred to the progenitor after birth. Thus, investigating any trends in metallicity is vital to place the progenitor and explosion properties in context.

Metallicities of host galaxies can be measured directly from emission lines in the host spectra. However, when spectroscopy is unavailable, indirect methods (described earlier in this chapter) can be used. One can infer the metallicity from galaxy luminosity (a tracer of a galaxy's stellar mass) using the long-established mass–metallicity relationship. As an alternative, the metallicity can also be inferred by using stellar population synthesis model fits to broadband multi-wavelength galaxy photometry (Conroy, 2013).

Graur et al. (2017a,b) investigated the relative rate of CCSNe subtypes across different galaxies and found that the relative rate of stripped-envelope Ib/c SNe versus non-stripped CCSNe declines in low-mass ($<10^{10}$ M$_\odot$) galaxies; they are underrepresented by a factor of $\sim$3. In addition, there appears to be a strong metallicity bias, with the relative rate of Ib/c to II SNe increasing with metallicity. However, this is not interpreted as evidence for the single-star scenario since the single-star stellar evolution models under predict the observed absolute numbers of SE-SN, therefore the binary scenario could be important and there could be multiple channels at play. In addition, the binary scenario can also show a strong metallicity dependency, although binary star channels are much more uncertain than the single-star channel.

Nevertheless, there are some subtle differences even within the stripped-envelope supernova population itself. Arcavi et al. (2010) found that while the relative rate

of Ic SNe vs non-stripped CCSNe increases in high-mass galaxies, the relative rates of all other SE-SNe types (Ic-BL, Ib, IIb) are lower in high-mass galaxies. These results could be interpreted as a metallicity effect – a similar progenitor will lose its hydrogen envelope and explode as a Ic SN in a metal-rich environment. However, in a low-mass galaxy, due to reduced metallicity-driven mass loss, it will retain some of its hydrogen and helium envelope and explode as Ib/IIb event.

This low-mass, low-metallicity preference is particularly strong for the more energetic cousins of Ic SN, Ic-BL (with and without LGRB associations) and SLSN-I which are often found in the lowest-mass hosts relative to all other classes of CCSNe (Kelly & Kirshner, 2012; Japelj et al., 2018; Modjaz et al., 2019; Neill et al., 2011), even though all these supernova types require that a massive progenitor star must lose its hydrogen envelope prior to death.

However, this stark host difference between ordinary and energetic stripped-envelope supernova (SLSN-I, LBRB-SN and Ic-BL), coupled with the fact that only a small fraction of massive stars explode as SLSNe and LGRB-SNe suggests that special circumstances must be involved in their production (i.e., not only do they require a massive star with >8 M$_\odot$ on the MS). There is probably a different formation scenario, where the star has to be *super-massive* and/or *rapidly rotating* when it explodes.

LGRB progenitors harbour a jet from a compact central engine, which requires a compact and rapidly rotating stellar core. In the single-star progenitor scenario, the star must be massive and rapidly rotating at birth and maintain a high rotation rate throughout its life which will mix the hydrogen envelope of the star, so that it evolves to be chemically homogeneous. This favours a low-metallicity progenitor $< 0.2 - 0.3$ Z$_\odot$, which leads to a more compact, faster rotating massive star, with weaker stellar winds (high mass loss would quickly sap the progenitor of its rotational energy) (e.g. Hirschi et al., 2005; Yoon & Langer, 2005; Woosley & Bloom, 2006). In contrast, the single-star progenitor scenario of ordinary Ic SNe probably requires a higher metallicity so that strong stellar winds cause the stars to shed its hydrogen and sometimes also its helium stellar envelope (Japelj

et al., 2018; Modjaz et al., 2019).

To produce a central engine powered SLSN-I, the progenitor would also need to possess a rapid rotation. In single-star models, the progenitor would require a low-metallicity so the rotational energy is not sapped from the progenitor due to wind-driven mass-loss. PISNe and PPISNe explosions of super-massive stars >90 $M_\odot$ could also power SLSNe. Such massive stars posses powerful stellar winds. Therefore, to enable the star to retain most of its stellar mass before the explosion, it would have to have a sub-solar metallicity.

However, binary interactions occur in three quarters of massive stars (Sana et al., 2012). When binary progenitor channels are considered, angular momentum and mass can be transferred to the progenitor after birth, right up to explosion, so the metallicity requirements are less stringent than in single-star models. A progenitor for the central engine model need not be as low metallicity since angular momentum can be transferred by a companion. In addition, a massive star that may produce a PISN or PPISN may be formed via dynamical interactions in young and dense star clusters. These stars would be exclusive to young and high-mass clusters that are compact in nature (Figer, 2005), but their rate may still be enhanced at low-metallicity (van den Heuvel & Portegies Zwart, 2013).

Analysis of host galaxy samples based on metallicity measurements taken locally at the transient explosion site suggests that the progenitors of SLSNe-I and LGRBs do have a strong preference for sub-solar metallicity: high-metallicity environments rarely produce LGRBs (Krühler et al., 2015; Vergani et al., 2015; Japelj et al., 2016a; Perley et al., 2016b; Palmerio et al., 2019) or SLSNe (Perley et al., 2016a; Schulze et al., 2018; Chen et al., 2017a). LGRB production is strongly suppressed at metallicities above ~0.3–1 $Z_\odot$ (Krühler et al., 2015; Vergani et al., 2015; Japelj et al., 2016a; Perley et al., 2016b; Palmerio et al., 2019), whereas SLSNe-I seem to require even lower metallicities than LGRBs or Ic-BL SNe: their production efficiency seems to be suppressed above ~0.4–0.5 $Z_\odot$ (Perley et al., 2016a; Chen et al., 2017a; Schulze et al., 2018). One must note that these metallicity threshold measurements are the preferred values that result from

a wide range of LGRB and SLSN samples and in some cases different methodologies, leading to some uncertainty in the threshold. For example, if there is global metallicity variation (Afflerbach et al., 1997), or small pockets of low-metallicity gas within the galaxies, then the measured host metallicity may be different from the progenitor metallicity. In addition, there are also uncertainties in the different line ratios used for metallicity estimation.

Individual studies have also shown that a small fraction of the SLSN-I population occur in very low metallicity hosts of less than 0.1 $Z_\odot$ (Lunnan et al., 2013; Chen et al., 2013). Some SLSNe could require even lower-metallicity environments than LGRBs, which could lend support to PISN models that require a low-metallicity or super-massive star to form. However, as the statistical sizes of nearby SLSN and LGRBs have increased, there have also been some massive spiral galaxies with high metallicities that have hosted SLSN-I (MLS121104, PTF10uhf, SN 2017egm, Lunnan et al., 2014; Perley et al., 2016c; Dong et al., 2017) and nearby LGRBs (e.g. Izzo et al., 2019). Also if there has been significant infall of low metallicity gas due to a merger, global metallicity gradients in the host, or even small pockets of low-metallicity gas, these scenarios would not require a low-mass galaxy. Thus it is likely that there may be a variety of progenitors and explosion models at play. The emerging picture is that the stringent metallicity conditions predicted by single-star models are not represented in the host galaxy populations, so binaries could be involved to some extent (e.g. Chrimes et al., 2020).

Comparatively, there have been few studies focusing on SLSNe-II host metallicities because most scientific attention has been given to SLSNe-I that likely require a different explosion mechanism and/or progenitor. In contrast, the luminosity of SLSNe-II is most likely determined by the strength of the interaction. SLSNe-II progenitors require an end-of-life mass-loss episode which is not a specific prediction of low-metallicity single-star models and the progenitors do not undergo chemically homogenous evolution.

SLSNe-II superficially resemble 'ordinary' IIn's and occur in galaxies which span

a wide range of masses and metallicities. But notably, some SLSN-II hosts do stand out from the bulk population. For example, two known SLSNe-II (SN 2006gy and PTF 10tpz) are in the circumnuclear regions of massive and metal-rich host galaxies, with roughly solar metallicites (Ofek et al., 2007; Perley et al., 2016c). This may suggest there is a distinct class of transient exclusive to galaxy nuclei that certainly do not favour a low-metallicity environment. Perhaps there is an alternative requirement for these SLSNe-II such as a top-heavy IMF in galaxy centres. Furthermore, some SLSNe-II have been found in faint dwarf galaxies, less massive than even some of the faintest SLSN-I hosts (Perley et al., 2016c; Schulze et al., 2018). In these low-metallicity environments, interaction models may be challenging because mass loss from stellar winds is reduced, so the CSM density should be lower. Thus, for SLSNe-II occurring in low-metallicity host galaxies another mass loss mechanism, such as PPISNe may be at play.

1.4.4 Star formation properties

There are some indications that metallicity alone may not fully explain the unusual properties of SLSN and LGRB hosts, and that the star-formation properties of the host may affect their production. In particular, many SLSN-I hosts are found in starburst[11] galaxies with exceptionally high star-formation rates (eg., Leloudas et al., 2015; Perley et al., 2016c; Schulze et al., 2018), in addition to their low metallicities, as evidenced by their high equivalent widths (Leloudas et al., 2015): as many as $\sim$50 per cent of SLSNe-I are found in extreme emission line galaxies (EELGs; Leloudas et al., 2015) with [O III] equivalent widths >100 Å. For example, a well-studied example of a young starburst hosting a SLSN is PTF12dam, with a stellar population of only $\sim$3 Myr (Thöne et al., 2015; Chen et al., 2015) and inferred progenitor mass >60 $M_\odot$.

Low-mass galaxies tend to experience bursty star-formation histories and are thus more likely to be starbursting at any given time in their history. Hence, if SLSNe

---

[11]We define a 'starburst' as a galaxy with a high specific star-formation rate (sSFR=SFR/M_*): specifically, a sSFR in excess of 10^{-9} yr^{-1}.

can be shown to exhibit a secondary dependence on sSFR (that is, a dependence in addition to the well-established dependence on metallicity), this would, at minimum, require a short-lived progenitor (Leloudas et al., 2015; Schulze et al., 2018). However, it could also point towards an *intrinsic* preference that favours the production of SLSNe in starbursting galaxies, such as a top-heavy IMF (e.g. Dabringhausen et al., 2009) or the collisional model of van den Heuvel & Portegies Zwart (2013). A top-heavy IMF would allow more massive stars to form, causing a preference for SLSN to occur in starburst galaxies and this could favour the PPISN and PISN scenarios because they require exceptionally massive stars.

The collision model (see Section 1.3.1 for more details) postulates that LGRBs or SLSNe are produced in the early stages of young and dense star cluster formation as the result of gravitational dynamical processes (such as runaway collisions) (van den Heuvel & Portegies Zwart, 2013) that produce super-massive progenitor stars. In this scenario, one would expect this to occur in young (<2 Myr) and massive star clusters ($>10^4$ $M_\odot$). These characteristics point to young clusters in small star-forming galaxies or the central regions of starburst galaxies. Therefore, one may expect to see a preference towards starburst galaxies and perhaps in galactic merger environments, even after accounting for the fact that any CCSN is proportionally more likely to occur in a galaxy with a high SFR.

Nevertheless, there is conflicting evidence for this scenario, since many (perhaps most) SLSN-I hosts are no more obviously star-forming than the general star-forming galaxy population. While many SLSN host galaxies do have high-UV SFR densities, attributing the SLSN host properties to an altered IMF is hard to reconcile because SLSNe do not usually form in the brightest regions of their host galaxies (Lunnan et al., 2015).

A complicating factor is that all of the key galaxy observational parameters we may want to use to diagnose the nature of the progenitor (e.g. stellar mass, metallicity and sSFR) correlate across the star-forming galaxy population (e.g. Tremonti et al., 2004; Salim et al., 2007). For example, a low-mass and low-metallicity galaxy tends to have a star-formation history with short bursts of

concentrated star-formation and therefore is more likely to be observed as a star-burst than a high-mass and high-metallicity galaxy. Thus, it is still unclear to what extent the environmental properties of SLSNe and LGRBs (low-mass, low metallicity and high sSFR) reflect their specific physical influences (progenitor and explosions mechanism).

Understanding these environmental trends is in part limited by our overall lack of knowledge about the low-metallicity dwarf galaxies, which the SLSN and LGRB populations tend to inhabit. Also, the high redshift nature of LGRBs and SLSNe makes detailed local environmental studies difficult, therefore, there are few spatially resolved studies (e.g. Chen et al., 2017d).

1.4.5 Core-collapse supernovae as probes of star-forming dwarf galaxies

Star forming dwarf galaxies (broadly defined as galaxies with stellar masses $< 10^9$ M$_\odot$) are the most common type of galaxy in the Universe. While small, they contribute significantly to cosmic star-formation. Their star formation histories are erratic, with brief (10^7–10^8 year) bursts of intense star formation, and they are chemically primitive, with low metallicities (Kunth & Östlin, 2000).

Their unique characteristics mean they are also key to solving many outstanding questions in galaxy formation and evolution. They offer the closest analogues to the very first galaxies which were the driving force behind cosmic reionisation. In addition, their chemical abundance patterns provide insight into the early Universe, their luminosity functions and kinematic properties place constraints on models of star-formation and feedback (Baldry et al., 2008) and they can be used to test the ΛCDM model (Bullock & Boylan-Kolchin, 2017).

Much of our detailed understanding of star forming dwarf galaxies originates from studies of *very* local dwarfs (predominantly Milky Way satellites and a few archetypal examples within the local group). The Local Volume Legacy Survey

is by far the most reliable catalogue to study the contribution of dwarfs to the local star-formation and the starburst fraction within the local Universe because it is volumetrically complete to ∼11 Mpc (Lee et al., 2011). However, this sample contains only ∼2 dwarf starburst galaxies because it covers a limited volume, and starbursts are rare in the local Universe.

The ability to reach more distant galaxies is important because it not only offers better statistics, but also allows us to study galaxies over a larger cosmic volume, increasing the range of environments to study (including objects that are too rare to appear in a small volume) and alleviates any bias associated with local conditions of the Milky Way environment.

Beyond the local group, a great deal of our knowledge of galaxy formation and evolution is tied to galaxy field surveys. Starburst galaxy searches either rely on *deep* narrow fields such as the Hubble Deep Field (Williams et al., 1996) and the Cosmological Evolution Survey (Scoville et al., 2007) that uncover distant ($z \sim$ 1.5–6) starbursts or *wide-field*, shallower surveys such as the Sloan Digital Sky Survey (SDSS; Frieman et al., 2008) that find more local ($z < 1$) starbursts. However, SDSS does not provide spectroscopic redshifts for most objects and photometric redshifts are unreliable in the local Universe. Hence, SDSS is poor at selecting dwarf starburst galaxies with stellar masses $<10^9$ $M_\odot$.

Starbursts fall into observationally defined classes. For example, the Blue Compact Dwarf Galaxies (BCDGs; Zwicky, 1965), which (as their name alludes to) appear blue in optical and ultraviolet colours. They have compact gas and stellar distributions (van Zee et al., 1998) and often show signs of recent mergers or interactions. They have observationally strong emission lines indicating intense star formation and exceptionally low gas-phase metallicities (Terlevich et al., 1991). One variant of BCDGs, are the so-called 'green peas', that were discovered as unresolved (at intermediate redshifts between $0.11 < z < 0.36$) small, green point sources in the Galaxy Zoo project using SDSS (Cardamone et al., 2009; Izotov et al., 2011). These galaxies are strong [OIII] 5007 Å emitters, giving them their

distinctive green colour in SDSS false colour images.[12] Green peas are thought to resemble primordial starbursts in the early Universe.

Studies of starburst-like galaxies do exist at higher redshifts too, and they contribute significantly to the star formation density at redshifts between $1 < z < 2$ (Chary & Elbaz, 2001). However, they are generally more massive galaxies $>10^{11}$ M$_\odot$ because smaller galaxies are more observationally challenging to study and metallicity and star formation measurements become increasingly difficult especially at $z > 1$ (Kewley et al., 2013). Even in the relatively local Universe (<100 Mpc), most dwarf galaxies are systematically missed by spectroscopic galaxy surveys. Thus, despite the importance of studies of more distant dwarf galaxies outside of the local volume (>11 Mpc), the starburst fraction in dwarf galaxies outside of the local volume is uncertain.

The evolution of the cosmic SFR provides a sensitive probe of galaxy formation and evolution. The cosmic SFR peaks at a redshift of $z = 1 - 2$ (Madau et al., 1996; Madau & Dickinson, 2014) and declines exponentially from $z \sim 1$ to $z = 0$ (Lilly et al., 1996). In addition, the 'cosmic downsizing' of star formation (Cowie et al., 1996; Juneau et al., 2005) is important since massive galaxies acquire the bulk of their stellar mass earlier than low-mass galaxies and their star formation rate decays faster, whereas since $z < 1$, most of the SFR activity occurs in lower-mass ($<10^{10}$ M$_\odot$) galaxies.

Mapping the SFR density requires detailed knowledge of the luminosity function and the flux limit of the survey. Since galaxy field surveys select galaxies based on their flux, they naturally under-represent dwarf galaxies – the small sizes and faint luminosities of these galaxies mean they often remain undetected (their flux falls below the detection limit of the survey). Due to the short progenitor lifetime of massive stars, CCSNe are a fantastic alternative method to directly probe star formation density. The CCSN rate can be used to measure the cosmic SFR and its evolution with time up to a redshift of $z \sim 2.5$ (Strolger et al., 2015). Likewise the LGRB rate has been used to extend this to very high redshifts because LGRBs

---

[12]For which 'green' is actually r-band but corresponds to green light in the rest frame.

can be detected out to $z \sim 6$ (e.g. Chornock et al., 2014; Melandri et al., 2015).

This thesis focuses on strictly low-redshift host galaxy samples. The SLSN and LGRB samples are at a redshift out to $z = 0.3$, with a comoving distance of ~ 1500 Mpc. The CCSN sample covers a redshift out to $z < 0.08$, with a comoving distance of ~ 340 Mpc. At these distances, redshift evolution of the star formation density and downsizing will play a marginal role, but when performing sample comparisons between the host galaxies, it is important enough to require a correction procedure.

CCSNe (Conroy & Bullock, 2015) and LGRBs can also be used to pinpoint extremely low-luminosity star-forming galaxies for detailed study and they provide an alternative method to build large and representative sample of galaxies because they select galaxies independently of their luminosity. These samples include dwarf galaxies that would otherwise be too faint to detect with standard techniques (e.g. Sedgwick et al., 2019). Also a high-quality sample of 'ordinary' CCSN hosts (which one can assume samples the explosions of 'typical' massive stars) can provide testable predictions for where we might expect SLSNe and LGRBs to occur under various hypothesis about their formation preferences. This can help to disentangle the role of metallicity and SFR and determine whether both properties are equally important in governing SLSN and LGRB production. The advantage of using a galaxies sample selected by CCSNe is that it is selected in the same manner as SLSNe or a LGRBs—via the explosion of a massive star as detected in a time-domain imaging survey. This minimises the large methodological differences between selecting dwarf galaxies via CCSNe vs. selecting via galaxy counts in flux-limited surveys that must then be weighted in proportion to their star formation rate.

Thus far, there have been a handful of individual studies specifically devoted to CCSNe that exploded in dwarf galaxies (Young et al., 2010; Prieto et al., 2012), but a large-scale statistically useful study has been lacking. Until recently supernovae were rarely discovered in dwarfs – traditional supernova surveys prioritised discovery efficiency by using a galaxy-targeted approach to search nearby

and relatively high-mass galaxies for transients (see Section 1.2.1 for a historical overview of supernova searches). These searches were insensitive to transients that might occur preferentially in faint hosts and they introduce obvious selection biases toward high-mass galaxies that may shift the observed galaxy mass distribution towards the high-mass end.

In more recent transient searches, wide-field cameras are used to survey the entire night sky on timescales of a few days. These untargeted searches are unbiased by host galaxy mass and find SNe over a much larger cosmic volume than galaxy targeted searches. A small but significant fraction of these SNe will explode in dwarf galaxies. However, even if a supernova survey's sky coverage is not biased towards particular galaxies, a variety of other biases can still result in a supernova sample that is not necessarily fully reflective of the underlying distribution.

Spectroscopic completeness is important for a number of reasons. Firstly, it allows one to distinguish between SN Ia and CCSNe, so that the CCSN sample contains only the hosts of dying massive stars and is not contaminated by other transient types which could bias the masses and star-formation rates of the sample. For example, SN Ia explode in a variety of environments in both young and old stellar populations, therefore including them would bias the host sample towards older populations. Secondly, it allows the CCSN population to be individually typed for comparisons of CCSN sub-types. Lastly, a spectroscopic classification provides a redshift estimate which is vital to determine a host galaxy luminosity. This is important for local dwarf galaxies, where photometric redshifts are unreliable and often do not have publicly available spectroscopic redshift estimates.

In addition, if selection criteria in discovery or in spectroscopic follow-up is dependent on the nature of the host galaxy then the sample will be biased towards the criteria that are used. Other spectroscopic follow-up biases can also lead to a biased sample, for example, the PTF untargeted CCSN sample (Arcavi et al., 2010) still suffers from biases where certain supernovae were given spectroscopic follow-up priority over others based on science goals at the time of observations. This results in incomplete sampling of the underlying CCSN population.

1.5 Thesis Outline

The primary result of my thesis is a new study of an untargeted and unbiased[13] sample of CCSNe to address the questions discussed in Section 1.4.5. Chapter 2 describes how this sample was compiled, analysed and compared to the host galaxies of SLSNe and LGRBs. Chapter 3 includes my work to help build future supernova catalogues that will be larger and have better systemics than any previous supernova survey. For example, the ZTF BTS sample is a project that spectroscopically classifies and publicly announces new bright transients (m < 18.5), with the overall aim to gather a large, well-defined supernova sample. This project relies on a number of spectroscopic resources, including a large role for LT. In addition, the ZTF SLSN sample, and efforts to find and study new classes of transients like AT2018cow. Finally, in Chapter 4, I present concluding remarks and ideas for future work that naturally follow on from the work described in this thesis.

Throughout this this we adopt ΛCDM cosmology, with $\Omega_0 = 0.27$, $\Omega_\Lambda = 0.73$ and $H_0 = 70 \mathrm{kms}^{-1}\mathrm{Mpc}^{-1}$ (Komatsu et al., 2011).

---

[13]In this thesis, 'unbiased' SN samples is used to refer to supernova samples that are gathered from all-sky, untargeted searches, as apposed to galaxy-targeted searches. These untargeted samples are unbiased by galaxy mass, so are a fantastic resource for host galaxy and demographic studies.

Chapter 2

Supernova host galaxies

2.1 Introduction

As discussed in the introduction, comparison between the host populations of different CCSN classes are among the most powerful tools to help constrain the progenitors. However, pre-existing studies of CCSN hosts suffered from various limitations and biases related to supernova discovery and follow-up.

In this chapter, I take advantage of unbiased supernova samples to provide new insights into the explosive endpoints of massive stars through their host galaxy environments. I compile a large, unbiased, representative sample of CCSN host galaxies (which sample the explosions of 'typical' massive stars, unlike SLSNe and LGRBs) using four years of the ASAS-SN survey. I provide UV-through-NIR photometry of this sample and derive stellar masses and star-formation rates by modelling the host galaxy spectral energy distribution, and make comparisons to samples of SLSNe and LGRB host galaxies.[1]

---

[1]This chapter has been submitted for publication in MNRAS.

2.2 Host galaxy samples

A supernova sample suitable for an unbiased statistical study of the explosion locations of massive stars must have several properties. First, it must enclose a sufficiently large volume such that it is not subject to strong cosmic variance effects. Second, the SNe must be discovered in an unbiased way (not via galaxy-targeted surveys). Third, the sample must be able to securely distinguish CCSNe from Ia SNe for all transients, ideally via spectroscopy. Finally, it must have multi-wavelength galaxy data from UV to NIR in order to derive physical parameters for the hosts. Few existing SN samples have these properties, and until recently, none of the samples are at low redshift where detailed host studies are most practical. Examples of other large, untargeted SN samples include SDSS (Frieman et al., 2008; Sako et al., 2008) and SNLS (Bazin et al., 2009) but these surveys are not spectroscopically complete, and this leads to ambiguities in the classifications.

2.2.1 Core-collapse supernovae

A variety of galaxy-untargeted SN catalogues exist, including the Dark Energy Survey (Flaugher, 2005), Catalina Real-Time Survey (Drake et al., 2009), the Palomar Transient Factory (Law et al., 2009), SuperNova Legacy Survey (Bazin et al., 2009), Pan-STARRS (Kaiser et al., 2002), La Silla Quest (Hadjiyska et al., 2012), the Gaia transient survey (Hodgkin et al., 2013), SkyMapper (Keller et al., 2007), SDSS Supernova Survey (Frieman et al., 2008) and the All-Sky Automated Survey for Supernovae (ASAS-SN; Shappee et al., 2014). I draw our CCSN sample from ASAS-SN for two reasons. Firstly, almost all SNe discovered by ASAS-SN are bright enough (even with small telescopes) for the global SN community to follow-up, spectroscopically classify and derive a redshift estimate. This is important since I need an unambiguous sample of CCSN selected host galaxies and a reliable SN redshift estimate for our host analysis. Second, ASAS-SN is shallow ($m_{V,\mathrm{limit}} \sim 17$ mag) but is all-sky, so the SNe it finds are generally very nearby,

where excellent photometric galaxy information exists in public catalogues. The ASAS-SN sample is spectroscopically complete for SNe with peak V-band light curve magnitudes $m_V < 15.8$ and is roughly 50 per cent complete at $m_V =\sim 17$ (Holoien et al., 2017a).

I compile all spectroscopically confirmed CCSN discovered by ASAS-SN (2013–2014, 2015, 2016, 2017; Holoien et al., 2017a,b,c, 2019), adopting any SN classifications and redshift estimates that were updated since the initial classification was made. I include any SNe that were not discovered by ASAS-SN and therefore do not have an ASAS-SN name designation, but were 'recovered' in their data. I refer to these SNe using the designated IAU name, or the discovery group name (6 SNe) when there is no IAU name to our knowledge. For the sake of brevity, I shorten any possible supernova (PSN) object names to the first 8 digits.

There are some ambiguous classifications which are removed from the sample. I remove two claimed SLSNe: ASAS-SN 15lh was classified as a SLSN-I (Dong et al., 2016), but was omitted from the CCSN sample since it is not well understood whether this event is a SLSN or a tidal disruption event (Leloudas et al., 2016; Margutti et al., 2017) and ASAS-SN 17jz was re-classified as a SLSN-II, but its classification is ambiguous; it could be a very luminous SN-II (Xhakaj et al., 2017) or alternatively it could be an AGN (Arcavi et al., 2017). In addition, I remove SN 2015bh since the classification is ambiguous. Despite having a dataset spanning a 21 year time period, it is unclear whether SN 2015bh is the terminal explosion of the star resulting in a CCSN or if it is a precursor LBV hyper-eruption (Elias-Rosa et al., 2016; Thöne et al., 2017).

I limit our sample to a declination greater than –30° because uniform, public, deep optical survey data is not available across the entire southern hemisphere. I also impose a galactic latitude cut ($|b| < 15°$) in order to eliminate those galaxies where stellar crowding significantly affects the photometry of the galaxies and thus remove SN 2015an, 2015W, 2016bpq, 2016G, 2017eaw, 2017gpn, ASAS-SN 17ny, 17kr, and PSNJ1828 from the sample. In addition, I also impose a minimum distance cut and remove any galaxy within a 10 Mpc volume, and

Table 2.1: Division of transient types within the host galaxy samples.

Transient Type	Number
CCSN-II	72
CCSN-IIP	26
CCSN-IIb	10
CCSN-Ib/Ic	19
CCSN-IIn/Ibn	21
CCSN-Ic-BL	2
CCSN Total	**150**
SLSN-I	29
Possible SLSN-I	3
SLSN-II	21
SLSN Total	**53**
LGRB-SN	12
SN-less LGRB	5
LGRB Total	**17**

therefore remove AT 2014ge. Two supernovae (SN 2016afa and 2017ivu) have the same host (NGC 5962) and this galaxy is included twice in the host galaxy analysis.

Our sample of CCSNe is comprised of 150 SNe discovered from 2013 to the end of 2017. The redshift distribution covers the range 0.00198–0.08, with a median value of 0.014. A table with details of these galaxies can be found in Table A.4. A mosaic showing our ASAS-SN CCSN host galaxy sample is provided in Fig. 2.1–2.2. I use methods detailed by Lupton et al. (2004) to convert PS1 *gri* images into a colour composite image. Each cutout has a constant physical size scale in the rest frame of the SN host of 21 kpc on each side and a scale bar showing an angular size of 10 arcsec is shown on each cutout.

2.2.2 Superluminous supernovae

I collate our initial SLSN sample based on archival SLSNe in the literature. I include SLSN hosts from Neill et al. (2011)[2], SUSHIES (Schulze et al., 2018)

---

[2]I do not include SN1995av and SN1997cy since their classifications are unclear, SN1997cy could be a SN Ia or IIn and may be associated with a LGRB.
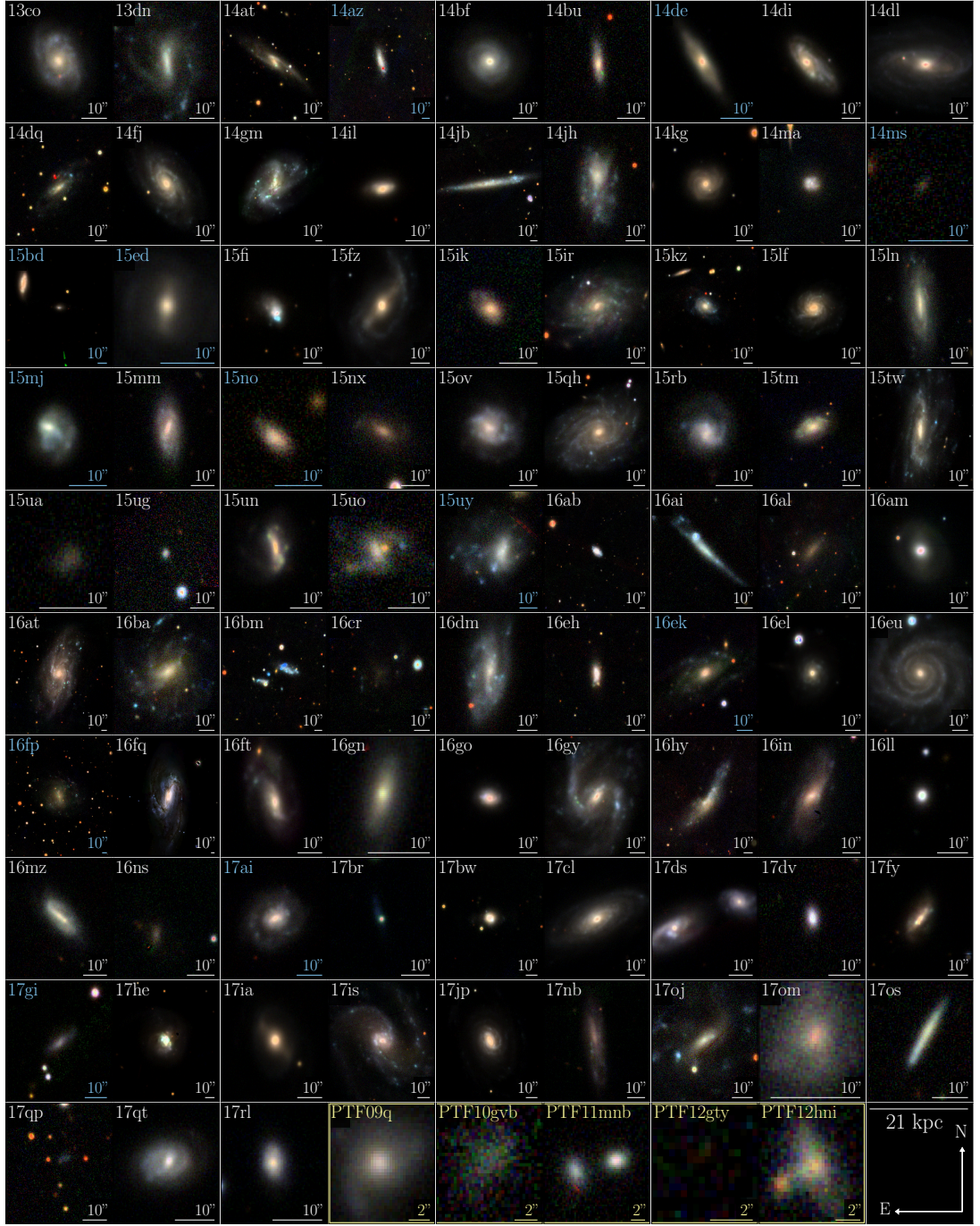
Figure 2.1: Mosaic showing RGB (*gri* PS1) colour composite images of our ASAS-SN CCSN host galaxy sample. Images labelled in white text are Type II CCSNe (excluding IIb) and images in blue are stripped-envelope SNe of type Ib/c or IIb. Each image has a constant physical size scale of 21 kpc in diameter at the redshift of the host galaxy and an angular scale of 10 arcsec is shown on each individual cutout. The image of low surface-brightness SN host 16ns is after the subtraction of a bright ($m_v \sim 17$) foreground star. The SLSN candidates that were discovered in archival PTF data are also included in the last row of the figure in yellow text. The same physical size as the CCSN is used, but with a scale bar of 2 arcsec due to their higher redshift nature.
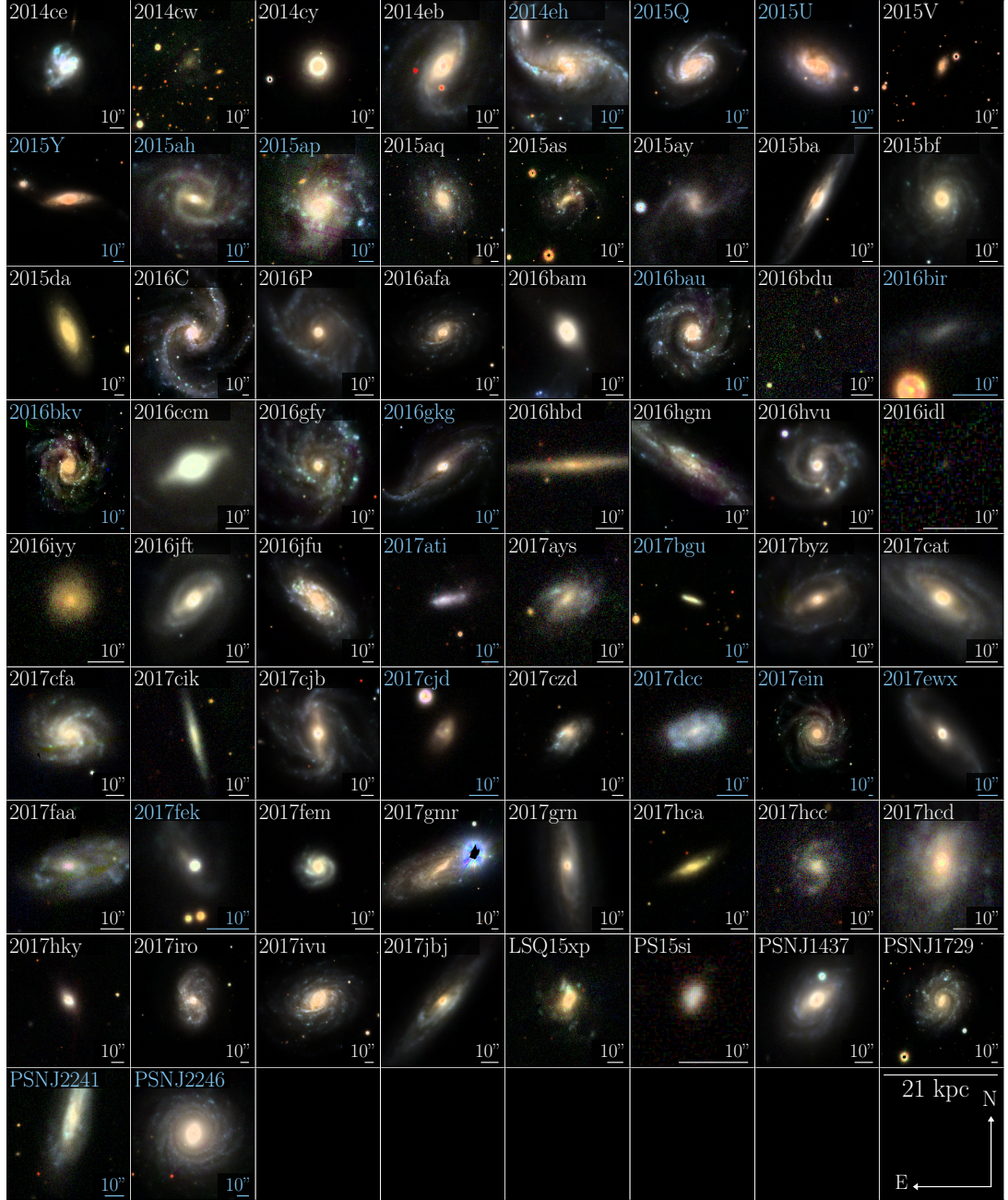
Figure 2.2: Mosaic showing RGB (*gri* PS1) colour composite images of hosts of additional CCSN recovered by ASAS-SN. Images labelled in white text are Type II CCSNe (excluding IIb) and images in blue are stripped-envelope SNe of type Ib/c or IIb. Each image has a constant physical size scale of 21 kpc in diameter at the redshift of the host galaxy and an angular scale of 10 arcsec is shown on each individual cutout.

Table 2.2: New PTF SLSN-I candidates from archival PTF search.

PTF ID	M_{peak}	$\alpha(2000)$	$\delta(2000)$	z	E(B-V)
09q*	$\sim$−20	12:24:50.11	+08:25:58.8	0.09	0.021
10gvb*	−19.6 [1]	12:15:32.28	+40:18:09.5	0.098	0.022
11mnb*	−18.9 [1]	00:34:13.25	+02:48:31.4	0.0603	0.016
12gty	−20.1 [2]	16:01:15.23	+21:23:17.4	0.1768	0.061
12hni	−19.9 [2]	22:31:55.86	−06:47:49.0	0.1056	0.054

Notes. Possible SLSN-I from Quimby et al. (2018) are indicated by a *; host analysis is done, but not included the SLSN statistical analysis due to uncertainty about the nature of the classification. 09q is reclassified as a SN Ia in (Modjaz et al., 2019).
References: [1] Quimby et al. (2018), [2] De Cia et al. (2018).

and PTF (Perley et al., 2016c). In addition, I include five candidates identified by Quimby et al. (2018) following their reanalysis of archival PTF spectra: two likely SLSNe-I (PTF12gty and PTF12hni) and three possible SLSNe-I (PTF09q, PTF10gvb and PTF11mnb) at slightly lower luminosities (M > -21 mag) than the PTF sample of SLSN host galaxies by Perley et al. (2016c). These SN properties are summarised in Table 2.2. Rest frame g-band magnitudes for PTF12gty and PTF12hni are taken from De Cia et al. (2018) and PTF09q, PTF10gvb and PTF11mnb from Quimby et al. (2018). Thumbnail images of each host are shown in the bottom row of Fig. 2.1; the physical scale is the same as for the CCSN hosts, with a yellow scale bar of 2 arcsec.

I restrict our analysis to SLSNe with a redshift of $z < 0.3$ for two main reasons. Firstly, a high-redshift SLSNe sample is more likely to be incomplete due to the increased difficulty in spectroscopically confirming members of this class without a bright associated host galaxy. Secondly, to reduce cosmic evolution effects when comparing to our $z \sim 0.02$ CCSN sample. After making this cut and excluding PTF09q, PTF10gvb and PTF11mnb, our final statistical sample consists of 29 SLSNe-I and 21 SLSNe-II in total.

2.2.3 Long-duration gamma-ray bursts

Our LGRB sample consists of all $z < 0.3$ LGRBs discovered prior to the end of 2017 with an associated optical counterpart: a supernova, an optical afterglow, or both. The requirement for an optical afterglow is imposed to better match the optical selection of SNe used for comparison and to ensure a high degree of confidence in the host-galaxy association: while many additional low-z LGRBs have been reported based on X-ray associations alone, it is difficult to rule out the possibility that these are higher-z events seen in coincidence with a foreground galaxy.

This sample is comprised of 17 LGRBs (see Table 2.3); 12 of which have confirmed SN associations. Of those 5 LGRBs without reported SNe, two are highly-publicised events from 2006 for which a SN was ruled out to deep limits, LGRBs 060505 and 060614 (Fynbo et al., 2006; Gal-Yam et al., 2006; Della Valle et al., 2006; Gehrels et al., 2006). These appear to have genuinely different progenitors and/or explosion mechanisms from ordinary SN-associated long-duration GRBs, a possibility that makes scrutiny of their host properties particularly relevant. The remaining events, LGRBs 050826, 080517 and 111225A, have relatively poor constraints on the extinction column towards the LGRB and/or on the presence of a SN peaking 1–3 weeks after the event (e.g. Stanway et al. 2015).

2.3 Photometry

2.3.1 Multi-wavelength data of CCSN host galaxies

The galaxies in our CCSN sample are nearby ($z < 0.08$), so most are detectable in all-sky multi-wavelength surveys. Therefore our primary image and source catalogues were public surveys. I use images from: the *Galaxy Evolution Explorer* (*GALEX*; Martin et al., 2005), the Panoramic Survey Telescope and Rapid Response System (PS1; Kaiser et al., 2010), the Sloan Digital Sky Survey (SDSS;

Table 2.3: Table of LGRB sources with and without SN associations. SN names and discovery reports are referenced and photometric (P) or spectroscopic (S) reports are indicated.

LGRB	SN name	SN Reference
980425	1998bw	[1,S]
020903	SN[†]	[1,S]
030329A	2003dh	[1,S]
031203	2003lw	[1,S]
050826	–	–
060218	2006aj	[1,S]
060505	–	–
060614	–	–
080517	–	–
100316D	2010bh	[1,S]
111225A	–	–
120422A	2012bz	[1,S]
130702A	2013dx	[1,S]
150518A	SN[†]	[1,P]
150818A	SN[†]	[1,S]
161219B	2016jca	[2–6,S]
171205	2017iuk	[7–13,S]

Notes. [†]In these cases, the LGRBs do have associated SNe but there is no known SN name designation on TNS.

References: [1] Refer to Table 4. in Cano et al. (2017b), [2] de Ugarte Postigo et al. (2016), [3]Volnova et al. (2017), [4] Chen et al. (2017d), [5] Ashall et al. (2019), [6] Cano et al. (2017a), [7] de Ugarte Postigo et al. (2017), [8] Cobb (2017), [9] Prentice et al. (2017), [10] D'Elia et al. (2018), [11] Wang et al. (2018), [12] Suzuki et al. (2019), [13] Izzo et al. (2019).

York et al., 2000) and the Two Micron All-Sky Survey (2MASS; Huchra et al., 2012).

Our aim is to derive consistent mass and star-formation estimates for our host galaxy sample, thus I match aperture sizes across the optical and NIR wavelengths. This is particularly important for nearby and massive galaxies, since the aperture size can significantly increase or decrease the flux measurements. In addition, the automated pipeline of *GALEX*, 2MASS and *WISE* often incorrectly deblends galaxies with a large angular diameter on the sky and does not capture the low surface brightness parts of the galaxy.

If available, I use SDSS *ugriz* and *GALEX* FUV and NUV photometry from the NASA Sloan Atlas (NSA) (NSA; Blanton et al., 2011). The NSA is a unified catalogue of galaxies out to $z \sim 0.05$, optimised for nearby extended objects since the flux measurements are derived from reprocessed SDSS images with a better background subtraction (Blanton et al., 2011). I use the elliptical petrosian aperture photometry, with an elliptical aperture radius defined by the shape of the light profile of the galaxy as in Blanton et al. (2011) and Yasuda et al. (2001). The NSA flux measurements are available for about half of the northern hemisphere sample. Otherwise, I perform the photometry using optical images downloaded from Pan-STARRS DR1 (PS1) (Chambers et al., 2016; Magnier et al., 2016) and if SDSS *u*-band is available, I also perform that photometry.

I use the 2MASS extended source catalogue to obtain NIR brightness measurements in the *J*, *H* and K_s filters (Huchra et al., 2012). The *WISE* photometry has a much wider PSF (6 arcsec) than the 2MASS photometry (2.5 arcsec) and therefore for nearby galaxies often required a deblending analysis. In addition, *W1* and *W2* are sensitive to evolved stellar populations and hot dust and *W3* is sensitive to PAH as well as the dust continuum. This makes SED modelling using the *WISE* bands difficult and may introduce additional uncertainties into the SED fits, therefore I do not use the *WISE* photometry in this analysis.

If the galaxy is in the NSA, I redo the 2MASS photometry with the same axis ratio

and aperture orientation and use the curve of growth technique to adjust the size of the aperture. If the galaxy is not within the NSA, I check whether the 2MASS extended aperture (which fits an ellipse to the 20 mag arcsec^{-2} isophote in the K_s band and uses a curve of growth technique to capture low surface brightness flux of the galaxy) is adequate. In the cases of galaxies with small angular size, the aperture is usually adequate, but in the case of high-mass, extended galaxies the aperture often misses a substantial fraction of the flux, thus I redo the 2MASS photometry.

2.3.2   Procedure for CCSN hosts

I perform aperture photometry using the python program PHOTUTILS[3]. I use an elliptical aperture and a curve-of-growth technique. I place the elliptical aperture at gradually increasing radii, measuring the flux in each aperture until the curve-of-growth levels, to the order of a few per cent, meaning the aperture is sufficiently large to include all of the host galaxy flux.

I derive the uncertainties on these photometric measurements by using the galaxy aperture to determine the brightness of the background sky. I place the galaxy aperture 30 times within the image on 'blank' patches of the sky, making sure there is no overlap between apertures. I take the standard deviation of the measurements. In some cases, the galaxy is sufficiently massive and nearby that it covers a large angular diameter on the sky: placing 30 apertures of this size on blank patches of the sky is not feasible in these instances (the aperture region will always contain field sources), and in many cases the image itself is simply not large enough to place the aperture in 30 non-overlapping locations. In these cases, I remove the sources from the image and calculate the standard deviation of the sky background. Because this procedure does not account for photon noise originating from the galaxy itself, it is technically a lower limit on the uncertainty. However, in cases where the galaxy is bright enough that the statistical

---

[3]https://github.com/astropy/photutils/tree/v0.3

uncertainty is dominated by galaxy photon counting noise instead of sky noise, systematic sources of uncertainty (flat-fielding and large-scale sky subtraction) generally dominate anyway and these are accounted for in the aperture-based analysis.

For image calibration, I have used catalogues of stars (PS1 Object Catalogue, 2MASS Point Source Catalogue and the SDSS Imaging Catalogue) to calculate a zero point for each image. Instrumental magnitudes were calibrated directly to the AB system with photometry from PS1. All magnitudes were converted into the AB system (Oke & Gunn, 1983). In addition, I correct all photometry for Galactic foreground extinction (Schlafly & Finkbeiner, 2011).[4]

2.3.3 Galaxies requiring special attention

Some host galaxies in our sample required extra care when performing photometry and when fitting SED models. These galaxies are either diffuse, low surface brightness galaxies, galaxies which show signs of interaction with nearby galaxies or where there are foreground stars (or other objects) in front of the galaxy, or galaxies where there is some prior indication of AGN. Below, I briefly describe each case where galaxies are treated individually.

Interacting galaxies

A significant number of host galaxies (in both the CCSN and extreme-SN samples) show evidence of physical companions, some of which appear to be in the process of interacting or merging. Our general philosophy is to mimic the photometry steps and subtraction I would do if these ASAS-SN galaxies were observed at $z \sim 0.2$ (for comparison to the LGRB and SLSN samples). I treat the merger as one system if it would not be resolved at $z \sim 0.2$ and is in the advanced merger

---

[4]SN 2003ma pierces through the Large Magellanic Cloud, and the Galactic extinction of E(B–V) = 0.348 mag is a lower limit of what one would expect in this direction (Rest et al., 2011).

stages, whereas if the galaxy could be resolved at those redshifts, then I measure the photometry of the single galaxy at the SN site.

ASAS-SN 14de: This galaxy is possibly undergoing an interaction or merger. This system would barely be detectable as two individual galaxies if it was discovered at a similar redshift to the SLSN/LGRB sample ($z \sim 0.2$), therefore I quote two different measurements for photometry: one of the entire system and one of the single galaxy from which the SN originated.

SN 2015Y: This SN exploded in NGC 2735 at $z = 0.00817$, which is interacting with MCG+04-22-003 at $z = 0.00827$. I do not include MCG+04-22-003 in the flux measurement.

ASAS-SN 16bm: This host galaxy does not have a catalogued redshift. However, it is possibly undergoing an interaction or merger since the SN redshift $z = 0.007$ is similar to the redshift of a companion galaxy at $z = 0.00686$. The galaxies are 35 arcsec apart, However if the system was at $z \sim 0.2$ their centres would be separated only by 1 arcsecond. Thus, this system would barely be detectable as two individual galaxies if it was discovered at a similar redshift to the SLSN/LGRB sample ($z \sim 0.2$), therefore I quote two different measurements for photometry: one of the entire system and one of the single galaxy from which the SN originated. I use the photometry of the system for the SED fit.

ASAS-SN 17ds: The host galaxy appears to have a companion in the PS1 imaging. However, an SDSS spectrum confirms that the redshift of this galaxy is $z = 0.046$, compared with the host galaxy with a redshift $z = 0.022$.

PTF12hni: There is a small, red object to east of the host galaxy (see panel 5 in Fig. 2.1). An archival KeckII/DEIMOS spectrum from 2017 July 13 confirms that this red object is at $z = 0.185$ and not associated with the host galaxy with redshift $z = 0.1056$. For this reason, I am careful not to include this object in the photometry aperture.

PTF11mnb: The host appears to have a companion galaxy (see bottom right

panel in Fig. 2.1). Thus, the galaxy on the west of the image was removed since the low surface brightness flux of the galaxy overlaps. Thus, I use the program GALFIT (Peng et al., 2002) to model and subtract any contaminating objects from the image and then use the procedure outlined in Section 2.3.2 to perform aperture photometry on the galaxy.

Unclear host galaxy

SN 2016bam: This SN was originally reported reported to TNS as being hosted by the elliptical galaxy NGC 2444, which is interacting with NGC 2445. The supernova exploded between these galaxies, so even at low-redshift, this is a difficult case to judge which is the true host. At the typical redshift of SLSNe it would also be tricky. However, I make the decision to attribute this supernova to NGC 2445 (the southern object) instead of NGC 2444 because it is a star-forming galaxy and the supernova position is near (3.54 arcsec away from) an H II region associated with NGC 2445.

SN 2017ati: was originally reported reported to TNS as a hostless supernova. However, when looking at a larger image of the field, the SN is located between two galaxies and is 36 arcsec from one galaxy nucleus and 76 arcsec from the other galaxy. This remote location is unusual for a CCSN, but these galaxies may be interacting and plausibly there could be a faint (unseen) bridge of star-formation between these galaxies. The redshift of the SN is consistent with the nearest galaxy (KUG 0946+674), but no spectra exist to confirm whether both galaxies are at the same redshift. This places the supernova $\sim$10 kpc (36 arcsec) away from the galaxy nucleus and although the remote location of the supernova defies any prescriptive attempt to assign a host galaxy, in our analysis I assign the SN to the nearest host galaxy since this would be how I would treat this SN if it were at a typical SLSN redshift.

Foreground star contamination

ASAS-SN 14dq, SN 2014cw, SN 2016bir and SN 2017fek: These hosts are large and extended objects low-surface brightness hosts. Flux from foreground stars in these image was subtracted from these hosts.

SN 2014eh: This host galaxy has a small background galaxy and a few foreground stars covering the host. I removed the flux from these objects.

SN 2015V, SN 2015ay, SN 2016P and 2016ccm: These host galaxies all have bright stars (between 12–16 mag) nearby. Therefore in each case, the aperture was chosen carefully so that the stellar flux was not included in the flux measurements.

2017gmr: There is a very bright, saturated star (HD 16152, $m_V \sim 7.1$) covering a large area (~ 50 per cent) of the host. The stellar flux is removed. However the host flux measurement is very uncertain.

ASAS-SN 16al: There is a very bright star (BD-12 4185, $m_V \sim 9.8$) in the nearby field, causing large variations in the sky background. In addition, this object is aligned with many foreground stars which contribute to around 50 per cent of the light from the galaxy aperture. I modelled and subtracted these stars from images, but accurate photometry of the galaxy remains difficult. Thus I estimate the uncertainty in the removal of the foreground stars and incorporate an extra photometric error of 0.1 magnitudes into the photometry measurements.

ASAS-SN 16ns: This system has a foreground star ($m \sim 17$ mag) which masks a large percentage of the galaxy flux due to the small and low surface brightness nature of the galaxy. I remove this star, but the subtraction residuals remain at approximately ~ 10 per cent of the object flux in the i and z bands. Photometric uncertainties were increased accordingly.

ASAS-SN 17oj: I remove foreground stars from this image. This is a low surface brightness galaxy, so a large aperture was used to incorporate the flux in the outskirts of the galaxy.

SN 2017fek: I remove multiple foreground stars from this image before performing aperture photometry.

Active Galactic Nuclei

I checked if any of the host galaxies in our sample had an observable AGN present.[5] First, I inspected the SDSS spectra where available (55/150 galaxies) to check for an AGN flag. Three host galaxies are flagged as an AGN in the SDSS spectra: ASAS-SN 14de (SN Ic), SN 2016afa/2017ivu (SN II/IIP) and PSNJ1437 (SN II).

The line ratio [N II]6583/H α can be used to identify the presence of an AGN (Baldwin et al., 1981; Carter et al., 2001). If log([N II]6583/H α)> –0.25, I assumed the spectrum could be dominated by an AGN. According to this metric, only ASAS-SN 14de (SN Ic) hosts an (observable) AGN (log([N II]6583/H $\alpha=-0.32$); strong [O III] emission confirms it as a Seyfert II galaxy. While visual inspection of the host galaxy suggests that the AGN is unlikely to contribute significantly to the optical flux measured in SDSS/PS1, it could contribute more significantly to the IR flux, which could in turn could affect the SED derived parameters including ages of the stellar populations, star-formation rates and also dust attenuation in the host galaxy. Hence, for 14de I exclude NIR photometry for the SED fit.

Since I do not have spectra for every galaxy in our sample, I also inspected the images of each host (see Fig. 2.1) to check for a clear nuclear point source. Almost all galaxies are well resolved and few show evidence for any sort of central point source (much less a photometrically-dominant AGN). However, the following sources in Fig. 2.1 do seem to have a red point source located at the centre of the host which could be either a galaxy bulge or an AGN: 14de (a Seyfert galaxy), 14di, 14dl, 14kg, 16am, 16go, 17br and 17cl.

The following sources in Fig. 2.2 also seem to have a red point source located

---

[5]It should be noted that if a galaxy hosts an AGN, it is possible that the observations of the host may be taken when the galaxy is undergoing an AGN flare which may lead to erroneous flux of the host. However, the chance of this occurring is very small, so we ignore this possibility.

at the centre of the host which could be either a galaxy bulge or an AGN: SN 2014cy, 2014eb, and 2015bf. However, in all cases given the huge and bright galaxies an AGN cannot contribute much ($<$20 per cent) to the integrated flux in any band relevant to our SED fitting procedure. I also check the ALLWISE colours ($W1$–$W2$ and $W3$–$W2$) of the host galaxies as another diagnostic to test whether an AGN is present (see Fig. 12 of Wright et al., 2010). Aside from 14de, I find that two galaxies (15fi and 14ma) have WISE colours suggestive of a possible AGN. ASAS-SN 15fi (Mrk 0884) has an SDSS spectrum and I find a ratio of log([N II]6583 /H α)=−1.13, therefore I estimate the maximum contribution to be ∼15 per cent. I obtained a spectrum of ASAS-SN 14ma in Taggart et al (in prep) from the WHT and I find log([N II]6583 /H α)=−0.83 indicating that AGN contribution is minimal in these host galaxies.

2.3.4 Literature photometry

Photometry of SLSN and LGRB hosts was gathered primarily from the published literature. For clarity, all sources are listed in Tables A.2– 2.4. Four host galaxies in the LGRB sample lacked an estimate of the photometric uncertainty in a few bands (specifically for 980425 (*BVRI*) from Michałowski et al. (2009), 020903 (*F606W*) from Wainwright et al. (2007), 060505 (*R*) from Hjorth et al. (2012), 060614 (*F814W*) from Gal-Yam et al. (2006)). In all these cases we have large telescopes observing relatively bright galaxies, and therefore the S/N is surely very high and the only significant source of error is systematics, assuming the authors did not make any mistakes. So I assigned an uncertainty of 0.01 mag when performing the SED modelling which is consistent with the systematic floor used elsewhere. I also confirmed that this assumption produced good fits with no measurements $>$ 3-σ out of line with the SED model.

I omitted photometric data points in the literature if they were inconsistent with the other photometric points at nearby wavelengths at high significance, if there may have been contamination from the transient given the time that the data were

taken, or (in cases where contamination with other galaxies was possible) if was unclear whether the authors took deblending into account with their photometry.

2.3.5 New LGRB host photometry

I supplement the LGRB photometry from the literature with new photometry from a variety of sources, detailed below. The image reduction were performed by Dr. Daniel Perley. A summary of the photometry is presented in Table 2.4.

Spitzer / IRAC

Most of the LGRB hosts in our sample were observed using the Infrared Array Camera (IRAC; Fazio et al. 2004) on the *Spitzer Space Telescope* (Werner et al., 2004) as part of the extended *Swift/Spitzer* Host Galaxy Legacy Survey (SHOALS; Perley et al. 2016a). These observations were generally carried out in channel 1 (3.6 μm) only, although LGRB 060218 was also observed in channel 2 (4.5 μm). I used the PBCD images from the *Spitzer* Heritage Archive and photometric techniques detailed in Perley et al. (2016b), including subtraction of all neighbouring objects that might contaminate the aperture or sky background. Data from some archival programs were also reanalysed using a consistent methodology. In most cases this was straightforward. In the case of LGRB 020903, isolating the host galaxy is challenging due to the presence of a dense group of merging galaxies with complicated light profiles in the foreground. The dwarf host of LGRB 130702A is part of a smaller and more distant galaxy group (Kelly et al., 2013). The companion spiral is approximately 6 magnitudes brighter and offset by 6.5 arcsec; subtraction of its halo also leaves some residuals in the sky background. As a result, in both these cases the uncertainty on the host flux is relatively large.

Keck / MOSFIRE

LGRB 130702A was observed in imaging mode using the Multi-Object Spectrograph for Infrared Exploration (MOSFIRE; McLean et al. 2010, 2012) at Keck Observatory on the night of 2014 Jun 16 in the J and K_s filters. These data were reduced using a custom pipeline. The resolution of these images (and of archival optical data) are sufficient that there are no issues with background contamination from the nearby galaxies. Aperture photometry is performed in a standard fashion using nearby 2MASS standards.

Palomar / WIRC

LGRB 120422A was observed with the Wide-Field Infrared Camera (WIRC; Wilson et al. 2003) on the Palomar 200–inch Hale telescope on the night of 2013 Feb 17 in the J and K_s filters. The data were reduced using a custom pipeline, which includes cleaning of noise signatures associated with the replacement-detector. Aperture photometry is performed in a standard fashion using nearby 2MASS standards.

Palomar / P60

LGRB 150818A was observed extensively with the CCD imager on the Palomar 60-inch robotic telescope (Cenko et al., 2006) as part of a campaign to follow-up the supernova associated with this event (Sanchez-Ramirez et al., in prep.). A series of late-time reference images in $griz$ filters were taken on 2016 February 14 for the purposes of galaxy subtraction against the earlier supernova imaging; I employ these here to measure the host flux in these bands.

Keck / LRIS

LGRB 150518A was observed in imaging mode with LRIS (Oke et al., 1995) in the *u*-band filter on 2016 June 07. The observations were reduced with LPipe (Perley, 2019) and aperture photometry of the host galaxy was measured relative to SDSS secondary standards in the field.

Magellan / FourStar

LGRB 150518A was observed in *J*-band with the near-infrared (NIR) camera FourStar (Persson et al., 2013) at the 6.5-m Magellan/Baade Telescope (Las Campanas Observatory, Chile) on 2016 March 27 as a part of the programme CN2016A-108. The observation sequence consisted of 39 dithered images with individual integration time of 32 s. These data were reduced with the software package THELI version 2.10.0 (Erben et al., 2005; Schirmer, 2013).

2.3.6   CCSN distances

I do not have our own spectroscopy for each CCSN host galaxy. Thus, I obtain distances to each galaxy from redshift measurements as published in the NASA Extragalactic Database (NED; https://ned.ipac.caltech.edu/) where available (114/150 galaxies).

Since our CCSN sample is primarily located in very low-redshift galaxies (median luminosity distance ∼70 Mpc and all galaxies < 400 Mpc), they have peculiar velocities relative to the motion due to the isotropic expansion of the Universe as described by the Hubble Flow. The fractional distance errors from peculiar velocities could have implications for the analysis of our hosts. Thus, I correct for peculiar velocity using the velocity field model in Mould et al. (2000). This model accounts for peculiar velocities due to the Virgo Cluster, the Great Attractor and the Shapley Supercluster and is typically a 6–8 per cent correction.

Table 2.4: New LGRB host galaxy photometry.

LGRB	Filter	AB Mag	Instrument	Date
020903	3.6μm	22.30 ± 0.30	*Spitzer*/IRAC	2006-06-07
030329A	3.6μm	23.71 ± 0.11	*Spitzer*/IRAC	2017-03-31
031203	3.6μm	18.19 ± 0.01	*Spitzer*/IRAC	2005-11-29
060218	3.6μm	20.77 ± 0.02	*Spitzer*/IRAC	2012-11-07
	4.5μm	21.06 ± 0.05	*Spitzer*/IRAC	2012-11-07
060614	3.6μm	22.96 ± 0.10	*Spitzer*/IRAC	2012-11-25
080517	J	16.90 ± 0.14	2MASS	-
	H	17.12 ± 0.24	2MASS	-
	K_s	16.87 ± 0.21	2MASS	-
111225A	3.6μm	24.00 ± 0.30	*Spitzer*/IRAC	2016-12-05
120422A	3.6μm	21.12 ± 0.03	*Spitzer*/IRAC	2017-02-21
	J	20.34 ± 0.09	P200/WIRC	2013-02-17
	K_s	20.35 ± 0.17	P200/WIRC	2013-02-17
130702A	J	22.63 ± 0.17	Keck/MOSFIRE	2014-06-16
	K	21.41 ± 0.45	Keck/MOSFIRE	2014-06-16
	3.6μm	23.80 ± 0.30	*Spitzer*/IRAC	2016-11-05
150518A	u'	22.78 ± 0.03	KeckI/LRIS	2016-06-07
	g'	22.07 ± 0.14	PS1	-
	r'	21.43 ± 0.08	PS1	-
	i'	21.25 ± 0.13	PS1	-
	z'	20.65 ± 0.11	PS1	-
	y'	20.80 ± 0.34	PS1	-
	J	19.78 ± 0.03	Magellan/FourStar	2016-03-27
150818A	g'	22.30 ± 0.16	P60	2016-02-14
	r'	22.10 ± 0.20	P60	2016-02-14
	i'	21.70 ± 0.20	P60	2016-02-14
	z'	> 21.30	P60	2016-02-14
	3.6μm	21.89 ± 0.05	*Spitzer*/IRAC	2017-02-03
161219B	3.6μm	20.70 ± 0.02	*Spitzer*/IRAC	2018-01-04

Notes. Photometry is not corrected for Galactic foreground extinction. Upper limits are 2-σ. All photometry is available online in a machine-readable form.

Table 2.5: New PTF SLSN host photometry.

PTF ID	Filter	AB Mag	Instrument
PTF09q	u'	18.20 ± 0.08	SDSS
	g'	17.13 ± 0.05	PS1
	r'	16.54 ± 0.04	PS1
	i'	16.14 ± 0.03	PS1
	z'	15.98 ± 0.03	PS1
	y'	15.74 ± 0.06	PS1
PTF10gvb	u'	21.10 ± 0.22	SDSS
	g'	20.14 ± 0.07	PS1
	r'	19.85 ± 0.07	PS1
	i'	19.70 ± 0.09	PS1
	z'	19.38 ± 0.12	PS1
	y'	19.89 ± 0.32	PS1
PTF11mnb	u'	20.42 ± 0.08	SDSS
	g'	19.42 ± 0.02	PS1
	r'	19.27 ± 0.02	PS1
	i'	18.96 ± 0.02	PS1
	z'	18.88 ± 0.03	PS1
	y'	18.91 ± 0.07	PS1
PTF12gty	u'	> 21.62	SDSS
	g'	> 24.23	PS1
	r'	> 24.27	PS1
	i'	23.78 ± 0.24	PS1
	z'	22.53 ± 0.21	PS1
	y'	> 24.28	PS1
PTF12hni	u'	20.16 ± 0.20	SDSS
	g'	19.19 ± 0.01	PS1
	r'	18.94 ± 0.03	PS1
	i'	18.86 ± 0.02	PS1
	z'	18.56 ± 0.04	PS1
	y'	18.50 ± 0.10	PS1

Notes. The photometry is not corrected for Galactic foreground extinction. Upper limits are 2-σ. All photometry is available online in a machine-readable form.

If a catalogued redshift is not available for the host galaxy (34/150), I adopt the redshift of the SN, since the supernova redshift is a good estimator of the host galaxy redshift (Fremling et al., 2020). I estimate the uncertainty based on data from the Bright Transient Survey Fremling et al. (2020) which finds the standard deviation of the derived supernova redshift versus the host galaxy redshift to be 0.005.

2.4 Physical parameters

2.4.1 Spectral energy distribution fitting

To quantify stellar parameters of the host galaxies including stellar mass and star-formation rate, I model each galaxy spectral energy distribution (SED) using UV through NIR photometry. I use the code LEPHARE[6] (Ilbert et al., 2006) which uses single-age stellar population synthesis model templates of Bruzual & Charlot (2003) summed according to a single-burst of exponentially declining star-formation history with a timescale τ, ranging from 0.1 to 30 Gyr. Exponentially declining SFHs (tau models) assume that star formation jumps from zero to its maximum value at some time T0, after which star formation declines exponentially with some timescale of τ=0.1,0.3,1,2,3,5,10,15,30 Gyr. The SEDs were generated on a grid of 57 time steps (smaller time steps for younger ages) between 10 Myrs up to 13.5 Gyr.

I assume a Chabrier initial mass function (Chabrier, 2003) and a stellar metallicity set between 0.2–1.0 $Z_\odot$. The contribution of emission lines to the modelled spectra is based on the Kennicutt (1998) relations between SFR and UV luminosity. The contribution of H α and [O II] lines to the photometry is included for galaxies with dust free colour bluer than $(NUV–r)_{ABS} \leq 4$ and the intensity of the emission lines is scaled according to the intrinsic UV luminosity of the galaxy. Dust attenuation in the galaxy is applied to the SED models using the

---

[6]http://www.cfht.hawaii.edu/ arnouts/LEPHARE/lephare.html

Calzetti et al. (2000) extinction law for starburst galaxies. Where spectroscopy of the host galaxy is available and shows little evidence for nebular emission, I fit a continuum driven SED.

To calculate the uncertainties involved in deriving the mass and star-formation rate parameters, I perform a simple Monte Carlo analysis. I choose a random number from a Gaussian distribution in flux space with standard deviation equal to the photometric uncertainty on the derived magnitude for each filter and for each host. I sample from the distribution 1000 times and then run the SED fit on each set of 'noisy' photometry and use the 16-to-84th percentile of each parameter as an estimate of its uncertainty. If the reduced $\tilde{\chi}^2 \gg 1$ (before the Monte Carlo sampling) and the SED photometry is well-sampled in the UV, optical and IR, I apply additional uncertainty to the photometry equally across all photometric points, before the Monte Carlo sampling, in order to more appropriately fit these data until the reduced $\tilde{\chi}^2$ is approximately one and then re-run the Monte Carlo sampling.

A polycyclic aromatic hydrocarbon (PAH; Leger & Puget, 1984) emission feature is present within the *WISE*/W1 and *Spitzer*/3.6μm bands at $z < 0.2$. In most galaxies this emission is insignificant compared to the stellar continuum. However, in low-mass galaxies with extreme star-formation, this non-stellar feature can significantly contribute to the flux in the mid-IR. LE PHARE does not account for this emission feature. Thus I investigate if there is any evidence that this feature at 3.6 μm may affect the flux in this band, given our photometry. The only case where this might be significant is for the host of LGRB 031203. However, Watson et al. (2011) studied the mid-infrared spectrum and did not find any evidence for PAH emission in the host of LGRB 031203.

I present the spectral energy distribution fits for CCSN in Fig. 2.3, LGRBs in Fig. 2.4 and SLSNe in Fig. 2.5.
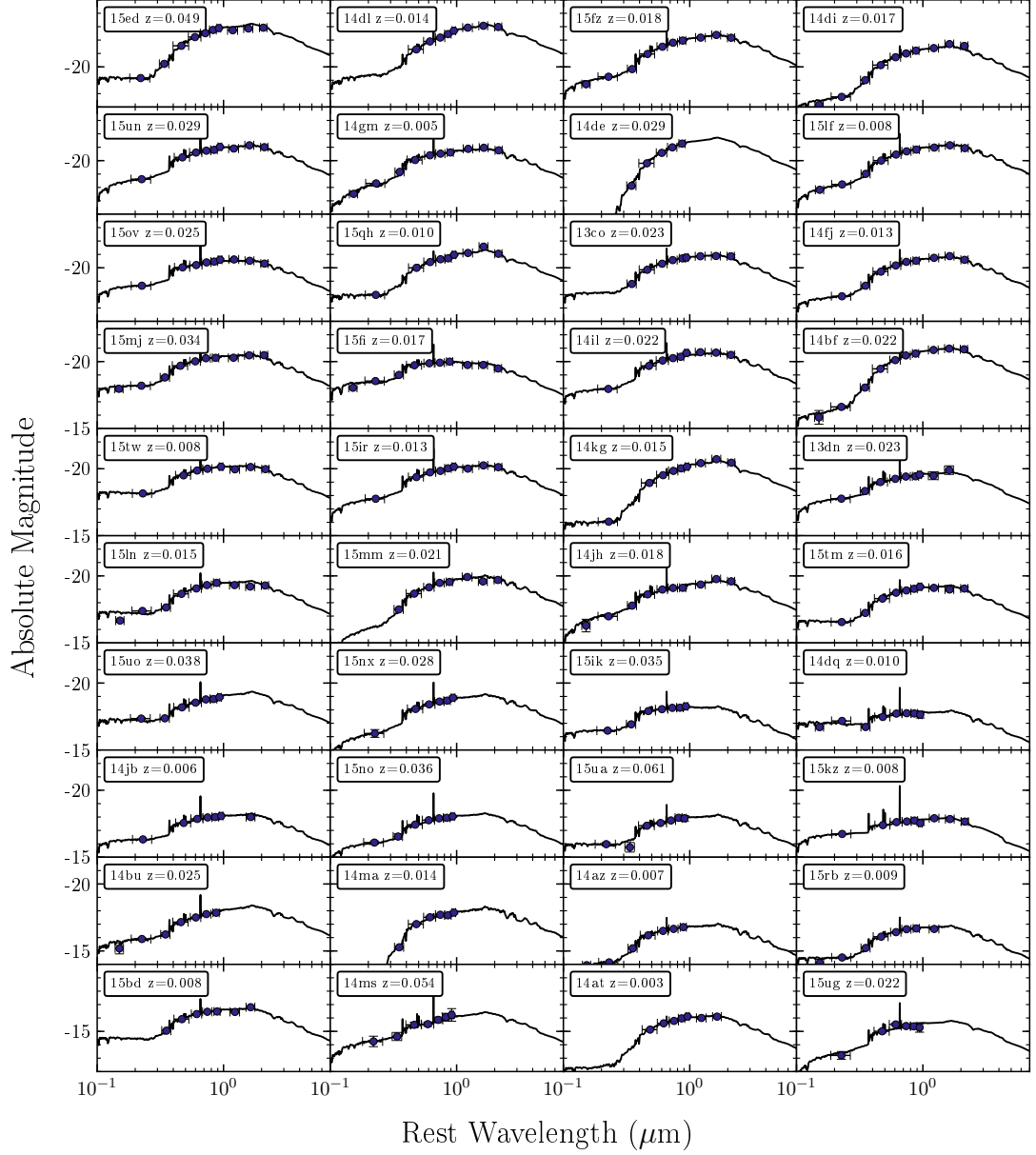
Figure 2.3: Spectral energy distributions of the CCSN host galaxy sample. The multi-band photometry is shown as blue markers and error bars show photometric uncertainties. The best-fitting SED model is displayed by the black curve, fitted to our data using the procedure outlined in Section 2.4.1. Galaxies are ordered in terms of their luminosity as measured in the r-band via the SED. The absolute magnitude axis uses appropriate limits for each row.
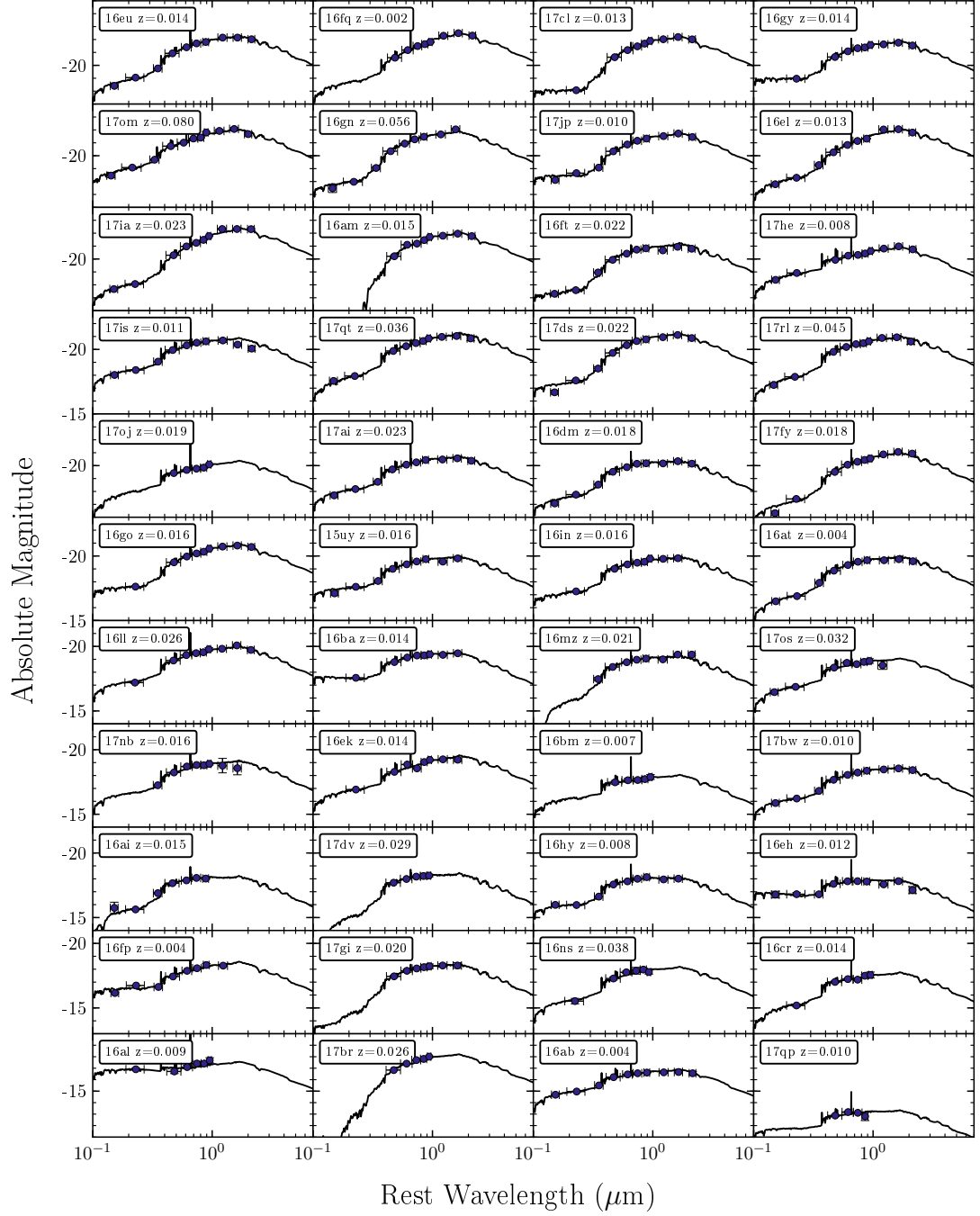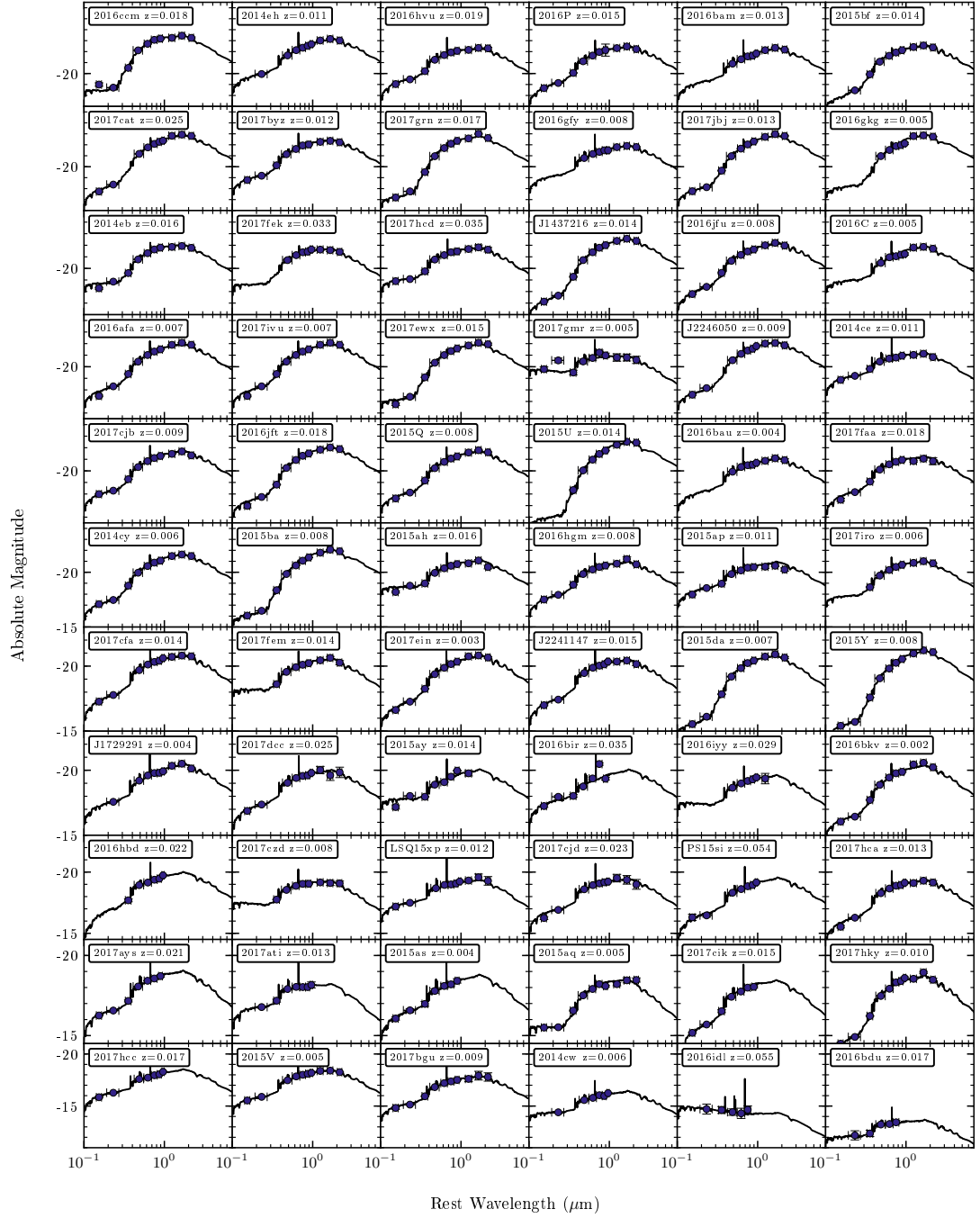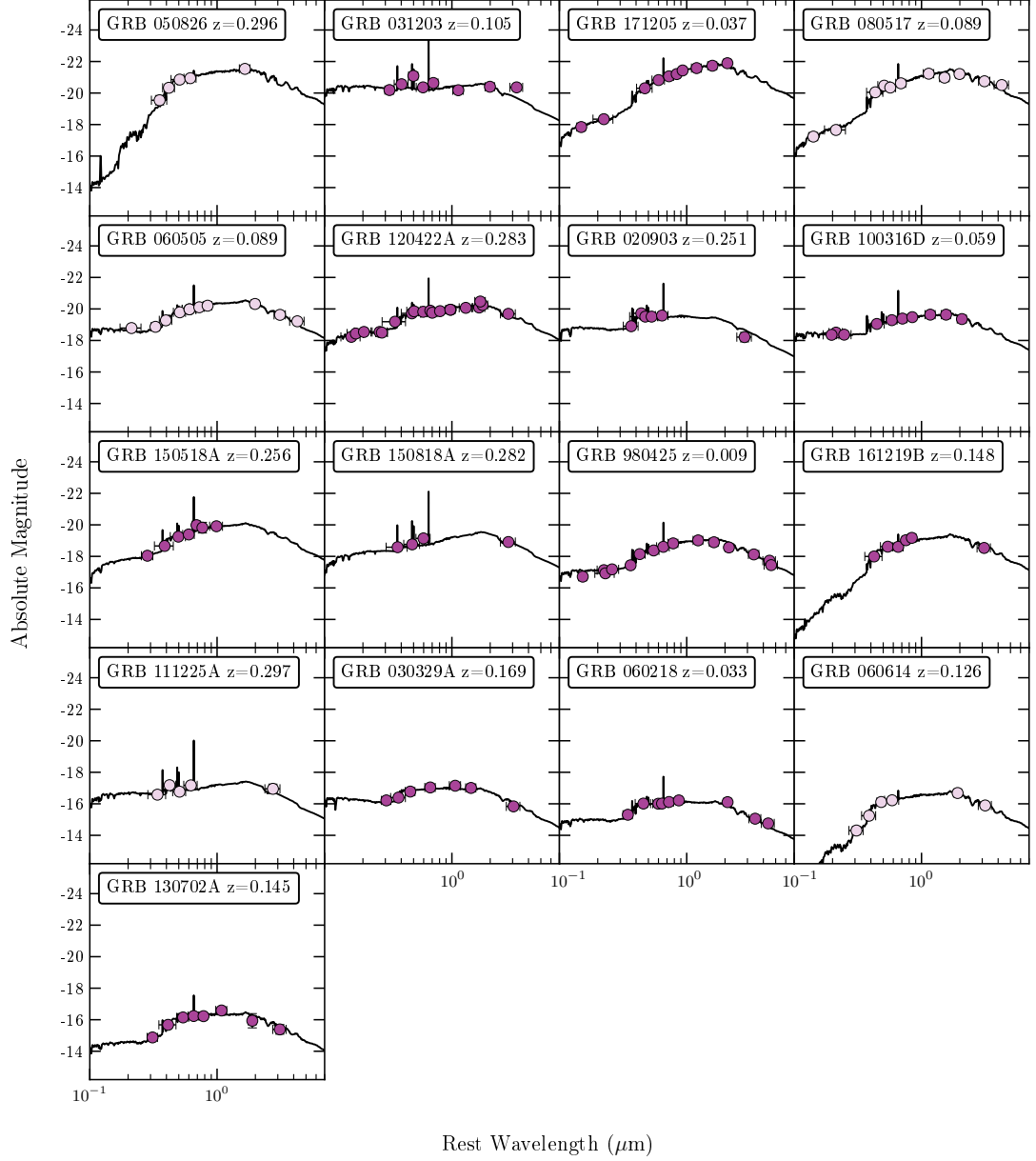
Figure 2.4: Spectral energy distributions of the LGRB sample. The multi-band photometry for LGRBs with SN are dark purple markers whereas LGRBs without SN are light purple and error bars show photometric uncertainties. The best-fitting SED model is displayed by the black curve, fitted to our data using the procedure outlined in Section 2.4.1. Galaxies are ordered in terms of their luminosity as measured in the r-band via the SED. The absolute magnitude axis uses appropriate limits for each row.
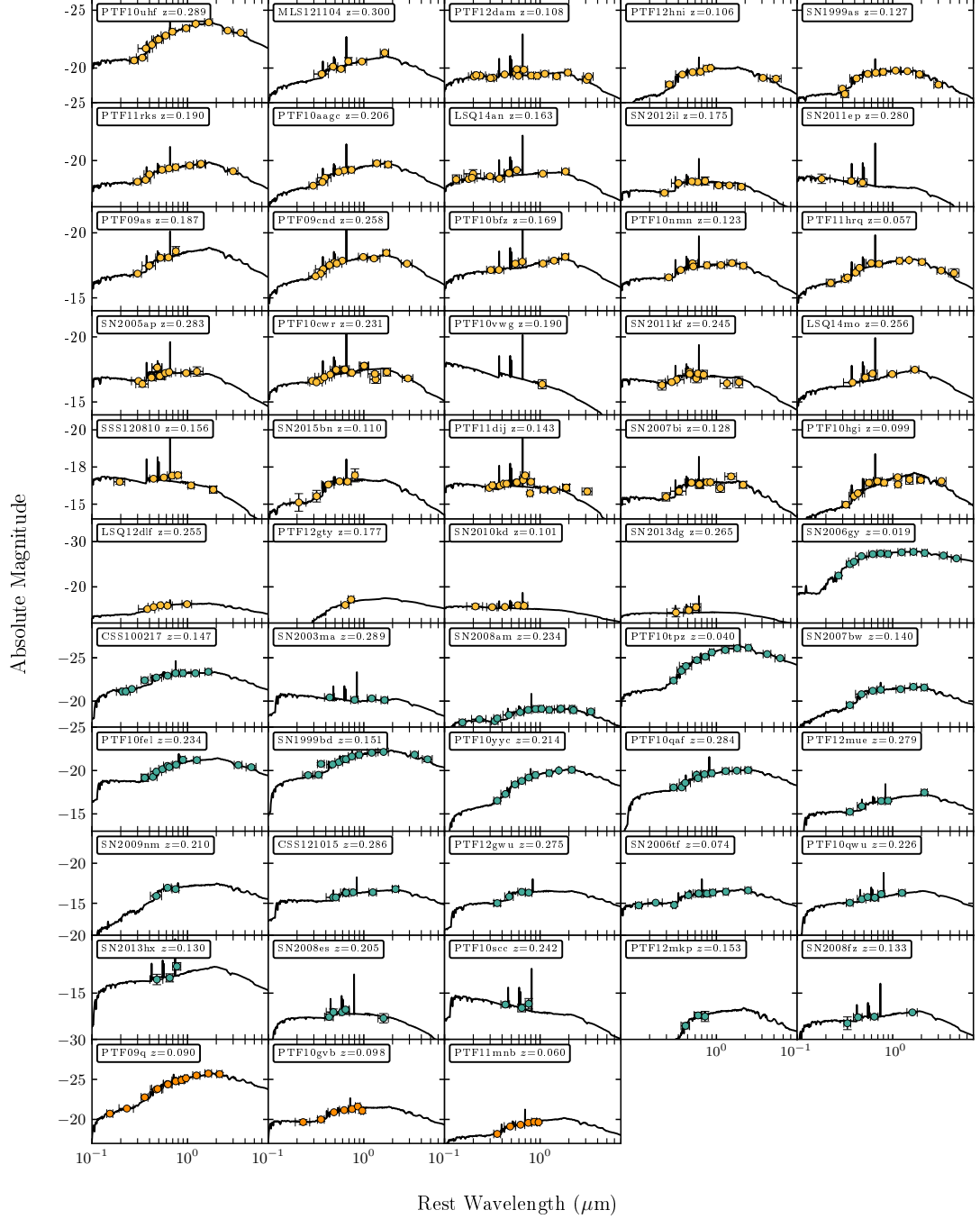
Figure 2.5: Spectral energy distributions of the SLSN sample. The multi-band photometry for SLSN-I are yellow markers, green for SLSN-II, and orange for possible SLSN-I and error bars show photometric uncertainties. The best-fitting SED model is displayed by the black curve, fitted to our data using the procedure outlined in Section 2.4.1. Galaxies are ordered in terms of their luminosity as measured in the r-band via the SED. The absolute magnitude axis uses appropriate limits for each row.

Table 2.6: Statistical properties of galaxy samples. 10th, 50th(median) and 90th percentiles are given for each physical parameter. 1-σ uncertainties are given on the median derived parameters. Star-formation rates are not corrected for redshift evolution. Ic-BL are not included as an individual subtype (only as part of the statistic for all subtypes) in this table since there are only two objects in this category.

Transient	N	z			$\log_{10}M_*$ (M$_\odot$)			$\log_{10}$SFR (M$_\odot$yr^{-1})			$\log_{10}$sSFR (yr^{-1})			$\log_{10}(\Delta S)$		
		10	50	90	10	50	90	10	50	90	10	50	90	10	50	90
CCSN (all subtypes)	150	0.005	0.014	0.033	8.1	9.5(0.1)	10.4	-1.4	-0.2(0.1)	0.5	-10.7	-9.6(0.1)	-8.9	-0.8	0.1(0.1)	0.7
CCSN II	98	0.005	0.014	0.025	8.2	9.5(0.1)	10.4	-1.3	-0.2(0.1)	0.6	-10.7	-9.6(0.1)	-8.8	-0.8	0.1(0.1)	0.7
CCSN IIb/Ib/Ic	29	0.004	0.014	0.035	8.3	9.5(0.2)	10.4	-1.4	-0.1(0.1)	0.4	-10.2	-9.6(0.1)	-8.9	-0.7	0.2(0.1)	0.7
CCSN IIn/Ibn	21	0.009	0.020	0.054	7.6	8.9(0.4)	10.2	-1.5	-0.4(0.3)	0.1	-10.9	-9.6(0.2)	-8.9	-0.7	-0.1(0.1)	0.3
SLSN-I	29	0.105	0.177	0.281	7.5	7.9(0.2)	9.1	-1.2	-0.5(0.2)	0.3	-9.6	-8.6(0.1)	-7.5	-0.3	0.3(0.1)	1.3
SLSN-II	21	0.074	0.210	0.284	7.2	8.8(0.5)	9.9	-1.9	-0.6(0.3)	0.2	-10.4	-9.2(0.3)	-7.8	-0.8	-0.1(0.1)	0.8
LGRB SN	12	0.033	0.146	0.280	7.7	8.7(0.2)	9.1	-1.4	-0.1(0.3)	0.4	-9.6	-9.1(0.1)	-8.5	-0.2	0.3(0.2)	0.8
SN-less LGRB	5	0.089	0.105	0.290	7.6	9.6(0.9)	9.8	-1.8	-0.1(0.6)	0.2	-10.2	-9.6(0.4)	-8.6	-1.0	0.1(0.5)	0.7

2.4.2 Redshift evolution correction

The overall SFR density of the Universe, and of individual galaxies, rises rapidly with increasing redshift (e.g. Lilly et al., 1996), making it likely that the rare, luminous SNe that are typically found at higher redshifts than common, less luminous SNe will tend to be found in galaxies with higher star-formation rates simply on account of the effects of cosmic evolution.
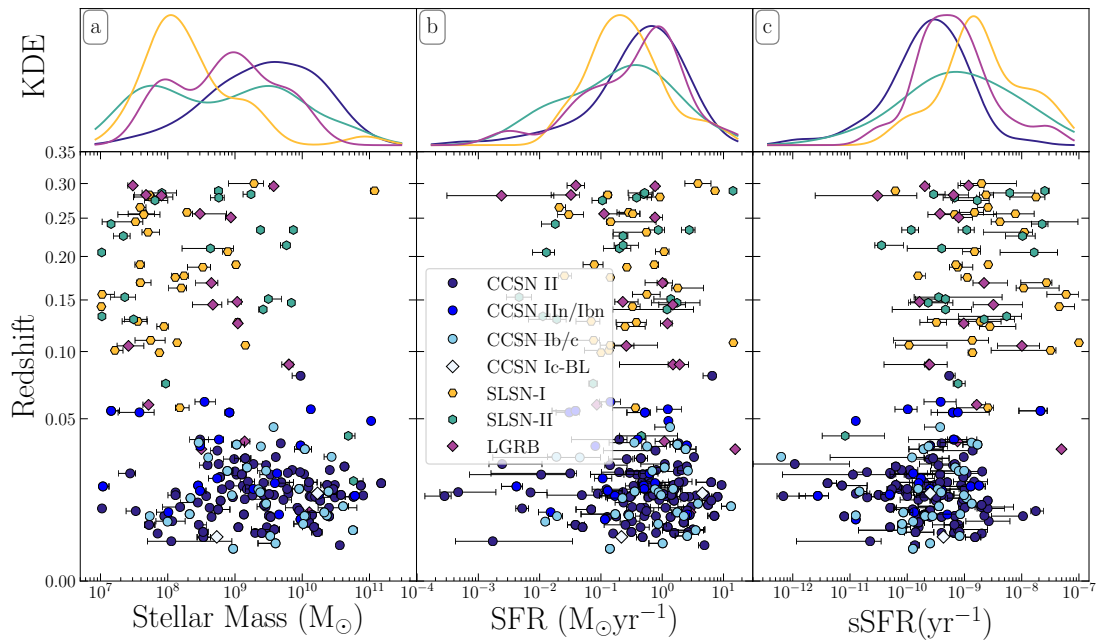
Figure 2.6: Distribution of the physical properties plotted against redshift for each host galaxy sample. Panel (a) shows the stellar mass, (b) the star formation rate, and (c) the specific star formation rate all plotted against redshift using a square root scale. Each upper panel is a Gaussian kernel density estimation of each physical property. For the kernel density estimation all subtypes of CCSNe are grouped together and plotted in dark blue. Redshift evolution is not corrected for in the physical parameters.

While I have restricted all our samples to relatively low-redshift ($z < 0.3$) and a small k–correction was applied by LE PHARE to all the host galaxies, Fig. 2.6 clearly shows that there are still redshift differences between our samples—in particular, between the CCSNe and the more extreme supernovae. The SLSN and LGRB samples are at a redshift out to $z = 0.3$, with a comoving distance of $\sim$1200 Mpc. Whereas the CCSN sample covers a redshift out to $z < 0.08$, with a comoving distance of $\sim$340 Mpc. At these distances, redshift evolution of the star formation density will play a marginal role, but since the ultimate goal is

to make direct comparisons between the physical properties of the host galaxy samples, it is important enough to require a correction procedure.

I aim to reduce any differences in the physical properties of the host galaxies that occur simply as a result of cosmic evolution as a result of the host galaxy samples covering different cosmic volumes. I correct for redshift evolution in SFR by empirically re-scaling all star formation rates to $z = 0$. I do this by measuring the ratio between the SFR expected for a $z = 0$ galaxy on the main-sequence (for a given host galaxy stellar mass) versus the expected SFR for this galaxy at the redshift of the host $\mathrm{SFR_{MS(M,0)}}/\mathrm{SFR_{MS(M,z)}}$. I use this ratio to scale the measured SFR and sSFR down to $z = 0$ as in Eq. 2.1.

$$\mathrm{SFR_{corrected}} \,=\, \mathrm{SFR_{measured}} \frac{\mathrm{SFR_{MS(M,0)}}}{\mathrm{SFR_{MS(M,z)}}} \tag{2.1}$$

I parametrize the main-sequence as a power-law, as in Eq. 2.2.

$$\mathrm{SFR_{MS}} \,=\, \mathrm{SFR_0} \left(\mathrm{M_*}/10^{10}\,\mathrm{M_\odot}\right)^{\alpha} \tag{2.2}$$

Parameter (α) is the slope of the galaxy main-sequence and ($\mathrm{SFR_0}$) describes the normalisation at a stellar mass of $10^{10}\,\mathrm{M_\odot}$, which varies as a function of redshift. Parameters were derived from observational data in Salim et al. (2007) ($z \sim 0.1$) and Noeske et al. (2007) ($z \sim 0.36$). The approximate values are ($\mathrm{SFR_0}$ / $\mathrm{M_\odot}$ $\mathrm{yr^{-1}}$, α) = (1.48,0.65) for the galaxy main-sequence at $z \sim 0.1$ and (2.3,0.67) for $z \sim 0.36$. I interpolate these parameters (α and $\mathrm{SFR_0}$) over the redshift range of our sample in order to calculate the SFR of a main sequence galaxy (with a certain stellar mass) at every host redshift and at redshift zero.

I apply this correction to the sSFR and SFR when I statistically compare the host galaxy populations of CCSNe, SLSNe and LGRBs. Once these corrections are applied, I find the median SFR is reduced by 0.02 dex for CCSN, 0.42 dex for SLSN-I, 0.15 dex for SLSN-II and 0.20 dex for LGRBs. Parameters have

not been corrected, unless specifically indicated in the text and figure caption. I provide the derived physical parameters from SED fits without applying this SFR correction in Tables A.4–A.6.

2.4.3 Sequence-offset parameter

As an alternative to applying a redshift evolution correction to the SFR to deal with cosmic evolution, I define an alternative metric of star-formation intensity, the 'sequence-offset' parameter (ΔS). This parameter, given by Eq. 2.3, measures the ratio between the actual, SED-measured star formation rate of a galaxy in our sample (SFR_{host}) vs. the predicted SFR (SFR_{MS}) for a galaxy on the star-forming galaxy main-sequence (at the same redshift with the same stellar mass), based on the parametrization in Eq. 2.2.

$$\Delta S = \frac{SFR_{host}(M_*, z)}{SFR_{MS}(M_*, z)} \tag{2.3}$$

2.5 Results

In this section I present the integrated galaxy properties derived from the SED fitting for nearby SLSN, LGRBs and the ASAS-SN CCSN. Basic statistical properties of each sample are summarised in Table 2.6. Uncertainties (1-σ) are calculated using a simple bootstrap.

2.5.1 Basic properties of CCSN hosts and comparisons to nearby star-forming galaxies

A key goal of our study is to produce a uniform and unbiased sample of CCSN hosts, providing a galaxy-luminosity-independent tracer of the sites of star-formation in the local universe. While our primary motivation for this exercise will be to

Figure 2.7: Cumulative distributions of the different galaxy samples with colours the same as in previous figures. I empirically re-scale all star formation rates to $z = 0$ for all host galaxy samples (CCSNe, SLSNe-I, SLSNe-II and LGRBs) using the procedure in 2.4.2. The LVLS galaxies (in grey) are weighted here by SFR (step size) to create a galaxy population that traces star-formation. Panel (a): cumulative distributions of all galaxy populations by mass. Panel (b): cumulative distributions of all galaxy populations by star-formation rate. Panel (c) & Panel (d) show measures of star-formation intensity via sSFR and sequence offsets from star-formation rate compared with the galaxy main sequence at that redshift. CCSN and the weighted LVLS are similar, although not identical.
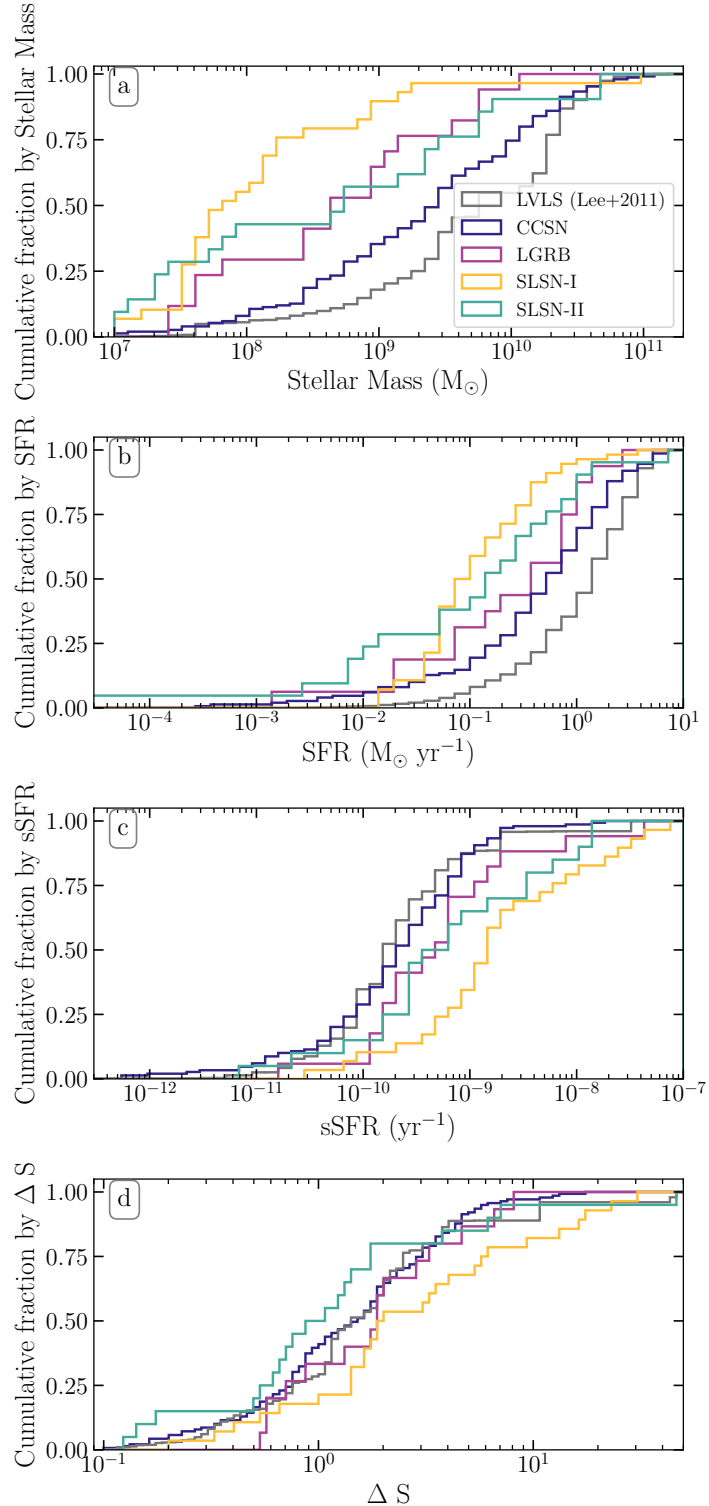
compare this sample to 'exotic' supernova types (SLSNe and LGRBs) in order to constrain their progenitors, our CCSN sample is also useful for studying the nature of star-formation at low-redshift: few galaxy surveys are complete beyond the dwarf galaxy $\lesssim 10^9$ M$_\odot$ limit. Those that are, are typically confined to small volumes limited by cosmic variance.

In Fig. 2.8a, I present the distribution of SFR vs. stellar mass for core-collapse SNe as compared to galaxies from the Local Volume Legacy Survey (LVLS). The LVLS is a volume-complete sample of galaxies within $\sim$11 Mpc, with stellar masses derived from SED fits (Johnson et al. in prep) and star formation rates derived from Hα flux (Lee et al., 2011)[7]. Most LVLS galaxies are observed to populate the main sequence of star-forming galaxies, where mass and star-formation rate are strongly correlated in a fairly narrow band of specific star-formation rate between 10^{-9}–10^{-10} yr^{-1}.

If the SN rate strictly tracks the star-formation rate, then the distribution of SN host masses should follow the distribution of galaxy masses, re-weighted by star-formation rate. As expected, CCSNe populate star-forming galaxies across their entire mass distribution—probing large spiral galaxies with stellar masses $\sim 10^{11}$ M$_\odot$ down to the low-mass dwarf galaxy regime with stellar masses of $\sim 10^7$ M$_\odot$. However, the SN host mass distribution is similar to the SFR-weighted galaxy mass distribution but they are not strictly consistent: the median SFR-weighted log stellar mass of LVLS galaxies is 9.8(0.1), 0.3 dex higher than the median mass of CCSN hosts 9.5(0.1) (the associated Anderson-Darling p-value is $p_{\mathrm{AD}} < 0.001$). This may be associated with cosmic variance effects in the small LVLS volume (e.g. an overabundance of large galaxies due to large-scale structure) and demonstrates the importance of obtaining a sample selected via SNe. Similar small but statistically significant differences are also seen in other parameters (SFR, sSFR, and sequence offset). I find the median stellar mass

---

[7]Note that this SFR indicator is different from the one employed in our SED analysis; I provide it as a visual comparison indicator and because it has been employed as the comparison sample in earlier transient host studies (in particular, Perley et al. 2016c). I statistically compare the LVLS vs. CCSN sample using both Hα and UV SFRs.
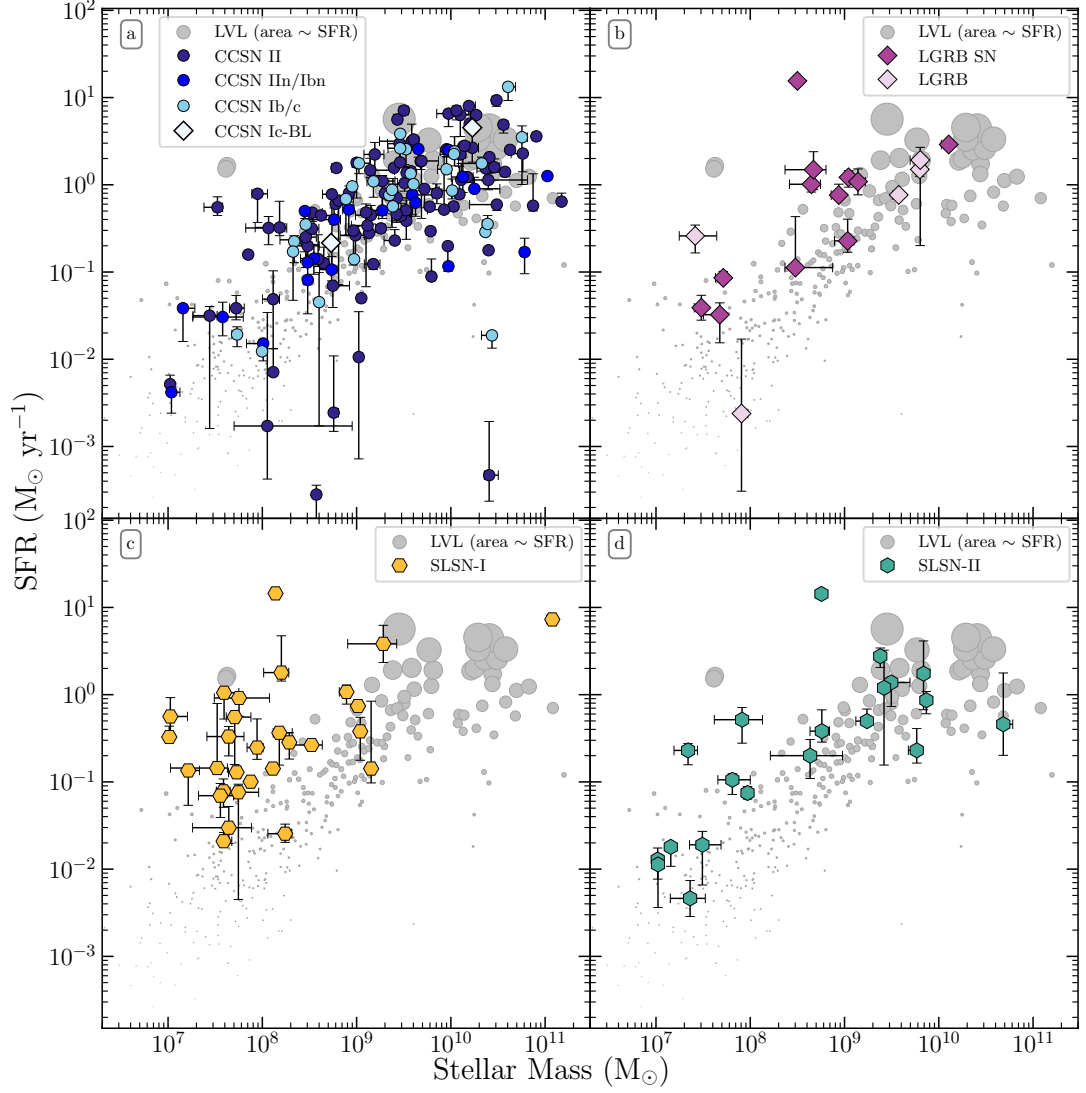
Figure 2.8: Star formation rate vs. stellar mass for each host galaxy population. SFR has not been corrected for redshift evolution. Grey points are the LVL survey galaxies with their sizes scaled in proportion to SFR to show the probability of producing a SN per unit time. Panel (a) shows the unbiased CCSN sample divided into subtypes. Panel (b) shows the LGRB sample in purple; the darker shade indicates where the LGRB was associated with a SN or optical afterglow. Panel (c) shows the SLSN-I sample. Panel (d) shows the SLSN-II sample.
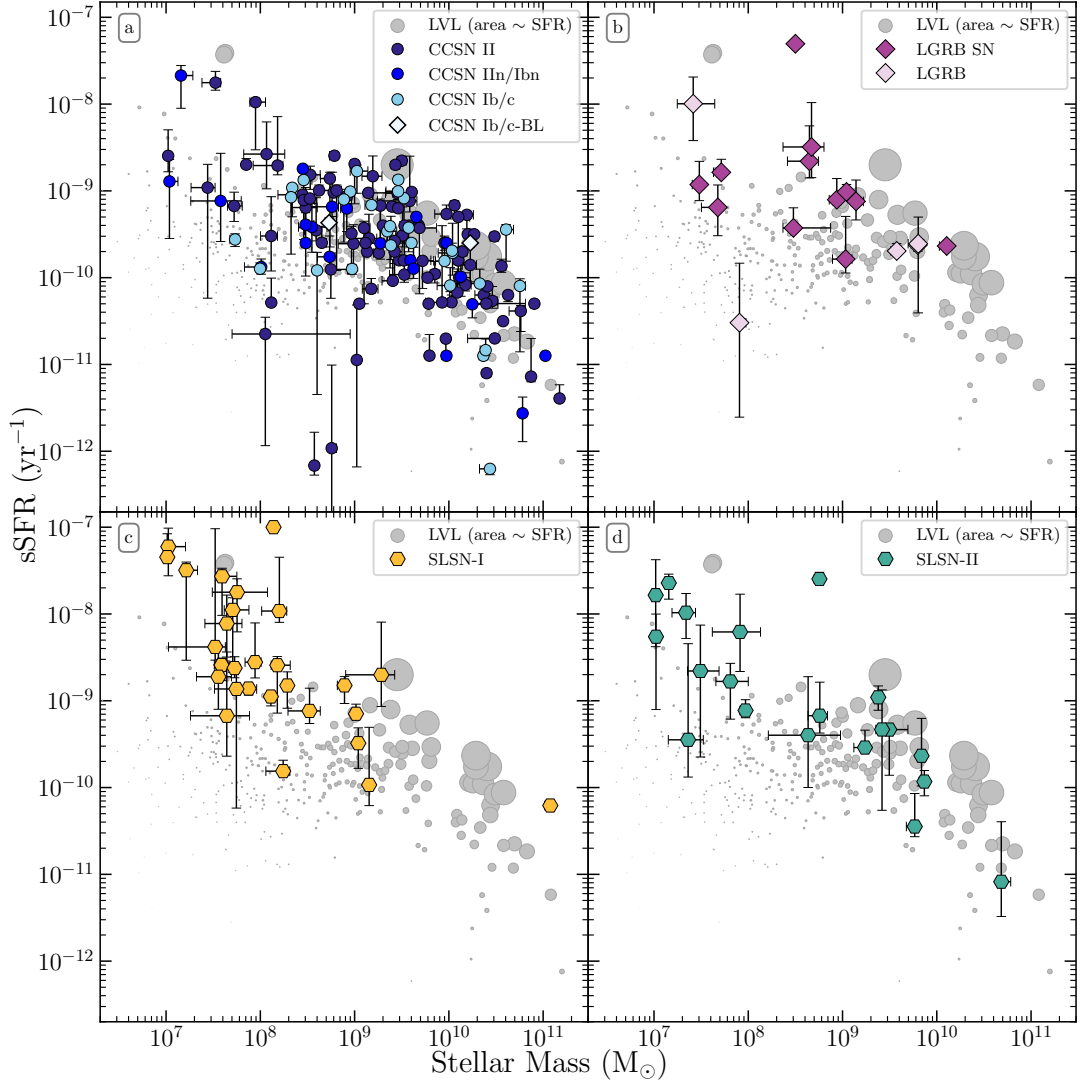
Figure 2.9: Specific star formation rate vs. stellar mass. The symbols and colours are the same as in Fig. 2.8. As in previous figure, SFRs have not been corrected for redshift evolution. SLSN-I show a strong preference for galaxies with high sSFR and/or low stellar mass, (top left of panel c), whereas CCSN are broadly consistent with the distribution of LVL galaxies (panel a). SLSN-II and LGRB hosts (panels a and d respectively) also seem to show a preference towards galaxies with high sSFR and/or low stellar mass compared to CCSNe. There are very few SLSN-II and LGRB hosts with low sSFR and high-mass, but this trend is clearly not as strong as for SLSNe-I.

9.5(0.1) is slightly higher in comparison to the Dark Energy Survey CCSN sample of 47 objects (9.4) (Wiseman et al., 2020), but still within the uncertainties of the measurements.

A few CCSN galaxies in Fig. 2.8a, specifically 14de and 16am, show very low star-formation rates despite high masses. Morphologically, these galaxies are not classical spiral galaxies, neither are they elliptical galaxies. They have red colours and the uncertainties on the SFRs derived for these galaxies, at minimum, are likely to be underestimated by our SED fitting procedure. When fitting the SEDs with LE PHARE, we model the star formation history of the galaxy with an exponentially declining burst of star formation (tau-model). However, for these cases, a two-population model may be a better approximation since these red galaxies likely have a population of old stars, as well as a recent star formation episode. Galaxies with these properties are expected to contribute very little to the cosmic supernova rate, although previous examples have been reported (e.g. Irani et al., 2019).

The fraction of star-formation in very faint or very rare galaxies that are poorly probed by traditional flux- or volume-limited galaxy surveys is of particular interest. In a SN survey, CCSNe select galaxies based on their star formation rate. Therefore if CCSNe are considered to be perfect tracers of star formation, within statistical uncertainties, the fraction of CCSNe that are in dwarfs can be used interchangeably with the fraction of star-formation that occurs in dwarfs. Therefore using our sample, I measure the fraction of CCSNe in dwarf galaxies and the fraction in 'starburst' galaxies.

I use the Bayesian beta distribution quantile technique to derive the 1-σ uncertainties following methods outlined in Cameron (2011). I find 33^{+4}_{-4} per cent of CCSNe (50/150 from our sample) occur in dwarf galaxies with stellar masses less than 10^9 M$_\odot$ and 7^{+3}_{-2} per cent of CCSNe (11/150 from our sample) occur in dwarf galaxies with stellar masses less than 10^8 M$_\odot$. These fractions are substantial, emphasising the importance of dwarf galaxies to the ongoing star formation rate density in the local Universe, together with potential future chemical enrichment

of their environments. However, only 2^{+2}_{-1} per cent (3/150) of CCSN hosts are undergoing very rapid star-formation in a starburst galaxy (sSFR$>10^{-8}$ yr^{-1}), all of which are dwarf galaxies. Thus, I find the vast majority of star-formation in the local Universe does not occur in starbursting galaxies. This is in agreement with the LVLS survey (Lee et al., 2009) which found that only a few per cent of the galaxies are now in a bursting mode (defined in their analysis as a H α equivalent width > 100 Å). Brinchmann et al. (2004) estimated that $\sim$20 per cent of local star-formation occurs in starburst galaxies using a volume-corrected sample of galaxies from SDSS DR2, although their definition of a starburst differs from ours and is much more generous (they require that the ratio of between the present SFR and the mean past SFR (b) is 2–3, which corresponds to a specific star-formation rate threshold of approximately $10^{-9.75}$ yr^{-1}). The fraction of strongly starbursting galaxies in SDSS is clearly much lower (see e.g. their Fig. 22), but cannot easily be quantified because most such star-formation is in galaxies with stellar masses below the SDSS completeness limit.

2.5.2 Basic properties of exotic SN hosts

In Fig. 2.8b–d I also plot the mass and SFRs of the 'exotic' SN samples in comparison to local galaxies. These populations are clearly quite different from ordinary CCSNe. The peak of the SLSN-I host mass distribution is much lower than that of the CCSN population, with a median log stellar mass of 7.9(0.2), though notably, there are a few outliers in galaxies with relatively high masses (PTF10uhf, SN2017egm and PTF09q). SLSN-II and LGRBs with observed associated SNe lie intermediate between the SLSN-I and CCSN samples with median logarithmic mass of 8.8(0.5) and 8.7(0.2) respectively (SN-less LGRBs have masses more consistent with CCSN with a median logarithmic stellar mass of 9.6(0.9), although this is poorly constrained).

Unlike CCSNe, SLSNe and LGRBs frequently populate galaxies above the galaxy main sequence with a median logarithmic sSFR of -8.6(0.1) for SLSNe-I, -9.2(0.3)

for SLSNe-II, and -9.1(0.1) for LGRB SNe. SN-less LGRBs have sSFR of -9.6(0.4) which is more consistent with the CCSN. This effect can be seen more clearly in Fig. 2.9. which shows specific star formation vs. stellar mass. The impartially selected CCSNe are consistent with star-forming local galaxies, whereas ∼70 per cent of SLSN-I lie above the star-forming galaxy main sequence with specific star-formation rates exceeding 10^{-9} yr^{-1}. This places many SLSN-I hosts in the top left of this diagram, with eight hosts which have specific star formation rates exceeding 10^{-8} yr^{-1}. This is more than expected if the SLSN rate purely traces SFR. This has also been noted by others (e.g. Lunnan et al., 2014; Perley et al., 2016c; Schulze et al., 2018). These galaxies (with specific star formation significantly above this main sequence) are sometimes referred to as starbursts. There are 8 (∼30 per cent) SLSN-I galaxies with specific star formation rates exceeding 10^{-8} yr^{-1} (which I will define as a 'starburst' for the purpose of this thesis). This is in qualitative agreement with other studies, such as in Leloudas et al. (2015) where ∼50 per cent of SLSN-I were found in EELGs indicative of an intense starburst episode within the galaxy. Perley et al. (2016c) and Schulze et al. (2018) also noted that many SLSN-I host galaxies in PTF and SUSHIES samples are undergoing intense star-formation.

2.5.3 Relative rates of SN subtypes

While I can qualitatively observe that the distributions of certain samples in Fig. 2.6–2.9 seem similar or dissimilar, this is not a statistical statement. I employ several different methods to quantify the significance and model the nature of these apparent differences below.

Cumulative Distribution Tests

In Fig. 2.7, I show the cumulative distributions of mass, star-formation rate, specific star formation rate and sequence offset for each of our galaxy samples. The step size of local galaxies in LVL are weighted by star-formation to create

Table 2.7: Two-sample Anderson-Darling probabilities between CCSNe, the LVLS weighted by SFR, SN host galaxy samples (SLSNe-I, SLSNe-II, LGRB-SNe and SN-less LGRBs) and between LGRBs with and without supernova. I empirically re-scale all star formation rates to $z = 0$ for all host galaxy samples (CCSNe, SLSNe-I, SLSNe-II and LGRBs) using the procedure in 2.4.2. Samples that differ at $p_{AD} < 0.05$ for that parameter are in boldface. The combined sample size of the two comparisons are given in the effective size column.

Parameter	Comparison	p_{AD}–value	Effective size
Mass	CCSN–LVLS	**<1e-03**	350
	CCSN–SLSN-I	**<1e-03**	179
	CCSN–SLSN-II	**1.90e-03**	171
	CCSN–LGRB SN	**5.67e-03**	162
	CCSN–SN-less LGRB	>0.25	155
	LGRB SN–SN-less LGRB	>0.25	17
	LGRB SN–SLSN-I	0.058	41
SFR	CCSN–LVLS (UV)	**<1e-03**	350
	CCSN–SLSN-I	**<1e-03**	179
	CCSN–SLSN-II	**4.96e-03**	171
	CCSN–LGRB SN	>0.25	162
	CCSN–SN-less LGRB	>0.25	155
	LGRB SN–SN-less LGRB	>0.25	17
	LGRB SN–SLSN-I	0.051	41
sSFR	CCSN–LVLS (UV)	**<1e-03**	350
	CCSN–SLSN-I	**1.05e-03**	179
	CCSN–SLSN-II	**3.36e-03**	171
	CCSN–LGRB SN	**2.49e-02**	162
	CCSN–SN-less LGRB	0.059	155
	LGRB SN–SN-less LGRB	**3.5e-02**	17
	LGRB SN–SLSN-I LGRB	0.11	41
ΔSFR	CCSN–LVLS (UV)	**<1e-03**	350
	CCSN–SLSN-I	**<1e-03**	179
	CCSN–SLSN-II	>0.25	171
	CCSN–LGRB SN	0.19	162
	CCSN–SN-less LGRB	>0.25	155
	LGRB SN–SN-less LGRB	>0.25	17
	LGRB SN–SN-SLSN-I	>0.25	41

a population consistent with one that traces star-formation. The CCSN and LVLS samples have remarkably similar sSFR and ΔS distributions, while the rarer SN subtypes seem to show different distributions in most properties. These differences can be tested formally using Anderson-Darling tests.

I compute the Anderson-Darling (AD) statistic, and associated *p*-value, for each pair of samples and for each parameter of interest: stellar mass, SFR, sSFR and the sequence offset parameter (ΔS). The results are summarised in Table 2.7. SLSN-I are statistically distinct from the CCSN in every parameter ($p_{AD} > 0.05$): mass ($p_{AD} <$1e-03), SFR ($p_{AD} <$1e-03) , sSFR ($p_{AD}=$1e-03) and ΔS ($p_{AD} <$1e-03). This population shows the most divergent properties out of all galaxy samples. SLSN-II fall intermediately between these two populations and are statistically distinct from CCSN in terms of mass ($p_{AD}=$2e-03), SFR ($p_{AD}=$5e-03), and sSFR ($p_{AD}=$3e-03).

In addition, CCSN host galaxies have shown diversity. Ic SNe have been previously reported to be found more frequently in high-metallicity galaxies (Prieto et al., 2008; Leloudas et al., 2011; Modjaz et al., 2011) with higher sSFRs (Kelly & Kirshner, 2012) than non-stripped envelope CCSNe and a sequence of decreasing metallicity has been established from Ic–(Ib/IIb) (Modjaz et al., 2019). Although, the Ic-BL subclass may prefer metal-poor galaxies (Modjaz et al., 2019). I do not find any statistically significant differences between stripped-envelope SNe and type II CCSNe in this sample. The ASAS-SN sample is dominated by Type II SNe (98) with only a small number of stripped-envelope events (19 Ib/Ic and 10 IIb and 2 Ib/c-BL), so our measurement is not very constraining, and in particular I am unable to address if there are differences in the Ic-BL population.

Relative rate formalism for uni-variate comparisons

While the Anderson-Darling tests above confirm that differences exist between some distributions, they do not tell us anything about the degree or quantitative nature of the differences between any two distributions.

To gain further insight into the differences between the distributions of different samples, I define a new quantity which I refer to as the *relative* rate (designated $\Re$). This quantity measures how more frequent a specific type of SN (type 'A', typically an exotic class of SN) is compared to another type of SN (type 'B', typically a normal class of SN) in a specific type of galaxy, compared to the Universe as a whole. Expressed in terms of a single parameter y (which can be mass, SFR, etc.), it is the ratio of the inferred probability density functions of the two SN types:

$$\Re_{A/B}(y) = \frac{\mathrm{PDF_A}(y)}{\mathrm{PDF_B}(y)} \tag{2.4}$$

A relative rate $\Re = 1$ for all values of y would indicate that the distributions over y for A and B are identical (although the *absolute* rates may not be the same). Otherwise, regions over y with $\Re > 1$ indicate environments where production of SNe of type A is enhanced relative to B; regions with $\Re < 1$ indicate environments where production of type A is suppressed relative to B.

In practice, I use a sliding-window method to estimate $\Re$ for each parameter of interest (stellar mass, star-formation rate, specific star-formation rate, or sequence offset). The PDF function for each parameter for each sample (A or B) is estimated by calculating the proportion P_i of host galaxies in that sample with parameter values within ± 0.5 dex of a grid of bin centres, y_i. If the number of galaxies within ± 0.5 dex of y_i is n_i and the sample size is N, this is then (for sample A):

$$P_A(y_i) = \frac{n_{A,i}}{N_A} \tag{2.5}$$

The (estimated) *relative* rate of one transient compared to another, $\Re_{A/B}$, is then the ratio of the two P arrays:

$$\Re_{A/B}(y_i) = \frac{P_A(y_i)}{P_B(y_i)} = \frac{n_{A,i}N_B}{n_{B,i}N_A} \tag{2.6}$$

The bin centres are defined in logarithmic intervals of 0.1 dex, such that every 10th window has no overlap with the first. For example, the window is evaluated between a mass of 1×10^6 $M_\odot$ to 1×10^7 $M_\odot$ (centred at 3.16×10^6 $M_\odot$), then at 1.26×10^6 $M_\odot$ to 1.26×10^7 $M_\odot$ (centred at 3.98×10^6 $M_\odot$), etc. Note that because windows within 1 dex overlap, values of $\Re$ within 1 dex of each other are not fully independent.

To calculate the confidence intervals on the relative rate I drew a new CCSN sample and a new SLSN sample from the original samples (with replacement) for 1000 bootstrap iterations. I derived a relative rate for each iteration and determined the 2-σ uncertainties based on the bootstrapped relative rate function.

Relative rate formalism for bivariate comparisons

Testing on a single parameter at a time will not be able to distinguish between fundamental differences vs. those that originate purely due to correlations with other parameters: many galaxy parameters (e.g. SFR and stellar mass) are strongly correlated, making it is difficult to tell which parameter is more directly related to the special conditions that appear necessary for SLSN-I or LGRB production.

However, our relative-rate formalism above can be extended to ascertain whether a difference in distributions associated with a control parameter (e.g. stellar mass) can completely explain an observed difference in distributions for another parameter (e.g. SFR). To test this, I *reweight* the comparison sample (sample 'B'). The weights for each galaxy in the comparison sample are interpolated from the relative-rate for the control parameter. For example, the host masses are weighted based on the relative rate weights for the sSFR. I use the same confidence intervals derived from the bootstrap procedure and rescale them using

the same factor to the weighted relative rate.

2.5.4 SLSNe-I vs. CCSNe

The relative rate, $\Re$, of SLSNe-I vs. CCSNe is plotted in the left panels of Fig. 2.10 as purple dashed lines with the 2-σ confidence intervals in a lighter colour against sSFR, sequence offset, redshift corrected sSFR scaled to z$\sim$0 and stellar mass. The grey line indicates the same relative rate.

SLSNe-I are enhanced in galaxies with sSFR exceeding 10^{-9} yr^{-1} (after correcting for redshift evolution) and strongly enhanced (by a factor of $\sim$10) for sSFR exceeding 10^{-8} yr^{-1}. The rate is also enhanced for galaxies with a sequence offset parameter $\Delta S > 5$, which corresponds to galaxies with SFR > 5 times that predicted of galaxies on the main sequence with the same stellar mass and redshift. The bottom left panel shows that the rate is increased for galaxies with stellar mass less than 2×10^8 M$_\odot$.

To investigate whether SLSN host galaxy mass (a proxy for metallicity) or specific star formation rate (a proxy for star-formation intensity) is more closely related to the factor driving the production of these events, I must correct for the co-variation between these two parameters. As described above, I remove the effects of a possible dependence in the relative rate of SLSNe to CCSNe as a function of specific star formation rate by controlling for the mass dependence in order to see whether specific star formation rate alone can explain the over-abundance of SLSNe-I relative to CCSNe. I also do the reverse, in order to see whether a specific star formation rate dependence alone would explain the observed apparent mass dependence in the relative rate.)

The right panels of Fig. 2.10 show the original relative rates as a purple dashed line. The light blue and red solid lines show the rates when one controls for mass dependence or sSFR dependence respectively. The covariance-corrected rates do appear to broadly level off (at a 2-σ confidence level) to an equal rate (grey line),

suggesting that either mass dependence or sSFR alone can explain the difference in relative rates between the CCSNe and SLSNe in our sample. However, in rows three and four, the covariance-corrected rates do show some deviation from an equal rate. Specifically, the redshift corrected sSFR shows deviation at at a 2-σ confidence level at sSFR $>8\times10^{-9}$ yr^{-1}. Also the mass shows some deviation at $<2\times10^8$ M$_\odot$ at the 2-σ confidence level. This may hint that the rate of SLSNe-I production is increased as a result of high sSFR *and* low stellar mass. A larger sample size should help to solidify this claim.

2.5.5 LGRBs vs. CCSNe

Using the same method as described above, I also calculate the relative rate $\Re$ of LGRBs vs. CCSNe in Fig. 2.11. Given the rather limited low-z LGRB sample the results are generally less constraining than for SLSNe, and I cannot conclusively (for any 1-dex bin) state that $\Re \neq 1$ for LGRBs versus SNe given this analysis.

Formally, the relative rate of LGRBs is enhanced in galaxies with sSFRs exceeding 10^{-9} yr^{-1} (after correcting for redshift evolution) by a factor of $\sim$3; it is enhanced in galaxies with sequence offsets >2 by a factor of approximately 2, and it is enhanced in low-mass dwarfs $<10^8$ M$_\odot$ by a factor of approximately 2.5. As with SLSNe, these effects are degenerate. Given the small sample sizes, I cannot yet determine which parameter (if any) is the primary cause of the differences.

2.5.6 SLSNe-I vs. LGRBs

I also compare the LGRB and SLSN-I host populations directly against each other. In our work, I find that SLSNe-I and LGRBs are statistically consistent with being drawn from the same galaxy populations in terms of all measured parameters (see Table 2.7), similar to (Japelj et al., 2018). However, the AD values for mass (p_{AD}=0.058) and SFR (p_{AD}=0.051) are right on the threshold (p_{AD}=0.05) for a statistically distinct population. I do find that SLSNe-I seem
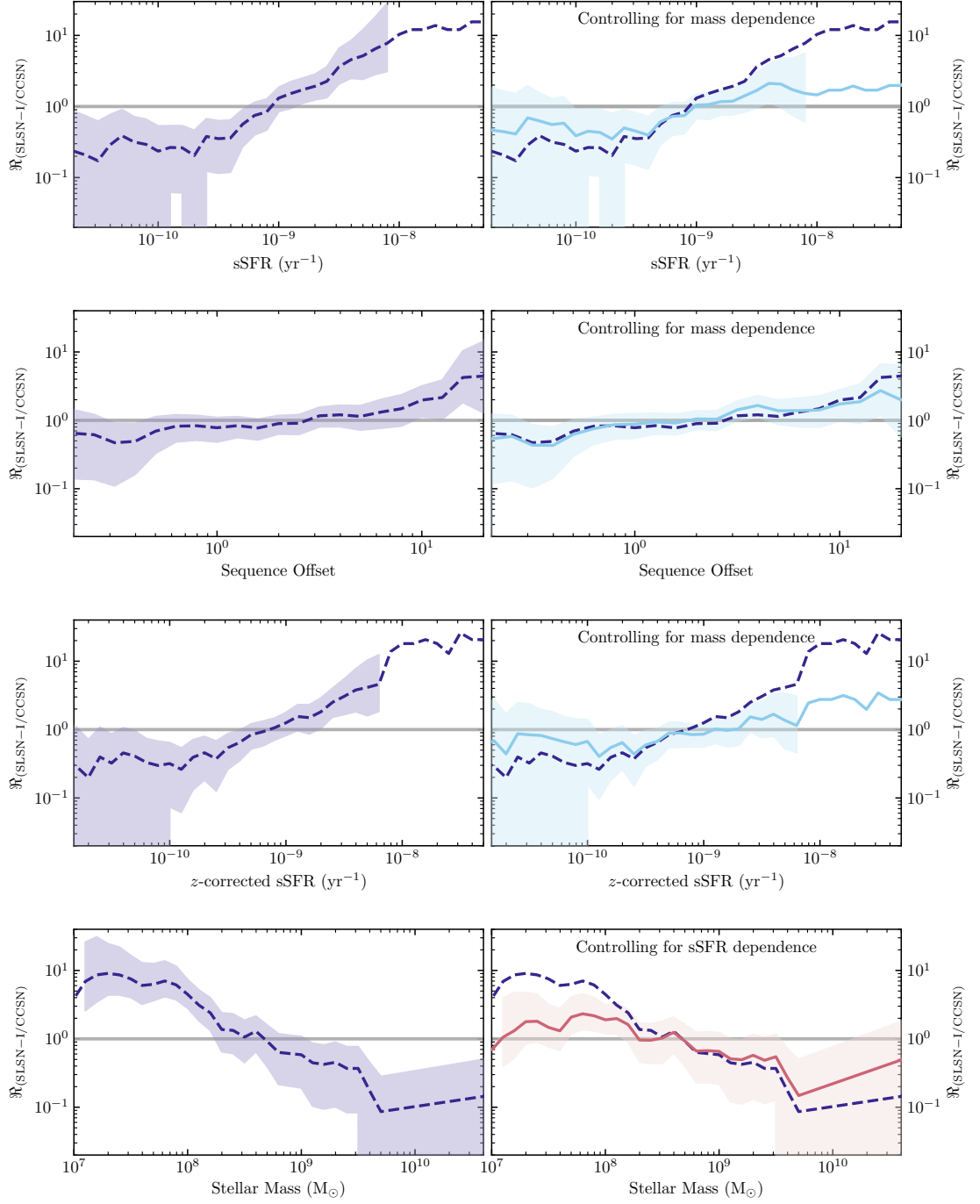
Figure 2.10: Relative rates of SLSN-I to CCSN for various host galaxy parameters. Left panels show the relative rates in purple given by the dashed lines for specific star formation rate, sequence offset (redshift corrected to z∼0) and stellar mass in a moving window function with a width of 1 dex. The window function moves such that after it has moved 10 times it has no overlap with the first window. 2-σ confidence intervals are shown in a lighter shade. Right panels show the same quantity, but after controlling for the modeled dependence on the alternative variable (stellar mass for SFR-related quantities, or SFR for mass-related quantities). Light blue lines are mass-controlled rates and red lines are the sSFR controlled rates.
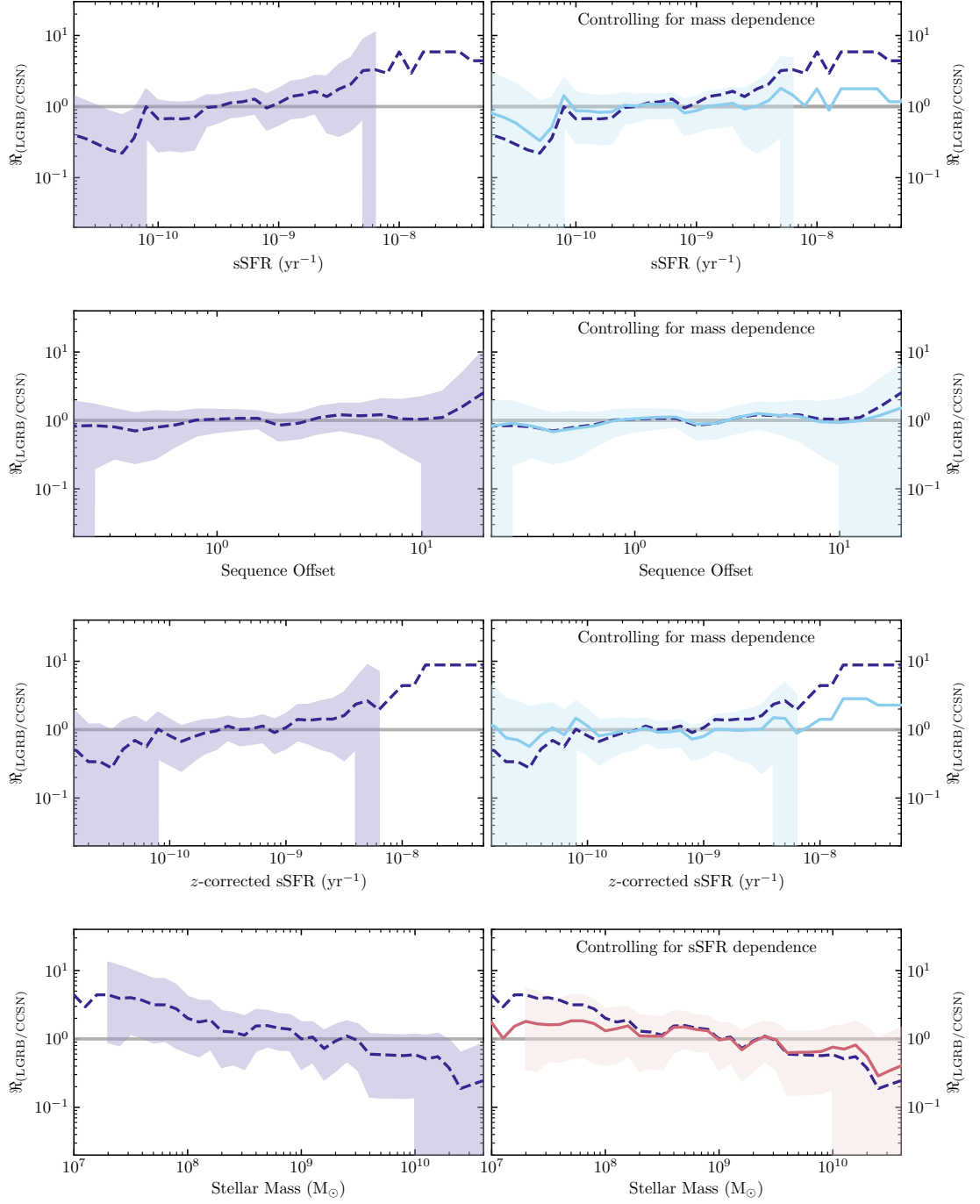
Figure 2.11: Relative rates of LGRB to CCSN for various host galaxy parameters. Left panels show the relative rates in purple given by the dashed lines for specific star formation rate, sequence offset (redshift corrected to z∼0) and stellar mass in a moving window function with a width of 1 dex. The window function moves such that after it has moved 10 times it has no overlap with the first window. 2-σ confidence intervals are shown in a lighter shade. Right panels show the same quantities, but after controlling for the alternative variable as in Fig. 2.10. Light blue lines are mass-controlled rates and red lines are the sSFR controlled rates.

to be in less massive galaxies in comparison to LGRBs. SLSNe-I have a median logarithmic stellar mass of 7.9(0.2), while LGRB SNe have a median stellar mass of 8.7(0.2). This is a similar conclusion to that found in Lunnan et al. (2014),Leloudas et al. (2015) and Schulze et al. (2018). However, I note that due to our selection of nearby events, our sample size for LGRBs is smaller than in these studies.

In terms of sSFR, I do not find any statistical differences (p_{AD}=0.11). Our results are fully consistent with those of Leloudas et al. (2015) who found the median sSFR (SFR determined via spectroscopic line measurements) was more strongly star-forming in SLSN-I compared to LGRBs with logarithmic sSFR of –8.53 for SLSNe-I and –9.15 for LGRBs. I find sSFRs –8.6(0.1) for SLSNe-I and –9.1(0.1) for LGRB-SNe. LGRBs and SLSNe-I both have a higher median logarithmic sSFR than CCSNe –9.6(0.1). However, SLSNe do seem to be more strongly star forming than LGRBs by 0.5 dex, in agreement with Leloudas et al. (2015) and Schulze et al. (2018), but our comparison is somewhat limited by the small sample of low-redshift LGRBs.

2.5.7 SN-less LGRBs vs. LGRB-SNe

To address whether the sub-population of 'SN-less' LGRBs may represent a distinct class from the remainder of LGRBs, I compare the host properties of the five events above to the remainder of the sample (Table. 2.6). While some SN-less LGRB hosts are individually unusual, their cumulative properties are not significantly different from the hosts of LGRBs with confirmed SNe (see Table 2.7), although the redshift corrected sSFR may show some difference (p_{AD}=0.04). However, this comparison is not strongly constraining given the small size of the SN-less sample (5 objects) and the possibility that some of these events hosted ordinary LGRB-SNe which were dust-obscured[8].

---

[8]A more detailed discussion of this issue can be found in Section 2.6.

2.6 Potential biases

Several biases may affect the conclusions drawn from our SN host galaxy samples. I briefly summarise these below.

2.6.1 CCSNe

Firstly, there may be biases in the CCSN sample associated with their discovery and follow-up. However, ASAS-SN is an untargeted survey, so the biases associated with targeted surveys are minimized and since the survey is shallow and their discovery numbers are relatively small, almost all ASAS-SN discoveries are followed-up spectroscopically. During 2013–2017 ASAS-SN discovered 595 SNe, of which 585 have known classifications (98 per cent were spectroscopically confirmed) on the ASAS-SN list on their website[9]. Stripped envelope are harder to classify than ordinary II SNe due to lack of strong emission lines, and for interacting SNe with narrow emission, the spectrograph needs to have high enough resolution to be able to resolve the narrow lines. However, of these 10 missed classifications (out of the total sample of 595), only 3 were within above our declination cut below –30 degrees. In addition, ASAS-SN discovers one quarter of its SNe in catalogued host galaxies without known redshifts (Holoien et al., 2017a), indicating that ASAS-SN is less biased against finding supernovae in uncatalogued hosts than previous low-redshift SN surveys; it also finds SNe closer to the galaxy nuclei than preceding projects (see Fig. 3 of; Holoien et al., 2017c). When compared with other surveys, the fraction of SNe within 5 arcsec of the host galaxy nucleus is 40 per cent, but only 20 per cent for other professional surveys — although the pixel scale for ASAS-SN is large (7 arcsec/pixel) and therefore the position is only known to $\sim$1 arcsec (Holoien et al., 2017c).

During 2013 through 2017, ASAS-SN had a $\sim$5 day cadence and surveyed to a limiting magnitude of $\sim$17 in $V-$band (after 2017 the cadence was increased

---

[9]http://www.astronomy.ohio-state.edu/~assassin/sn_list.txt

to every 2–3 days, and the limiting magnitude deepened to 18 mag due to the use of a $g-$band filter which goes deeper than $V-$band in dark time). Thus, slow and bright transient would be unlikely to be missed, but a bright, rapidly-evolving transient such as an FBOTs (Drout et al., 2014) may be missed due to undersampling of the light curve. In any case, these events are likely to be rare, and may not represent the death of an 'ordinary' massive star.

The ASAS-SN survey is effectively flux-limited, so luminous types of CCSNe will be overpopulated in our sample compared to a volume-limited survey, possibly meaning our sample is not a true representation of the sites of (all) massive star-formation. In particular, the Type IIn subclass of SNe (which likely represents a fairly exotic, mass-loss-intense end-phase of stellar evolution itself) and Ibn SNe (analogous to IIn SN but with narrow helium lines) tend to exhibit substantially higher luminosities, causing them to be over-represented. The median redshift of type II and also type Ibc is 0.014, which corresponds to a luminosity distance of 60.6 Mpc, whereas for IIn/Ibn SNe it is 0.020, which corresponds to a luminosity distance of 87.0 Mpc. These events make up 21/150 of our sample, so even if they are over-represented somewhat they are unlikely to exert substantial impact on the properties of the sample. Luminous (ordinary) II SNe could in principle trend towards a different host population than sub-luminous II if, for some reason, the peak luminosity of a SN was a metallicity-dependent quantity. However, Gutiérrez et al. (2018a) found no significant difference between the properties of CCSN explosions produced in faint, low-mass galaxies and those produced in bright, high-mass galaxies, so this effect is probably also not significant.

2.6.2 SLSNe

Our SLSN sample is comprised of objects from a variety of surveys. About half of our sample of SLSNe were discovered by PTF (Perley et al., 2016c; Quimby et al., 2018), a devoted transient survey during which substantial effort was placed in securing spectroscopic classifications of as many objects as possible. Even so, only

a small fraction of PTF SNe could be followed-up and thus there may be biases associated with this in terms of SN classification. There may also be selection biases (associated with the contrast between the transient and the host galaxy), as explained in more detail by Frohmaier et al. (2017). However, efforts to identify additional SLSNe in archival PTF data have produced no high-quality candidates other than those mentioned in Table 2.5, so it is not likely that large numbers of SNe were missed by this effort, but I cannot strictly rule this out this possibility.

I constructed the rest of our sample from the literature; since I focus on low-redshift objects, many of these objects were discovered by reanalysis of old data. This SLSN sample may thus, potentially, be quite heterogeneous. Future surveys with a stronger emphasis on an unbiased selection and follow-up will be needed to ensure this is not the case.

2.6.3 LGRBs

To avoid cosmic evolution effects, I restricted our sample of LGRBs to events closer than $z = 0.3$, even though these represent a tiny fraction (a few per cent) of all LGRBs with known redshifts. However, because most observed LGRBs do not have a successful redshift measurement, it is difficult to know whether the LGRBs that are *known* to be at $z < 0.3$ are fully representative of *all* detected LGRBs at $z < 0.3$. Low-z LGRBs are often first identified to be nearby on the basis of the appearance of their host galaxies themselves: a catalogued galaxy coincident with an afterglow is a strong motivator for spectroscopic follow-up. This means that, at a fixed redshift, a LGRB host may be more likely to enter our sample if it is luminous than if it is faint. Furthermore, because of the huge pool of LGRBs occurring at higher redshifts, it is quite possible for a LGRB to be *misidentified* as a low-z burst if it happens to align with a lower-redshift galaxy. Many of these biases are mitigated by requiring a spectroscopically-confirmed supernova in association: not only does this guarantee that the redshift is correct, but the ability to conduct such a search also ensures that the LGRB could be observed

readily and excludes a wider pool of events with poor observability which were inferred to be at low redshift *only* because of a bright host galaxy.

Still, some of these SN campaigns may have been conducted only because of the initial detection and redshift measurement of a bright host galaxy in the first place, leaving the possibility of a bias in favour of luminous galaxies and against dim ones in our sample. Whether this is likely to be a significant bias can be investigated case-by-case within our sample. For about half of the events in our sample, the LGRB was either so close that the host galaxy would have been evident almost no matter how luminous or dim it was ($z < 0.1$), or the afterglow was so bright that its redshift would have been immediately evident from absorption spectroscopy regardless of its host. About half of our events fall in this category. The remaining events (which may have been missed if their host was fainter or less star-forming) include 031203, 120422A, 150518A, 150818A and perhaps 130702A (on account of its companion). However, omitting these targets would not change our conclusions.

A more delicate issue concerns the use of LGRBs without observed associated SNe, many of which specifically have observations ruling *out* the presence of a SN at or near the luminosity of SN 1998bw. As I have noted, these could in principle represent background objects in dim high-z hosts. They could also represent variants of the short LGRB phenomenon (with T90's at the extreme of the distribution or 'extended emission' episodes; e.g. Norris & Bonnell 2006; Perley et al. 2009), or even something else entirely. On the other hand, they could also be genuine LGRBs whose SN was missed, dim, or dust-extinguished, and/or failed entirely (Fynbo et al., 2006).

The origins of this class are probably heterogeneous: based on examination of individual no-SN events, there is reason to think almost all of the above events are at play. For example, GRB 060614's redshift is unambiguous but a very distinct host galaxy with almost no star-formation may point towards a different progenitor; GRB 051109B had no SN follow-up due to poor observability (despite a massive host), and may simply be a missed low-z LGRB, though it could also

be a background event; the SN in GRB 020903 has been interpreted as having been dust-extinguished (Soderberg et al., 2004).

Given these uncertainties, I have run our tests both including and excluding the no-SN events; our basic conclusion is unaffected by this choice, although this largely reflects the small sample size of no-SN events. Further work will be needed to securely ascertain whether the no-SN events are associated with a different progenitor.

2.6.4 Redshift evolution

Our CCSN sample spans redshifts between $0.002 < z < 0.08$. In contrast, our SLSN and LGRB samples are predominately at redshifts greater than 0.08. While I have used a simple procedure to correct for evolution in star-formation rate, I have not made any correction for stellar mass build-up from $z = 0.3$ to 0 (as a result of galaxy mergers and from the conversion of gas into new stars) because this change is very slow across the redshift range of our sample: much less than the differences that we see or the size of our statistical errors (See Fig. 2 of Furlong et al. (2015) who find almost no evolution in the galaxy masses between $z = 0.3$ to 0, except for high-mass galaxies). However, since the number of very high-mass ($\gtrsim 10^{11}$ M$_\odot$) galaxies is small (1/29 SLSNe-I, 2/150 CCSNe and no SLSNe-II, LGRBs) I do not attempt to correct for this effect.

Changes in star-formation rate over this redshift range ($z = 0$–0.3) are present—and while I have corrected for the offset of the main sequence, I have not corrected for possible changes in the distribution of SFR as a function of stellar mass along the main sequence. While these changes are anticipated to be small for most galaxy masses, the number of actively star-forming, very massive galaxies ($\gtrsim 10^{11}$ M$_\odot$) strongly decreases from $z = 0.3$ to current day due to high-mass galaxy quenching. For example, see Fig. 6 from Fontanot et al. (2009) which shows the star formation rate density with redshift by galaxies of different stellar mass. There is an obvious drop in the star formation rate density between $z = 0$ to

$z = 1$ from galaxies with stellar masses exceeding $10^{11.5}$ M$_\odot$, but for galaxies with stellar masses between 10^{9-11} M$_\odot$, the change in star formation rate density is small. Thus, high-z transients are more likely to be found in very high-mass galaxies than low-z transients. This is not taken into account by our analysis, but the number of very high-mass galaxies is small in all samples, so its effect is likely to be minor.

2.6.5   Extinction effect

All our SN samples are selected via an optical search and thus are subject to biases if the transient is not easily visible or identifiable due to significant obscuration by dust. This bias is common among all SN searches that discover SN at optical wavelengths. This is especially important if the transient itself is intrinsically low-luminosity or if it is discovered at high redshift (and thus selected in the rest-frame UV). Since all of our samples are exclusively at low-redshift ($z \sim 0 - 0.3$), this effect should be relatively minor and it would affect all three samples in similar ways.

2.6.6   Age effect

An additional effect we must consider is the result of differences in stellar population ages and the possible difference in progenitor lifetimes between our samples. Stars that explode as SLSNe and LGRBs are likely >12 M$_\odot$ and hence have short lifetimes of a few million years. Conversely, our sample of CCSNe is dominated by type II SNe which typically originate from less massive stars of 8–12 M$_\odot$ which may take up to a few tens of millions of years to explode. Therefore, the galaxy populations hosting CCSNe could evolve significantly more that the galaxies hosting SLSN/LGRBs after the actual star-formation episode—such that even if the properties of the galaxies were identical at the time that the SN progenitors were formed, the observable properties may in some cases be different at the time of

the SN explosion.

This effect is crucial when considering precise spatial positions within the galaxy, and to some extent when dealing with emission-line metrics. Fortunately, this issue is lessened in our study because our investigations are limited to quantities derived from the broadband photometry. These wavelengths trace star-formation over a much longer timescale (10–100 Myr) than other tracers of star formation such as H α which measure the 'instantaneous' star-formation (1–10 Myr). Thus, the difference between SLSNe and CCSNe is not likely to be an age effect. If a galaxy is starting from a very small stellar population and then a starburst begins, many more young stars will have formed in the tens of millions of years between the explosions of the first very high-mass stars and the explosions of stars with longer lifetimes. Thus, there may be a mass 'build-up' effect seen in CCSNe which may not be seen in SLSNe and LGRBs, leading to systematically higher masses in the CCSNe sample.

As shown in Table 2.6, the 90th percentile of the specific star formations rates for the transients in our samples are: -8.9 for CCSNe, -7.5 for SLSNe-I, -7.8 for SLSNe-II and -8.5 for LGRB SNe. The SLSN-I host, PTF12dam, has the highest specific star formation rate in our sample of -7.0. The derived SFR for PTF12dam is $\sim$14.5 M$_\odot$ yr^{-1}. In this vigorously star forming galaxy, a progenitor with a short life of 2 Myrs would see a mass build up effect in the galaxy over the progenitors lifetime of 2.9×10^7 M$_\odot$, whereas a progenitor with a lifetime of 100 Myrs would allow a stellar mass build in the host galaxy of 1.4×10^9 M$_\odot$, which would significantly alter the measured stellar mass of this galaxy. However, this also assumes the starburst would continue for 100 Myr without abating, which is unlikely and is only important for the very youngest, lowest-mass galaxies.

2.6.7 SED fitting procedure

I fit the host SEDs using LE PHARE in order to derive stellar masses and SFRs of each galaxy within the sample. There are a number of uncertainties associated

with SED fitting. For example, measuring the age and hence SFR of the galaxy can be difficult due to the degeneracy between the age, metallicity. However, since our samples are low-redshift, we have high-quality data from UV to NIR which helps to overcome this degeneracy.

Assuming that the stellar models are perfect to begin with, one can estimate the stellar masses of normal galaxies to within ~0.3 dex (Conroy, 2013). However, using single stellar population models will tend to underestimate the mass to light ratio and hence the stellar mass since young stellar populations can outshine older stellar populations, causing older stellar populations to be missed in these types of galaxies (e.g. Papovich et al., 2001).

A few CCSN hosts (specifically 14de and 16am) were found to have low star formation rates, despite having high stellar masses. In these cases, the star formation rates derived from the SED fitting procedure are are likely to be underestimated. Thus, in these cases fitting a more complex star formation history with a two-population model may be a better approximation since these red galaxies likely have a population of old stars, as well as a recent star formation episode. However, galaxies with these properties are expected to contribute very little to the cosmic supernova rate, although previous examples have been reported (e.g. Irani et al., 2019). In addition, for the starburst galaxies in our sample, the star formation histories are often complex and see stars formed in bursty episodes. Therefore the tau model especially in these cases may be over simplified.

I use the Bruzual & Charlot (2003) libraries, which are single-star stellar isochrones. However, a number of other stellar population synthesis codes exist such as PE-GASE (Fioc & Rocca-Volmerange, 1997) FSPS (Conroy et al., 2009) and BPASS (Eldridge & Stanway, 2009) or CIGALE (Boquien et al., 2019) and each set of models. However, since binary interactions are thought to occur in three quarters of massive stars (Sana et al., 2012) and certain types of CCSNe, such as stripped-envelope supernovae, are thought to be produced (at least in part) though binary channels, this could introduce some biases. However, at the time this work has been completed, no easily accessible set of isochrones existed and binary stellar

evolution pathways include assumptions of the binary fraction, and the distribution of initial binary parameters in the population, which are uncertain outside of the local Universe. In addition to the biases introduced by the choice of SED models, the choice of program to fit the models may also introduce a systematic offset in the derived parameters.

In addition, the choice of program used to measure physical parameters of stellar populations by fitting the models to data to broad band SEDs could systematically affect the measured physical parameters. LE PHARE uses a χ^2 grid-based minimisation. However, Markov Chain Monte Carlo techniques also exist. For example, PROSPECTOR (Johnson et al., 2019) uses this technique and the choice of chosen priors can impact the derived physical parameters. In host galaxies where there there may be bimodal fits, it may be beneficial to derive the best-fit parameters via the marginalised posterior distribution, instead of the χ^2 minimisation technique (Bundy et al., 2005).

However, I self-consistently run LePhare in the same way on all the different samples discussed in this Chapter. Therefore although the absolute numbers in the derived parameters are affected by all these systematics mentioned above, the *differences* between different samples are more secure and this is an important distinction from most previous work on the topic.

2.6.8 Differences in photometry procedure

The photometry for PTF SLSN hosts and ASAS-SN CCSN hosts is carried out using a similar method. There may, however, be differences in background and aperture treatment for photometry measurements I have taken from the literature—but in most cases this photometry is directly validated by comparison to our own measurements, with measurements that disagree to high significance excluded.

In addition, the dominant source of uncertainty for the photometry of nearby and massive galaxies in the CCSN sample is from the background subtraction.

Therefore the photometric uncertainties may be underestimated for these sources. However, photometry from the NSA has a special background optimised subtraction (Blanton et al., 2011) and these host galaxies are not offset from the rest of the sample.

2.7 Conclusions

In this chapter, I have presented a large and unbiased sample of 150 CCSNe from ASAS-SN. I have performed UV to NIR photometry of this sample. I have also compiled a sample of low-redshift exotic transients from the literature for direct comparison to CCSN hosts, including 29 SLSNe-I, 21 SLSNe-II and 17 LGRBs detected and publicly announced before 2017.

I model each host galaxy SED to derive the stellar masses and star formation rates. CCSNe generally exhibit similar star-formation properties to star-formation-weighted local galaxies (LVL), consistent with the expectation that CCSNe should trace star-formation. However, I find the CCSN-selected galaxy median logarithmic stellar mass distribution to be weighted towards slightly lower mass galaxies 9.5(0.1) than the SFR-weighted LVLS galaxy stellar mass distribution with median logarithmic stellar mass of 9.8, possibly indicating that the local-volume sample is affected by cosmic variance. I find that 33^{+4}_{-4} per cent of CCSNe (50/150) from our sample) occur in dwarf galaxies with stellar masses less than 10^9 $M_{\odot}$ and 7^{+3}_{-2} per cent of CCSNe (11/150 from our sample) occur in dwarf galaxies with stellar masses less than 10^8 $M_{\odot}$, representing a substantial fraction of the population.

The hosts of SLSNe-I were shown to be consistently less massive than every other host galaxy sample in this analysis and there is a large starburst fraction (28^{+10}_{-7} per cent) consistent with an intrinsic preference for starbursting galaxies, whereas only a few per cent (2^{+2}_{-1}) of CCSN hosts are undergoing starbursts. If star formation density is the main driver of SLSNe instead of a metallicity bias, it

could be an important clue to uncovering the nature of the progenitors of SLSNe. This may suggest a variable top-heavy IMF in these environments, or possibly the SLSN rate may be enhanced by the interactions of massive stars in extremely dense star clusters. However, this high starburst fraction for SLSNe-I is also consistent with a strong SLSN-I mass dependence in covariance with a larger starburst fraction in dwarf galaxies. I cannot yet conclusively identify or rule out a role for intense star-formation in increasing the SLSN-I rate in starbursting dwarf galaxies.

In principle, the distribution of late bursts of low-metallicity star formation in galaxies could have some impact on the implications of a dwarf-exclusive SLSN population. For example, in the local Universe, observational IFU studies MANGA shows that the metallicity of the outskirts of galaxies of different stellar masses tend to converge to a common metallicity, similar to the observed metallicity in the centres of low-mass galaxies (Belfiore et al., 2017). Thus if galaxies with high stellar masses had a substantial amount metal-poor star-formation (e.g. in their outer reaches, due to gas infall in mergers) perhaps something other than metallicity could be responsible for driving the trend. However, this convergence at large radii is not seen in CALIFA (Sánchez et al., 2014) where there appears to be a characteristic effective radius-normalised metallicity gradient. The results from cosmological simulations such as EAGLE (Tissera et al., 2019) show the oxygen abundances at 2 effective radii for galaxies with negative metallicity gradients (typically lower-mass galaxies) and positive gradients (typically higher mass galaxies) have values around $12+\log(O/H)=8.0$. However, the resolution means that the lower logarithmic mass range of this sample of 9.7 is higher than the majority of the SLSN-I sample.Future work on this question will be needed to produce clear predictions of the SLSN rate in the outer regions of massive galaxies to determine whether our observations are consistent with this picture.

LGRB SN and SLSN-I host populations exhibit similar host galaxy properties. The peak of their host mass distributions is clearly much lower and spans a much smaller mass range than the CCSN population which trace star-formation with

median logarithmic mass of 7.9(0.2) for SLSNe-I, 8.7(0.2) for LGRB SNe, and 9.5(0.1) for CCSNe. Since galaxy stellar mass correlates well with the average galaxy metallicity, this difference in stellar mass of the host galaxies indicates there could be a metallicity bias in the progenitors of LGRB SNe and SLSNe-I in comparison to CCSNe. If one assumes the galaxy mass-metallicity relation (Tremonti et al., 2004), this implies that the 12+log(O/H) median integrated metallicity values for host galaxies of SLSNe-I are 8.1(0.1), for LGRB SNe are 8.5(0.1), in comparison to CCSNe which have metallicities of 8.8(0.1). This corresponds to 0.3 $Z_\odot$ for SLSNe-I, 0.6 $Z_\odot$ for LGRBs and 1.3 $Z_\odot$ for CCSNe. These values are in agreement with the metallicity dependence proposed in the literature, which suggests that SLSNe-I and LGRBs seem to exhibit a preference for sub-solar metallicity host galaxies. The LGRB production efficiency seems to be strongly suppressed at metallicities above ∼0.3–1 $Z_\odot$ (Krühler et al., 2015; Vergani et al., 2015; Japelj et al., 2016a; Perley et al., 2016b; Palmerio et al., 2019) and the production efficiency of SLSNe-I seems to be suppressed above ∼0.4–0.5 $Z_\odot$ (Perley et al., 2016a; Chen et al., 2017a; Schulze et al., 2018).

Single-star PISN models that could produce SLSNe-I predict that pair-instability supernovae should only be produced by low-metallicity stars Z<0.2 $Z_\odot$ (which corresponds to a logarithmic stellar mass of ∼7.7) and the rate of PISN explosions should be low at metallicities above 0.5 $Z_\odot$. Thus, our results suggest that PISNe contribute at most a fraction of SLSNe-I in our sample and some other mechanism that still operates at higher metallicities is responsible for most or perhaps all known SLSNe-I at higher metallicities.

LGRB SNe explode, on average, in higher mass galaxies than SLSNe-I. This lends further support to models in which LGRBs and SLSNe-I form only in certain environmental conditions related to low-mass and metallicity, and may reflect similar favoured progenitors. I also made comparisons between LGRB-SNe and SN-less LGRBs. However, I do not find any statistically significant differences. However, this comparison is limited by the sample size of five SN-less events.

I find a statistical difference between the hosts of SLSNe-II and CCSNe. SLSNe-

II seem to occur in generally lower mass and more strongly star-forming hosts that CCSNe. However, the difference is not as stark as SLSNe-I and SLSNe-II do arise in galaxies spanning a surprisingly large range of stellar masses and star formation rates. This is difficult to explain if the progenitor population is subject to a simple metallicity bias and this diversity could suggest multiple progenitor channels.

Since we are analysing host galaxies with ongoing massive star formation, the effects of binary evolution on such stars will play an important role in the stellar population synthesis models, and this will change the observable properties, particularly for young and low-metallicity stellar populations. For example, Eldridge (2012) argued that binary models will create more massive stars than the initial maximum imposed on the stellar population due to mass transfer and mergers, which may lead to uncertainties in the isochrones impact the UV spectra of star-forming galaxies and the resulting SPS model predictions.

The choice of IMF is one of the largest sources of systematic uncertainty in the modelling of stellar populations. Thus, the choice of IMF will affect the stellar population synthesis models. In particular, it will affect the normalisation of the mass-to-light ratio, which is used to estimate the stellar mass and the star formation rate host galaxy parameters. In this thesis, we assumed a Chabrier IMF. However, if we had assumed the Salpeter (bottom-heavy) IMF, there would be a larger fraction of long-lived, low-mass stars and our derived values of SFR and stellar mass would be higher with a Salpeter IMF assumption. However, in this thesis I self-consistently re-derive all the physical parameters. Thus while the absolute numbers may be affected by these systematics, the differences between the samples would still be present.

Chapter 3

Liverpool Telescope integration with the Zwicky Transient Facility

3.1 Introduction

Increasingly sophisticated transient discovery methods (described early in Sections 1.2.1 and 1.2.3) have now enabled a diverse range of transient science to be effected, including:

- The search for electromagnetic counterparts to gravitational waves.

- Characterising transients in high-cadence search efforts, including: studying the effects of shock breakout in young supernovae caught within hours of explosion, and uncovering the explosion mechanism of rapidly-evolving transients (<10 day rise to peak), such as fast blue optical transients.

- Building large, representative samples of different transient populations for supernova rate calculations and demographic studies.

However, survey telescopes provide photometry in only a few filters, to limited

depth, and generally follow a fixed observing schedule. Thus, for these science goals to be achieved, search efforts must be coupled with systematic photometric and spectroscopic follow-up.

Spectroscopy is vital to identify interesting transients, to secure redshifts and to understand the physics of the explosion. It is especially important for population studies requiring large, representative samples (100–1000's) of SNe. In addition, photometric follow-up allows high-quality light curves to be obtained in multiple filters, that go much deeper than survey telescopes. This is important for light curve modeling and for obtaining late-time light curve coverage.

Moreover, when follow-up facilities are distributed globally, this allows for higher-cadenced follow-up because when the sun rises in one location, observations can still be taken at other observatories. Also if the weather is poor it enables data to be gathered from another location, reducing significant gaps in photometric or spectroscopic coverage.

The robotic Liverpool Telescope (LT; Steele et al., 2004) is well suited for this type of follow-up (see Section 3.3 for a summary of LT's specifications). Specifically, data is gathered on a nightly basis for various LT science programs for the Zwicky Transient Facility (ZTF). Often it is crucial to analyse the new data immediately to inform future follow-up plans, and this motivates the need for an automated approach to reduce and analyse the data efficiently. In this chapter, I present my work within ZTF, including the integration of the Liverpool Telescope and my automated digital image subtraction pipeline.

3.2 Zwicky Transient Facility

The Zwicky Transient Facility (ZTF) is an optical wide-area survey focused on discovering transients. ZTF has been on sky since 2017, and its transient surveys began in 2018. It is the successor of the Palomar Transient factory (Law et al., 2009) that ran from 2009–2012, and the intermediate Palomar Transient factory

([Cao et al., 2016](#)) that ran from 2013–2017. ZTF uses the same 48-inch telescope, but with a much larger camera, upgraded from a 7.26 deg^2 to 47 deg^2 field of view ([Bellm et al., 2019](#)). A comparison of the ZTF camera against PTF and other wide-field surveys is shown in Fig. [3.1](#). Since ZTF is very wide-field, it discovers many bright ($m_r < 20.5$ mag) transients. Thus, many ZTF discoveries are accessible even with modest diameter telescopes.

ZTF scans the sky every night in the g- and r-bands, with a 3-day cadenced public data stream, and with several high-cadence surveys to find young and fast events. Additionally, target-of-opportunity programs are used to conduct searches for gravitational wave counterparts by tiling LIGO/VIRGO error regions following the detection of a candidate merger event.

ZTF has a dedicated website (the GROWTH MARSHAL; [Kasliwal et al. 2019](#)) for filtering the ZTF alert stream based on science-program filters written by different science groups. The GROWTH MARSHAL also allows follow-up resources to be scheduled and has the ability to trigger some telescopes directly, such as the Spectral Energy Distribution Machine (SEDM) integral field spectrograph on the Palomar 60-inch Telescope (P60; [Blagorodnova et al., 2018](#)).

3.3 Liverpool Telescope follow-up

The Liverpool Telescope (LT; [Steele et al., 2004](#)) is a fully robotic, 2-m telescope located at the Roque de Los Muchachos Observatory on La Palma. LT's robotic nature makes it very well suited for ZTF follow-up. Current instrumentation on LT includes: an optical wide-field imager (IO:O)[1], a fast-readout wide-field camera built for precise timing of transiting exoplanets, (RISE; [Steele et al., 2008](#)), a low-resolution (18 Å) spectrograph for the rapid acquisition of transients (SPRAT; [Piascik et al., 2014](#)), a dual beam integral-field input spectrograph (FRODOSpec; [Barnsley et al., 2012](#)) and a separate wide-field imager (SkyCam)[2]

---

[1]https://telescope.livjm.ac.uk/TelInst/Inst/IOO/
[2]https://telescope.livjm.ac.uk/TelInst/Inst/SkyCam/
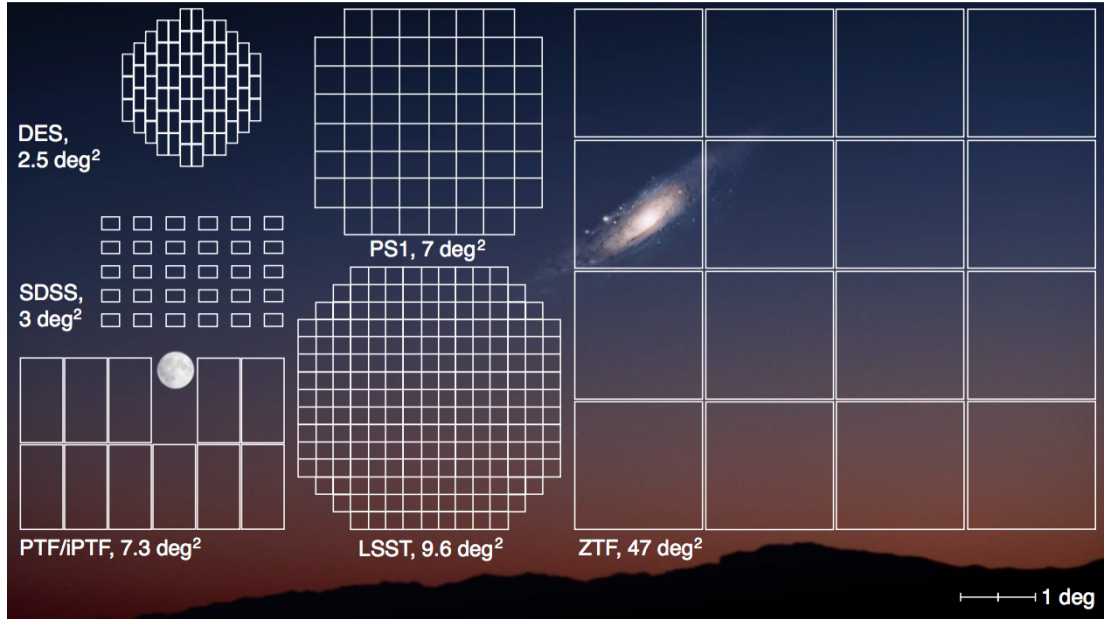
Figure 3.1: Field of view of the ZTF camera compared against other wide-field surveys. The moon and the Andromeda galaxy are shown to scale. A one degree scale bar is indicated (Credit: Joel Johansson; Laher et al. 2018).

that is mounted on the side wall of the LT enclosure, and operates in parallel with LT's normal data taking operations.

Before the start date of my PhD, LT had not been integrated and was rarely used with PTF (although there were a few special cases for nova and gravitational wave science that were uncoupled to the survey itself). Thus, the follow-up strategy was put into place in mid-2018 at the start of ZTF and further developed over the course of ZTF. I was not closely involved with the development of the strategy or in triggering, but I took charge of the software and data analysis aspect.

For the data reduction aspect, most groups do image subtraction on a case by case basis for publication worthy photometry. However, the Global Supernova Project (Howell & Global Supernova Project, 2017), while not a search survey, has software tools for triggering and data reduction tools as part of this follow-up project, coupled to a Marshal-like interface. Also recently (in the past year) there has been a significant focus on developing common interfaces for triggering (TOM) across different telescopes.

To my knowledge the only other comparable end-to-end system coupling a tele-

scope with a single search survey is Palomar 60-inch telescope coupled to PTF/ZTF. The Palomar 60-inch was first coupled to PTF in a limited sense for only imaging and there was no automated image subtraction pipeline. In 2018 Palomar 60-inch (with SEDM) was then coupled to ZTF for imaging and spectra. The Fremling et al. (2016) image-subtraction pipeline for Palomar 60-inch was the first to be able to run completely hands-off for PTF/ZTF follow-up. The LT-ZTF integration shortly followed and the LT with integrated with ZTF for both spectroscopy and automated image subtracted photometry.

We primarily concentrate on the SPRAT (spatial pixel scale 0.44"/pixel) for classification of bright (<18.5 mag) transients and IO:O for multi-colour ($ugriz$) photometric follow-up. These data are complementary to ZTF, which is a primarily g and $r-$band survey. Multi-colour light curves are useful for constraining the temperature evolution of SLSNe and are also vital to have as a high-fidelity light curve training sample to help prepare for LSST (which will have six optical bands $ugrizy$).

The pixel scale for IO:O is 0.3"/pixel with the default 2×2 binning. Observational constraints are flexible since useful data can be taken even in sub-optimal seeing conditions. Exposure times typically vary between 30–120 s, with a corresponding saturation r-band limit of 13.2–14.7 mag. The shutter causes the exposure time to vary as a function of position in the image, with the centre being exposed by 80 ms longer[3]. This effect is increased for short exposure times and reduces the photometric accuracy of the images. Thus, even for bright transients, we keep the minimum exposure time to 30 s. This allows photometry to be obtained to an r-band limiting magnitude of $\sim$22 mag for single-exposure subtractions. By stacking the images, the signal-to-noise ratio can be improved (the noise is reduced by $1/\sqrt{N}$ for N exposures at these depths). Stacking allows photometry to be obtained to a limiting magnitude of $\sim$23 mag for multiple r-band exposures[4]. For data taken in bright time, with a large contribution by the moon, imaging

---

[3]See https://telescope.livjm.ac.uk/TelInst/Inst/IOO/ for more detail.

[4]For u and z-band limits are shallower. Single u-band exposures typically have a magnitude limit of $\sim$21 mag, and $\sim$22 mag for multiple exposures.

can be obtained to a depth of ∼20 mag. However, if the host galaxy is bright or complex such that it does not subtract away cleanly and the subtraction residuals dominate the sky noise, then signal-to-noise will not improve much with increasing exposure time.

The LT images are reduced with the IO:O instrument calibration pipeline, including bias and dark subtraction, trimming of the overscan regions, and flat fielding. The new LT data is available every morning. However, the LT also offers rapid data reductions on a quicklook webpage[5] within ∼5 minutes of the exposure being taken. These images are essentially fully reduced and are usually of very similar quality to the archive data, except they may not use the most up-to-date calibration files nor have been quality inspected by the LT staff.

3.4 Liverpool Telescope interface for ZTF

For typical users, LT observations are generally triggered from the JAVA PHASE2UI, a graphical user interface which allows users to configure their programs and submit their observation blocks to the LT observing database. The observations are ranked alongside other users' requests and against the observing constraints. The scheduler then establishes a ranked list of observations that are sent to the robotic control system. For regular monitoring programs where one may require observations over a long period at some specific cadence, such as gathering multi-band weekly photometry to construct a SLSN light curve, this triggering method is preferred. However, when rapid follow-up is required (e.g. LIGO/VIRGO optical counterpart candidates), a more streamlined approach is needed.

A method to trigger the LT from the ZTF GROWTH MARSHAL is preferable for rapid follow-up because in large collaborations not all users will be familiar with the PHASE2UI system, and without credential access some time-critical observations may not take place. A web-enabled triggering method also allows the

---

[5]http://telescope.livjm.ac.uk/DataProd/quicklook/

Figure 3.2: LT-ZTF GROWTH marshal interface. (a) The image request form allows users to select a variety of observations with different filter combinations. (b) The spectrum request form allows users to select the integration times, and the grating configuration for optimum sensitivity on either the blue or red side.

object name and coordinates to be taken directly from the GROWTH MAR-SHAL, meaning there are no mistakes due to human errors.

LT can process observation requests using the Remote Telescope Markup Language (RTML), which means that observation requests can be generated via the command line and be sent directly to the LT database. Therefore an user interface was implemented on the GROWTH MARSHAL (see Fig. 3.2) using RTML. Fig. 3.2 shows the LT request form. For the image requests, different filter combinations can be selected. For the spectrum request form, the integration times and grating configuration can be chosen. Requests are managed on a designated webpage on the ZTF GROWTH marshal (see Fig. 3.3). To keep track of the ZTF-MARSHAL submitted observations, I have implemented nightly summary e-mails listing any newly submitted observations which are sent to immediate collaborators. This helps to prevent over-submission, possible duplication of submissions since currently the ZTF-MARSHAL submitted observations cannot be deleted directly from the MARSHAL and have to be deleted from the JAVA PHASE2UI.

9999	LT - IOO	gri 1x90s :ACCEPTED	5	2020-01-28	2020-01-29	Fast Transients	ZTF20aajnksq	annayqho	ACCEPTED	✖
10003	LT - IOO	ugriz 1x60s :ACCEPTED	5	2020-01-28	2020-01-29	Fast Transients	ZTF20aagexvg	dperley	ACCEPTED	✖
10035	LT - IOO	gri 1x90s :ACCEPTED	5	2020-01-30	2020-01-31	Fast Transients	ZTF20aaiikae	annayqho	ACCEPTED	✖
10081	LT - IOO	r 3x180s :ACCEPTED	5	2020-01-31	2020-02-01	Fast Transients	ZTF19acykibn	KTaggart	ACCEPTED	✖
10111	LT - IOO	gri 1x90s :ACCEPTED	5	2020-02-03	2020-02-04	Fast Transients	ZTF20aaifaqt	annayqho	ACCEPTED	✖
10112	LT - IOO	griz 1x60s :ACCEPTED	5	2020-02-03	2020-02-04	Fast Transients	ZTF20aaifaqt	annayqho	ACCEPTED	✖
10172	LT - SPRAT	blue 2x300s :ACCEPTED	5	2020-02-04	2020-02-05	Infant Supernovae	ZTF20aalxlis	RachelBruch	ACCEPTED	✖
10204	LT - SPRAT	blue 1x600s :ACCEPTED	5	2020-02-05	2020-02-06	Infant Supernovae	ZTF20aalxlis	steveschulze	ACCEPTED	✖
10254	LT - SPRAT	blue 1x600s :ACCEPTED	5	2020-02-07	2020-02-08	Infant Supernovae	ZTF20aalxlis	steveschulze	ACCEPTED	✖
10287	LT - SPRAT	blue 1x600s :ACCEPTED	5	2020-02-09	2020-02-10	Infant Supernovae	ZTF20aamgdkb	steveschulze	ACCEPTED	✖
10308	LT - IOO	gri 1x90s :ACCEPTED	1	2020-02-11	2020-02-12	Superluminous Supernovae II	ZTF19ackzvdp	lyan	ACCEPTED	✖
10309	LT - IOO	gri 1x90s :ACCEPTED	1	2020-02-11	2020-02-12	Superluminous Supernovae II	ZTF19acsajxn	lyan	ACCEPTED	✖
10310	LT - IOO	gri 1x90s :ACCEPTED	1	2020-02-11	2020-02-12	Superluminous Supernovae II	ZTF19abfvnns	lyan	ACCEPTED	✖
10341	LT - SPRAT	blue 2x600s :ACCEPTED	1	2020-02-12	2020-02-13	Redshift Completeness Factor	ZTF20aafmdzj	jesper	ACCEPTED	✖
10358	LT - IOO	gri 1x90s :ACCEPTED	1	2020-02-13	2020-02-14	Electromagnetic Counterparts to Gravitational Waves	ZTF20aamvqxl	ChrisCopperwheat	ACCEPTED	✖
10429	LT - IOO	r 3x180s :ACCEPTED	5	2020-02-16	2020-02-17	Infant Supernovae	ZTF20aanzplk	steveschulze	ACCEPTED	✖
10443	LT - IOO	gri 1x90s :ACCEPTED	1	2020-02-17	2020-02-18	Electromagnetic Counterparts to Gravitational Waves	ZTF20aamvmzj	ChrisCopperwheat	ACCEPTED	✖
10444	LT - SPRAT	blue 1x600s :ACCEPTED	5	2020-02-17	2020-02-18	Infant Supernovae	ZTF20aaocqkr	nora	ACCEPTED	✖
10460	LT - SPRAT	blue 1x600s :ACCEPTED	5	2020-02-18	2020-02-19	Electromagnetic Counterparts to Gravitational Waves	ZTF20aanakcd	ChrisCopperwheat	ACCEPTED	✖
10461	LT - IOO	gri 1x90s :ACCEPTED	1	2020-02-18	2020-02-19	Electromagnetic Counterparts to Gravitational Waves	ZTF20aanakcd	ChrisCopperwheat	ACCEPTED	✖
10462	LT - IOO	gri 1x90s :ACCEPTED	5	2020-02-18	2020-02-19	Electromagnetic Counterparts to Gravitational Waves	ZTF20aanakcd	ChrisCopperwheat	ACCEPTED	✖
10463	LT - IOO	r 3x180s :ACCEPTED	5	2020-02-18	2020-02-19	Electromagnetic Counterparts to Gravitational Waves	ZTF20aanakcd	ChrisCopperwheat	ACCEPTED	✖

Figure 3.3: Summary of Liverpool Telescope requests submitted by ZTF users.

3.5 Image subtraction pipeline

In addition to needing a capability to rapidly *request* observations from a central project website (GROWTH MARSHAL), we also need a capability to rapidly *analyse* the observations and feed them back to the same website, to enable science and to inform future follow-up decisions. On average, 11 images are taken per night for various LT programs. Photometry must be performed for these images and be uploaded to the GROWTH MARSHAL. Without automation, this is a laborious task and could take up to a few hours per day. This motivates the need for a more efficient approach for the supernova photometry, in the form of an automated image subtraction pipeline.

In this Section, I present my implementation of the final science pipeline for LT-ZTF data. The image subtraction pipeline is written in PYTHON, calling on SWARP (Bertin, 2010), PANSTAMPS[6], SExtractor (Bertin & Arnouts, 1996) and PSFEx (Bertin, 2011). It is fully automated, fully implemented and runs continually on the LJMU cluster computers every night. For the real-time data reduction and sharing with ZTF users, the quicklook LT images are used in the reductions. For publications, the pipeline can be run on the fully-reduced images that are available the following morning. However, this photometry is usually identical to the quicklook reductions, therefore tailoring prior to publication is usually unnecessary.

On average, 11 images are taken per night and for each image (or stack, if multiple exposures in one band are taken) the pipeline uses 0.9 megabytes of memory and takes approximately 90 seconds to obtain fully reduced, image-subtracted photometry. The pipeline is fast enough to do processing in real-time so that the fully reduced photometry is available the following morning. In the morning, a detailed overview of the observations and reductions is sent the immediate collaborators and the photometry is automatically fed back to the ZTF GROWTH MARSHAL. This photometry is in full usage and is available for all ZTF GROWTH MAR-

---

[6] https://pypi.org/project/panstamps

SHAL users and has been used in a number of publications, science topics, and LT proposals for different LT users (see Table. 3.1 for more detail). The pipeline is extremely reliable. The typical precision achieved in the reductions is between 1–5 per cent for the vast majority of cases – similar to the ZTF photometry. But for cases such as SNe in nuclei or in very high surface-brightness starbursts, or when LT has focus problems, there can be larger uncertainties.

To some extent, all supernovae will have some flux contribution from their respective host galaxy. For accurate supernova photometry, this galaxy light must be removed by image subtraction. A pre-existing reference image ($\text{Image}_{\text{Ref}}$) of the same region of the sky (or a reference image taken when the supernova has sufficiently faded) is subtracted from the science image ($\text{Image}_{\text{Sci}}$) containing the transient object, leaving the supernova light.

An important difficulty in image subtraction is that the Point Spread Function (PSF) will vary significantly on short timescales of minutes. These variations arise due to seeing, tracking errors and atmospheric dispersion for significant zenith distances. Thus, even if the images are taken consecutively, in order to make a perfect subtraction of two images, one must precisely match the PSF in each image to account for PSF variation.

The images relevant to this work, are usually taken on different dates, with the reference image taken in a different year, and with a different telescope. Therefore PSF matching is of critical importance. To do this usually requires an extremely accurate convolution kernel (Alard, 2000).

One commonly used method is partial deconvolution, where one image is convolved to match the PSF of the other image.

$$\text{Image}_{\text{Sci}}(x, y) - \text{K}(u, v) \otimes \text{Image}_{\text{Ref}}(x, y) = \text{Image}_{\text{Sub}}(x, y) \qquad (3.1)$$

Here $\otimes$ represents convolution and K, is the convolution kernel. Subtraction packages that implement this method include ISIS (Alard, 2000) and HOTPANTS

(Becker, 2015). The kernel model, K, is a set of basis functions which are linear combinations of Gaussians that are fitted to point sources in the image. K is then multiplied by low-order polynomials over the image in order to account for spatial variations in the PSF across the image.

Another method is the cross filtering, or sometimes called the common PSF method (Gal-Yam et al., 2008), where the $\text{Image}_{\text{Sci}}$ is convolved with the PSF of the reference image and the $\text{Image}_{\text{Ref}}$ is convolved with the PSF of the science image:

$$\text{PSF}_{\text{Ref}}(x,y) \otimes \text{Image}_{\text{Sci}}(x,y) - \text{PSF}_{\text{Sci}} \otimes \text{Image}_{\text{Ref}}(x,y) = \text{Image}_{\text{Sub}}(x,y) \quad (3.2)$$

One advantage of this method is there are no parameters to be tuned except the size of the box region used to measure the PSF. A pipeline implementing this method can be easily modified. For example, one has full control of the selection of PSF stars. Whereas packages such as ISIS and HOTPANTS are like a 'black box' in the sense that one has almost no control on the selections made by the program, which occasionally causes failures.

The drawback of the common PSF method is that *both* images are degraded, therefore the final PSF is broader than the PSF of the worse image. However, it is well-suited for subtractions with varying conditions where the reference image was obtained from another telescope. For example, it has been implemented with great effect for the P60 Telescope for ZTF photometric follow-up (Fremling et al., 2016).

I have implemented a script to automatically run image subtraction in PYTHON. A simplified outline of the pipeline is shown in Fig. 3.4 and a description of the pipeline (from data collection to upload) is detailed below:

Science image preparation– Firstly, all new images are downloaded in parallel as they are made available on the quicklook website[7]. Before image subtraction

---

[7] http://telescope.livjm.ac.uk/DataProd/quicklook/
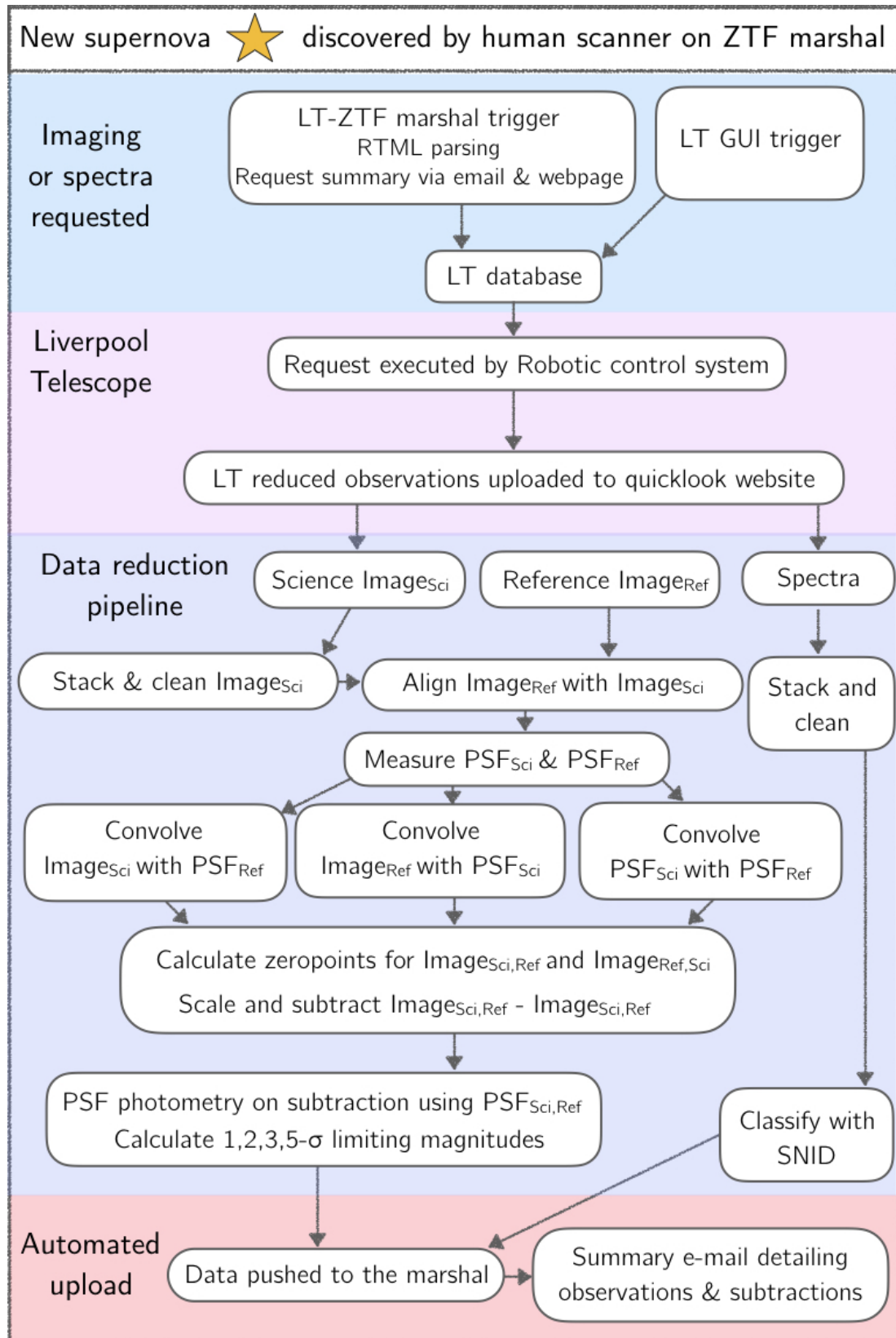
Figure 3.4: The workflow of the LT pipeline. It can be roughly split into three main steps: the triggering of LT, the data reduction, and feeding the data back to the GROWTH MARSHAL automatically.

can be carried out, some steps are taken to ensure the new images will give scientifically useful subtractions:

- The image header is read to check the seeing conditions. If the seeing could not be determined, this is flagged as '996' or '999' which means either the seeing is very poor ($\gtrsim 5$ arcseconds), or is indicative of shutter problems. These conditions usually make it impossible to determine a PSF within the image, so in these cases, the pipeline will exit and write an error message in the output log, containing the estimated and the predicted seeing for the image.

- Next, the pipeline stacks images using SWARP (Bertin, 2010) if multiple exposures are taken in the same filter. This serves two primary purposes: to increase the signal to noise of the supernova detection, and it allows for the rejection of some cosmic rays in the image. Since the exposures are typically less than 120 seconds, the pipeline runs 5 minutes after the latest image is taken to ensure the observation block for a particular object has ceased before the combination step is performed.

- Single exposures cannot be stacked to remove cosmic rays and longer integrations are more prone to cosmic ray contamination. Thus, I remove cosmic rays using a spatial filtering algorithm (Laplacian edge detection) as described in van Dokkum (2001)[8] for images with exposure times exceeding 60 seconds.

- The optical set up and the observing conditions will produce background variations that vary between frames. Therefore, the images are background subtracted to ensure any background variations are reduced, which may lead to an erroneous flux estimation. The science image is divided into a 2D grid using a box size (150×150 pixels) larger than the typical source size in the image. The background level in each mesh is calculated using the SEXTRACTOR (Bertin & Arnouts, 1996) background algorithm ((2.5 *

---

[8]https://lacosmic.readthedocs.io/en/latest/

median) - (1.5 * mean)) on the sigma-clipped mesh to create a low-resolution background image.

After the background level has been determined in each of the boxes, the low-resolution background image is median filtered, using a window of size 3×3 boxes to suppress local discrepancies in one mesh (for instance, if there is a bright galaxy in one mesh). The final background image is generated and subtracted from the science image. The main source of non-instrumental background variations is usually moonlight (when observations are taken in bright time).

Reference image– The next step is to gather an appropriate reference image for the subtraction. In the ideal scenario, with unlimited telescope resources, I would obtain the reference template from LT because the subtraction is far easier with the same aperture telescope, the same instrument, and with the same photometric filters. However, in practice, this would require a deep reference image ($\sim$5 minutes of exposure time per filter) which would need to be taken at least six months after the supernova explosion, when it has sufficiently faded. This is not possible on the timescale over which we need photometry and would demand substantial additional telescope resources.

The best alternative is to gather references from public all-sky optical surveys which are freely available to download. For the *griz*-bands, Pan-STARRS1 (PS1; Kaiser et al., 2002) images are retrieved using PANSTAMPS[9] which allows the user to specify the central RA and Dec coordinates and also the required image size. For the *u*-band, reference images are pulled from the Sloan Digital Sky Survey DR12[10] (SDSS; York et al., 2000). These SDSS reference images are not centred on our science image and do not have the same dimensions. Thus, a grid of coordinates (spaced by 0.1 degrees) is queried to retrieve all images in our field of view. The images are combined using SWARP to produce a single image that covers the same field as the science image.

---

[9]https://pypi.org/project/panstamps
[10]https://dr12.sdss.org

Image alignment– The reference images need to be registered against the science image so that the calibration stars and the supernova all have the same x and y pixel coordinates in both images. This is important because an astrometric offset can result in a non-optimal subtraction and leave subtraction residuals often in the form of 'dipoles'. An example of a poorly aligned image is shown in Fig. 3.5.
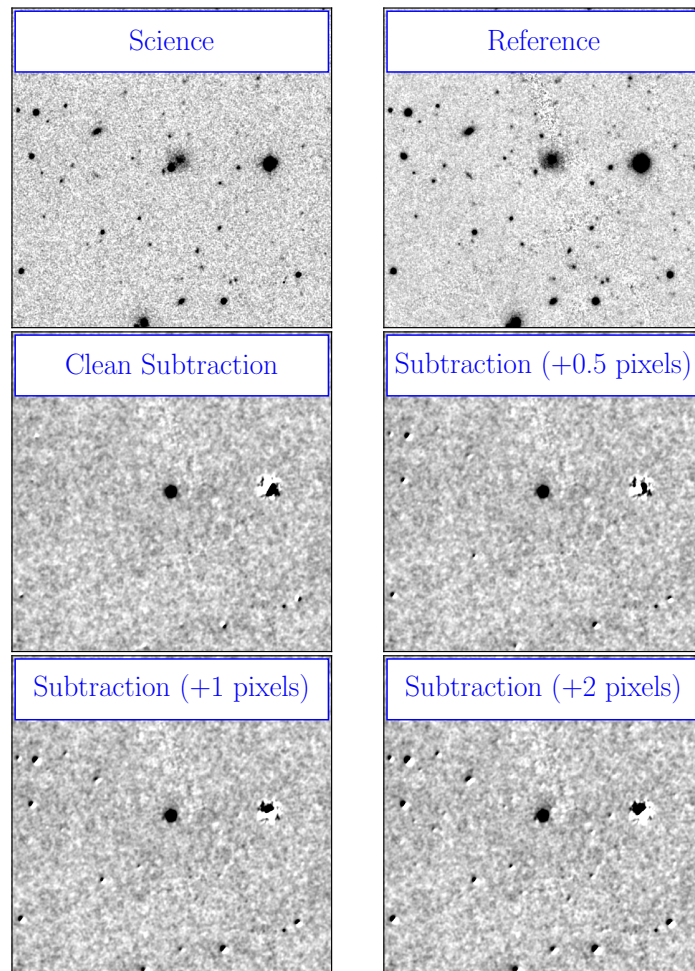
Figure 3.5: An example image subtraction. The top row shows the science and reference images. The second and third rows show image subtractions with a correctly aligned image and poorly aligned images. Even with an astrometric offset of 0.5 pixels, the subtraction residuals begin to appear as 'dipoles'.

- The science images already have a World Coordinate System (WCS) solution after reduction. Therefore the WCS need only be shifted slightly for optimum image alignment. The centroids of familiar point sources in

the reference and background subtracted science images are first identified using SExtractor (Bertin & Arnouts, 1996), and the distances between them are returned. The standard deviation between the centroids in the reference and the science frame is typically less than 0.3 pixels. The median RA and Dec offsets are applied to the relative pixel coordinates at the origin.

- Once the reference image has been correctly registered to the science image, SWarp (Bertin, 2010) is used to project the images on the same pixel grid, using the modified WCS. SWarp uses Lanczos re-sampling for the sub-pixel accuracy required for image subtraction.

Convolution– The science and reference images are from different telescopes and have varying observational conditions. Since the subtractions are non-trivial, I use the common PSF method (CPM) for image subtraction (Gal-Yam et al., 2008).

The science image ($\text{Image}_{\text{Sci}}$) is convolved with the reference image PSF (PSF_{Ref}) and vice versa. The CPM does degrade the final subtracted image. However, it is well-suited for subtractions with varying conditions. Furthermore, there are no parameters to be tuned except the size of the box region used to measure the PSF.

- To obtain the PSFs for the $\text{Image}_{\text{Sci}}$ and $\text{Image}_{\text{Ref}}$, I use SExtractor in combination with PSFEx. Firstly, SExtractor extracts a catalogue of the stars for $\text{Image}_{\text{Sci}}$ and $\text{Image}_{\text{Ref}}$. The star catalogues are then filtered by PSFEx (Bertin, 2011) to prevent any artefacts, saturated, low signal-to-noise or elongated sources from inclusion in the PSF model-building procedure. These filtered catalogues (to avoid introducing noise within the measured PSF by only using isolated, bright stars) are used to extract the non-parametric PSF model by median stacking all remaining stars in the catalogue. Firstly the PSFs are measured by deriving a first-order estimate

of the PSF model, then PSF model is fitted to the point sources and a map of residuals is made so that any poorly fitted objects are rejected. This iterative rejection process is repeated three times. The derived PSF model (dimensions 59×59 pixels) assumes a single, non-spatially-varying PSF and there appears to be evidence for a varying PSF in the subtracted image.

To determine whether the PSF models for the science and reference images are adequate, one useful test is to visually inspect the residuals in the subtracted images. However, the pipeline image control must be automated to ensure consistency in the photometry. To assess the PSF quality, I use the reduced χ^2 for the PSF model fit. If this is greater than 3, the pipeline issues a warning flag that the PSF model may be not be adequate for the subtraction.

- Next, three separate convolutions are done using a Fast Fourier Transform. $Image_{Sci}$ is convolved with PSF_{Ref}, $Image_{Ref}$ is convolved with PSF_{Sci} and PSF_{Sci} is convolved with PSF_{Ref}.

PSF fitting and zero point determination– To calibrate the images, and determine the zeropoint (ZP), the flux of the stars with known magnitudes from (SDSS or PS1) star catalogues are compared to the instrumental magnitudes.

- A cutout of each star in the image is made and then registered to the normalised, convolved $PSF_{Sci,Ref}$ model using cross-correlation. Offsets are applied in the x- and y-direction using spline interpolation. The shift is restricted to move <5 pixels in each direction because if the field is crowded and there are multiple stars in the cutout, the fit should be centered on another maximum in the image.

- Next, the arrays are flattened to 1D, and least-squares linear regression is used to fit the convolved $PSF_{Sci,Ref}$ to the star cutouts. The correlation coefficient (r) is used to measure the quality of the fit. If the quality of the PSF fit is poor ($r^2 < 0.7$) these stars are excluded from the ZP calculation.

- The remaining sources are matched to the catalogues with known magnitudes and the ZP is determined for each star. The ZP measurements are clipped to 5-σ through two iterations to remove any anomalous ZP estimates such as on variable or saturated objects. The median ZP is then calculated for the convolved reference and the convolved science image, respectively.

Image subtraction and magnitude estimates– The ZP information is used to scale the counts of the convolved reference image, resulting in a common ZP_{Sci}. The aligned, convolved, and scaled reference image is subtracted from the convolved science image. Some examples of image subtractions (with seeing <2 arcseconds) are presented in Fig. 3.6. Poor subtractions generally suggests poor removal of the host galaxy flux. Common reasons include: elongation, poor seeing, few stars in the field for calibration and the alignment process and filter differences. Some examples of image subtractions with poor observing conditions (with seeing >5 arcseconds) or with poor signal to noise are presented in Fig. 3.7.

After the image subtraction is performed, I make a cutout in the subtracted image at the expected location of the transient (see the blue box in Fig. 3.8) and perform PSF photometry on the source using the same method as outlined above.

To calculate the signal to noise ratio of the detection and a limiting magnitude for the field, the sky background in the general vicinity of the supernova position is estimated. Forced PSF photometry (i.e. the position is fixed along with the PSF shape, and only the flux is measured) is done on the subtracted image (using the same method as outlined above) to determine the background level of 80 off-target apertures centred around the supernova location (on a 9×9 grid separated by the PSF cutout size so that there is no overlap of the sky background). Fig. 3.8 shows these 80 cutouts in orange, with the fixed cutout centres as orange circles. The typical variation in the sky background is measured by taking the standard deviation of the flux values in the aperture grid and the median of the flux values is used as the typical background level.

If the supernova flux is above 3-σ of the typical background level, a supernova
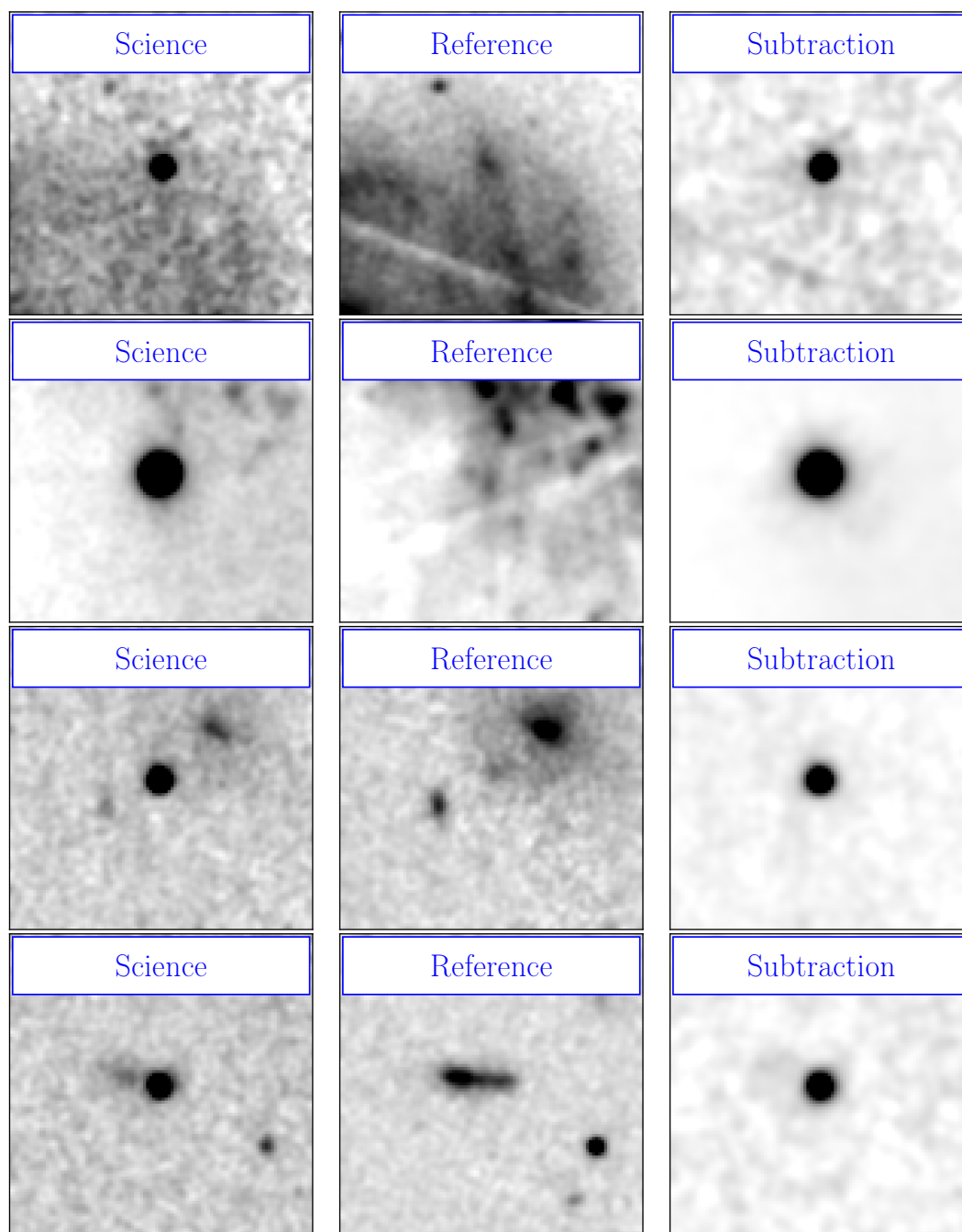
Figure 3.6: Example image subtractions. The left panel shows the aligned science images, the middle column shows the aligned reference images and the right column shows the image subtractions. Each image is 100 pixels (15 arcsec) on each side.
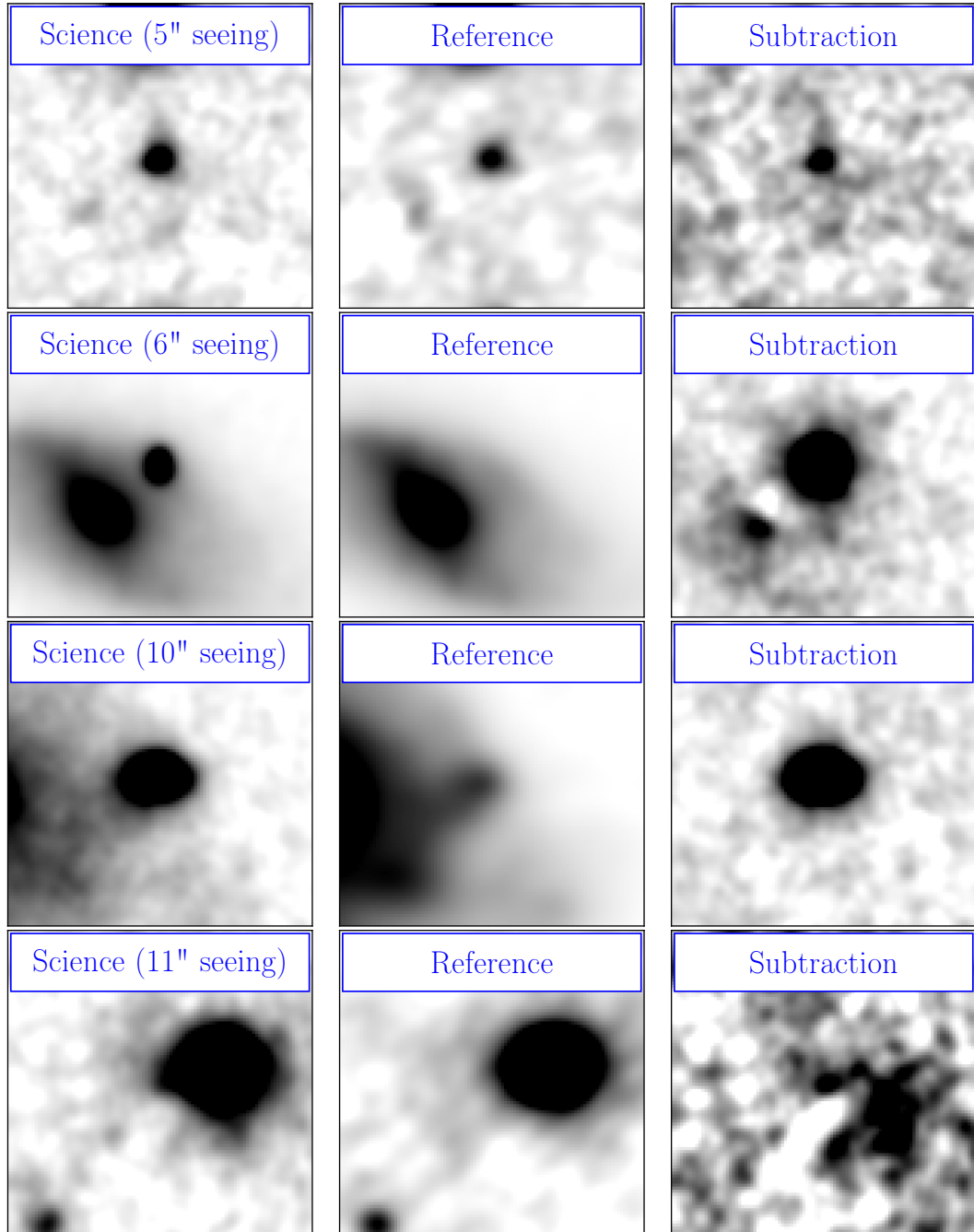
Figure 3.7: Example image subtractions with poor seeing conditions. The left panel shows the aligned science images, the middle column shows the aligned reference images and the right column shows the image subtractions. Each image is 100 pixels (15 arcsec) on each side.
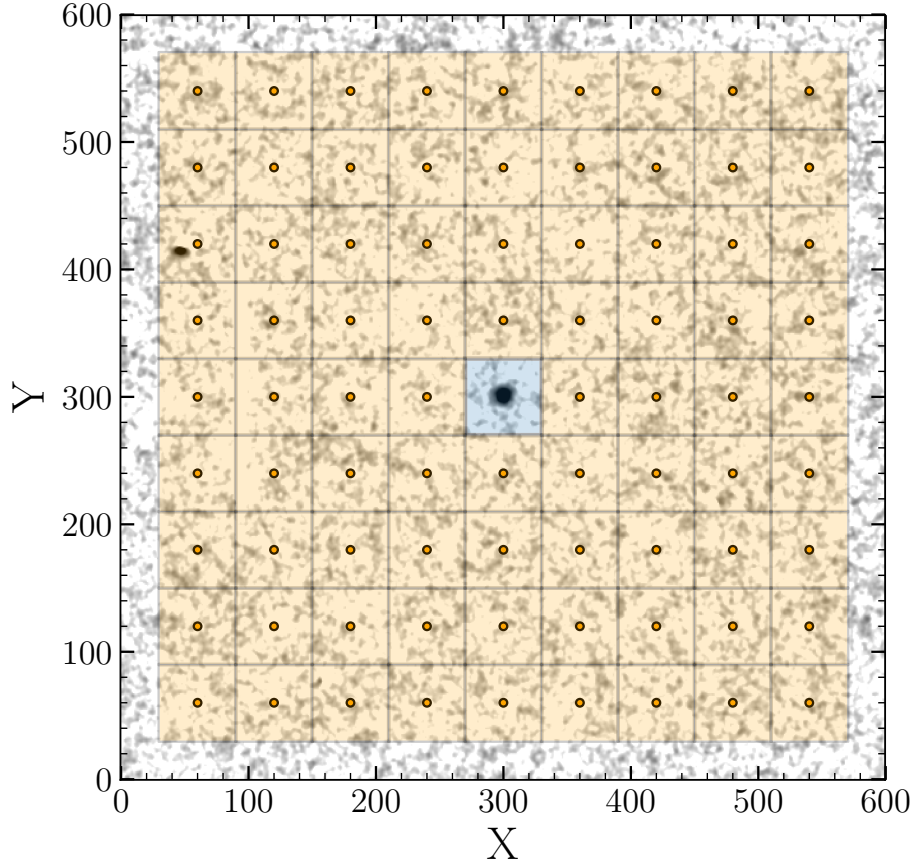
Figure 3.8: Grid for calculating the limiting magnitudes of the LT photometry. The image is after image-subtraction and the supernova is in the centre of the image. The blue box in the centre shows the cutout of the supernova that the PSF is fitted to. The orange circles show the 80 off-target aperture centres, and the orange boxes are the background cutouts that the PSF model is also fitted to in order to determine the limiting magnitude for the image.

magnitude is calculated (and an upper limit for the field is reported to 2-σ). The uncertainty on the supernova magnitude is calculated by inserting the PSF model of the supernova onto the 80 off-target apertures centres and performing PSF photometry on the artificial supernovae. The scatter in the measured artificial supernova flux is added in quadrature to the standard deviation of the science ZP determination to determine the uncertainty on the supernova flux.

If the supernova flux is below a 3-σ detection, then the most conservative limiting magnitude is chosen: either the 3-σ limit, or the flux corresponding to the (marginal) detection plus 2-σ. Reliable photometry can be usually be achieved to r-band limits of $\sim$22 mag, or $\sim$23 mag using stacked images. There are some spec-

tral sensitivity differences between LT and ZTF (see Fig. 3.10), leading to small systematic differences in the photometry. However, the light curves are generally consistent with ZTF $g-$ and r-band observations to within ±0.02 mag. Thus, the filter differences are sufficiently small that no colour-correction is deemed necessary.

However, even with the image registration steps outlined above, Poisson noise sets the signal-to-noise ratio for bright sources. In addition, all extremely bright stars will have subtraction residuals due to atmospheric effects, spatially varying PSFs, astrometric distortions, the effects of the different filter transmission between LT and PS1/SDSS, and for bright objects with high pixel counts, they may enter the regime of non-linearity for the detector.

For images of the same depth and seeing, image subtraction increases the noise level of the resulting subtracted image by $\sqrt{2}$ because the (randomly distributed) photon noise from the reference image is added to the science image. However, since the LT images are usually shallower and have worse seeing than the PS1/SDSS reference images, the noise added by image subtraction is minimal. Additionally, some of the noise is reduced further by smoothing the reference image with the LT PSF. However, on the rare occasion that we do require deep imaging (e.g. late-time SLSN or kilonova follow-up), the depth of the reference image is the limiting factor: one can never go deeper than the reference image.

3.6 Spectroscopy reduction and data sharing

All spectra are reduced with the SPRAT pipeline (Piascik et al., 2014). If multiple exposures are taken, the spectra are stacked and cosmic rays are identified and removed by comparing the flux values at the same wavelength in each spectrum. When single spectra are taken, a different method is required in order to remove cosmic rays. A median filter is applied to the 1D spectra counts, using a kernel size of 2 points either side of the desired wavelength.
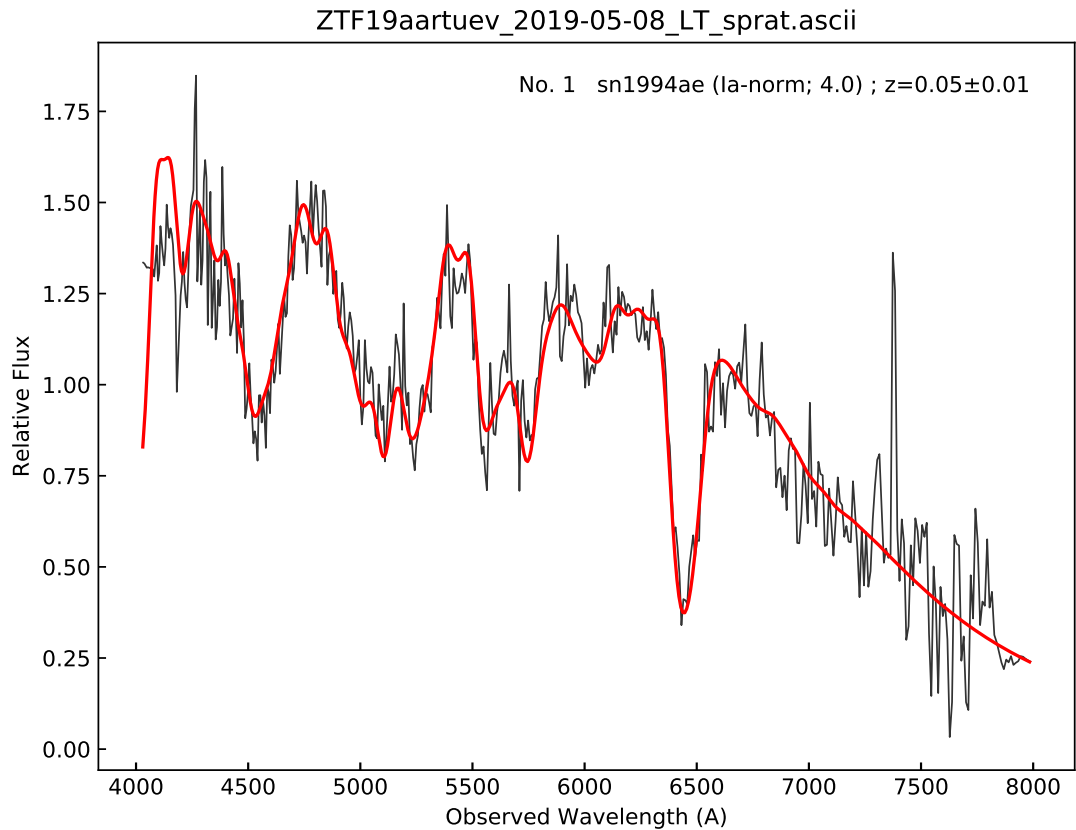
Figure 3.9: Example SPRAT spectrum of a ZTF19aartuev in black and a spectral fit in red showing a best template match to a SN Ia and $z = 0.05$.

The median filtered counts are then subtracted from the raw counts and divided by the standard deviation of the counts. This method gives an indication of how far a count value is from the average in units of standard deviation. If this is above a threshold of 100 then the wavelength of the individual count value is noted and the spectra flux at this wavelength is replaced with a median filtered flux value. SNID (Blondin & Tonry, 2007) is automatically run on each spectrum for a redshift determination and to establish a supernova classification and a PDF of the best fitting spectral template and the spectrum is generated.

Automated data sharing and uploads to the ZTF GROWTH Marshal– Once all photometry is completed, a compatible photometry file is automatically generated and is uploaded to the GROWTH MARSHAL. The supernovae spectra and classifications are also uploaded to the GROWTH MARSHAL.

Every morning an e-mail is sent for each science program containing any new

data. The e-mail includes cutouts of the subtractions, a light curve showing the new photometry and ZTF photometry, and a table of the observing conditions and observation sequence. As an example, I present the observations obtained on the night of the 13th March 2020 in Fig. 3.11 and I give an overall summary of all LT reductions performed to date in Table 3.1.

3.7 Weaknesses and future work

The ZTF GROWTH MARSHAL interface and the pipeline is fully implemented and has been used throughout the full ZTF survey. For future efforts with ZTF-II, the ZTF GROWTH MARSHAL is being fully replaced from the ground up. Thus, while the LT-ZTF triggering codes will be replaced, the data reduction and image subtraction pipeline written is this thesis is planned to continue, based on the code written in this thesis.

Although the LT pipeline is extremely reliable for the vast majority of images, for some specific cases, such as for supernovae located in galaxy nuclei or in very high surface-brightness galaxies, or if LT has focus problems, the subtraction residuals can be large and introduce large uncertainties in the photometry. In these cases, one simple improvement could be modifying the pipeline to use deep LT reference images to give a better subtraction. In addition, an implementation of the (ZOGY; Zackay et al., 2016) instead of the (Gal-Yam et al., 2008; Fremling et al., 2016) subtraction method may improve the subtractions since this technique is free from an assumptions that the reference image is noise free.

In order to improve processing time which is particularly important for follow up of fast-evolving transients, a number of improvements could be implemented. Firstly, the reference images that are automatically downloaded from PS1 or SDSS could be pre-downloaded once any LT observations are requested from the database. This would cut down the time required to download and stitch the reference images together. This may be particularly useful for SDSS u-band
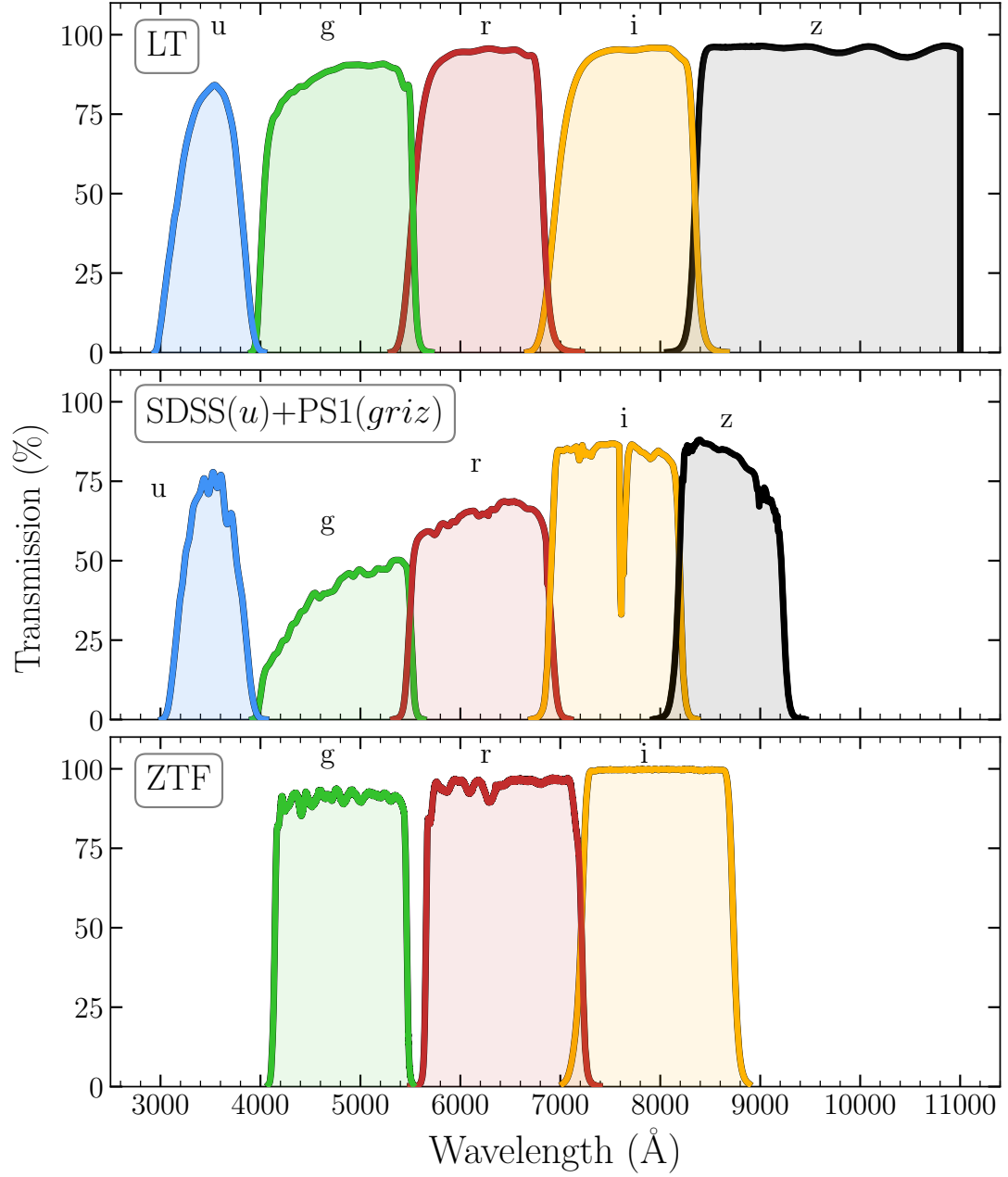
Figure 3.10: Transmission profiles for the LT filters on IO:O[11], the SDSS and PS1 filters used for calibration and the ZTF filters.
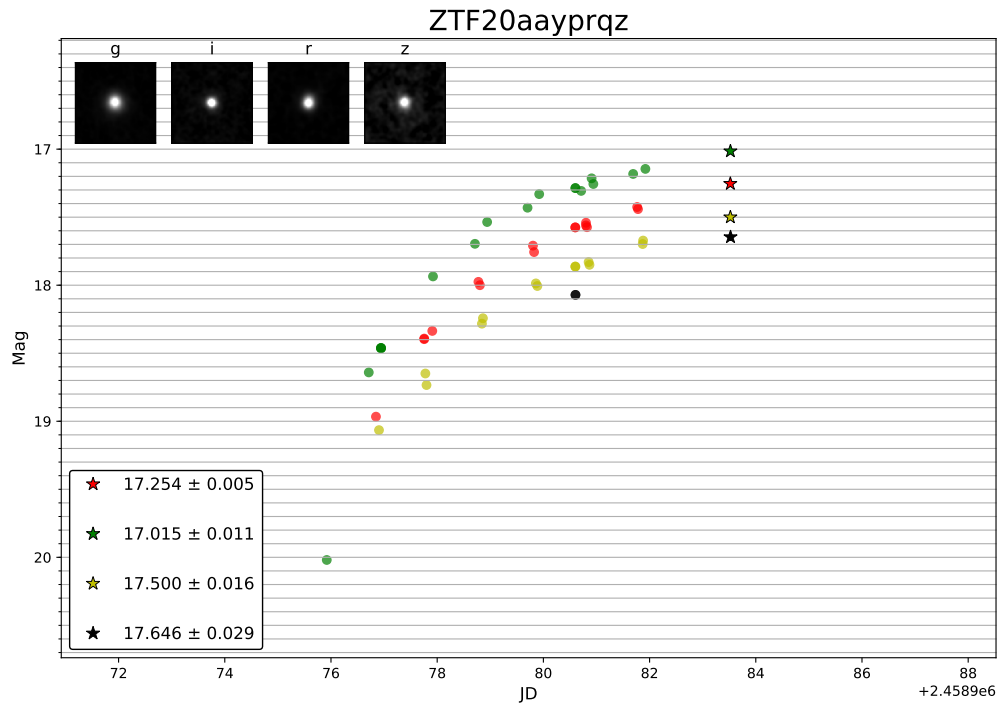
Figure 3.11: Plot of the automated light curve plot sent every morning, with the new photometry plotted as stars and the ZTF GROWTH Marshal photometry plotted as circles. Cutouts of the subtracted images are shown in the top left corner.

Program	Code	Spectra		Imaging		Paper References
		Total	Objects	Total	Objects	
RCF	JL18B06	72	25	301	29	Fremling et al. (2020)
	JL19A23	80	27	194	28	
	JL20A08	100	32	71	8	
SLSNe	JL18B07	–	–	330	24	Lunnan et al. (2020)
	JL19A24	–	–	395	33	
	JL19B11	14	5	603	67	
	JL20A09	3	1	467	40	
Fast Transients	JL18B08	41	8	214	13	Ho et al. (2020)
	JL19A25	68	17	787	49	
	JL19B12	89	28	615	66	
	JL20A10	45	14	287	27	
EM GW	JL19A33	44	11	427	53	Coughlin et al. (2019)
	JL19B09	36	9	325	29	Andreoni et al. (2020)
						Kasliwal et al. (2020)
Filler	JZ19A01	34	11	1000	85	Yao et al. (2019)
	JZ19B01	313	95	870	83	Stein et al. (2020)
						Soumagnac et al. (2020)
						van Velzen et al. (2020)
Total		**939**	**283**	**6886**	**634**	

Table 3.1: Summary of the Liverpool Telescope observations from 30th August 2018 to 21st May 2020, and the resulting publications.

reference images since to obtain a reference image of the correct footprint, one must downloaded images for a grid of positional coordinates and then combine these images with SWarp (Bertin, 2010). Another way to speed up the pipeline would be to work on a method to determine the image sequence to be observed with the LT – this information is currently not provided by LT. If this could be determined, there could be a better implementation of the pipeline that processes exposures taken in multiple bands in parallel.

Chapter 4

Summary

4.1 Conclusions

In this thesis, I have presented the results of extensive investigation into the global properties of an unbiased sample of 150 CCSN host galaxies discovered by ASAS-SN ($z < 0.08$). I directly compared the CCSN hosts using a consistent analysis of all known SLSN and LGRB host galaxies at low redshift $z < 0.3$. These catalogues are public and can be used for broad host galaxy applications, including unusual classes of object — such as the emerging category of rapidly-evolving transients (e.g. Drout et al., 2014; Pursiainen et al., 2018).

I briefly summarise the key conclusions below:

I. CCSNe generally exhibit similar star-formation properties to star-formation-weighted local galaxies (LVL), consistent with the expectation that CCSNe should trace star-formation. However, we find the CCSN-selected galaxy stellar mass distribution to be weighted towards slightly lower-mass galaxies 9.5(0.1) than the SFR-weighted LVLS galaxy stellar mass distribution with median log stellar mass of 9.8, possibly indicating that the local-volume sample is affected by cosmic variance.

II. 33^{+4}_{-4} per cent of CCSNe (50/150) from our sample) occur in dwarf galaxies with stellar masses less than 10^9 M$_\odot$ and 7^{+3}_{-2} per cent of CCSNe (11/150 from our sample) occur in dwarf galaxies with stellar masses less than 10^8 M$_\odot$, representing a substantial fraction of the population.

III. Only a few per cent (2^{+2}_{-1}) of CCSN hosts are undergoing starbursts with rapid star-formation (sSFR$>10^{-8}$ yr^{-1}), all of which are dwarf galaxies with stellar masses $<10^9$ M$_\odot$.

IV. LGRB SN and SLSN-I host populations exhibit similar host galaxy properties. The peak of their host mass distributions is clearly much lower and spans a much smaller mass range than the CCSN population which trace star-formation (with median logarithmic mass of 8.7(0.2) for LGRB SNe, 7.9(0.2) for SLSNe-I, and 9.5(0.1) for CCSNe. LGRB SNe explode, on average, in higher mass galaxies than SLSNe-I. This lends further support to models in which LGRBs and SLSN-I form only in certain environmental conditions related to low-mass and metallicity.

V. We do not find statistically significant differences between LGRB-SNe and SN-less LGRBs. However, this comparison is limited by the small sample size of SN-less events (only 5).

VI. Many (8/29) SLSNe-I are found in starbursts. This greater fraction is consistent with an intrinsic preference for starbursting galaxies, but it is also consistent with a strong SLSN-I mass dependence in covariance with a larger starburst fraction in dwarf galaxies. We cannot yet conclusively identify or rule out a role for intense star-formation in increasing the SLSN-I rate in starbursting dwarf galaxies.

VII. In addition, I present work I have done to help to build future supernova catalogues with the Zwicky Transient Facility (ZTF) including the Bright Transient Survey and the Superluminous Supernova Survey, with a large role played by the Liverpool Telescope. I have integrated the Liverpool Telescope with ZTF, which allows follow-up spectroscopy and photometry to

be requested and reduced via an automated reduction and image-subtraction pipeline.

These new samples will be larger, with even better control of systematics relative to ASAS-SN and other previous CCSN and SLSN samples. This will be vital to determine whether host-galaxy mass (a proxy for metallicity) or specific star-formation rate (a proxy for star-formation intensity and potential IMF variation) is more fundamental in driving the preference for SLSNe and LGRBs in unusual galaxy environments.

4.2 Future Work

Even though ASAS-SN is untargeted and the spectroscopic completeness fraction is high for bright supernovae, the shallow nature of the survey means that demographic studies are limited by the sample size and building samples of 1000's of SNe requires many years of data. In addition, the low-z samples of rare LGRB and superluminous supernova are limited by their low volumetric rate. Thus, our conclusions are still limited by the modest numbers of different classes of transients. For example, selecting dwarf galaxies based on 100's of CCSNe will still only provide a modest sample of dwarf galaxies for deriving statistics on star forming dwarf galaxies in the local volume. In addition, in this thesis, we found some indications to 2σ that both sSFR and stellar mass affect the production of SLSNe-I. However, since these parameters are intrinsically tied, it was difficult to assess whether both factors are causal.

To address these questions we need even larger samples of transients of each class. This is now becoming possible since deeper untargeted surveys are being coupled with large-scale classification projects, offering large, homogenous samples that have clear constraints on follow up priority. Indeed, part of the research presented in this thesis has helped to build these new, more extensive supernova catalogues, which can be used to address the questions remaining and to explore

many promising areas of supernova and galaxy science. One resource that was worked on in this thesis was the Bright Transient Survey (BTS; Fremling et al., 2020), which aims to classify every bright transient (m < 18.5) discovered by ZTF and publicly announce the classification. This untargeted survey is coupled with a large-scale classification effort, including the Liverpool Telescope playing a significant role (as described earlier in the thesis in Chapter 3). The sample selection is based only on peak magnitude, and neither the filtering of the alert stream nor the spectroscopic follow-up are dependent on the nature of the host galaxy. Thus, the sample is well-defined and has high (>90 per cent) spectroscopic completeness. The survey is ongoing and will continue with ZTF-II. So far it has classified 2174 transients[1], with 587 CCSN classifications. This sample exceeds the ASAS-SN CCSNe sample by a factor of ∼4, therefore is well-suited to use for comparisons between sub-classifications of specific types of SNe and intrinsically rare types of SNe (there are 33 SLSNe in the sample and 68 IIn).

A straightforward analysis would be to apply the techniques used in this thesis to the BTS sample to establish a large supernova galaxy catalogue containing the integrated host galaxy properties of ∼3,000 SNe. Fig. 4.1 shows a preliminary analysis of the entire BTS sample for the first nine months of ZTF, with some of the lowest mass galaxies highlighted as cutouts on the right of the plot. One could take this further by automating this process to some extent in order to maintain a database of galaxy photometry, SED fits and host properties as the sample grows. Once this catalogue has been established, many potential research questions could be addressed.

SN Ia to the ultra-faint end of the galaxy luminosity function– Measuring the slope of the faint end of the galaxy luminosity function is an important constraint on theories of galaxy formation. However, current survey methods do not provide a complete census of all galaxy populations within the volume of interest. Many galaxies are close to or below the detection limits of the surveys in which they were discovered, and spectroscopic redshifts are difficult to obtain

---

[1] As of 7th July 2020.
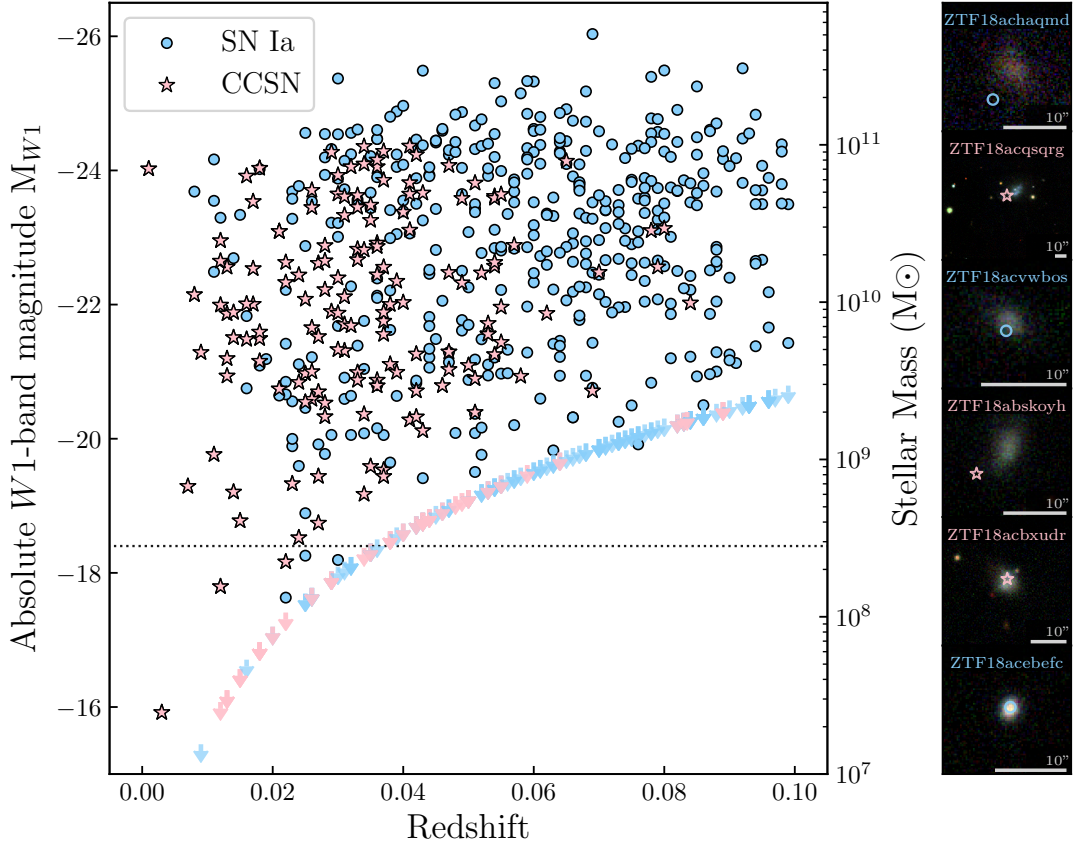
Figure 4.1: *Left*: Absolute $W1$–band magnitudes of 707 supernova host galaxies from the first nine months of the ZTF flux-limited survey, plotted as a function of redshift ($z < 0.1$). CCSNe are pink stars, and SNe Ia are blue circles. Stellar mass estimates from $W1$ are plotted. *Right*: Mosaic showing RGB (*gri* PS1) colour composite images of 6 dwarf galaxies that are detected in WISE and with magnitudes $W1 > -18.5$. Each image has a constant physical size scale of 10 kpc in diameter at the redshift of the host galaxy, and an angular scale of 10 arcsec is shown on each individual cutout. SN positions are indicated; colour and symbol conventions are as in the left panel.

for all but the very nearest dwarf galaxies, so they do not have accurate distance (thus luminosity) estimates. Thus, the observed dwarf galaxy luminosity function is incomplete.

SN Ia explode in a variety of environments, and trace stellar mass relatively uniformly. Using a SN Ia sample will allow the stellar mass to be constrained in this low-mass regime and has the advantage that even for the galaxies lacking a host redshift (in particular dwarf galaxies), one can still use the supernova redshift (Sedgwick et al., 2019). Therefore this method does not require large amounts of spectroscopic follow-up time on large aperture telescopes. Using the BTS sample which contains 1000's of low-z Ia SNe will help to address this question. This sample of SN Ia hosts would also be an excellent low-redshift companion sample for the *Nancy Grace Roman Space Telescope* SN survey (formerly the *Wide Field Infrared Survey Telescope*; Spergel et al., 2015) and to act as an anchor for the high-redshift sample.

CCSNe as beacons to probe the faintest star-forming galaxies– Using the CCSN in this galaxy catalogue, one can select star-forming galaxies. In particular, from the integrated properties one can select star-forming dwarf galaxies because a small but significant fraction (7^{+3}_{-2} per cent) of these spectroscopically classified CCSNe explode in dwarf galaxies with stellar masses below 10^8 $M_\odot$, resulting in a SN-selected sample of approximately 40 local star-forming dwarf galaxies.

Expanding the current small sample of dwarf galaxies with precise star formation histories is an especially high priority for understanding the effects of reionisation and environment on star formation in the faintest dwarfs. It is unclear how much star-formation in the Universe happens in ultra-faint and low-metallicity galaxies (<0.1 $Z_\odot$) due to the scarcity of extremely low-metallicity galaxies.

Using this sample, one could obtain a more precise estimate of the host redshifts by obtaining spectra using a large aperture telescope. Metallicity-line diagnostics could be calculated via a variety of strong line ratios to determine chemical abundances and the specific star-formation rate as measured by the Hα luminosity

relative to the continuum. This will allow us to put limits on the spatial density of low-metallicity galaxies in the local Universe, investigate the metallicity distribution of dwarf galaxies and to assess the fundamental metallicity relation in dwarf galaxies in an unbiased sample. Because low-metallicity galaxies have not undergone much chemical evolution. These galaxies could be used to determine the primordial helium-4 abundance (e.g. Izotov et al., 1994).

Characterising the environments of SNe with IFU studies– IFU studies provide simultaneous spectra for all spatial resolution elements and they offer superior spatial and spectral resolution in comparison to broad-band host studies. This allows the metallicity and star-formation to be derived for the local stellar population at the supernova site, and across the whole host galaxy environment, for better characterisation of the underlying progenitor.

While IFU studies such as PISCO and AMUSING have characterised large samples of core-collapse supernovae (e.g. Galbany et al., 2018; Kuncarayakti et al., 2018), providing a unique window to study the association of different SN types to the star-formation of their environment, these samples are still heavily biased towards high-mass galaxies due to discovery biases in the samples. Thus, the BTS would be a good feeder survey for an IFU blind follow-up program since it is a large, low-redshift and homogenous sample. For example, for the first time a study of 25 very local CCSNe (<40 Mpc) could be done for the first study of a homogenous CCSN sample. In addition, we now have large samples of rare types of SNe, such as interacting Ibn/IIn SNe for which an an IFU study of a large sample (particularly rare types) of SNe is lacking and is vital in working towards characterising the environments of interacting transients.

Constraining the rates of rare and exotic types of SNe– For the first time, we are beginning to gather large samples of intrinsically rate types of SNe, including Ibn SNe. At present, there fewer than 40 Ibn's in the literature, and there are 10 Ibn SNe in the BTS sample. However, in the future with ZTF-II and with VRO(LSST), a full analysis of their environments can be conducted.

The rates of the exotic supernovae such as SLSNe and fast blue optical transients (FBOTs; Drout et al., 2014; Pursiainen et al., 2018)[2] are currently very uncertain. To tie down progenitor models for these events, a robust rate determination can now be achieved with the BTS sample.

Characterising the environments of interacting SNe– This work has shown the diversity in SLSNe-II hosts spanning a broad range of stellar masses and star formation rates. Some of the host galaxies in this sub-class are even lower mass than some of the SLSN-I. In contrast, a few SLSN-II are found in the circumnuclear rings of massive galaxies. Such diversity in the host environments suggests that either their production may not be tied to their host environment, or perhaps that there are multiple formation channels for SLSNe-II. Perhaps, some SLSNe-II are PISNe that require low-metallicity environments, whereas other SLSNe-II are powered by 'ordinary' CSM interaction and require large CSM masses.

This ambiguity can really only be solved with more detailed samples of SLSN-II and their host galaxies. More attention has been focused on SLSN-I, in both their supernova properties and their host galaxies. Therefore using the new large samples that are becoming available, a full analysis of SLSNe-II and SLSNe-IIn environments can be undertaken and compared to the environments of 'ordinary' SNe II and SNe IIn.

Large demographic studies with VRO(LSST)– Looking further into the future, the volume and alert rate of VRO, will require additional spectroscopic capabilities in order to maximise the science output from VRO. Instruments such as 4MOST (Emerson et al., 2006) that are well suited for transient follow-up on a large scale will be used for VRO. 4MOST will be mounted on the 4-m Visible and Infrared Survey Telescope for Astronomy (VISTA), which will simultaneously obtain 2,400 spectra. VISTA will help to classify the vast number of supernovae that will be detected by VRO and enable even larger population studies.

---

[2]FBOTs are usually characterised by their blue optical colours and fast-evolving light curves, with evolutionary timescales within $\sim$10 days.

Future limitations– Although the new resources discussed in this Chapter will allow us to address many open questions in the field, in the medium to short term, there will still be many outstanding questions:

- SN 1987A which was discovered in the LMC is still the only core-collapse supernova whose progenitor has been detected spectroscopically as well as photometrically (Sanduleak, 1970; Rousseau et al., 1978). Extragalactic supernovae are indirect probes of the supernova mechanism, and spectroscopically observing individual stars at extragalactic distances requires multi-hour integrations on the largest telescopes. Thus, unless we observe a Galactic supernova (or one in the LMC/SMC), it is unlikely that we will be able to spectroscopically characterise another supernova progenitor in pre-existing data to directly link the supernova progenitor to its explosion mechanism. In addition, observing a Galactic supernova opens up the possibility to study the explosion using probes such as neutrinos or possible gravitational wave signals, that are not possible for the many extragalactic SNe. Studying the neutrino production would allow us to answer fundamental questions about the physical conditions in the core at the instant of collapse, the shock breakout phase, the detailed spectral evolution at late-times, and allow us to connect the progenitor with the observed explosion properties, any interaction with the surrounding circumstellar material and to the compact object formed in the explosion.

- Due to the low volumetric rate of SLSNe and LGRBs, it is unlikely that we will be able to pinpoint the progenitors of SLSNe and LGRBs though deep, pre-explosion imaging since even HST/adaptive optics imaging will not be of high enough resolution and deep enough for an unambiguous identification of the progenitor star. A SLSN/LGRB SN progenitor detection would help to bridge the gap between exotic SNe and the massive stars from which they arise. It would allow us to directly constrain the progenitor mass, map out any CSM interaction, and possibly a central engine.

Appendix A

Appendix

A.1   References for photometry

This section contains references to all the photometry gathered from archival sources and the new photometry used in the spectral energy distribution fits for all the host galaxies in our sample.

A.2   Physical properties of host galaxies

Tables of physical properties of all host galaxies, including their stellar masses and star-formation rates. Redshifts are derived from host galaxy, or the supernova if there no redshift available.

Table A.1: LGRB photometry sources. For cases where LGRBs do have SNe, but there is no known SN name designation on TNS, we use SN in the name column.

LGRB	SN name	Reference
980425	1998bw	[2,3,4]
020903	SN	[1,5,6]
030329A	2003dh	[1,7]
031203	2003lw	[1,8,9,10]
050826	–	[1,11,12]
060218	2006aj	[1,13,14]
060505	–	[4,14,15,16]
060614	–	[1,14,17,18]
080517	–	[1,19]
100316D	2010bh	[20,21]
111225A	–	[1,22]
120422A	2012bz	[1,23]
130702A	2013dx	[1,24]
150518A	SN	[1]
150818A	SN	[1]
161219B	2016jca	[1,25]
171205	2017iuk	[1,26,27]

References:
[1] This work, [2] Michałowski et al. (2009), [3] Michałowski et al. (2014), [4] Castro Cerón et al. (2010), [5] Bersier et al. (2006), [6] Wainwright et al. (2007), [7] Gorosabel et al. (2005), [8] Margutti et al. (2007), [9] Mazzali et al. (2006), [10] Prochaska et al. (2004), [11] Ovaldsen et al. (2007), [12] Mirabal et al. (2007), [13] Sollerman et al. (2006), [14] Hjorth et al. (2012), [15] Thöne et al. (2008), [16] Wright et al. (2010), [17] Mangano et al. (2007), [18] Gal-Yam et al. (2006), [19] Stanway et al. (2015), [20] Starling et al. (2011), [21] Michałowski et al. (2015), [22] Niino et al. (2017), [23] Schulze et al. (2014), [24] Toy et al. (2016), [25] Cano et al. (2017b), [26] Bianchi et al. (2011), [27] Huchra et al. (2012).
Notes. New photometry measurements for the LGRBs are detailed in Section 2.3.5 and is included in online machine-readable table.

Table A.2: SLSN archival photometry sources

SLSN	TNS Name	Type	Reference
LSQ12dlf	—	I	[1,2]
LSQ14an	—	I	[1,3]
LSQ14mo	—	I	[1]
MLS121104	—	I	[1,4]
PTF09as	SN2009cb	I	[5]
PTF09cnd	—	I	[5,6]
PTF10aagc	—	I	[5]
PTF10bfz	—	I	[5]
PTF10cwr	SN2010gx	I	[1,4,5,6]
PTF10hgi	SN2010md	I	[1,4,5,6]
PTF10nmn	—	I	[5]
PTF10uhf	—	I	[5,7]
PTF10vwg	SN2010hy	I	[5]
PTF11dij	SN2011ke	I	[1,5,6]
PTF11hrq	—	I	[5,7]
PTF11rks	SN2011kg	I	[1,5]
PTF12dam	—	I	[1,5,7]
SN1999as	—	I	[1,5,6,7]
SN2005ap	—	I	[1,4,6,8]
SN2007bi	—	I	[1,6]
SN2010kd	—	I	[1,3]
SN2011ep	—	I	[1,3]
SN2011kf	—	I	[1,4,6]
SN2012il	—	I	[1,4,6]
SN2013dg	—	I	[1]
SN2015bn	—	I	[1,3]
SSS120810	—	I	[1]

References: [1] Schulze et al. (2018), [2] Nicholl et al. (2014), [3] Bianchi et al. (2011), [4] Lunnan et al. (2014), [5] Perley et al. (2016c), [6] Angus et al. (2016), [7] Cutri & et al. (2013), [8] Adami et al. (2006), [9] Cutri & et al. (2014), [10] Neill et al. (2011), [11] Kato et al. (2007), [12] Rest et al. (2011), [13] Lawrence et al. (2007), [14] Blanton et al. (2011), [15] Huchra et al. (2012).

SLSN	TNS Name	Type	Reference
CSS100217	—	II	[1]
CSS121015	—	II	[1]
PTF10fel	—	II	[5,7]
PTF10qaf	—	II	[5]
PTF10qwu	—	II	[5]
PTF10scc	—	II	[5]
PTF10tpz	—	II	[5,9]
PTF10yyc	—	II	[5]
PTF12gwu	—	II	[5]
PTF12mkp	—	II	[5]
PTF12mue	—	II	[5]
SN1999bd	—	II	[1,6,7,10]
SN2003ma	—	II	[11,12]
SN2006gy	—	II	[6,7]
SN2006tf	—	II	[1,3]
SN2007bw	—	II	[1]
SN2008am	—	II	[1,3,6,9,13]
SN2008es	—	II	[1,6]
SN2008fz	—	II	[6]
SN2009nm	—	II	[1]
SN2013hx	—	II	[1]

References: [1] Schulze et al. (2018), [2] Nicholl et al. (2014), [3] Bianchi et al. (2011), [4] Lunnan et al. (2014), [5] Perley et al. (2016c), [6] Angus et al. (2016), [7] Cutri & et al. (2013), [8] Adami et al. (2006), [9] Cutri & et al. (2014), [10] Neill et al. (2011), [11] Kato et al. (2007), [12] Rest et al. (2011), [13] Lawrence et al. (2007), [14] Blanton et al. (2011) , [15] Huchra et al. (2012).

Table A.3: Photometry of all galaxy samples including ASAS-SN CCSN, LGRBs and SLSN used in our analysis. These data include new photometry, photometry from public data and data gathered from the literature. Only the first few lines are shown; the full table will be made available online.

Type	Name	Filter	Mag	Unc	System	Extinction	Instrument	Ref
CCSN	ASAS-SN13co	u'	16.54	0.05	std	no	SDSS	(1)
CCSN	ASAS-SN13co	g'	15.39	0.01	std	no	SDSS	(1)
CCSN	ASAS-SN13co	r'	14.88	0.01	std	no	SDSS	(1)
CCSN	ASAS-SN13co	i'	14.57	0.01	std	no	SDSS	(1)
CCSN	ASAS-SN13co	z'	14.39	0.01	std	no	SDSS	(1)
CCSN	ASAS-SN13co	y'	14.34	0.05	std	no	PS1	(4)
CCSN	ASAS-SN13co	J	13.31	0.03	std	no	2MASS	(2)
CCSN	ASAS-SN13co	H	12.79	0.07	std	no	2MASS	(2)
CCSN	ASAS-SN13co	K_s	12.34	0.11	std	no	2MASS	(2)

References: [1] Nasa Sloan Atlas; Blanton et al. (2011), [2] 2MASS; this work, [3] *GALEX*; Martin et al. (2005), [4] PS1; this work, [5] 2MASS Extended Source Catalogue; Huchra et al. (2012), [6] SDSS; this work [7], 2MASS Large Galaxy Atlas; Jarrett et al. (2003).

Notes. All photometry is available online in a machine-readable form. Magnitudes are expressed in the conventional frame, this is indicated as 'std' under the System column, unless given in AB form in the literature where is indicated as 'AB'. For SDSS *gri* and PS1 filters, 'std' is identical to 'AB'. Magnitudes are not corrected for foreground extinction and under the Extinction column as 'no', unless unless corrected for Galactic foreground extinction in the literature, indicated by 'yes'.

Table A.4: Properties of ASAS-SN CCSN host galaxies, including physical parameters derived from the SED fitting procedure.

ASAS-SN	Class	α(2000)	δ(2000)	$z_{\rm sn}$	$z_{\rm host}$	Distance† Mpc	E(B-V)	$\log_{10}(M_*)$ $M_\odot$	SFR $M_\odot$ yr^{-1}	sSFR‡ yr^{-1}
13co	IIP	21:40:38.74	+06:30:36.87	0.023	0.0234	100.2±7.0	0.052	$9.85\,^{+0.05}_{-0.05}$	$0.800\,^{+0.224}_{-0.193}$	$-9.96\,^{+0.14}_{-0.10}$
13dn	II	12:52:58.20	+32:25:09.30	0.023	0.0228	105.6±7.4	0.014	$9.01\,^{+0.04}_{-0.04}$	$1.791\,^{+0.021}_{-1.086}$	$-8.69\,^{+0.01}_{-0.46}$
14at	II	17:55:05.43	+18:15:26.45	0.010	0.0104	52.0±3.6	0.073	$8.05\,^{+0.90}_{-0.35}$	$0.002\,^{+0.033}_{-0.001}$	$-10.65\,^{+0.19}_{-1.29}$
14az	IIb	23:44:48.00	−02:07:03.17	0.007	0.0067	29.3±2.1	0.028	$8.00\,^{+0.01}_{-0.01}$	$0.012\,^{+0.002}_{-0.001}$	$-9.90\,^{+0.07}_{-0.01}$
14bf	IIP	13:58:12.75	+17:31:53.66	0.022	0.0225	105.4±7.4	0.026	$9.97\,^{+0.02}_{-0.01}$	$0.198\,^{+0.001}_{-0.096}$	$-10.70\,^{+0.01}_{-0.24}$
14bu	II	11:18:41.03	+25:09:59.88	0.025	0.0255	115.9±8.1	0.014	$8.59\,^{+0.05}_{-0.12}$	$0.141\,^{+0.126}_{-0.025}$	$-9.46\,^{+0.38}_{-0.12}$
14de	Ic	10:40:39.33	+39:03:52.70	0.029	0.0293	130.7±9.2	0.015	$10.44\,^{+0.01}_{-0.11}$	$0.019\,^{+0.001}_{-0.005}$	$-12.20\,^{+0.02}_{-0.07}$
14di	II	02:01:46.39	+26:32:41.96	0.017	0.0167	69.6±4.9	0.064	$10.09\,^{+0.03}_{-0.08}$	$0.780\,^{+0.857}_{-0.080}$	$-10.17\,^{+0.27}_{-0.04}$
14dl	II	12:21:51.38	−24:09:54.00	0.014	0.0139	65.2±4.6	0.068	$10.91\,^{+0.01}_{-0.04}$	$3.589\,^{+0.058}_{-0.323}$	$-10.30\,^{+0.01}_{-0.04}$
14dq	II	21:57:59.97	+24:16:08.10	0.010	0.0104	46.9±3.3	0.062	$8.01\,^{+0.07}_{-0.23}$	$0.344\,^{+0.291}_{-0.046}$	$-8.46\,^{+0.46}_{-0.13}$
14fj	II	14:40:39.50	+38:37:58.55	0.013	0.0125	61.8±4.3	0.014	$9.72\,^{+0.12}_{-0.02}$	$0.897\,^{+0.008}_{-0.352}$	$-9.81\,^{+0.01}_{-0.32}$
14gm	II	00:59:47.83	−07:34:19.30	0.005	0.0055	23.2±1.6	0.099	$9.47\,^{+0.11}_{-0.02}$	$0.443\,^{+0.171}_{-0.039}$	$-9.80\,^{+0.01}_{-0.01}$
14il	IIn	00:45:32.55	−14:15:34.60	0.022	0.0220	92.3±6.5	0.020	$9.62\,^{+0.06}_{-0.04}$	$0.622\,^{+0.231}_{-0.187}$	$-9.90\,^{+0.25}_{-0.11}$
14jb	IIP	22:23:16.12	−28:58:30.78	0.006	0.0060	27.3±1.9	0.017	$8.46\,^{+0.11}_{-0.01}$	$0.251\,^{+0.006}_{-0.138}$	$-9.11\,^{+0.01}_{-0.45}$
14jh	II	08:40:44.27	+57:15:04.91	0.018	0.0175	78.4±5.5	0.055	$8.92\,^{+0.05}_{-0.04}$	$0.807\,^{+0.161}_{-0.214}$	$-9.06\,^{+0.08}_{-0.05}$
14kg	II	01:44:38.38	+35:48:20.45	0.014	0.0145	60.8±4.3	0.041	$9.79\,^{+0.04}_{-0.02}$	$0.089\,^{+0.052}_{-0.001}$	$-10.90\,^{+0.24}_{-0.01}$
14ma	IIP	23:55:09.13	+10:12:54.21	0.014	0.0137[1]	59.3±4.7	0.091	$8.57\,^{+0.04}_{-0.03}$	$0.001\,^{+0.001}_{-0.001}$	$-12.16\,^{+0.38}_{-0.11}$
14ms	Ibn	13:04:08.69	+52:18:46.50	0.054	0.0540[1]	241.0±19.3	0.010	$7.58\,^{+0.22}_{-0.32}$	$0.030\,^{+0.015}_{-0.012}$	$-9.12\,^{+0.55}_{-0.47}$
15bd	IIb	15:54:38.33	+16:36:38.06	0.008	0.0078	42.1±2.9	0.030	$7.73\,^{+0.03}_{-0.06}$	$0.019\,^{+0.004}_{-0.005}$	$-9.56\,^{+0.07}_{-0.08}$
15ed	Ibn	16:48:25.16	+50:59:30.72	0.049	0.04866[1]	216.4±17.3	0.022	$11.02\,^{+0.01}_{-0.01}$	$1.259\,^{+0.003}_{-0.007}$	$-10.90\,^{+0.01}_{-0.01}$
15fi	II	16:31:48.80	+20:24:38.50	0.017	0.0172	82.1±5.8	0.050	$9.12\,^{+0.01}_{-0.17}$	$0.341\,^{+0.121}_{-0.091}$	$-9.60\,^{+0.20}_{-0.01}$
15fz	II	13:35:25.14	+01:24:33.00	0.017	0.0175	84.4±5.9	0.022	$10.48\,^{+0.01}_{-0.05}$	$9.311\,^{+0.261}_{-1.368}$	$-9.53\,^{+0.02}_{-0.05}$
15ik	IIn	11:02:04.75	+03:30:02.66	0.035	0.0346[2]	152.2±12.2	0.048	$8.48\,^{+0.01}_{-0.04}$	$0.081\,^{+0.003}_{-0.007}$	$-9.60\,^{+0.01}_{-0.01}$
15ir	II	10:48:30.30	−21:38:07.95	0.013	0.0127	59.2±4.2	0.056	$9.14\,^{+0.26}_{-0.02}$	$1.469\,^{+0.545}_{-0.250}$	$-9.02\,^{+0.02}_{-0.04}$
15kz	IIP	13:37:18.67	−28:39:23.55	0.008	0.0080	30.5±2.2	0.053	$7.95\,^{+0.11}_{-0.06}$	$0.789\,^{+0.072}_{-0.420}$	$-7.98\,^{+0.04}_{-0.55}$
15lf	IIn	12:06:45.56	+67:09:24.00	0.008	0.0084	41.9±2.9	0.016	$9.65\,^{+0.01}_{-0.01}$	$2.570\,^{+0.024}_{-0.495}$	$-9.30\,^{+0.01}_{-0.01}$
15ln	II	00:53:41.40	+18:05:29.00	0.015	0.0150	62.8±4.4	0.042	$9.40\,^{+0.03}_{-0.11}$	$0.230\,^{+0.077}_{-0.007}$	$-10.04\,^{+0.25}_{-0.03}$
15mj	Ib	14:02:15.64	+33:39:40.29	0.034	0.0344	155.0±10.9	0.013	$9.38\,^{+0.04}_{-0.02}$	$0.566\,^{+0.618}_{-0.102}$	$-9.63\,^{+0.34}_{-0.16}$

ASAS-SN	Class	$\alpha(2000)$	$\delta(2000)$	z_{sn}	z_{host}	Distance[†] Mpc	E(B-V)	$\log_{10}(\mathrm{M_*})$ $\mathrm{M_\odot}$	SFR $\mathrm{M_\odot\ yr^{-1}}$	sSFR[‡] $\mathrm{yr^{-1}}$
15mm	II	15:25:23.50	+29:10:24.50	0.021	0.0215	100.5±7.1	0.021	9.53 $^{+0.04}_{-0.16}$	0.386 $^{+0.281}_{-0.149}$	-9.96 $^{+0.41}_{-0.09}$
15no	Ic	15:38:25.30	+46:54:06.60	0.043	0.03638[1]	160.3±12.8	0.015	8.46 $^{+0.09}_{-0.03}$	0.351 $^{+0.022}_{-0.215}$	-8.88 $^{+0.03}_{-0.55}$
15nx	II-pec	04:43:53.19	−09:42:11.22	0.026	0.02823[1]	123.6±9.9	0.074	8.99 $^{+0.09}_{-0.16}$	0.264 $^{+0.068}_{-0.131}$	-9.61 $^{+0.22}_{-0.31}$
15ov	II	03:30:59.15	−18:33:23.19	0.025	0.0255	106.7±7.5	0.034	9.46 $^{+0.01}_{-0.03}$	1.807 $^{+0.038}_{-0.061}$	-9.20 $^{+0.01}_{-0.01}$
15qh	II	22:45:13.22	−22:43:39.82	0.010	0.0102	45.0±3.2	0.026	9.93 $^{+0.01}_{-0.18}$	0.519 $^{+1.715}_{-0.012}$	-10.29 $^{+0.88}_{-0.01}$
15rb	IIn	10:08:08.24	+19:17:59.38	0.034	0.0336	149.0±10.4	0.023	8.01 $^{+0.03}_{-0.18}$	0.015 $^{+0.001}_{-0.006}$	-9.88 $^{+0.09}_{-0.08}$
15tm	IIP	23:27:35.60	+29:24:31.17	0.016	—	69.4±21.9	0.116	9.18 $^{+0.07}_{-0.09}$	0.123 $^{+0.013}_{-0.016}$	-10.13 $^{+0.12}_{-0.05}$
15tw	IIP	12:50:28.05	−10:50:29.15	0.008	0.0080	36.7±2.6	0.040	9.52 $^{+0.05}_{-0.03}$	0.510 $^{+0.001}_{-0.012}$	-9.80 $^{+0.02}_{-0.04}$
15ua	IIn	13:34:54.47	+10:59:04.69	0.061	—	273.7±23.4	0.026	8.55 $^{+0.16}_{-0.14}$	0.143 $^{+0.065}_{-0.049}$	-9.42 $^{+0.27}_{-0.29}$
15ug	II	06:45:01.68	+63:14:59.89	0.022	0.0221[1]	96.3±7.7	0.077	7.44 $^{+0.08}_{-0.18}$	0.032 $^{+0.009}_{-0.030}$	-8.96 $^{+0.27}_{-1.28}$
15un	II	02:40:41.38	+16:49:51.82	0.029	0.0292	121.7±8.5	0.074	9.61 $^{+0.01}_{-0.04}$	3.304 $^{+0.277}_{-0.319}$	-9.01 $^{+0.01}_{-0.06}$
15uo	IIn-pec	01:17:00.00	−04:56:34.10	0.038	—	167.6±22.6	0.040	8.76 $^{+0.07}_{-0.27}$	0.399 $^{+0.143}_{-0.047}$	-9.18 $^{+0.40}_{-0.11}$
15uy	IIb	14:32:15.31	+26:19:32.02	0.016	0.0160	77.5±5.5	0.017	9.35 $^{+0.10}_{-0.04}$	0.762 $^{+0.113}_{-0.106}$	-9.46 $^{+0.05}_{-0.14}$
16ab	II	11:55:04.25	+01:43:06.77	0.004	0.0043	26.0±1.9	0.019	7.85 $^{+0.01}_{-0.01}$	0.159 $^{+0.007}_{-0.001}$	-8.70 $^{+0.07}_{-0.01}$
16ai	IIP	14:39:44.73	+23:23:43.27	0.015	0.0149	72.8±5.1	0.028	8.12 $^{+0.01}_{-0.01}$	0.007 $^{+0.006}_{-0.001}$	-10.29 $^{+0.28}_{-0.01}$
16al	IIP	15:00:27.47	−13:33:09.00	0.009	0.0093	44.2±3.1	0.088	7.52 $^{+0.05}_{-0.14}$	0.552 $^{+0.176}_{-0.107}$	-7.75 $^{+0.13}_{-0.09}$
16am	II	04:45:21.28	+73:23:41.09	0.015	0.0150	66.3±4.7	0.151	10.41 $^{+0.10}_{-0.05}$	0.001 $^{+0.001}_{-0.001}$	-13.90 $^{+0.66}_{-0.15}$
16at	II	12:55:15.50	+00:05:59.70	0.004	0.0044	26.7±1.9	0.020	9.30 $^{+0.01}_{-0.01}$	0.794 $^{+0.001}_{-0.001}$	-9.40 $^{+0.01}_{-0.01}$
16ba	II	09:42:29.22	−16:58:26.88	0.014	0.0139	64.6±4.5	0.058	9.26 $^{+0.03}_{-0.05}$	0.316 $^{+0.031}_{-0.029}$	-9.72 $^{+0.01}_{-0.03}$
16bm	II	11:51:56.24	−13:25:03.07	0.007	0.0068[1]	29.3±2.3	0.038	8.07 $^{+0.19}_{-0.24}$	0.320 $^{+0.113}_{-0.114}$	-8.58 $^{+0.37}_{-0.40}$
16cr	II	11:42:34.65	−25:54:45.22	0.014	—	60.6±21.8	0.042	8.12 $^{+0.07}_{-0.11}$	0.049 $^{+0.054}_{-0.036}$	-9.52 $^{+0.45}_{-0.40}$
16dm	IIP	11:37:20.64	−04:54:36.84	0.018	0.0183	86.7±6.1	0.046	9.42 $^{+0.08}_{-0.02}$	0.462 $^{+0.039}_{-0.092}$	-9.70 $^{+0.01}_{-0.26}$
16eh	II	15:40:29.23	+00:54:36.38	0.012	0.0117	58.6±4.1	0.263	8.45 $^{+0.01}_{-0.26}$	0.234 $^{+0.010}_{-0.063}$	-9.04 $^{+0.04}_{-0.03}$
16ek	IIb	07:20:24.16	+32:51:02.58	0.014	—	60.6±21.8	0.052	8.95 $^{+0.03}_{-0.01}$	0.959 $^{+0.013}_{-0.139}$	-9.01 $^{+0.01}_{-0.05}$
16el	II	08:56:39.08	+52:06:10.01	0.014	0.0135	61.9±4.4	0.017	10.13 $^{+0.03}_{-0.02}$	2.748 $^{+0.032}_{-0.038}$	-9.70 $^{+0.01}_{-0.01}$
16eu	IIP	08:44:11.05	+34:42:55.80	0.014	0.0141	64.4±4.5	0.028	10.20 $^{+0.01}_{-0.01}$	5.012 $^{+0.001}_{-0.080}$	-9.50 $^{+0.01}_{-0.01}$
16fp	Ib/c-BL	21:59:04.14	+18:11:10.50	0.004	0.0037	18.8±1.3	0.075	8.73 $^{+0.01}_{-0.03}$	0.216 $^{+0.004}_{-0.002}$	-9.37 $^{+0.05}_{-0.04}$
16fq	IIP	11:20:19.09	+12:58:57.20	0.002	0.00243	11.5±0.8	0.030	10.56 $^{+0.05}_{-0.04}$	4.887 $^{+0.325}_{-0.969}$	-9.87 $^{+0.08}_{-0.07}$
16ft	II	23:56:13.74	−00:32:28.44	0.022	0.0222	93.6±6.6	0.028	9.79 $^{+0.01}_{-0.02}$	0.294 $^{+0.016}_{-0.029}$	-10.30 $^{+0.01}_{-0.01}$

ASAS-SN	Class	α(2000)	δ(2000)	$z_{\rm sn}$	$z_{\rm host}$	Distance† Mpc	E(B-V)	$\log_{10}(M_*)$ $M_\odot$	SFR $M_\odot\,{\rm yr}^{-1}$	sSFR‡ ${\rm yr}^{-1}$
16gn	IIn	12:06:57.59	+27:18:04.93	0.056	0.0560	246.4±17.3	0.018	$10.13^{+0.03}_{-0.05}$	$1.236^{+0.845}_{-0.421}$	$-9.99^{+0.16}_{-0.22}$
16go	II	13:02:44.26	−26:56:26.81	0.016	0.0161	80.1±5.6	0.070	$9.78^{+0.01}_{-0.01}$	$0.561^{+0.004}_{-0.046}$	$-10.00^{+0.01}_{-0.03}$
16gy	II	02:21:22.77	+16:33:54.56	0.014	0.0137	56.7±4.0	0.129	$10.11^{+0.12}_{-0.01}$	$1.140^{+0.614}_{-0.005}$	$-10.00^{+0.05}_{-0.01}$
16hy	II	15:26:29.52	+41:44:03.32	0.008	0.0078	41.5±2.9	0.022	$8.65^{+0.05}_{-0.01}$	$0.127^{+0.066}_{-0.017}$	$-9.60^{+0.18}_{-0.01}$
16in	IIn	04:59:30.07	−28:51:39.43	0.016	0.0161	68.5±4.8	0.012	$9.27^{+0.04}_{-0.12}$	$0.508^{+0.717}_{-0.097}$	$-9.60^{+0.51}_{-0.05}$
16ll	II	19:00:32.43	+54:34:09.70	0.028	0.026[1]	113.6±9.1	0.054	$9.27^{+0.13}_{-0.04}$	$1.102^{+0.175}_{-0.654}$	$-9.17^{+0.04}_{-0.62}$
16mz	II	12:04:16.91	+21:48:03.30	0.021	0.0215	99.8±7.0	0.020	$9.02^{+0.04}_{-0.01}$	$0.011^{+0.025}_{-0.010}$	$-10.95^{+0.63}_{-1.23}$
16ns	II	10:04:18.59	+43:25:29.13	0.038[2]	—	167.6±22.8	0.011	$8.48^{+0.12}_{-0.15}$	$0.200^{+0.067}_{-0.166}$	$-9.19^{+0.23}_{-0.79}$
17ai	Ib	12:07:18.83	+16:50:26.02	0.023	0.0231	107.0±7.5	0.041	$9.46^{+0.02}_{-0.13}$	$2.624^{+0.136}_{-0.857}$	$-9.01^{+0.01}_{-0.09}$
17br	IIP	15:52:00.31	+66:18:55.27	0.026	—	113.6±22.2	0.024	$8.76^{+0.05}_{-0.03}$	$0.002^{+0.008}_{-0.001}$	$-11.96^{+0.96}_{-0.73}$
17bw	II	16:58:37.69	+50:29:26.50	0.01	0.01020	44.0±3.1	0.019	$8.62^{+0.18}_{-0.02}$	$0.445^{+0.057}_{-0.029}$	$-8.99^{+0.06}_{-0.01}$
17cl	II	05:02:19.58	−10:21:22.78	0.013	0.0133	56.2±3.9	0.078	$10.49^{+0.01}_{-0.29}$	$0.593^{+0.017}_{-0.084}$	$-10.70^{+0.01}_{-0.01}$
17ds	II	08:03:55.21	+26:31:12.73	0.022	0.0217	95.2±6.7	0.038	$10.03^{+0.04}_{-0.02}$	$0.565^{+0.063}_{-0.049}$	$-10.28^{+0.08}_{-0.03}$
17dv	Ib/c	09:52:31.22	−21:57:54.59	0.029	—	127.0±22.3	0.037	$8.60^{+0.04}_{-0.02}$	$0.045^{+0.053}_{-0.043}$	$-9.92^{+0.21}_{-1.42}$
17fy	IIn	09:03:32.47	−21:20:02.73	0.018	0.0182	82.7±5.8	0.140	$9.59^{+0.22}_{-0.00}$	$0.766^{+0.258}_{-0.313}$	$-9.80^{+0.05}_{-0.11}$
17gi	Ibn	14:14:48.94	−29:33:37.01	0.020	—	87.0±22.0	0.057	$8.73^{+0.06}_{-0.13}$	$0.107^{+0.044}_{-0.028}$	$-9.76^{+0.24}_{-0.15}$
17he	II	09:45:48.36	−14:22:05.60	0.008	0.0081	37.4±2.6	0.053	$9.50^{+0.05}_{-0.05}$	$7.096^{+0.811}_{-0.727}$	$-8.65^{+0.05}_{-0.04}$
17ia	IIP	13:10:59.29	+78:24:37.16	0.023	0.0234	100.3±7.1	0.033	$10.41^{+0.01}_{-0.01}$	$2.075^{+0.058}_{-0.052}$	$-10.10^{+0.01}_{-0.01}$
17is	II	02:11:06.94	+03:50:36.63	0.011	0.0105	44.9±3.1	0.036	$9.46^{+0.02}_{-0.13}$	$2.965^{+0.283}_{-1.166}$	$-9.03^{+0.03}_{-0.07}$
17jp	II	02:54:02.09	+02:58:07.71	0.010	0.0102	41.9±2.9	0.095	$10.40^{+0.01}_{-0.16}$	$1.135^{+0.221}_{-0.258}$	$-10.30^{+0.11}_{-0.01}$
17nb	II	07:27:37.32	+35:36:30.64	0.016	—	69.4±21.9	0.048	$8.81^{+0.05}_{-0.06}$	$0.659^{+0.033}_{-0.587}$	$-9.00^{+0.06}_{-0.92}$
17oj	II	21:44:22.95	−29:54:59.30	0.016	0.01874	82.6±22.0	0.040	$9.19^{+0.10}_{-0.12}$	$2.228^{+0.834}_{-0.953}$	$-8.83^{+0.23}_{-0.36}$
17om	II	03:34:11.10	−13:56:09.37	0.08	—	363.9±24.0	0.042	$9.97^{+0.04}_{-0.12}$	$6.546^{+0.420}_{-1.906}$	$-9.27^{+0.10}_{-0.04}$
17os	II	04:33:05.88	−26:07:41.34	0.032	0.0323	138.4±9.8	0.035	$8.74^{+0.03}_{-0.10}$	$0.778^{+0.063}_{-0.668}$	$-8.86^{+0.07}_{-0.79}$
17qp	II	20:28:49.80	−04:22:57.29	0.01[2]	—	43.3±21.7	0.050	$7.02^{+0.01}_{-0.01}$	$0.005^{+0.001}_{-0.001}$	$-8.60^{+0.30}_{-0.18}$
17qt	II	02:27:36.59	−20:42:56.18	0.036	—	158.6±22.5	0.023	$9.68^{+0.04}_{-0.03}$	$1.854^{+0.193}_{-0.354}$	$-9.40^{+0.02}_{-0.05}$
17rl	Ib/c	07:15:00.04	+46:22:43.79	0.045	—	199.5±22.8	0.073	$9.57^{+0.02}_{-0.02}$	$1.343^{+0.140}_{-0.587}$	$-9.42^{+0.03}_{-0.28}$

Name	Class	$\alpha(2000)$	$\delta(2000)$	$z_{\rm sn}$	$z_{\rm host}$	Distance[†] Mpc	E(B-V)	$\log_{10}(\mathrm{M_*})$ $\mathrm{M_\odot}$	SFR $\mathrm{M_\odot\ yr^{-1}}$	sSFR[‡] $\mathrm{yr^{-1}}$
SN2014ce	II	23:27:40.86	+23:35:21.4	0.011000	0.011000	49.00±3.43	0.039	$9.43^{+0.04}_{-0.01}$	$5.598^{+0.832}_{-0.051}$	$-8.70^{+0.01}_{-0.01}$
SN2014cw	II	22:15:26.55	-10:28:34.6	0.006000	—	25.82±21.70	0.051	$7.72^{+0.09}_{-0.07}$	$0.038^{+0.015}_{-0.010}$	$-9.17^{+0.16}_{-0.18}$
SN2014cy	IIP	23:44:16.03	+10:46:12.5	0.005547	0.005547	24.65±1.73	0.049	$10.18^{+0.06}_{-0.17}$	$1.227^{+0.097}_{-0.161}$	$-10.08^{+0.14}_{-0.07}$
SN2014eb	II	09:52:55.58	+42:50:51.1	0.016000	0.016000	73.37±5.14	0.011	$10.46^{+0.05}_{-0.09}$	$1.589^{+0.393}_{-0.195}$	$-10.27^{+0.17}_{-0.08}$
SN2014eh	Ic	20:25:03.86	-24:49:13.3	0.010614	0.010614	49.45±3.46	0.056	$10.61^{+0.08}_{-0.04}$	$13.270^{+1.048}_{-4.019}$	$-9.45^{+0.06}_{-0.36}$
SN2015da	IIn	13:52:24.11	+39:41:28.6	0.00722	0.00722	39.11±2.75	0.013	$9.97^{+0.01}_{-0.01}$	$0.116^{+0.002}_{-0.002}$	$-10.90^{+0.01}_{-0.01}$
SN2015U	Ibn	07:28:53.87	+33:49:10.6	0.01379	0.01379	61.36±4.30	0.051	$10.78^{+0.02}_{-0.04}$	$0.169^{+0.075}_{-0.074}$	$-11.56^{+0.19}_{-0.33}$
LSQ15xp	IIP	11:32:42.79	-16:44:01.2	0.01226	0.01226	57.34±4.07	0.034	$8.79^{+0.01}_{-0.05}$	$1.560^{+0.073}_{-0.134}$	$-8.60^{+0.04}_{-0.03}$
PS15si	IIn	11:10:22.93	-04:21:31.5	0.05390	0.05390	237.74±16.67	0.046	$8.92^{+0.05}_{-0.06}$	$0.522^{+0.113}_{-0.257}$	$-9.20^{+0.05}_{-0.26}$
SN2015V	IIP	17:49:27.05	+36:08:36.0	0.00457	0.00457	26.64±1.87	0.034	$8.53^{+0.07}_{-0.03}$	$0.314^{+0.005}_{-0.005}$	$-9.09^{+0.05}_{-0.01}$
SN2015Y	IIb	09:02:37.87	+25:56:04.2	0.00817	0.00817	39.50±2.77	0.034	$10.37^{+0.01}_{-0.02}$	$0.288^{+0.003}_{-0.009}$	$-10.90^{+0.01}_{-0.01}$
PSNJ14372160+3634018	II	14:37:21.60	+36:34:01.8	0.01409	0.01409	68.72±4.81	0.015	$10.57^{+0.02}_{-0.01}$	$1.406^{+0.003}_{-0.171}$	$-10.50^{+0.01}_{-0.03}$
SN2015Q	Ib	11:47:35.08	+55:58:14.7	0.00803	0.00803	40.99±2.87	0.010	$10.03^{+0.04}_{-0.03}$	$2.254^{+0.526}_{-0.061}$	$-9.69^{+0.09}_{-0.02}$
PSNJ17292918+7542390	II	17:29:29.18	+75:42:39.0	0.00438	0.00438	24.68±1.73	0.036	$9.40^{+0.03}_{-0.01}$	$1.567^{+0.135}_{-0.128}$	$-9.18^{+0.05}_{-0.03}$
PSNJ22460504-1059484	Ib	22:46:05.04	-10:59:48.4	0.00895	0.00895	39.55±2.77	0.054	$10.33^{+0.03}_{-0.25}$	$1.758^{+0.318}_{-0.323}$	$-10.07^{+0.17}_{-0.02}$
SN2015ah	Ib	23:00:24.63	+01:37:36.8	0.01613	0.01613	69.18±4.91	0.071	$9.95^{+0.02}_{-0.10}$	$1.507^{+0.597}_{-0.081}$	$-9.81^{+0.29}_{-0.04}$
PSNJ22411479-2147421	Ib	22:41:14.79	-21:47:42.1	0.01495	0.01495	65.10±4.56	0.026	$9.38^{+0.01}_{-0.01}$	$0.875^{+0.016}_{-0.550}$	$-9.41^{+0.01}_{-0.48}$
SN2015ap	Ib	02:05:13.32	+06:06:08.4	0.01138	0.01138	47.02±3.29	0.038	$9.46^{+0.01}_{-0.04}$	$3.837^{+0.190}_{-0.173}$	$-8.87^{+0.05}_{-0.02}$
SN2015aq	II	09:25:44.53	+34:16:36.1	0.00550	0.00550	28.74±2.01	0.015	$9.05^{+0.01}_{-0.01}$	$0.050^{+0.001}_{-0.001}$	$-10.30^{+0.01}_{-0.01}$
SN2015ay	II	01:09:46.77	+13:18:28.9	0.01407	0.01407	58.61±4.10	0.024	$9.43^{+0.11}_{-0.04}$	$0.708^{+0.021}_{-0.189}$	$-9.58^{+0.05}_{-0.26}$
SN2015as	II	10:08:11.37	+51:50:40.9	0.00365	0.00365	21.30±1.49	0.009	$8.53^{+0.11}_{-0.09}$	$0.479^{+0.023}_{-0.100}$	$-8.81^{+0.10}_{-0.17}$
SN2015ba	II	14:32:29.19	+49:53:34.5	0.00795	0.00795	41.79±2.93	0.016	$10.40^{+0.01}_{-0.01}$	$0.178^{+0.002}_{-0.002}$	$-11.10^{+0.01}_{-0.01}$
SN2015bf	IIn	23:24:49.03	+15:16:52.0	0.01423	0.01423	60.76±4.26	0.059	$10.25^{+0.27}_{-0.01}$	$0.899^{+0.320}_{-0.018}$	$-10.31^{+0.03}_{-0.16}$
SN2016C	IIP	13:38:05.30	-17:51:15.3	0.00452	0.00452	20.32±1.42	0.079	$10.23^{+0.07}_{-0.09}$	$2.655^{+1.272}_{-0.836}$	$-9.85^{+0.32}_{-0.19}$
SN2016P	Ic-BL	13:57:31.10	+06:05:51.0	0.01462	0.01462	71.73±5.02	0.024	$10.23^{+0.01}_{-0.02}$	$4.519^{+0.116}_{-0.113}$	$-9.60^{+0.01}_{-0.01}$
SN2016afa[3]	II	15:36:32.47	+16:36:36.7	0.00653	0.00653	35.70±2.50	0.048	$10.10^{+0.05}_{-0.03}$	$2.239^{+0.440}_{-0.031}$	$-9.80^{+0.10}_{-0.03}$
SN2016bam	II	07:46:52.72	+39:01:21.8	0.01350	0.01335	59.93±4.20	0.045	$10.19^{+0.07}_{-0.02}$	$7.998^{+0.552}_{-1.544}$	$-9.28^{+0.04}_{-0.16}$
SN2016bau	Ib	11:20:59.02	+53:10:25.6	0.00386	0.00386	23.16±1.62	0.015	$9.52^{+0.05}_{-0.02}$	$2.559^{+0.228}_{-0.933}$	$-9.08^{+0.04}_{-0.27}$
SN2016bdu	IIn	13:10:13.95	+32:31:14.1	0.01700	0.01700	73.79±22.07	0.013	$7.04^{+0.09}_{-0.01}$	$0.004^{+0.001}_{-0.002}$	$-8.89^{+0.25}_{-0.66}$

Name	Class	α(2000)	δ(2000)	z_{sn}	z_{host}	Distance[†] Mpc	E(B-V)	$\log_{10}(\mathrm{M}_*)$ $\mathrm{M}_\odot$	SFR $\mathrm{M}_\odot\ \mathrm{yr}^{-1}$	sSFR[‡] yr^{-1}
SN2016bir	IIb	13:14:05.90	+33:55:09.7	0.03535	0.03535	155.61±22.68	0.010	$9.03^{+0.12}_{-0.07}$	$1.766^{+0.062}_{-0.425}$	$-8.77^{+0.07}_{-0.25}$
SN2016bkv	IIb	10:18:19.31	+41:25:39.3	0.00198	0.00198	10.55±0.74	0.015	$8.97^{+0.01}_{-0.01}$	$0.140^{+0.003}_{-0.010}$	$-9.90^{+0.01}_{-0.06}$
SN2016ccm	IIP	14:09:58.91	+17:45:49.4	0.01816	0.01816	87.04±6.09	0.022	$11.17^{+0.01}_{-0.02}$	$0.641^{+0.161}_{-0.016}$	$-11.39^{+0.16}_{-0.01}$
SN2016gfy	II	07:26:45.93	+85:45:51.2	0.00806	0.00806	38.73±2.71	0.088	$10.06^{+0.02}_{-0.04}$	$7.096^{+0.921}_{-1.552}$	$-9.17^{+0.05}_{-0.16}$
SN2016gkg	IIb	01:34:14.46	-29:26:25.0	0.00490	0.00490	20.53±1.44	0.017	$10.75^{+0.06}_{-0.04}$	$3.508^{+1.224}_{-2.501}$	$-10.10^{+0.08}_{-0.76}$
SN2016hbd	IIP	02:56:06.21	+27:42:06.8	0.02159	0.02159	90.00±6.30	0.122	$9.10^{+0.06}_{-0.01}$	$0.482^{+0.121}_{-0.414}$	$-9.43^{+0.08}_{-0.87}$
SN2016hgm	II	01:22:11.73	+00:57:07.8	0.00780	0.00780	32.53±2.28	0.029	$9.53^{+0.01}_{-0.01}$	$1.371^{+0.013}_{-0.019}$	$-9.40^{+0.01}_{-0.01}$
SN2016hvu	IIP	22:35:55.56	+20:19:12.6	0.01852	0.01852	79.75±5.58	0.042	$10.10^{+0.12}_{-0.01}$	$6.310^{+0.675}_{-2.737}$	$-9.30^{+0.01}_{-0.40}$
SN2016idl	IIn	10:06:29.13	+22:26:43.8	0.05800	0.05800	259.67±23.42	0.029	$7.16^{+0.13}_{-0.02}$	$0.038^{+0.001}_{-0.022}$	$-7.67^{+0.12}_{-0.38}$
SN2016iyy	II	06:56:34.62	+46:53:38.6	0.02860	—	125.25±22.46	0.060	$9.15^{+0.08}_{-0.16}$	$0.449^{+0.131}_{-0.094}$	$-9.55^{+0.28}_{-0.15}$
SN2016jft	IIP	09:43:55.87	+41:41:17.8	0.01750	0.01750	79.68±5.59	0.014	$10.37^{+0.01}_{-0.09}$	$1.542^{+0.043}_{-0.435}$	$-10.20^{+0.01}_{-0.01}$
SN2016jfu	IIP	12:54:42.60	+28:56:26.0	0.00829	0.00829	43.50±3.05	0.011	$10.14^{+0.05}_{-0.01}$	$2.799^{+0.006}_{-0.076}$	$-9.70^{+0.01}_{-0.03}$
SN2017ati	IIb	09:49:56.7	+67:10:59.56	0.013050	0.013050	56.47±21.94	0.106	$8.34^{+0.03}_{-0.04}$	$0.224^{+0.036}_{-0.097}$	$-8.96^{+0.02}_{-0.33}$
SN2017ays	II	12:12:45.99	+00:24:28.11	0.020515	0.020515	89.29±22.19	0.025	$8.78^{+0.03}_{-0.04}$	$0.604^{+0.020}_{-0.043}$	$-9.02^{+0.05}_{-0.03}$
SN2017bgu	Ib	16:55:59.47	+42:33:36.01	0.008503	0.008503	45.30±3.17	0.019	$8.33^{+0.03}_{-0.04}$	$0.171^{+0.004}_{-0.124}$	$-9.07^{+0.04}_{-0.66}$
SN2017byz	II	11:23:30.78	-08:39:11.84	0.012285	0.012285	58.52±4.10	0.037	$10.27^{+0.01}_{-0.06}$	$6.310^{+0.001}_{-1.832}$	$-9.50^{+0.01}_{-0.10}$
SN2017cat	II	17:58:52.09	+34:00:09.32	0.024894	0.024894	112.77±7.9	0.042	$10.63^{+0.02}_{-0.01}$	$2.512^{+0.001}_{-0.216}$	$-10.20^{+0.01}_{-0.08}$
SN2017cfa	IIP	09:57:3.89	-07:52:51.14	0.014063	0.014063	65.71±4.62	0.088	$9.58^{+0.04}_{-0.01}$	$1.429^{+0.156}_{-0.033}$	$-9.40^{+0.02}_{-0.01}$
SN2017cik	IIn	07:54:13.07	+21:47:36.49	0.015474	0.015474	67.08±22.02	0.054	$8.48^{+0.09}_{-0.01}$	$0.129^{+0.093}_{-0.003}$	$-9.39^{+0.14}_{-0.01}$
SN2017cjb	II	12:53:50.45	+09:42:17.70	0.009443	0.009443	47.67±3.34	0.020	$9.95^{+0.04}_{-0.02}$	$2.553^{+0.024}_{-0.475}$	$-9.60^{+0.04}_{-0.08}$
SN2017cjd	Ic	11:50:30.17	-18:35:44.96	0.023000	0.023000	100.30±22.27	0.032	$8.89^{+0.08}_{-0.01}$	$0.687^{+0.046}_{-0.426}$	$-9.10^{+0.01}_{-0.49}$
SN2017czd	II	14:51:47.05	+43:38:40.96	0.008410	0.008410	43.81±3.07	0.022	$9.13^{+0.01}_{-0.04}$	$0.280^{+0.001}_{-0.016}$	$-9.70^{+0.03}_{-0.01}$
SN2017dcc	Ic	12:49:4.89	-12:12:22.42	0.024500	0.024500	106.96±22.32	0.041	$9.18^{+0.04}_{-0.07}$	$1.094^{+0.122}_{-0.374}$	$-9.16^{+0.04}_{-0.05}$
SN2017ein	Ic	11:52:53.25	+44:07:26.20	0.002699	0.002699	16.20±1.14	0.019	$9.60^{+0.01}_{-0.26}$	$1.016^{+0.028}_{-0.409}$	$-9.60^{+0.01}_{-0.01}$
SN2017ewx	Ib	14:02:16.52	+07:40:44.21	0.015217	0.015217	74.44±5.21	0.024	$10.39^{+0.03}_{-0.06}$	$0.356^{+0.090}_{-0.039}$	$-10.84^{+0.13}_{-0.06}$
SN2017faa	II	13:19:03.90	-02:30:45.81	0.018480	0.018480	88.81±6.22	0.030	$9.69^{+0.18}_{-0.02}$	$1.875^{+0.120}_{-1.463}$	$-9.43^{+0.03}_{-0.76}$
SN2017fek	IIb	20:21:47.44	-10:43:53.27	0.033000	0.033000	145.01±22.61	0.066	$10.04^{+0.10}_{-0.15}$	$2.410^{+1.146}_{-0.764}$	$-9.71^{+0.34}_{-0.26}$
SN2017fem	IIP	14:32:27.32	+27:25:36.75	0.014337	0.014337	70.23±4.94	0.019	$9.51^{+0.05}_{-0.07}$	$1.047^{+0.660}_{-0.202}$	$-9.51^{+0.33}_{-0.13}$
SN2017gmr	II	02:35:30.15	-09:21:14.95	0.005037	0.005037	20.77±1.46	0.024	$9.59^{+0.08}_{-0.34}$	$3.162^{+1.792}_{-0.599}$	$-9.12^{+0.52}_{-0.13}$

Name	Class	α(2000)	δ(2000)	z_{sn}	z_{host}	Distance[†] Mpc	E(B-V)	$\log_{10}$(M$_*$) M$_\odot$	SFR M$_\odot$ yr^{-1}	sSFR[‡] yr^{-1}
SN2017grn	II	23:31:53.6	-05:00:43.40	0.017312	0.017312	73.59±5.15	0.040	$10.87^{+0.01}_{-0.01}$	$0.575^{+0.761}_{-0.074}$	$-11.14^{+0.44}_{-0.06}$
SN2017hca	II	08:49:41.07	-08:05:31.25	0.013403	0.013403	61.35±4.30	0.037	$8.97^{+0.01}_{-0.03}$	$0.298^{+0.033}_{-0.178}$	$-9.49^{+0.08}_{-0.38}$
SN2017hcc	IIn	00:03:50.58	-11:28:28.78	0.017300	0.017300	75.11±22.08	0.029	$8.45^{+0.02}_{-0.03}$	$0.500^{+0.012}_{-0.090}$	$-8.74^{+0.02}_{-0.10}$
SN2017hcd	IIn	01:42:51.83	+31:28:56.57	0.034847	0.034847	146.17±10.23	0.054	$9.97^{+0.01}_{-0.01}$	$2.512^{+0.106}_{-0.097}$	$-9.60^{+0.02}_{-0.02}$
SN2017hky	II	11:23:30.51	+63:21:59.43	0.009725	0.009725	47.44±3.32	0.011	$8.75^{+0.18}_{-0.01}$	$0.070^{+0.002}_{-0.030}$	$-9.90^{+0.01}_{-0.33}$
SN2017iro	Ib/c	14:06:23.11	+50:43:20.20	0.006191	0.006191	34.32±2.40	0.016	$10.01^{+0.04}_{-0.14}$	$0.859^{+0.305}_{-0.170}$	$-10.09^{+0.21}_{-0.07}$
SN2017ivu[3]	IIP	15:36:32.7	+16:36:19.40	0.006528	0.006528	35.70±2.50	0.048	$10.10^{+0.05}_{-0.03}$	$2.239^{+0.440}_{-0.031}$	$-9.80^{+0.10}_{-0.01}$
SN2017jbj	II	00:48:5.42	-02:47:22.40	0.013492	0.013492	56.42±3.95	0.040	$10.76^{+0.01}_{-0.12}$	$2.280^{+0.158}_{-0.873}$	$-10.38^{+0.06}_{-0.24}$

Notes. SN Type, Host Galaxy, and Discovery Reference columns come from http://www.astronomy.ohio-state.edu/~assassin/sn_list.txt, except where noted.

[†] Hubble flow distances are derived from the host galaxy if available in NED and the uncertainty is derived from the velocity calculator which accounts for the Virgo Cluster, Great Attractor and Shapley Supercluster infall velocities. If a redshift is not available in NED, we search the literature for redshifts derived from a host galaxy spectrum or narrow emission lines from the SN spectrum, in these cases we adopt an 8 per cent uncertainty in the distance (since this is the maximum uncertainty derived for the NED velocity uncertainties). Finally, if the host galaxy redshift is unknown, we use the SN redshift and give the luminosity distance, with an uncertainty on the redshift of z=0.005.

[‡] sSFR is based on the PDF marginalised over all the other parameters in the SED fit. Thus it is slightly different from the derived SFR/Mass.

[1] Host redshift was not obtained from NED, but from another source. For 14m, 14ms and 15nx the redshift was derived from narrow emission lines of the host galaxy in the SN spectrum (Zhang & Wang, 2014; Vallely et al., 2018; Bose et al., 2018b). For 15ed and 15no the redshift was derived from unresolved emission lines in the host galaxy spectrum (Pastorello et al., 2015; Benetti et al., 2018). For 16ll, the redshift was derived from narrow emission lines of the host galaxy in the SN spectrum (Tomasella et al., 2016). For 16ns, there is no available host galaxy redshift, therefore we use the best estimate SN redshift of z=0.038 Turatto et al. (2016). Finally for 17qp, we use the best available redshift estimate from Benetti et al. (2017) with a 50 per cent uncertainty.

[2] For these cases, SN redshift was not obtained from the ASAS-SN website, but from another source. For 16ns, there is no available host galaxy redshift, therefore we use the best estimate SN redshift of z=0.038 Turatto et al. (2016). Finally for 17qp, we use the best available redshift estimate from Benetti et al. (2017) with a 50 per cent uncertainty. All others are derived from spectroscopy of the host galaxies in Taggart et al. (in prep).

[3] SN2016afa and SN2017ivu have the same host galaxy NGC 5962.

Table A.5: Photometric properties of LGRB host galaxies.

LGRB	Class	α(2000)	δ(2000)	z	E(B-V)	$\log_{10}(\mathrm{M_*})$ $\mathrm{M_\odot}$	SFR $\mathrm{M_\odot\ yr^{-1}}$	sSFR[‡] $\mathrm{yr^{-1}}$
980425	SN	19:35:03.12	−52:50:44.88	0.009	0.060	$8.48\,^{+0.40}_{-0.11}$	$0.113\,^{+0.319}_{-0.010}$	$-9.43\,^{+0.23}_{-0.02}$
020903	SN	22:48:42.24	−20:46:09.12	0.251	0.030	$8.65\,^{+0.10}_{-0.23}$	$1.014\,^{+0.465}_{-0.188}$	$-8.66\,^{+0.41}_{-0.19}$
030329A	SN	10:44:49.99	+21:31:17.76	0.169	0.030	$7.71\,^{+0.03}_{-0.08}$	$0.086\,^{+0.016}_{-0.006}$	$-8.79\,^{+0.15}_{-0.06}$
031203	SN	08:02:29.04	−39:51:11.88	0.105	0.937	$8.50\,^{+0.01}_{-0.01}$	$15.520\,^{+0.844}_{-0.318}$	$-7.30\,^{+0.02}_{-0.01}$
050826	SN-less	05:51:01.58	−02:38:35.88	0.296	0.600	$9.80\,^{+0.06}_{-0.11}$	$1.923\,^{+0.764}_{-1.722}$	$-9.61\,^{+0.31}_{-0.80}$
060218	SN	03:21:39.67	+16:52:01.92	0.033	0.150	$7.48\,^{+0.04}_{-0.08}$	$0.039\,^{+0.015}_{-0.011}$	$-8.93\,^{+0.27}_{-0.19}$
060505	SN-less	22:07:03.43	−27:48:51.84	0.089	0.020	$9.57\,^{+0.02}_{-0.06}$	$0.766\,^{+0.097}_{-0.012}$	$-9.69\,^{+0.08}_{-0.03}$
060614	SN-less	21:23:32.11	−53:01:36.12	0.126	0.020	$7.91\,^{+0.07}_{-0.04}$	$0.002\,^{+0.015}_{-0.002}$	$-10.52\,^{+0.69}_{-1.09}$
080517	SN-less	06:48:58.06	+50:44:05.64	0.089	0.110	$9.80\,^{+0.03}_{-0.02}$	$1.500\,^{+0.096}_{-0.249}$	$-9.62\,^{+0.03}_{-0.07}$
100316D	SN	07:10:30.53	−56:15:19.80	0.059	0.120	$8.94\,^{+0.03}_{-0.08}$	$0.762\,^{+0.254}_{-0.086}$	$-9.10\,^{+0.24}_{-0.06}$
111225A	SN-less	00:52:37.22	+51:34:19.5	0.297	0.229	$7.42\,^{+0.23}_{-0.17}$	$0.259\,^{+0.086}_{-0.094}$	$-8.00\,^{+0.31}_{-0.42}$
120422A	SN	09:07:38.42	+14:01:07.68	0.283	0.030	$9.04\,^{+0.03}_{-0.03}$	$1.219\,^{+0.233}_{-0.280}$	$-9.01\,^{+0.09}_{-0.06}$
130702A	SN	14:29:14.78	+15:46:26.40	0.145	0.040	$7.68\,^{+0.03}_{-0.17}$	$0.032\,^{+0.012}_{-0.017}$	$-9.19\,^{+0.26}_{-0.33}$
150518A	SN	15:36:48.27	+16:19:47.1	0.256	0.046	$9.14\,^{+0.08}_{-0.05}$	$1.086\,^{+0.434}_{-0.319}$	$-9.12\,^{+0.25}_{-0.21}$
150818A	SN	15:21:25.43	+68:20:33.0	0.282	0.021	$8.67\,^{+0.13}_{-0.30}$	$1.489\,^{+0.906}_{-0.611}$	$-8.49\,^{+0.51}_{-0.35}$
161219B	SN	06:06:51.43	−26:47:29.52	0.148	0.028	$9.03\,^{+0.07}_{-0.14}$	$0.228\,^{+0.176}_{-0.059}$	$-9.79\,^{+0.49}_{-0.16}$
171205A	SN	11:09:39.52	−12:35:18.34	0.037	0.045	$10.11\,^{+0.02}_{-0.08}$	$2.897\,^{+0.158}_{-0.261}$	$-9.63\,^{+0.03}_{-0.02}$

Notes.[‡]sSFR is based on the PDF marginalised over all the other parameters in the SED fit. Thus it is slightly different from the derived SFR/Mass.

Table A.6: Photometric properties of the SLSN host galaxies.

SLSN	Class	α(2000)	δ(2000)	z	E(B-V)	$\log_{10}\left(\mathrm{M_*}\right)$ $\mathrm{M_\odot}$	SFR $\mathrm{M_\odot\ yr}^{-1}$	sSFR[‡] yr^{-1}
LSQ12dlf	I	01:50:29.80	-21:48:45.4	0.255	0.011	$7.64^{+0.24}_{-0.39}$	$0.030^{+0.022}_{-0.010}$	$-9.17^{+0.73}_{-0.46}$
LSQ14an	I	12:53:47.83	-29:31:27.2	0.163	0.074	$8.20^{+0.08}_{-0.19}$	$1.791^{+2.941}_{-0.358}$	$-7.97^{+0.62}_{-0.13}$
LSQ14mo	I	10:22:41.53	-16:55:14.4	0.256	0.065	$7.64^{+0.16}_{-0.23}$	$0.331^{+0.101}_{-0.133}$	$-8.11^{+0.33}_{-0.39}$
MLS121104	I	02:16:42.51	$+20$:40:08.5	0.30	0.150	$9.28^{+0.14}_{-0.38}$	$3.828^{+2.411}_{-1.485}$	$-8.70^{+0.61}_{-0.37}$
PTF09as	I	12:59:15.864	$+27$:16:40.58	0.187	0.008	$8.52^{+0.11}_{-0.23}$	$0.265^{+0.028}_{-0.029}$	$-9.12^{+0.26}_{-0.14}$
PTF09cnd	I	16:12:08.839	$+51$:29:16.01	0.258	0.021	$8.29^{+0.05}_{-0.04}$	$0.284^{+0.083}_{-0.101}$	$-8.82^{+0.16}_{-0.26}$
PTF10aagc	I	09:39:56.923	$+21$:43:17.09	0.206	0.022	$8.89^{+0.04}_{-0.08}$	$1.076^{+0.215}_{-0.297}$	$-8.82^{+0.10}_{-0.21}$
PTF10bfz	I	12:54:41.288	$+15$:24:17.08	0.169	0.018	$7.59^{+0.16}_{-0.06}$	$1.052^{+0.073}_{-0.526}$	$-7.57^{+0.09}_{-0.45}$
PTF10cwr	I	11:25:46.73	-08:49:41.9	0.231	0.035	$7.71^{+0.17}_{-0.09}$	$0.553^{+0.073}_{-0.395}$	$-7.95^{+0.14}_{-0.72}$
PTF10hgi	I	16:37:47.074	$+06$:12:31.83	0.099	0.074	$7.88^{+0.03}_{-0.04}$	$0.101^{+0.003}_{-0.006}$	$-8.86^{+0.05}_{-0.08}$
PTF10nmn	I	15:50:02.809	-07:24:42.38	0.123	0.138	$7.94^{+0.06}_{-0.11}$	$0.248^{+0.280}_{-0.066}$	$-8.55^{+0.45}_{-0.18}$
PTF10uhf	I	16:52:46.696	$+47$:36:21.76	0.289	0.018	$11.08^{+0.01}_{-0.06}$	$7.278^{+0.596}_{-0.941}$	$-10.21^{+0.03}_{-0.04}$
PTF10vwg	I	18:59:32.881	$+19$:24:25.74	0.1901	0.467	$7.59^{+0.07}_{-0.08}$	$0.078^{+0.030}_{-0.027}$	$-8.58^{+0.02}_{-0.01}$
PTF11dij	I	13:50:57.798	$+26$:16:42.44	0.143	0.011	$7.01^{+0.01}_{-0.01}$	$0.327^{+0.108}_{-0.009}$	$-7.34^{+0.27}_{-0.03}$
PTF11hrq	I	00:51:47.22	-26:25:10.0	0.057	0.012	$8.18^{+0.14}_{-0.06}$	$0.366^{+0.050}_{-0.210}$	$-8.59^{+0.10}_{-0.55}$
PTF11rks	I	01:39:45.528	$+29$:55:27.43	0.19	0.038	$9.02^{+0.03}_{-0.05}$	$0.741^{+0.128}_{-0.056}$	$-9.15^{+0.11}_{-0.05}$
PTF12dam	I	14:24:46.228	$+46$:13:48.64	0.108	0.100	$8.14^{+0.01}_{-0.01}$	$14.490^{+0.578}_{-0.199}$	$-7.00^{+0.01}_{-0.01}$
SN1999as	I	09:16:30.86	$+13$:39:02.2	0.127	0.096	$9.04^{+0.03}_{-0.03}$	$0.379^{+0.170}_{-0.202}$	$-9.49^{+0.18}_{-0.29}$
SN2005ap	I	13:01:14.83	$+27$:43:32.3	0.283	0.026	$7.73^{+0.05}_{-0.09}$	$0.129^{+0.020}_{-0.018}$	$-8.62^{+0.13}_{-0.11}$
SN2007bi	I	13:19:20.00	$+08$:55:44.0	0.128	0.084	$7.55^{+0.14}_{-0.23}$	$0.070^{+0.026}_{-0.030}$	$-8.72^{+0.36}_{-0.38}$
SN2010kd	I	12:08:01.11	$+49$:13:31.1	0.101	0.021	$7.21^{+0.12}_{-0.03}$	$0.135^{+0.014}_{-0.081}$	$-7.50^{+0.09}_{-1.04}$
SN2011ep	I	17:03:41.78	$+32$:45:52.6	0.28	0.020	$7.75^{+0.32}_{-0.26}$	$0.916^{+0.059}_{-0.349}$	$-7.75^{+0.15}_{-0.46}$
SN2011kf	I	14:36:57.53	$+16$:30:56.6	0.245	0.069	$7.52^{+0.11}_{-0.50}$	$0.144^{+0.649}_{-0.021}$	$-8.38^{+1.36}_{-0.15}$
SN2012il	I	09:46:12.91	$+19$:50:28.7	0.175	0.069	$8.11^{+0.02}_{-0.03}$	$0.142^{+0.016}_{-0.012}$	$-8.95^{+0.06}_{-0.11}$
SN2013dg	I	13:18:41.38	-07:04:43.1	0.265	0.042	$7.59^{+0.09}_{-0.02}$	$0.021^{+0.005}_{-0.001}$	$-8.59^{+0.03}_{-0.18}$
SN2015bn	I	11:33:41.57	$+00$:43:32.2	0.11	0.022	$7.75^{+0.21}_{-0.23}$	$0.076^{+0.018}_{-0.072}$	$-8.86^{+0.28}_{-1.37}$
SSS120810	I	23:18:01.82	-56:09:25.7	0.156	0.017	$7.02^{+0.18}_{-0.01}$	$0.562^{+0.362}_{-0.235}$	$-7.22^{+0.21}_{-0.34}$

Photometric properties of the SLSN-I and SLSN-II host galaxies.

SLSN	Class	α(2000)	δ(2000)	z	E(B-V)	$\log_{10}(\mathrm{M_*})$ $\mathrm{M_\odot}$	SFR $\mathrm{M_\odot\ yr^{-1}}$	sSFR[‡] $\mathrm{yr^{-1}}$
PTF09q	I[†]	12:24:50.11	+08:25:58.8	0.09	0.021	$10.45\,^{+0.01}_{-0.01}$	$3.155\,^{+0.007}_{-0.017}$	$-9.90\,^{+0.01}_{-0.01}$
PTF10gvb	I[†]	12:15:32.28	+40:18:09.5	0.098	0.022	$8.76\,^{+0.08}_{-0.17}$	$0.330\,^{+0.097}_{-0.187}$	$-9.25\,^{+0.22}_{-0.37}$
PTF11mnb	I[†]	00:34:13.25	+02:48:31.4	0.0603	0.016	$8.67\,^{+0.06}_{-0.07}$	$0.297\,^{+0.184}_{-0.099}$	$-9.20\,^{+0.28}_{-0.23}$
PTF12gty	I	16:01:15.23	+21:23:17.4	0.1768	0.061	$8.24\,^{+0.07}_{-0.18}$	$0.025\,^{+0.007}_{-0.005}$	$-9.81\,^{+0.13}_{-0.01}$
PTF12hni	I	22:31:55.86	−06:47:49.0	0.1056	0.054	$9.15\,^{+0.05}_{-0.03}$	$0.142\,^{+0.700}_{-0.045}$	$-9.97\,^{+0.66}_{-0.24}$
CSS100217	II	10:29:12.56	+40:42:20.0	0.147	0.013	$9.84\,^{+0.02}_{-0.03}$	$11.510\,^{+1.827}_{-2.175}$	$-9.63\,^{+0.43}_{-0.35}$
CSS121015	II	00:42:44.34	+13:28:26.5	0.286	0.076	$7.91\,^{+0.22}_{-0.29}$	$0.516\,^{+0.195}_{-0.238}$	$-8.21\,^{+0.44}_{-0.46}$
PTF10fel	II	16:27:31.103	+51:21:43.45	0.234	0.017	$9.87\,^{+0.04}_{-0.06}$	$0.863\,^{+0.223}_{-0.259}$	$-9.93\,^{+0.13}_{-0.16}$
PTF10qaf	II	23:35:42.887	+10:46:32.57	0.284	0.070	$9.24\,^{+0.03}_{-0.12}$	$0.498\,^{+0.187}_{-0.022}$	$-9.54\,^{+0.20}_{-0.05}$
PTF10qwu	II	16:51:10.572	+28:18:07.62	0.226	0.040	$7.34\,^{+0.10}_{-0.15}$	$0.230\,^{+0.045}_{-0.072}$	$-7.99\,^{+0.22}_{-0.30}$
PTF10scc	II	23:28:10.495	+28:38:31.10	0.242	0.093	$7.16\,^{+0.01}_{-0.04}$	$0.018\,^{+0.002}_{-0.007}$	$-7.64\,^{+0.10}_{-0.19}$
PTF10tpz	II	21:58:31.74	−15:33:02.6	0.040	0.041	$10.68\,^{+0.10}_{-0.05}$	$0.458\,^{+1.316}_{-0.256}$	$-11.09\,^{+0.69}_{-0.40}$
PTF10yyc	II	04:39:17.297	−00:20:54.5	0.214	0.041	$9.77\,^{+0.04}_{-0.09}$	$0.230\,^{+0.178}_{-0.066}$	$-10.45\,^{+0.38}_{-0.12}$
PTF12gwu	II	15:02:32.876	+08:03:49.47	0.275	0.033	$7.81\,^{+0.19}_{-0.15}$	$0.106\,^{+0.018}_{-0.034}$	$-8.78\,^{+0.21}_{-0.44}$
PTF12mkp	II	08:28:35.092	+65:10:55.60	0.153	0.046	$7.36\,^{+0.16}_{-0.21}$	$0.005\,^{+0.003}_{-0.002}$	$-9.45\,^{+1.11}_{-0.43}$
PTF12mue	II	03:18:51.072	−11:49:13.55	0.279	0.062	$8.76\,^{+0.08}_{-0.12}$	$0.382\,^{+0.288}_{-0.096}$	$-9.17\,^{+0.39}_{-0.20}$
SN1999bd	II	09:30:29.17	+16:26:07.8	0.151	0.096	$9.50\,^{+0.20}_{-0.02}$	$1.380\,^{+0.092}_{-0.650}$	$-9.33\,^{+0.02}_{-0.53}$
SN2003ma	II	05:31:01.88	−70:04:15.9	0.289	0.348	$8.76\,^{+0.03}_{-0.06}$	$14.290\,^{+0.743}_{-0.293}$	$-7.60\,^{+0.08}_{-0.04}$
SN2006gy	II	03:17:27.06	+41:24:19.5	0.019	0.493	$10.76\,^{+0.14}_{-0.04}$	$0.001\,^{+0.001}_{-0.001}$	$-16.48\,^{+0.79}_{-0.73}$
SN2006tf	II	12:46:15.82	+11:25:56.3	0.074	0.023	$7.97\,^{+0.04}_{-0.06}$	$0.075\,^{+0.014}_{-0.011}$	$-9.11\,^{+0.12}_{-0.08}$
SN2007bw	II	17:11:01.99	+24:30:36.4	0.14	0.046	$9.42\,^{+0.03}_{-0.07}$	$1.199\,^{+2.038}_{-1.043}$	$-9.33\,^{+0.46}_{-0.93}$
SN2008am	II	12:28:36.25	+15:35:49.1	0.234	0.078	$9.38\,^{+0.04}_{-0.03}$	$2.761\,^{+0.667}_{-0.706}$	$-8.96\,^{+0.13}_{-0.15}$
SN2008es	II	11:56:49.13	+54:27:25.7	0.205	0.037	$7.02\,^{+0.01}_{-0.01}$	$0.013\,^{+0.005}_{-0.005}$	$-7.78\,^{+0.41}_{-0.59}$
SN2008fz	II	23:16:16.60	+11:42:47.5	0.133	0.132	$7.02\,^{+0.01}_{-0.01}$	$0.011\,^{+0.003}_{-0.008}$	$-8.26\,^{+0.26}_{-0.84}$
SN2009nm	II	10:05:24.54	+51:16:38.7	0.21	0.011	$8.63\,^{+0.34}_{-0.42}$	$0.200\,^{+0.107}_{-0.091}$	$-9.40\,^{+0.67}_{-0.60}$
SN2013hx	II	01:35:32.83	−57:57:50.6	0.13	0.022	$7.49\,^{+0.20}_{-0.14}$	$0.019\,^{+0.008}_{-0.012}$	$-8.66\,^{+0.53}_{-0.99}$

Notes.[†] Possible SLSN-I are indicated
[‡]sSFR is based on the PDF marginalised over all the other parameters in the SED fit. Thus it is slightly different from the derived SFR/Mass.

Bibliography

Adami C., et al., 2006, A&A, 451, 1159

Afflerbach A., Churchwell E., Werner M. W., 1997, ApJ, 478, 190

Aglietta M., et al., 1987, EPL (Europhysics Letters), 3, 1315

Alard C., 2000, A&AS, 144, 363

Anderson J. P., James P. A., 2008, MNRAS, 390, 1527

Anderson J. P., Covarrubias R. A., James P. A., Hamuy M., Habergham S. M., 2010, MNRAS, 407, 2660

Anderson J. P., Habergham S. M., James P. A., Hamuy M., 2012, MNRAS, 424, 1372

Anderson J. P., et al., 2014, ApJ, 786, 67

Anderson J. P., et al., 2018, Nature Astronomy, 2, 574

Ando S., Beacom J. F., Yüksel H., 2005, Phys. Rev. Lett., 95, 171101

Andreoni I., et al., 2020, ApJ, 890, 131

Angus C. R., Levan A. J., Perley D. A., Tanvir N. R., Lyman J. D., Stanway E. R., Fruchter A. S., 2016, MNRAS, 458, 84

Arafune J., Fukugita M., 1987, Phys. Rev. Lett., 59, 367

Arcavi I., et al., 2010, ApJ, 721, 777

Arcavi I., et al., 2012, ApJl, 756, L30

Arcavi I., et al., 2016, ApJ, 819, 35

Arcavi I., McCully C., Hosseinzadeh G., Howell D. A., Valenti S., Trakhtenbrot B., 2017, The Astronomer's Telegram, 10668

Arnett W. D., 1982, ApJ, 253, 785

Arnett W. D., 1987, ApJ, 319, 136

Arnett W. D., Bahcall J. N., Kirshner R. P., Woosley S. E., 1989, ARA&A, 27, 629

Ashall C., et al., 2019, MNRAS, 487, 5824

Baade W., 1943, ApJ, 97, 119

Baade W., Zwicky F., 1934, Proceedings of the National Academy of Science, 20, 254

Bahcall J. N., Dar A., Piran T., 1987, Nature, 326, 135

Baldry I. K., Glazebrook K., Driver S. P., 2008, MNRAS, 388, 945

Baldwin J. A., Phillips M. M., Terlevich R., 1981, PASP, 93, 5

Baltay C., et al., 2013, PASP, 125, 683

Band D., et al., 1993, ApJ, 413, 281

Barbon R., Ciatti F., Rosino L., 1979, A&A, 72, 287

Barkat Z., Rakavy G., Sack N., 1967, Physical Review Letters, 18, 379

Barnsley R. M., Smith R. J., Steele I. A., 2012, Astronomische Nachrichten, 333, 101

Bartunov O. S., Tsvetkov D. Y., Filimonova I. V., 1994, PASP, 106, 1276

Bastian N., Covey K. R., Meyer M. R., 2010, ARA&A, 48, 339

Bazin G., et al., 2009, A&A, 499, 653

Beasor E. R., Davies B., Smith N., van Loon J. T., Gehrz R. D., Figer D. F., 2020, MNRAS, 492, 5994

Becker A., 2015, HOTPANTS: High Order Transform of PSF ANd Template Subtraction (ascl:1504.004)

Belfiore F., et al., 2017, MNRAS, 469, 151

Bellm E. C., et al., 2019, PASP, 131, 018002

Benetti S., et al., 2014, MNRAS, 441, 289

Benetti S., Ochner P., Cappellaro E., Tomasella L., Turatto M., Colombo L., 2017, The Astronomer's Telegram, 11072, 1

Benetti S., et al., 2018, MNRAS, 476, 261

Bersier D., et al., 2006, ApJ, 643, 284

Bertin E., 2010, SWarp: Resampling and Co-adding FITS Images Together (ascl:1010.068)

Bertin E., 2011, in Evans I. N., Accomazzi A., Mink D. J., Rots A. H., eds, Astronomical Society of the Pacific Conference Series Vol. 442, Astronomical Data Analysis Software and Systems XX. p. 435

Bertin E., Arnouts S., 1996, A&AS, 117, 393

Bethe H. A., Wilson J. R., 1985, ApJ, 295, 14

Bianchi L., Herald J., Efremova B., Girardi L., Zabot A., Marigo P., Conti A., Shiao B., 2011, Ap&SS, 335, 161

Bianco F. B., Modjaz M., Oh S. M., Fierroz D., Liu Y. Q., Kewley L., Graur O., 2016, Astronomy and Computing, 16, 54

Bionta R. M., et al., 1987, Phys. Rev. Lett., 58, 1494

Blagorodnova N., et al., 2018, PASP, 130, 035003

Blain A. W., Smail I., Ivison R. J., Kneib J. P., Frayer D. T., 2002, Phys. Rep., 369, 111

Blanton M. R., Kazin E., Muna D., Weaver B. A., Price-Whelan A., 2011, AJ, 142, 31

Bloemen S., Groot P., Nelemans G., Klein-Wolt M., 2015, The BlackGEM Array: Searching for Gravitational Wave Source Counterparts to Study Ultra-Compact Binaries. p. 254

Blondin S., Tonry J. L., 2007, ApJ, 666, 1024

Boissier S., Prantzos N., 2009, A&A, 503, 137

Boquien M., Burgarella D., Roehlly Y., Buat V., Ciesla L., Corre D., Inoue A. K., Salas H., 2019, A&A, 622, A103

Bose S., et al., 2018a, ApJ, 853, 57

Bose S., et al., 2018b, ApJ, 862, 107

Boyle W. S., Smith G. E., 1970, Bell System Technical Journal, 49, 587

Brinchmann J., Charlot S., White S. D. M., Tremonti C., Kauffmann G., Heckman T., Brinkmann J., 2004, MNRAS, 351, 1151

Bromm V., Coppi P. S., Larson R. B., 1999, ApJl, 527, L5

Bruenn S. W., 1985, ApJS, 58, 771

Bruzual G., Charlot S., 2003, MNRAS, 344, 1000

Bufano F., et al., 2010, GRB Coordinates Network, 10543, 1

Bullock J. S., Boylan-Kolchin M., 2017, ARA&A, 55, 343

Bundy K., Ellis R. S., Conselice C. J., 2005, ApJ, 625, 621

Burbidge E. M., Burbidge G. R., Fowler W. A., Hoyle F., 1957, Reviews of Modern Physics, 29, 547

Calzetti D., Armus L., Bohlin R. C., Kinney A. L., Koornneef J., Storchi-Bergmann T., 2000, ApJ, 533, 682

Cameron E., 2011, Publications of the Astronomical Society of Australia, 28, 128

Cano Z., et al., 2017a, A&A, 605, A107

Cano Z., Wang S.-Q., Dai Z.-G., Wu X.-F., 2017b, Advances in Astronomy, 2017, 8929054

Cantiello M., Yoon S. C., Langer N., Livio M., 2007, A&A, 465, L29

Cao Y., et al., 2013, ApJl, 775, L7

Cao Y., Nugent P. E., Kasliwal M. M., 2016, PASP, 128, 114502

Cardamone C., et al., 2009, MNRAS, 399, 1191

Carter B. J., Fabricant D. G., Geller M. J., Kurtz M. J., McLean B., 2001, ApJ, 559, 606

Castro Cerón J. M., Michałowski M. J., Hjorth J., Malesani D., Gorosabel J., Watson D., Fynbo J. P. U., Morales Calderón M., 2010, ApJ, 721, 1919

Cenko S. B., et al., 2006, PASP, 118, 1396

Cenko S. B., Gal-Yam A., Kasliwal M. M., Stern D., Markey K., Alduena E., Alduena A., Kuo S., 2013, GRB Coordinates Network, 14998, 1

Chabrier G., 2003, ApJl, 586, L133

Chambers K. C., et al., 2016, preprint, (arXiv:1612.05560)

Chary R., Elbaz D., 2001, ApJ, 556, 562

Chatzopoulos E., Wheeler J. C., 2012, ApJ, 760, 154

Chen T.-W., et al., 2013, ApJl, 763, L28

Chen T. W., et al., 2015, MNRAS, 452, 1567

Chen T.-W., Smartt S. J., Yates R. M., Nicholl M., Krühler T., Schady P., Dennefeld M., Inserra C., 2017a, MNRAS, 470, 3566

Chen T. W., et al., 2017b, A&A, 602, A9

Chen T.-W., et al., 2017c, ApJl, 849, L4

Chen T.-W., et al., 2017d, GRB Coordinates Network, Circular Service, No. 20380, #1 (2017), 20380

Chen K.-J., Woosley S. E., Whalen D. J., 2020, ApJ, 893, 99

Chevalier R. A., 1977, ARA&A, 15, 175

Chevalier R. A., Irwin C. M., 2011, ApJl, 729, L6

Chomiuk L., et al., 2011, ApJ, 743, 114

Chornock R., et al., 2010, arXiv e-prints, p. arXiv:1004.2262

Chornock R., Berger E., Fox D. B., Fong W., Laskar T., Roth K. C., 2014, arXiv e-prints, p. arXiv:1405.7400

Chrimes A. A., Stanway E. R., Eldridge J. J., 2020, MNRAS, 491, 3479

Chugai N. N., Danziger I. J., 1994, MNRAS, 268, 173

Clausen D., Piro A. L., Ott C. D., 2015, ApJ, 799, 190

Cobb B. E., 2017, GRB Coordinates Network, 22270, 1

Colgate S. A., 1968, Canadian Journal of Physics, 46, S476

Colgate S. A., White R. H., 1966, ApJ, 143, 626

Collins George W. I., Claspy W. P., Martin J. C., 1999, PASP, 111, 871

Conroy C., 2013, ARA&A, 51, 393

Conroy C., Bullock J. S., 2015, ApJl, 805, L2

Conroy C., Gunn J. E., White M., 2009, ApJ, 699, 486

Corsi A., et al., 2016, ApJ, 830, 42

Coughlin M. W., et al., 2019, ApJl, 885, L19

Cowie L. L., Songaila A., Hu E. M., Cohen J. G., 1996, AJ, 112, 839

Crowther P., 2012, Astronomy and Geophysics, 53, 4.30

Crowther P. A., 2013, MNRAS, 428, 1927

Crowther P. A., et al., 2016, MNRAS, 458, 624

Cutri R. M., et al. 2013, VizieR Online Data Catalog, 2328

Cutri R. M., et al. 2014, VizieR Online Data Catalog, 2328

D'Elia V., et al., 2013, GRB Coordinates Network, 15000, 1

D'Elia V., et al., 2018, A&A, 619, A66

Dabringhausen J., Kroupa P., Baumgardt H., 2009, MNRAS, 394, 1529

Dale D. A., et al., 2009, ApJ, 703, 517

De Cia A., et al., 2018, ApJ, 860, 100

Della Valle M., et al., 2006, Nature, 444, 1050

Denicoló G., Terlevich R., Terlevich E., 2002, MNRAS, 330, 69

Dexter J., Kasen D., 2013, ApJ, 772, 30

Dilday B., et al., 2012, Science, 337, 942

Dong S., et al., 2016, Science, 351, 257

Dong S., et al., 2017, The Astronomer's Telegram, 1049

Drake A. J., et al., 2009, ApJ, 696, 870

Drout M. R., et al., 2014, ApJ, 794, 23

Drout M. R., Prieto J. L., Dong S., Shappee B. J., 2017, The Astronomer's Telegram, 10970

Duchêne G., Kraus A., 2013, ARA&A, 51, 269

Dutton A. A., van den Bosch F. C., Dekel A., 2010, MNRAS, 405, 1690

Duyvendak J. J. L., 1942, PASP, 54, 91

Dyer M. J., Dhillon V. S., Littlefair S., Steeghs D., Ulaczyk K., Chote P., Galloway D., Rol E., 2018, in Proc. SPIE. p. 107040C, doi:10.1117/12.2311865

Eftekhari T., et al., 2019, ApJl, 876, L10

Elbaz D., et al., 2007, A&A, 468, 33

Eldridge J. J., 2012, MNRAS, 422, 794

Eldridge J. J., Stanway E. R., 2009, MNRAS, 400, 1019

Eldridge J. J., Fraser M., Smartt S. J., Maund J. R., Crockett R. M., 2013, MNRAS, 436, 774

Eldridge J. J., Fraser M., Maund J. R., Smartt S. J., 2015, MNRAS, 446, 2689

Eldridge J. J., Xiao L., Stanway E. R., Rodrigues N., Guo N. Y., 2018, Publications of the Astronomical Society of Australia, 35, 49

Elias-Rosa N., et al., 2016, MNRAS, 463, 3894

Emerson J., McPherson A., Sutherland W., 2006, The Messenger, 126, 41

Ensman L., Burrows A., 1992, ApJ, 393, 742

Erben T., et al., 2005, Astronomische Nachrichten, 326, 432

Ertl T., Janka H. T., Woosley S. E., Sukhbold T., Ugliano M., 2016, ApJ, 818, 124

Falco E., Berlind P., Challis P., Kirshner R., Prieto J. L., 2016, The Astronomer's Telegram, 8543

Falk S. W., 1978, ApJl, 225, L133

Fatkhullin T. A., Sokolov V. V., Moiseev A. V., Guziy S., Castro-Tirado A. J., 2006, GRB Coordinates Network, 4809, 1

Fazio G. G., et al., 2004, ApJS, 154, 10

Figer D. F., 2005, Nature, 434, 192

Filippenko A. V., 1982, PASP, 94, 715

Filippenko A. V., 1997, ARA&A, 35, 309

Filippenko A. V., et al., 1992, ApJl, 384, L15

Filippenko A. V., Li W. D., Treffers R. R., Modjaz M., 2001, The Lick Observatory Supernova Search with the Katzman Automatic Imaging Telescope. p. 121

Fioc M., Rocca-Volmerange B., 1997, A&A, 500, 507

Flaugher B., 2005, International Journal of Modern Physics A, 20, 3121

Folatelli G., et al., 2014, ApJl, 793, L22

Folatelli G., Bersten M. C., Kuncarayakti H., Benvenuto O. G., Maeda K., Nomoto K., 2015, ApJ, 811, 147

Folatelli G., et al., 2016, ApJl, 825, L22

Fontanot F., De Lucia G., Monaco P., Somerville R. S., Santini P., 2009, MNRAS, 397, 1776

Fowler W. A., Hoyle F., 1964, ApJS, 9, 201

Fremling C., et al., 2016, A&A, 593, A68

Fremling C., Kulkarni S. R., Taggart K., Perley D., 2018, The Astronomer's Telegram, 11615, 1

Fremling C., et al., 2020, ApJ, 895, 32

Frieman J. A., et al., 2008, AJ, 135, 338

Frohmaier C., Sullivan M., Nugent P. E., Goldstein D. A., DeRose J., 2017, The Astrophysical Journal Supplement Series, 230, 4

Fruchter A. S., et al., 2006, Nature, 441, 463

Fryer C. L., 1999, ApJ, 522, 413

Fukuda I., 1982, PASP, 94, 271

Fukugita M., Shimasaku K., Ichikawa T., 1995, PASP, 107, 945

Furlong M., et al., 2015, MNRAS, 450, 4486

Fynbo J. P. U., et al., 2006, Nature, 444, 1047

Fynbo J. P. U., et al., 2009, The Astrophysical Journal Supplement Series, 185, 526

Gal-Yam A., 2012, Science, 337, 927

Gal-Yam A., 2019, ARA&A, 57, 305

Gal-Yam A., Leonard D. C., 2009, Nature, 458, 865

Gal-Yam A., et al., 2006, Nature, 444, 1053

Gal-Yam A., et al., 2007, ApJ, 656, 372

Gal-Yam A., Maoz D., Guhathakurta P., Filippenko A. V., 2008, ApJ, 680, 550

Gal-Yam A., et al., 2009, Nature, 462, 624

Gal-Yam A., et al., 2014, Nature, 509, 471

Galama T. J., et al., 1998, Nature, 395, 670

Galbany L., et al., 2018, ApJ, 855, 107

Garnavich P. M., Tucker B. E., Rest A., Shaya E. J., Olling R. P., Kasen D., Villar A., 2016, ApJ, 820, 23

Gehrels N., et al., 2006, Nature, 444, 1044

Gehrels N., Ramirez-Ruiz E., Fox D. B., 2009, ARA&A, 47, 567

Georgy C., Meynet G., Ekström S., Wade G. A., Petit V., Keszthelyi Z., Hirschi R., 2017, A&A, 599, L5

Gezari S., et al., 2015, ApJ, 804, 28

Ginzburg S., Balberg S., 2012, ApJ, 757, 178

Gomez S., et al., 2019, ApJ, 881, 87

Gorosabel J., et al., 2005, A&A, 444, 711

Graham J. F., Fruchter A. S., 2013, ApJ, 774, 119

Graham M. J., et al., 2019, PASP, 131, 078001

Graur O., Bianco F. B., Huang S., Modjaz M., Shivvers I., Filippenko A. V., Li W., Eldridge J. J., 2017a, ApJ, 837, 120

Graur O., Bianco F. B., Modjaz M., Shivvers I., Filippenko A. V., Li W., Smith N., 2017b, ApJ, 837, 121

Greiner J., et al., 2015, Nature, 523, 189

Groh J. H., Georgy C., Ekström S., 2013, A&A, 558, L1

Gutiérrez C. P., et al., 2018a, Monthly Notices of the Royal Astronomical Society, 479, 3232

Gutiérrez C. P., et al., 2018b, MNRAS, 479, 3232

Hadfield L. J., Crowther P. A., 2006, MNRAS, 368, 1822

Hadjiyska E., et al., 2012, in New Horizons in Time Domain Astronomy. pp 324–326, doi:10.1017/S1743921312000944

Hakobyan A. A., Petrosian A. R., McLean B., Kunth D., Allen R. J., Turatto M., Barbon R., 2008, A&A, 488, 523

Hakobyan A. A., Mamon G. A., Petrosian A. R., Kunth D., Turatto M., 2009, A&A, 508, 1259

Hakobyan A. A., Adibekyan V. Z., Aramyan L. S., Petrosian A. R., Gomes J. M., Mamon G. A., Kunth D., Turatto M., 2012, A&A, 544, A81

Hamanowicz A., Gromadzki M., Wyrzykowski L., Buckley D., 2017, The Astronomer's Telegram, 10424

Hamuy M., Phillips M. M., Suntzeff N. B., Schommer R. A., Maza J., Aviles R., 1996, AJ, 112, 2391

Hanke F., Müller B., Wongwathanarat A., Marek A., Janka H.-T., 2013, ApJ, 770, 66

Harwit M., 1988, Astrophysical Concepts

Heger A., Woosley S. E., 2002, ApJ, 567, 532

Heger A., Fryer C. L., Woosley S. E., Langer N., Hartmann D. H., 2003, ApJ, 591, 288

Heger A., Woosley S. E., Spruit H. C., 2005, ApJ, 626, 350

Hillebrandt W., Niemeyer J. C., 2000, ARA&A, 38, 191

Hirano S., Hosokawa T., Yoshida N., Omukai K., Yorke H. W., 2015, MNRAS, 448, 568

Hirata K., et al., 1987, Phys. Rev. Lett., 58, 1490

Hirschi R., Meynet G., Maeder A., 2005, A&A, 443, 581

Hjorth J., Bloom J. S., 2012, The Gamma-Ray Burst - Supernova Connection. pp 169–190

Hjorth J., et al., 2003, Nature, 423, 847

Hjorth J., et al., 2012, ApJ, 756, 187

Ho A. Y. Q., et al., 2020, ApJ, 902, 86

Hodgkin S. T., Wyrzykowski L., Blagorodnova N., Koposov S., 2013, Philosophical Transactions of the Royal Society of London Series A, 371, 20120239

Holoien T. W.-S., et al., 2017a, MNRAS, 464, 2672

Holoien T. W.-S., et al., 2017b, MNRAS, 467, 1098

Holoien T. W.-S., et al., 2017c, MNRAS, 471, 4966

Holoien T. W.-S., et al., 2019, MNRAS, 484, 1899

Hopkins A. M., 2018, , 35, e039

Horiuchi S., Beacom J. F., Kochanek C. S., Prieto J. L., Stanek K. Z., Thompson T. A., 2011, ApJ, 738, 154

Howell D. A., Global Supernova Project 2017, in American Astronomical Society Meeting Abstracts #230. p. 318.03

Hoyle F., Fowler W. A., 1960, ApJ, 132, 565

Huchra J. P., et al., 2012, ApJS, 199, 26

Humphreys R. M., Davidson K., 1994, PASP, 106, 1025

Humphreys R. M., Davidson K., Smith N., 1999, PASP, 111, 1124

Hunt L. K., et al., 2014, A&A, 565, A112

Ilbert O., et al., 2006, A&A, 457, 841

Inserra C., 2019, Nature Astronomy, 3, 697

Inserra C., et al., 2013, ApJ, 770, 128

Inserra C., et al., 2017, MNRAS, 468, 4642

Inserra C., et al., 2020, arXiv e-prints, p. arXiv:2004.12218

Irani I., et al., 2019, ApJ, 887, 127

Ivezic Z., et al., 2008, Serbian Astronomical Journal, 176, 1

Izotov Y. I., Thuan T. X., Lipovetsky V. A., 1994, ApJ, 435, 647

Izotov Y. I., Schaerer D., Blecha A., Royer F., Guseva N. G., North P., 2006, A&A, 459, 71

Izotov Y. I., Guseva N. G., Fricke K. J., Papaderos P., 2009, A&A, 503, 61

Izotov Y. I., Guseva N. G., Thuan T. X., 2011, ApJ, 728, 161

Izzard R. G., Ramirez-Ruiz E., Tout C. A., 2004, MNRAS, 348, 1215

Izzo L., et al., 2018, A&A, 610, A11

Izzo L., et al., 2019, Nature, 565, 324

James P. A., Anderson J. P., 2006, A&A, 453, 57

Janka H.-T., 2012, Annual Review of Nuclear and Particle Science, 62, 407

Janka H.-T., 2017, Neutrino-Driven Explosions. p. 1095, doi:10.1007/978-3-319-21846-5˙109

Janka H. T., Mueller E., 1996, A&A, 306, 167

Janka H.-T., Melson T., Summa A., 2016, Annual Review of Nuclear and Particle Science, 66, 341

Japelj J., et al., 2016a, A&A, 590, A129

Japelj J., Vergani S. D., Salvaterra R., Hunt L. K., Mannucci F., 2016b, A&A, 593, A115

Japelj J., Vergani S. D., Salvaterra R., Renzo M., Zapartas E., de Mink S. E., Kaper L., Zibetti S., 2018, A&A, 617, A105

Jarrett T. H., Chester T., Cutri R., Schneider S. E., Huchra J. P., 2003, AJ, 125, 525

Johnson B. D., Leja J. L., Conroy C., Speagle J. S., 2019, Prospector: Stellar population inference from spectra and SEDs (ascl:1905.025)

Jones D. O., et al., 2019, The Astronomer's Telegram, 13330, 1

Juneau S., et al., 2005, ApJl, 619, L135

Kaiser N., et al., 2002, in Survey and Other Telescope Technologies and Discoveries. pp 154–164, doi:10.1117/12.457365

Kaiser N., et al., 2010, in Ground-based and Airborne Telescopes III. p. 77330E, doi:10.1117/12.859188

Kanbur S. M., Ngeow C., Nikolaev S., Tanvir N. R., Hendry M. A., 2003, A&A, 411, 361

Kangas T., et al., 2017, MNRAS, 469, 1246

Kasen D., Bildsten L., 2010, ApJ, 717, 245

Kasliwal M. M., et al., 2019, PASP, 131, 038003

Kasliwal M. M., et al., 2020, arXiv e-prints, p. arXiv:2006.11306

Kaspi V. M., Beloborodov A. M., 2017, ARA&A, 55, 261

Kato D., et al., 2007, PASJ, 59, 615

Keller S. C., et al., 2007, Publications of the Astronomical Society of Australia, 24, 1

Kelly P. L., Kirshner R. P., 2012, ApJ, 759, 107

Kelly P. L., Kirshner R. P., Pahre M., 2008, ApJ, 687, 1201

Kelly P. L., Filippenko A. V., Fox O. D., Zheng W., Clubb K. I., 2013, ApJl, 775, L5

Kennicutt Jr. R. C., 1998, ARA&A, 36, 189

Kennicutt Jr. R. C., Keel W. C., van der Hulst J. M., Hummel E., Roettiger K. A., 1987, AJ, 93, 1011

Kewley L. J., Dopita M. A., 2002, ApJS, 142, 35

Kewley L. J., Dopita M. A., Leitherer C., Davé R., Yuan T., Allen M., Groves B., Sutherland R., 2013, ApJ, 774, 100

Kilpatrick C. D., et al., 2017, MNRAS, 465, 4650

Kilpatrick C. D., et al., 2018, MNRAS, 480, 2072

Klebesadel R. W., Strong I. B., Olson R. A., 1973, ApJl, 182, L85

Klein R. I., Chevalier R. A., 1978, ApJl, 223, L109

Knust F., et al., 2017, A&A, 607, A84

Kobulnicky H. A., Kewley L. J., 2004, ApJ, 617, 240

Kochanek C. S., 2019, MNRAS, 483, 3762

Kochanek C. S., Beacom J. F., Kistler M. D., Prieto J. L., Stanek K. Z., Thompson T. A., Yüksel H., 2008, ApJ, 684, 1336

Koen C., 2006, MNRAS, 365, 590

Komatsu E., et al., 2011, ApJS, 192, 18

Kroupa P., 2001, MNRAS, 322, 231

Krühler T., et al., 2015, A&A, 581, A125

Kulkarni S. R., Perley D. A., Miller A. A., 2018, ApJ, 860, 22

Kumar P., Zhang B., 2015, Phys. Rep., 561, 1

Kuncarayakti H., et al., 2018, A&A, 613, A35

Kunth D., Östlin G., 2000, A&A Rev., 10, 1

Lada C. J., Lada E. A., 2003, ARA&A, 41, 57

Laher R. R., et al., 2018, Robotic Telescope, Student Research and Education Proceedings, 1, 329

Law N. M., et al., 2009, Publications of the Astronomical Society of the Pacific, 121, 1395

Lawrence A., et al., 2007, MNRAS, 379, 1599

Le Floc'h E., et al., 2003, A&A, 400, 499

Lee J. C., Kennicutt Robert C. J., Funes S. J. J. G., Sakai S., Akiyama S., 2009, ApJ, 692, 1305

Lee J. C., et al., 2011, ApJS, 192, 6

Leger A., Puget J. L., 1984, A&A, 500, 279

Leloudas G., et al., 2011, A&A, 530, A95

Leloudas G., et al., 2015, MNRAS, 449, 917

Leloudas G., et al., 2016, Nature Astronomy, 1, 0034

Levan A. J., Read A. M., Metzger B. D., Wheatley P. J., Tanvir N. R., 2013, ApJ, 771, 136

Levan A. J., et al., 2014, ApJ, 781, 13

Levan A., Crowther P., de Grijs R., Langer N., Xu D., Yoon S.-C., 2016, Space Sci. Rev., 202, 33

Levesque E. M., Kewley L. J., Graham J. F., Fruchter A. S., 2010, ApJl, 712, L26

Li W., et al., 2003, PASP, 115, 453

Li W., et al., 2011a, MNRAS, 412, 1441

Li W., Chornock R., Leaman J., Filippenko A. V., Poznanski D., Wang X., Ganeshalingam M., Mannucci F., 2011b, MNRAS, 412, 1473

Lilly S. J., Le Fevre O., Hammer F., Crampton D., 1996, ApJl, 460, L1

Liu Y.-Q., Modjaz M., Bianco F. B., 2017, ApJ, 845, 85

Loveday J., 2004, MNRAS, 347, 601

Lundmark K., 1921, PASP, 33, 225

Lunnan R., et al., 2013, ApJ, 771, 97

Lunnan R., et al., 2014, ApJ, 787, 138

Lunnan R., et al., 2015, ApJ, 804, 90

Lunnan R., et al., 2016, ApJ, 831, 144

Lunnan R., et al., 2018, ApJ, 852, 81

Lunnan R., et al., 2020, ApJ, 901, 61

Lupton R., Blanton M. R., Fekete G., Hogg D. W., O'Mullane W., Szalay A., Wherry N., 2004, PASP, 116, 133

Lyman J. D., et al., 2017, MNRAS, 467, 1795

Madau P., Dickinson M., 2014, ARA&A, 52, 415

Madau P., Ferguson H. C., Dickinson M. E., Giavalisco M., Steidel C. C., Fruchter A., 1996, MNRAS, 283, 1388

Maeda K., et al., 2007, ApJ, 666, 1069

Maeda K., et al., 2015, ApJ, 807, 35

Maeder A., Meynet G., 2000, ARA&A, 38, 143

Magnier E. A., et al., 2016, preprint, (arXiv:1612.05242)

Maiolino R., et al., 2008, A&A, 488, 463

Malesani D., et al., 2012, GRB Coordinates Network, 13277, 1

Mangano V., et al., 2007, A&A, 470, 105

Mannucci F., Della Valle M., Panagia N., Cappellaro E., Cresci G., Maiolino R., Petrosian A., Turatto M., 2005, A&A, 433, 807

Maoz D., Sharon K., Gal-Yam A., 2010, ApJ, 722, 1879

Margutti R., et al., 2007, A&A, 474, 815

Margutti R., et al., 2017, ApJ, 836, 25

Margutti R., et al., 2018, ApJ, 864, 45

Marino R. A., et al., 2013, A&A, 559, A114

Marks M., Kroupa P., Dabringhausen J., Pawlowski M. S., 2012, MNRAS, 422, 2246

Martin D. C., et al., 2005, ApJl, 619, L1

Maund J. R., Smartt S. J., Kudritzki R. P., Podsiadlowski P., Gilmore G. F., 2004, Nature, 427, 129

Mayall N. U., Oort J. H., 1942, PASP, 54, 95

Maza J., van den Bergh S., 1976, ApJ, 204, 519

Mazzali P. A., et al., 2006, ApJ, 645, 1323

McLean I. S., et al., 2010, in Ground-based and Airborne Instrumentation for Astronomy III. pp 77351E–77351E–12, doi:10.1117/12.856715

McLean I. S., et al., 2012, in Ground-based and Airborne Instrumentation for Astronomy IV. p. 84460J, doi:10.1117/12.924794

Melandri A., et al., 2012, A&A, 547, A82

Melandri A., et al., 2015, A&A, 581, A86

Metzger B. D., Giannios D., Thompson T. A., Bucciantini N., Quataert E., 2011, MNRAS, 413, 2031

Metzger B. D., Margalit B., Kasen D., Quataert E., 2015, MNRAS, 454, 3311

Metzger B. D., Berger E., Margalit B., 2017, ApJ, 841, 14

Michałowski M. J., et al., 2009, ApJ, 693, 347

Michałowski M. J., et al., 2012, ApJ, 755, 85

Michałowski M. J., et al., 2014, A&A, 562, A70

Michałowski M. J., et al., 2015, A&A, 582, A78

Minkowski R., 1941, PASP, 53, 224

Mirabal N., Halpern J. P., O'Brien P. T., 2007, ApJl, 661, L127

Mitchell P. D., Lacey C. G., Baugh C. M., Cole S., 2013, MNRAS, 435, 87

Modjaz M., Kewley L., Bloom J. S., Filippenko A. V., Perley D., Silverman J. M., 2011, ApJl, 731, L4

Modjaz M., Liu Y. Q., Bianco F. B., Graur O., 2016, ApJ, 832, 108

Modjaz M., Gutiérrez C. P., Arcavi I., 2019, Nature Astronomy, 3, 717

Moriya T., Tominaga N., Tanaka M., Maeda K., Nomoto K., 2010, ApJl, 717, L83

Moriya T. J., Blinnikov S. I., Tominaga N., Yoshida N., Tanaka M., Maeda K., Nomoto K., 2013, MNRAS, 428, 1020

Mould J. R., et al., 2000, ApJ, 529, 786

Müller B., Smartt S. J., 2017, Astronomy and Geophysics, 58, 2.32

Müller B., Heger A., Liptai D., Cameron J. B., 2016, MNRAS, 460, 742

Nagao T., Maiolino R., Marconi A., 2006, A&A, 459, 85

Neill J. D., et al., 2011, ApJ, 727, 15

Nicholl M., Smartt S. J., 2016, MNRAS, 457, L79

Nicholl M., et al., 2013, Nature, 502, 346

Nicholl M., et al., 2014, MNRAS, 444, 2096

Nicholl M., Berger E., Margutti R., Blanchard P. K., Milisavljevic D., Challis P., Metzger B. D., Chornock R., 2017a, ApJl, 835, L8

Nicholl M., Berger E., Margutti R., Blanchard P. K., Guillochon J., Leja J., Chornock R., 2017b, ApJl, 845, L8

Nicholl M., et al., 2020, Nature Astronomy,

Niemela V. S., Ruiz M. T., Phillips M. M., 1985, ApJ, 289, 52

Niino Y., et al., 2017, PASJ, 69, 27

Nikutta R., Hunt-Walker N., Nenkova M., Ivezić Ž., Elitzur M., 2014, MNRAS, 442, 3361

Noeske K. G., et al., 2007, ApJl, 660, L43

Nomoto K., Thielemann F. K., Yokoi K., 1984, ApJ, 286, 644

Norris J. P., Bonnell J. T., 2006, ApJ, 643, 266

Nugent P. E., et al., 2011, Nature, 480, 344

Nugis T., Lamers H. J. G. L. M., 2000, A&A, 360, 227

O'Connor E., Ott C. D., 2011, ApJ, 730, 70

Ochner P., Benetti S., Cappellaro E., Tomasella L., Turatto M., 2017, The Astronomer's Telegram, 11063

Ofek E. O., et al., 2007, ApJl, 659, L13

Oke J. B., Gunn J. E., 1983, ApJ, 266, 713

Oke J. B., et al., 1995, PASP, 107, 375

Omand C. M. B., Kashiyama K., Murase K., 2018, MNRAS, 474, 573

Oppenheimer J. R., Volkoff G. M., 1939, Physical Review, 55, 374

Ostriker J. P., Gunn J. E., 1971, ApJl, 164, L95

Ott C. D., 2009, Classical and Quantum Gravity, 26, 063001

Ovaldsen J.-E., et al., 2007, ApJ, 662, 294

Pagel B. E. J., Edmunds M. G., Blackwell D. E., Chun M. S., Smith G., 1979, MNRAS, 189, 95

Palmerio J. T., et al., 2019, A&A, 623, A26

Pan T., Patnaude D., Loeb A., 2013, MNRAS, 433, 838

Papovich C., Dickinson M., Ferguson H. C., 2001, ApJ, 559, 620

Pastorello A., et al., 2010, ApJl, 724, L16

Pastorello A., et al., 2015, MNRAS, 453, 3649

Peng C. Y., Ho L. C., Impey C. D., Rix H.-W., 2002, AJ, 124, 266

Perley D. A., 2019, PASP, 131, 084503

Perley D. A., et al., 2009, ApJ, 696, 1871

Perley D. A., et al., 2013, ApJ, 778, 128

Perley D. A., et al., 2016a, ApJ, 817, 7

Perley D. A., et al., 2016b, ApJ, 817, 8

Perley D. A., et al., 2016c, ApJ, 830, 13

Perley D. A., et al., 2020, ApJ, 904, 35

Perlmutter S., Muller R. A., Newberg H. J. M., Pennypacker C. R., Sasseen T. P., Smith C. K., 1992, A doubly robotic telescope: the Berkeley Automated Supernova Search. pp 67–71

Persson S. E., et al., 2013, PASP, 125, 654

Petit V., et al., 2017, MNRAS, 466, 1052

Petrosian A., McLean B., Allen R. J., MacKenty J. W., 2007, ApJS, 170, 33

Pettini M., Pagel B. E. J., 2004, MNRAS, 348, L59

Phillips M. M., 1993, ApJl, 413, L105

Piascik A. S., Steele I. A., Bates S. D., Mottram C. J., Smith R. J., Barnsley R. M., Bolton B., 2014, in Proc. SPIE. p. 91478H, doi:10.1117/12.2055117

Podsiadlowski P., 1992, PASP, 104, 717

Podsiadlowski P., Joss P. C., Hsu J. J. L., 1992, ApJ, 391, 246

Popov D. V., 1993, ApJ, 414, 712

Pozanenko A., Mazaeva E., Sergeev A., Reva I., Volnova A., Klunko E., Korobtsev I., 2015, GRB Coordinates Network, Circular Service, No. 17903, #1 (2015), 17903

Prajs S., et al., 2017, MNRAS, 464, 3568

Prantzos N., Boissier S., 2003, A&A, 406, 259

Prentice S., et al., 2017, The Astronomer's Telegram, 11060, 1

Prieto J. L., Stanek K. Z., Beacom J. F., 2008, ApJ, 673, 999

Prieto J. L., et al., 2012, ApJ, 745, 70

Prochaska J. X., et al., 2004, ApJ, 611, 200

Pursiainen M., et al., 2018, MNRAS, 481, 894

Quimby R. M., Aldering G., Wheeler J. C., Höflich P., Akerlof C. W., Rykoff
E. S., 2007, ApJl, 668, L99

Quimby R. M., et al., 2011, Nature, 474, 487

Quimby R. M., Yuan F., Akerlof C., Wheeler J. C., Warren M. S., 2012, AJ, 144,
177

Quimby R. M., Yuan F., Akerlof C., Wheeler J. C., 2013, MNRAS, 431, 912

Quimby R. M., et al., 2018, ApJ, 855, 2

Rakavy G., Shaviv G., 1967, ApJ, 148, 803

Rau A., et al., 2009, PASP, 121, 1334

Rest A., et al., 2011, ApJ, 729, 88

Richardson D., Jenkins Robert L. I., Wright J., Maddox L., 2014, AJ, 147, 118

Riess A. G., et al., 1998, AJ, 116, 1009

Rossi A., et al., 2014, A&A, 572, A47

Rousseau J., Martin N., Prévot L., Rebeirot E., Robin A., Brunet J. P., 1978,
A&AS, 31, 243

Saio H., Kato M., Nomoto K., 1988, ApJ, 331, 388

Sako M., et al., 2008, AJ, 135, 348

Salim S., et al., 2007, ApJS, 173, 267

Salim S., et al., 2016, ApJS, 227, 2

Salpeter E. E., 1955, ApJ, 121, 161

Sana H., et al., 2012, Science, 337, 444

Sanchez-Ramirez R., et al., 2012, GRB Coordinates Network, 13281, 1

Sánchez S. F., et al., 2014, A&A, 563, A49

Sanders D. B., Mirabel I. F., 1996, ARA&A, 34, 749

Sanders N. E., et al., 2012, ApJ, 758, 132

Sanduleak N., 1970, Contributions from the Cerro Tololo Inter-American Observatory, 89

Savaglio S., 2006, New Journal of Physics, 8, 195

Schady P., 2017, Royal Society Open Science, 4, 170304

Schawinski K., et al., 2008, Science, 321, 223

Schirmer M., 2013, ApJS, 209, 21

Schlafly E. F., Finkbeiner D. P., 2011, ApJ, 737, 103

Schneider N., et al., 2015, A&A, 575, A79

Schulze S., et al., 2014, A&A, 566, A102

Schulze S., et al., 2018, MNRAS, 473, 1258

Scoville N., et al., 2007, ApJS, 172, 1

Sedgwick T. M., Baldry I. K., James P. A., Kelvin L. S., 2019, MNRAS, 484, 5278

Shappee B. J., et al., 2014, ApJ, 788, 48

Shu F. H., Adams F. C., Lizano S., 1987, ARA&A, 25, 23

Silverman J. M., et al., 2013, ApJS, 207, 3

Smartt S. J., 2009, ARA&A, 47, 63

Smartt S. J., 2015, Publications of the Astronomical Society of Australia, 32, e016

Smith N., 2014, ARA&A, 52, 487

Smith N., 2017, Philosophical Transactions of the Royal Society of London Series A, 375, 20160268

Smith N., et al., 2007, ApJ, 666, 1116

Smith N., Chornock R., Silverman J. M., Filippenko A. V., Foley R. J., 2010, ApJ, 709, 856

Smith N., Li W., Filippenko A. V., Chornock R., 2011, MNRAS, 412, 1522

Sobral D., Best P. N., Smail I., Mobasher B., Stott J., Nisbet D., 2014, MNRAS, 437, 3516

Soderberg A. M., et al., 2004, ApJ, 606, 994

Soderberg A. M., et al., 2008, Nature, 453, 469

Soderberg A. M., et al., 2010, Nature, 463, 513

Sollerman J., et al., 2006, A&A, 454, 503

Sorokina E., Blinnikov S., Nomoto K., Quimby R., Tolstov A., 2016, ApJ, 829, 17

Soumagnac M. T., et al., 2020, arXiv e-prints, p. arXiv:2001.05518

Spergel D., et al., 2015, arXiv e-prints, p. arXiv:1503.03757

Stanek K. Z., 2017, Transient Name Server Discovery Report, 2017-1398, 1

Stanek K. Z., et al., 2003, ApJl, 591, L17

Stanway E. R., Levan A. J., Tanvir N., Wiersema K., van der Horst A., Mundell C. G., Guidorzi C., 2015, MNRAS, 446, 3911

Stanway E. R., Eldridge J. J., Becker G. D., 2016, MNRAS, 456, 485

Starling R. L. C., et al., 2011, MNRAS, 411, 2792

Steele I. A., et al., 2004, The Liverpool Telescope: performance and first results. pp 679–692, doi:10.1117/12.551456

Steele I. A., Bates S. D., Gibson N., Keenan F., Meaburn J., Mottram C. J., Pollacco D., Todd I., 2008, in Proc. SPIE. p. 70146J, doi:10.1117/12.787889

Steidel C. C., Pettini M., Hamilton D., 1995, AJ, 110, 2519

Stein R., et al., 2020, arXiv e-prints, p. arXiv:2005.05340

Stoll R., Prieto J. L., Stanek K. Z., Pogge R. W., 2013, ApJ, 773, 12

Strolger L.-G., et al., 2015, ApJ, 813, 93

Sukhbold T., Woosley S. E., 2014, ApJ, 783, 10

Sullivan M., et al., 2006, ApJ, 648, 868

Suzuki A., Maeda K., Shigeyama T., 2019, ApJ, 870, 38

Svensson K. M., Levan A. J., Tanvir N. R., Fruchter A. S., Strolger L.-G., 2010, MNRAS, 405, 57

Szécsi D., Langer N., Yoon S.-C., Sanyal D., de Mink S., Evans C. J., Dermine T., 2015, A&A, 581, A15

Taddia F., et al., 2018, A&A, 609, A136

Taggart K., Perley D., 2019, arXiv e-prints, p. arXiv:1911.09112

Terlevich R., Melnick J., Masegosa J., Moles M., Copetti M. V. F., 1991, A&AS, 91, 285

Thöne C. C., et al., 2008, ApJ, 676, 1151

Thöne C. C., et al., 2011, Nature, 480, 72

Thöne C. C., de Ugarte Postigo A., García-Benito R., Leloudas G., Schulze S., Amorín R., 2015, MNRAS, 451, L65

Thöne C. C., et al., 2017, A&A, 599, A129

Tissera P. B., Rosas-Guevara Y., Bower R. G., Crain R. A., del P Lagos C., Schaller M., Schaye J., Theuns T., 2019, MNRAS, 482, 2208

Tomasella L., et al., 2016, The Astronomer's Telegram, 9610, 1

Tonry J. L., et al., 2018, PASP, 130, 064505

Toy V. L., et al., 2016, ApJ, 818, 79

Tremonti C. A., et al., 2004, ApJ, 613, 898

Trimble V., 1988, Reviews of Modern Physics, 60, 859

Tucker M. A., et al., 2020, MNRAS, 493, 1044

Turatto M., Benetti S., Tomasella L., Cappellaro E., Elias-Rosa N., Ochner P., Terreran G., 2016, The Astronomer's Telegram, 9829, 1

Ugliano M., Janka H.-T., Marek A., Arcones A., 2012, ApJ, 757, 69

Vallely P. J., et al., 2018, MNRAS, 475, 2344

Van Dyk S. D., Peng C. Y., Barth A. J., Filippenko A. V., 1999, AJ, 118, 2331

Van Dyk S. D., et al., 2018, ApJ, 860, 90

Vanbeveren D., Mennekens N., Van Rensbergen W., De Loore C., 2013, A&A, 552, A105

Vergani S. D., et al., 2015, A&A, 581, A102

Villar V. A., Nicholl M., Berger E., 2018, ApJ, 869, 166

Vink J. S., de Koter A., Lamers H. J. G. L. M., 2001, A&A, 369, 574

Volnova A., et al., 2017, GRB Coordinates Network, Circular Service, No. 20442, #1 (2017), 20442

Vreeswijk P. M., et al., 2017, ApJ, 835, 58

Wainwright C., Berger E., Penprase B. E., 2007, ApJ, 657, 367

Wang J., et al., 2018, ApJ, 867, 147

Watson D., et al., 2011, ApJ, 741, 58

Weaver T. A., Zimmerman G. B., Woosley S. E., 1978, ApJ, 225, 1021

Weidner C., Kroupa P., Pflamm-Altenburg J., 2011, MNRAS, 412, 979

Werner M. W., et al., 2004, ApJS, 154, 1

Whelan J., Iben Icko J., 1973, ApJ, 186, 1007

Whitworth A., 1979, MNRAS, 186, 59

Wiersema K., et al., 2012, GRB Coordinates Network, 13276, 1

Williams R. E., et al., 1996, AJ, 112, 1335

Wilson J. R., 1985, in Numerical Astrophysics. p. 422

Wilson J. C., et al., 2003, in Iye M., Moorwood A. F. M., eds, Society of Photo-Optical Instrumentation Engineers (SPIE) Conference Series Vol. 4841, Proc. SPIE. pp 451–458, doi:10.1117/12.460336

Wiseman P., et al., 2020, MNRAS, 495, 4040

Wolf C., Podsiadlowski P., 2007, MNRAS, 375, 1049

Wolf C. J. E., Rayet G., 1867, Academie des Sciences Paris Comptes Rendus, 65, 292

Wongwathanarat A., Müller E., Janka H. T., 2015, A&A, 577, A48

Woosley S. E., 1988, ApJ, 330, 218

Woosley S. E., 1993, ApJ, 405, 273

Woosley S. E., 2010, ApJl, 719, L204

Woosley S. E., 2017, ApJ, 836, 244

Woosley S. E., Bloom J. S., 2006, ARA&A, 44, 507

Woosley S. E., Heger A., 2005, in Humphreys R., Stanek K., eds, Astronomical Society of the Pacific Conference Series Vol. 332, The Fate of the Most Massive Stars. p. 407

Woosley S. E., Pinto P. A., Martin P. G., Weaver T. A., 1987, ApJ, 318, 664

Woosley S. E., Heger A., Weaver T. A., 2002, Reviews of Modern Physics, 74, 1015

Woosley S. E., Blinnikov S., Heger A., 2007, Nature, 450, 390

Wright E. L., et al., 2010, AJ, 140, 1868

Xhakaj E., Rojas-Bravo C., Foley M. M., Kilpatrick C. D., Pan Y.-C., Foley R. J., 2017, The Astronomer's Telegram, 10620

Yan L., et al., 2015, ApJ, 814, 108

Yan L., et al., 2017, ApJ, 848, 6

Yao Y., et al., 2019, ApJ, 886, 152

Yaron O., Gal-Yam A., 2012, PASP, 124, 668

Yasuda N., et al., 2001, AJ, 122, 1104

Yoon S.-C., Langer N., 2005, A&A, 443, 643

Yoon S.-C., Langer N., Norman C., 2006, A&A, 460, 199

York D. G., et al., 2000, AJ, 120, 1579

Yoshida T., Okita S., Umeda H., 2014, MNRAS, 438, 3119

Young D. R., et al., 2010, A&A, 512, A70

Yusof N., et al., 2013, MNRAS, 433, 1114

Zackay B., Ofek E. O., Gal-Yam A., 2016, ApJ, 830, 27

Zhang J., Wang X., 2014, The Astronomer's Telegram, 6827, 1

Zhao F.-Y., Strom R. G., Jiang S.-Y., 2006, , 6, 635

Zinnecker H., Yorke H. W., 2007, ARA&A, 45, 481

Zwicky F., 1938, PASP, 50, 215

Zwicky F., 1965, ApJ, 142, 1293

de Nisco K. R., Bruenn S. W., Mezzacappa A., 1998, in Mezzacappa A., ed.,
Stellar Evolution, Stellar Explosions and Galactic Chemical Evolution. p. 571
(arXiv:astro-ph/9808048)

de Ugarte Postigo A., et al., 2015, GRB Coordinates Network, Circular Service,
No. 18213, #1 (2015), 18213

de Ugarte Postigo A., et al., 2016, GRB Coordinates Network, Circular Service,
No. 20342, #1 (2016), 20342

de Ugarte Postigo A., Izzo L., Kann D. A., Thoene C. C., Pesev P., Scarpa R.,
Perez D., 2017, GRB Coordinates Network, 22204, 1

de Vaucouleurs G., Corwin H. G. J., 1985, ApJ, 295, 287

van Dokkum P. G., 2001, PASP, 113, 1420

van Dyk S. D., 1992, AJ, 103, 1788

van Velzen S., et al., 2020, arXiv e-prints, p. arXiv:2001.01409

van Zee L., Skillman E. D., Salzer J. J., 1998, AJ, 116, 1186

van den Heuvel E. P. J., Portegies Zwart S. F., 2013, ApJ, 779, 114